UNIVERSIDADE DA BEIRA INTERIOR
Engenharia

Project and Validation of an Electromagnetic Field Generator for MECSE CubeSat under Controlled Environment

(versão corrigida após defesa)

Paulo Jorge Ferreira

Dissertação para a obtenção do Grau de Mestre em
Engenharia Aeronáutica
(Ciclo de estudos integrado)

Orientadores: Profª Doutora Anna Guerman
Engenheiro Paulo Figueiredo
Co-orientadores: Prof. Doutor António Espírito Santo
Engenheiro André João

Covilhã, dezembro de 2018

Acknowledgments

First and foremost, I would like to thank the two greatest women I have known in my life for all the support they have given me throughout every good and bad moment, my mother Luísa and my sister Sílvia. My father, Bernardino, my biggest example, I've always tried to emulate you throughout all my actions. I am the man that I am today because of you. Thank you for your teachings, support and love. I am proud to be your son.

I wouldn't be here today without the help and support I received from Professor Anna Guerman and Professor António Espírito Santo. Thank you for pushing me forward, the guidance and all the essential lessons throughout this wonderful phase that was creating and finishing this dissertation.

Likewise, a wholehearted thank you to my tutor at CEiiA Paulo Figueiredo, his tireless attitude, passion and brilliance never cease to amaze me. Also, my mentor João André whose eagerness for discovery is commendable. Both of you inspire me to improve myself not only as a researcher but also as a professional. For all the advices, assistance, encouragement and patience. Your tutelage will never be forgotten.

As such, I would also like to thank CEiiA's academy, especially Madalena Pinheiro and Inês Martins for the opportunity to work with CEiiA and for all the support they have given me. Working with you and the whole Sea and Space team has made me grow as a professional and a Man. Also, I can not forget the people who worked alongside me. Alexandre, André, Gonçalo, Miguel, Oleh, Luís and Rafael, thank you for all the support and positive energy you gave me.

My friends, my closest anchor in all aspects, by accompanying me through and through, every up and every down that this journey was. I will always carry you with me. I know I can always count on you to be there for me and that distance is inconsequential. To Ana, Bruna, Bruno, Coelho, Daniel, Gonçalo, Luís, Maria, Nelson, Nuno, Pedro, Rodolfo and Romeiro I am honored to have you in my life. Huge thanks to Luis Reis e Gabriel Carrolo, your patience and energy while working with me, were fundamental.

Professor Paulo Fael, Rui, Lucas, Miguel and Alexandre, I will forever be in your debt, for every hour, every sweat and effort you have put in helping me with my experimental activity. Thank you for all the laughs and support amidst the adversity.

For the privilege of sharing the best stages and playing music along side you all, to Desertuna, Tuna Académica da Universidade da Beira Interior. To all its members, I will never stop praising you. I will always acknowledge the values this association taught me, the skills I developed, every improvement on myself that arose as a direct consequence of every situation I've been through all because of every single one of you.

Dedication

This M. Sc. Thesis is dedicated to the two women of my life…

… to my beloved Mother, Maria Luísa Morais Ferreira
… to my dear Sister, Sílvia Margarida Ferreira

“To the American Red Cross, New York City.

The retrospect is glorious, the prospect is inspiring: Much might be said of both. But one idea dominates my mind. This — my best, my dearest — is for your noble cause.

I have observed electrical actions, which have appeared inexplicable. Faint and uncertain though they were, they have given me a deep conviction and foreknowledge, that ere long all human beings on this globe, as one, will turn their eyes to the firmament above, with feelings of love and reverence, thrilled by the glad news: "Brethren! We have a message from another world, unknown and remote. It reads: one… two… three…"

Christmas 1900

Nikola tesla”

Resumo

Durante a fase de reentrada atmosférica, o blackout de comunicações entre o veículo espacial e o centro de controlo ou satélite, é um fenómeno comum de todas as missões aeroespaciais. Enquanto o veículo espacial se desloca a velocidades hipersónicas em relação à atmosfera, o ar é comprimido e aquecido, gerando uma onda de choque na frente do veículo, assim como uma camada de plasma em torno do mesmo. À medida que a plataforma aeroespacial se move em direção ao planeta, essa camada de plasma irá tornar-se cada vez mais densa, causando a interrupção ou atenuação significativa das comunicações, levando mesmo ao blackout total. O método da janela magnética sugere a aplicação de um campo magnético, suficientemente robusto, de forma a manipular o blackout criando assim uma janela de comunicação.

Esta dissertação é dedicada à análise da carga útil da missão MECSE CubeSat, atualmente em desenvolvimento em Portugal, por uma equipa conjunta da UBI (Universidade da Beira Interior) e do CEiiA (Centro de Engenharia e Desenvolvimento de Produto). O objetivo da missão é realizar diversas medições das propriedades da camada de plasma em torno de uma plataforma CubeSat 3U e manipular essas propriedades através de um campo magnético estático a bordo. De forma a manipular a camada de plasma, será proposto o estudo analítico, numérico e experimental acerca do comportamento do campo magnético (B), em função da distância à superfície da aeronave. À medida que se afasta da superfície do gerador de campo magnético a magnitude da densidade do fluxo magnético diminui, convergindo para um estado neutro, igual a zero. Através do software FEMM 4.2 ™ é criado um modelo cilíndrico gerador de campo magnético, que fornece 0.0375 tesla a uma distância de 25 mm da sua superfície; a configuração é idealizada de forma a reduzir a potência requerida. Na fase de design, foram considerados materiais com alta permeabilidade para o núcleo (Ferro Puro) e de alta condutividade para o enrolamento (Fio de Cobre). O número de voltas e a corrente induzida determinam a magnitude da densidade do fluxo magnético. A análise das propriedades geométricas e das características dos materiais, permite determinar a massa final do gerador, de acordo com os requisitos de massa da missão MECSE CubeSat (3U com menos de 4 kg, carga útil 1,2 kg).

Posteriormente, o modelo é construído em laboratório e a densidade de fluxo magnético é medida em diferentes posições, com o objetivo de validar o modelo analítico de determinação de massa do gerador e os resultados numéricos do software FEMM 4.2 ™ para restrições magnéticas. Finalmente, esta dissertação discute a possibilidade de mitigar o blackout criando um gerador de campo magnético compatível com uma unidade dos 3Us do MECSE CubeSat.

Palavras-chave

Reentrada atmosférica; Mitigação de plasma; Comunicação Blackout de reentrada; MECSE CubeSat; Manipulação de campo magnético; Densidade do fluxo magnético.

Abstract

One of the major concerns of the descent phase of spacecraft missions are problems on communication with spacecraft that appear during its atmospheric re-entry. While the spacecraft moves at hypersonic velocity with respect to the atmosphere, the air is compressed and heated, generating a shock wave in front of the vehicle, and a plasma layer around it. As the spacecraft moves towards the planet, this plasma layer becomes increasingly dense causing communications disruption, significant attenuation or even total communications blackout. Applying the magnetic window method which suggests the use of a static magnetic field to open communication window, it is possible to manipulate the blackout.

This dissertation is dedicated to the analysis of the payload for MECSE CubeSat mission currently under development in Portugal by a joint team of the UBI (University of Beira Interior) and CEiiA (Centre of Engineering and Product Development). The mission goal is to perform several measurements of the properties of the plasma layer around a 3U CubeSat and to manipulate these properties generating a static magnetic field on board. In order to manipulate the plasma layer, an analytical, numerical, and experimental study is performed to examine the behavior of the magnetic field (B), as a function of the distance from the magnetic field generator to the spacecraft surface. The strength of the magnetic flux density decreases as it moves away from the surface of the model, converging to a neutral state equal to zero. The FEMM 4.2™ open source software is used to create a model of an axisymmetric generator that provides 0.0375 tesla at a distance of 25mm from the generator surface; the configuration is selected to reduce the power demand. In the design phase, materials with high permeability for the core (Pure Iron) and for the winding with high conductivity (Copper Wire) are considered. The number of turns and current determine the magnitude of the magnetic flux density. Analysis of the construction and design parameters, in order to determine the final mass of the generator, matching MECSE CubeSat Experiment mass requirements (3U under 4 kg and 1,2 kg for the payload).

After the design, a laboratory model is built, and the magnetic field is measured in different locations in order to validate the analytical model of the generator mass determination and FEMM 4.2™ software for magnetic constraints. Finally, this dissertation discusses the possibility to mitigate the blackout by creating a robust magnetic field generator capable to fit in one unit of the 3Us of the MECSE CubeSat.

Keywords

Atmospheric re-entry; Plasma mitigation; Re-entry communication Blackout; MECSE CubeSat; Magnetic Field manipulation; Magnetic flux density.

Contents

List of Figures

List of Tables

List of Acronyms

ABS	Acrylonitrile Butadiene Styrene
AWG	American Wire Gauge
C-MAST	Center for mechanical and Aerospace Science and Technologies
CAD	Computer Aided Design
CEiiA	Center of Engineering and Product Development
C-MAST	Center for Mechanical and Aerospace Science and Technologies
ECSS	European Cooperation for Space Standardization
EHD	ElectroHydroDynamics
EDR	Electron Density Reduction
EMF	Electromotive Force
EMG	Electromagnetic Field Generator
ENVISENSE	Environmental Sensors
ESA	European Space Agency
EUV	Extreme UltraViolet
FEM	Finite Element Method
FEMM	Finite Element Method Magnetics
FUV	Far UltraViolet
GNSS	Global Navigation Satellite System
GPS	Global Positioning System
LEO	Low Earth Orbit
LEOP	Early Orbit Phase
LP	Langumir Probe
MECSE	Magneto/Electrohydrodynamics CubeSat Experiment
MHD	MagnetoHydroDynamics
MMF	MagnetoMotive Force
MMS	Magnetospheric MultiScale
mNLP	Multi Needle Langumir Probe
NASA	National Aeronautics and Space Administration
O	Orbital Re-entry Experiment
P-POD	Poly Picosatellite Orbital Deployer
PDS	Plasma Dynamics Study
PL	Payload
PLME	Plasma Layer Mitigation Experiment
RAA	Remote Antenna Assemblies
RAM	Radio Attenuation Measurments
RF	Radio Frequancy
SMO	Secondary Mission Objective
STEM	Science, Technology, Engineering and Math
SWG	Standard Wire Gauge
TTC	Telemetry, Tracking and Command
UBI	Universidade da Beira Interior
UHF	Ultra High Frequency
USA	United States of America
U	CubeSat Unit
UV	UltraViolet

Nomenclature

A_c	Coercivity
Ar	Argon
B	Magnetic Flux Density
D	Electric Flux Density
D_{real}	Real Diameter
$D_{theoretical}$	Theoretical Diameter
e	Eccentricity
E	Electric Filed Intensity
EDR	Electron Density Reduction
Fr	Frequency
H(Vector)	Magnetic Field Intensity Vector
He	Helium
I	Current in the Wire
J(vetor)	Current Density Vector
Kr	Krypton
L	Length of the Solenoid
mair	Mass of Air
mcore	Total Mass of the Case Study Core
mpure iron	Mass of Pure Iron
mWire	Represents the Total Mass of Copper Wire Used in the Winding Process
N	North
N	Number of Turns
Ne	Neon
p	Pressure
Pcircle (1st turn)	Represents the Perimeter of the First Turn
Pcircle (2nd turn)	Represents the Perimeter of the Second Turn
S	South
Sm	Specific Mass
T	Temperature
Vcoil	Coil Volume
Vcore	Core Volume
Vwire	Wire Volume
W	Width
Xe	Xenon

Greek Letters

$\o_h$	Relative Hysteresis Lag
$\varepsilon0$	Electric Permittivity of Vacuum
ε	Electric Permittivity
εr	Relative Electric Permittivity
$\eta0$	Initial Electron Density of Plasma
$\eta critical$	Critical Electron Density of Plasma
μ	Permeability
$\mu0$	Permeability of Vaccum
μr	Relative Permeability
ρE	Electrical Restivity
ρch	Carge Density
σ	Electrical Conductivity
υ	Reluctivity Tensor
$\upsilon0$	Reluctivity of Vaccum
υr	Relative Reluctivity

Chapter 1

1 Introduction

1.1 Motivation

The magnetosphere is the region around the planet dominated by its magnetic field. But not all magnetospheres are created equal. Venus and Mars do not have magnetospheres at all, while the other planets have ones that are surprisingly different from Earth's in several aspects [1]. Earth's magnetosphere is part of a dynamic, interconnected system which has played a vital part in our planet's ecosystem. In fact, life on Earth was initially developed and continues to be sustained under the protection of this magnetic environment. Consequently, it is essential to comprehend the relationship between the magnetosphere and the space environment to prevent future catastrophes assuring the continuity of biodiversity on Earth [2].

Several space missions implemented by NASA (National Aeronautics and Space Administration) and ESA (European Space Agency) aim to study the Earth's magnetosphere in order to better understand its role in our space environment. The Magnetospheric MultiScale mission program, or MMS, is a solar-terrestrial probe constellation from USA launched on March 12, 2015 that orbits Earth. The MMS mission consists of four identically instrumented spacecraft that work together to study a little-understood phenomenon called magnetic reconnection: the explosive phenomenon that can send powerful bursts of particles hurtling towards Earth, potentially damaging satellites. The process of magnetic reconnection is fundamental to our understanding of astrophysical, solar system plasmas, and space weather. Although this phenomenon only occurs in the Earth's magnetosphere, it is promptly accessible for sustained study through the *in situ* measurement of plasma properties and of the electric and magnetic fields that govern the behavior of plasmas. Additionally, the properties of the magnetosphere, where many of our spacecraft reside, can have adverse effects on space technology as well as communications systems [3].

All manned and unmanned spacecraft must contain a communication system associated with telemetry, control, and tracking in order to guarantee the operation of the satellite. Therefore, communication is an imperative element for the whole mission, and especially necessary during the reentry phase. During all space missions, when the vehicle enters the atmosphere at hypersonic velocity, a common phenomenon called Blackout occurs. The Blackout is verified when the radio waves used for communication between the satellite and the ground station are attenuated and/or reflected by the plasma layer that is created during hypersonic reentry flight.

Even today, after much research on the subject, spacecraft still experience radio blackout during re-entry [4] which is particularly critical for safety because it can jeopardize the success of the mission and, in manned missions, the human lives on board. Therefore, solutions which can solve or at least reduce this period without communication are of high priority in scientific and technological aerospace sector [4, 5, 6, 7, 8, 9, 10, 11, 12, 13].

In the light of this matter, the Magnetohydrodynamics / Electrohydrodynamics CubeSat Experiment (MECSE) project proposes an investigation on the plasma properties and a complex research on the Blackout mitigation which will promote future investigations in these scientific subjects as well as promising strategies and technologies applied in the aerospace industry. The MECSE project has the cooperation of UBI, University da Beira Interior and CEiiA, a Centre of Engineering and Product Development, and aims to innovate and contribute to the development of the aerospace sector in Portugal. Globally, by aspiring to help finding the solution for a fundamental problem arising during hypersonic flight and Earth's atmospheric reentry, the communication blackout. If deemed successful, the outcomes of the project will have high impact in scientific and technological terms [4, 5, 6, 7, 8, 9, 10, 11, 12, 13], stimulating and increasing the competitiveness of the Portugal's knowledge-based economy.

1.2 Purpose and Contribution

The MECSE is a nanosatellite based on a standardized modular platform (CubeSat). The project main objective is to investigate the mitigation of the communication blackout during the atmospheric reentry phase. The solution to this blackout problem is to reduce the electron density present in plasma flow in order to allow the communication between the satellite and the ground station. The use of a magnetic field, in order to create a window for communication, is an elegant technique suitable for small spacecraft, such as the MECSE CubeSat. It is crucial to explore the magnetic field generator, considering all the parameters both related to the formation of plasmas under the reentry conditions, as well as the requirements of the entire MECSE mission.

Thus, the author of this thesis proposes the analytical and numerical analysis as well as the construction of an electromagnetic model matching with payload and mass requirements of the MECSE CubeSat Experiment (3U under 4 kg and to fit in 1U payload) in order to reduce the power demand by exploring the properties of the winding and core materials.

To accomplish the main purpose, firstly it is essential to understand the shape of the magnetic field at different positions using the analytical model driven by mathematical concepts based on Maxwell's equations. Consequently, the FEMM 4.2™ open source software is used to design an axisymmetric magnetic generator which provides a significant magnetic field at an specific distance from its surface. Furthermore, in order to manipulate the plasma layer, numerical and experimental studies are performed in order to examine the magnetic flux density (B), as a function of the distance from the magnetic field generator to the spacecraft surface, and the current passing through the electric conductor wire. Hereupon, there are several reasons to promote such innovative space project as well as to develop a magnetic field generator technology.

Firstly, considering that continuous communication, real-time telemetry, and GNSS signal reception are imperative in order to safeguard the operation of manned and unmanned spacecraft, thus, solutions that might solve or attenuate the radio frequencies blackout, mainly during atmospheric reentry, are of high priority in scientific and technological terms [4, 14, 15, 16, 17]. The work presented in this thesis executes a significant contribution to the progress of the MECSE CubeSat project by making payload dimensioning and analysis possible. Furthermore, this dissertation has the fundamental role of materializing the payload by creating the bridge between the scientific knowledge and the design and test of the electromagnetic system.

Secondly, C-MAST, a Center for Mechanical and Aerospace Science and Technologies based at University of Beira Interior (UBI), which is elaborating and validating a Magnetohydrodynamics (MDH) numerical model for hypersonic vehicles under reentry conditions with focus on magnetic window manipulation method, will take advantage of the work of this dissertation. A number of researchers [11, 12], including the C-MAST team, consider that through electromagnetic manipulation at a localized region it is possible to reduce the plasma density that surrounds the spacecraft during hypersonic reentry. In this perspective, the validation of the analytical and numerical method of the magnetic field generator model will improve the development of more efficient numerical studies on the manipulation of plasma flow as well as to promote the possibility of MHD experimental model validation by using the electromagnetic physical model in a plasma chamber.

Thirdly, CEiiA, a Centre of Engineering and Product Development, based in Matosinhos, which architects, develops and operates innovative products and technological systems for extensive markets, has recently started to explore the space sector. CEiiA, which aims to fast-forward the Portuguese space industry, is stimulated by the innovative mission of the MECSE project. Hence, in partnership with UBI, they have accepted to support technically and financially the project promoting the materialization of the CubeSat concept. Considering the work presented in this dissertation, CEiiA will be able to implement these concepts in new projects and products applicable to its developmental departments, as well as to commercialize the product which can potentially surpass the RF Blackout.

Fourthly, the final product resulting by the project and validation of an electromagnetic generator for MECSE payload might create an innovative space technology, which can provide a solution for a general unsolved space mission problem, communication Blackout. Designed to fit in 1U of a CubeSat, as a consequence, the electromagnet model could be adapted to any spacecraft category even to conventional satellites which frequently perform more complex missions than small satellites. In addition, a team composed of 9 companies and 10 research centres, including CEiiA and UBI [18, 19, 20, 21], will focus on the propulsion system of INFANTE which can include electromagnetic propulsion as an option. In light of this matter, the electromagnetic validation of the analytical and numerical method may be useful in the research on the viability of the spacecraft's thrusters.

Finally, the experimentally tested and validated magnetic generator model may be able to associate the satellite communication system which provides a new product mainly to the aerospace market. The development and design of a new breakthrough technology provides a more competitive market which is associated with a reduction in the manufacturing and marketing costs [22].

1.3 Research and Objectives

The work presented in this document follows two main purposes. Firstly, CEiiA, challenged the author of this dissertation to design, validate, and manufacture an electromagnetic generator capable of manipulate the plasma density allowing the communication between an hypersonic vehicle and the ground station during atmospheric reentry. Secondly, as a part of MECSE CubeSat Experiment, this dissertation intends to be able to actively contribute for the progress of the project as well as to boost future studies on the mitigation of plasma flow, currently conducted by C-MAST. The design and validation of an electromagnetic generator for MECSE CubeSat, initially depends on the payload requirements in order to understand the constraints for the design of the magnetic model. The next step is to provide an analytical, numerical and experimental validation of the electromagnetic model to conclude the feasibility of the payload in the MECSE mission.

Therefore, the objectives of this dissertation are to:

- Review the mission requirements of the MECSE project and identify those that have the most impact on the construction of an electromagnetic field generator model to better understand the feasibility of the MECSE mission;
- Analyze the payload requirements and objectives in order to determine the mass, power demand, and dimensions restrictions for the creation of an electromagnetic generator model;
- Explore the properties of the plasma throughout the Ionosphere layer, with greater focus on the electron density and plasma density present in the fluid, in order to create a theoretical model of these parameters for different altitudes;
- Investigate the different approaches for the design of the electromagnetic field generator based on a cost-benefit approach;
- Study the magnetic impact of different materials for the core and winding of the electromagnetic model;
- Perform analytical validation for typical axisymmetric solenoid model to interpret the behavior of the magnetic field intensity (B) from its geometrical center to considerable distances from the surface of the model;
- Numerically validate three types of electromagnetic models considering the magnetic field intensity, power, adaptability, and mass requirements;
- Experimentally validate an electromagnetic field generator model based on cost-effectiveness approach;
- Compare and interpret the data from analytical, numerical and, experimental tests.

1.4 Thesis Outline

Chapter 1 introduces the motivation of this dissertation and develops its importance both for CEiiA and for MECSE Project and its contribution for the aerospace industry as well as a product of increased value.

Chapter 2 contextualizes the current plan for CubeSat missions with payloads with the objective of studying the atmosphere, magnetosphere and ionosphere. Afterwards it cites the whole theory behind the design of the magnetic field generator, including the MECSE project requirements and its mission scientific objectives.

Chapter 3 analyses several magnetic equations considering both the geometric characteristics and the generic solenoid electromagnet composition. Also displays the projects' whole validation of the analytical process model.

Chapter 4 exposes the characteristics of design, pre-processor and post-processor of the software used in the simulation and study of the magnetic field of the EMG model. Moreover it provides the simulation environment setup according to the requirements of the MECSE CubeSat payload. Furthermore, it presents, with basis on the generic model simulation, the optimization method of the numerical model as well as its final result of an optimized EMG model.

Chapter 5 explain the objectives, the method of construction and data collection, in addition to other specifications and considerations, taken into account during the EMG model experimental tests. Finally it presents and analyses the experimental results of the winding as well as the EMG model under the influence of the magnetic core.

In Chapter 6 the author discusses the analytical, numerical and experimental results. Some significative conclusions will be drawn for the validation of the project as well as the validation of the EMG model. Furthermore, it analyses and presents the optimization of the EMG models design, with the purpose of providing satisfactory results for the MECSE CubeSat project requirements.

Finally, Chapter 7 presents the final conclusions of this dissertation, considering future tasks for the MECSE CubeSat payload project and the ongoing work as well as publications and conferences.

Chapter 2

2 State of Art

It is essential to understand background knowledge and fundamental milestones of the blackout mitigation phenomenon, as well as, similar studies made by other authors. It is also important to understand the reasons for the application of a magnetic field in the manipulation of the plasma layer and some notable achievements.

2.1 Overview Satellites Missions

In astronomy, a natural satellite is by definition a celestial body orbiting around a planet or another celestial body, as dwarf planets and even asteroids. One natural satellite that everyone knows about is the Moon. On the other hand, artificial satellites are human-made space objects intentionally placed in specific orbit around the Earth and other planets in the Solar System. This artificial bodies are used to collect information from the Earth and from other planets, to enable communications, and even to observe the distance Universe.

In 1957 a major event marked the beginning of a new spatial era in Earth: the first artificial satellite Sputnik 1 was launched by the Soviet Union and precipitated a predominantly military and political response, triggering the well-known space race of the 1960s. Since then, the number of objects launched into space, has increased and more than 4000 satellites have successfully been launched [23].

In present times, the daily life of modern society depends heavily on all the information shared and provided by space technology. Without that information, such evolution would not be possible. Considering that today's advanced economy relies on the capacity to develop knowledge and on the productivity to drive growth, innovation and technology are high priority themes on every nation's agenda [24, 25]. Portugal began its space activity in September 1993 by launching the POSAT-1 satellite, mainly used for military communications. In the aerospace industry, the mission is defined as the objective of the satellite, which is required in order to reconcile the needs imposed by the stakeholders involves in the project. *Figure 2.1* describes the various mission ranges alongside with their various applications and some examples of artificial satellites for each type of mission.

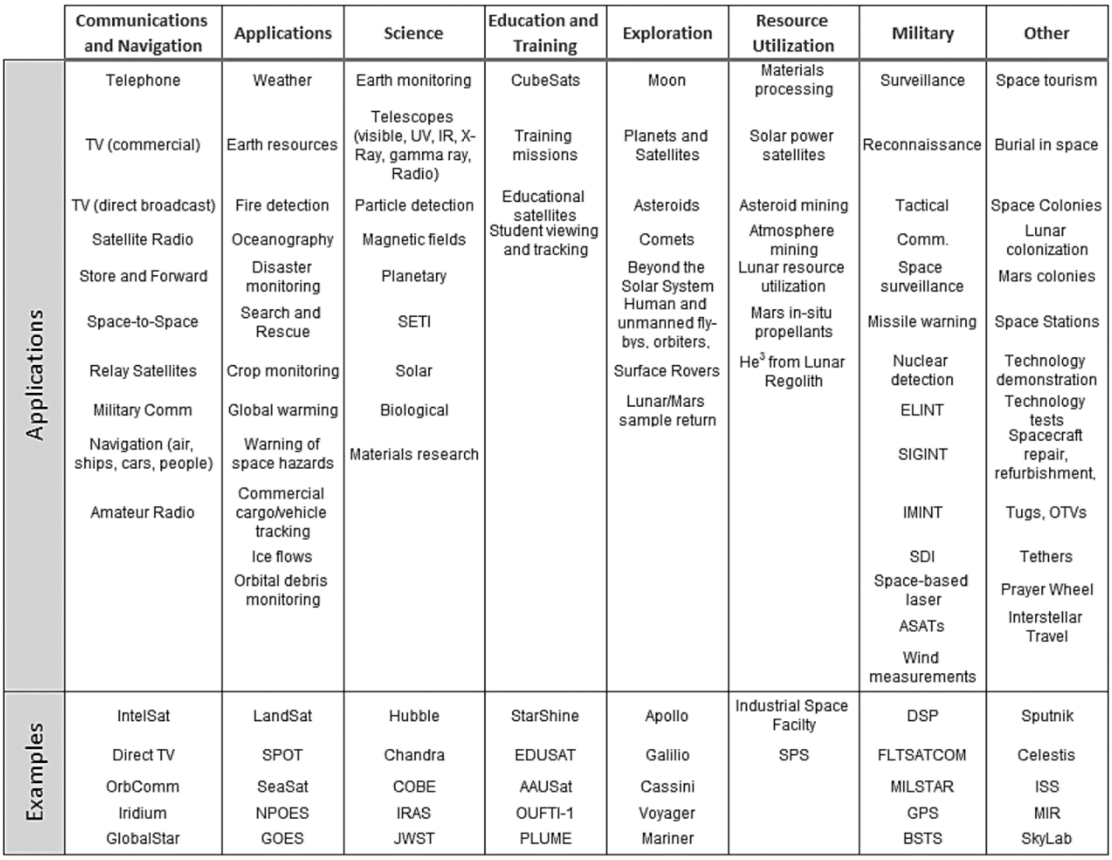

	Communications and Navigation	Applications	Science	Education and Training	Exploration	Resource Utilization	Military	Other
Applications	Telephone TV (commercial) TV (direct broadcast) Satellite Radio Store and Forward Space-to-Space Relay Satellites Military Comm Navigation (air, ships, cars, people) Amateur Radio	Weather Earth resources Fire detection Oceanography Disaster monitoring Search and Rescue Crop monitoring Global warming Warning of space hazards Commercial cargo/vehicle tracking Ice flows Orbital debris monitoring	Earth monitoring Telescopes (visible, UV, IR, X-Ray, gamma ray, Radio) Particle detection Magnetic fields Planetary SETI Solar Biological Materials research	CubeSats Training missions Educational satellites Student viewing and tracking	Moon Planets and Satellites Asteroids Comets Beyond the Solar System Human and unmanned fly-bys, orbiters, Surface Rovers Lunar/Mars sample return	Materials processing Solar power satellites Asteroid mining Atmosphere mining Lunar resource utilization Mars in-situ propellants He^3 from Lunar Regolith	Surveillance Reconnaissance Tactical Comm. Space surveillance Missile warning Nuclear detection ELINT SIGINT IMINT SDI Space-based laser ASATs Wind measurements	Space tourism Burial in space Space Colonies Lunar colonization Mars colonies Space Stations Technology demonstration Technology tests Spacecraft repair, refurbishment, Tugs, OTVs Tethers Prayer Wheel Interstellar Travel
Examples	IntelSat Direct TV OrbComm Iridium GlobalStar	LandSat SPOT SeaSat NPOES GOES	Hubble Chandra COBE IRAS JWST	StarShine EDUSAT AAUSat OUFTI-1 PLUME	Apollo Galilio Cassini Voyager Mariner	Industrial Space Facilty SPS	DSP FLTSATCOM MILSTAR GPS BSTS	Sputnik Celestis ISS MIR SkyLab

Figure 2.1: The broad range of space missions (from [36])

There are many different ways to classify artificial satellites – by function, type of orbit, cost, size, and so forth. Satellites are generally grouped according to their mass [26]. Small spacecraft regard minisatellites with a mass of 100-500 kg, microsatellites with a mass of 10-100 kg, nanosatellites with a mass of 1-10 kg, picosatellites with a mass of 0.1-1 kg and femtosatellite with a mass below 0.1 kg [27]. Their different classes are schematized in *Table 2.1*.

Space vehicles weighing less than 500kg are defined as small satellites [28]. Because of its mass and size limitations, this class of satellites becomes progressively more used in space programs [28]. Conventional satellites, weighing more than 500 kg, require larger rockets with higher thrust that also have a higher cost to finance. In contrast, smaller and lighter satellites require smaller and cheaper launch vehicles, and in most cases are launched in multiples, but have the disadvantage of much shorter lifetimes than conventional satellites. This growth in the use of small satellites was driven primarily by technological advancements to the miniaturization and performance of electronics which have fostered the development of increasingly sophisticated and smaller satellites without the sacrifice of performance [29].

Table 2.1: Classification of satellites by the mass (from *[26]*)

Category	Mass Range [kg]
Large Satellite	> 1000
Medium Satellite	500 - 1000
Minisatellite	100 - 500
Microsatellite	10 - 100
Nanosatellite	1 - 10
Picosatellite	0.1 - 1
Femtosatellite	< 0.1

Figure 2.2 shows the rise of small satellites as well as the projection for the following years as full market potential. Small satellites have an incredible number of other uses, largely in telecommunications. One of the biggest names in private spaceflight is getting into the small satellite industry. SpaceX, founded by Elon Musk back in 2002, plans to use small satellites to blanket the globe with fast and inexpensive satellite internet.

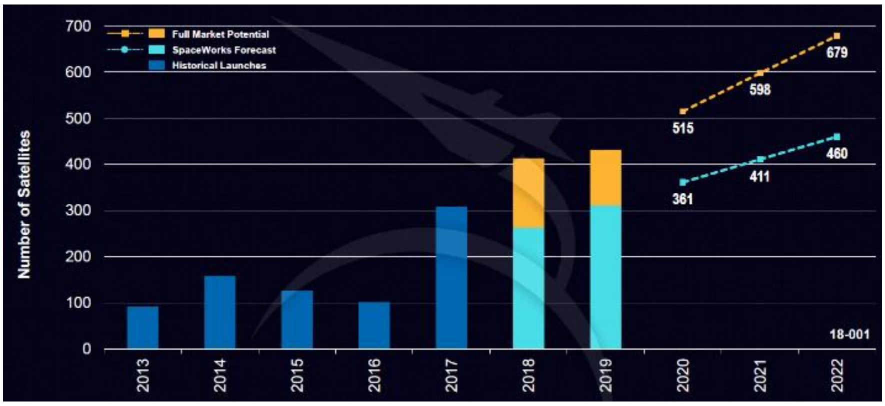

Figure 2.2: Nano-microsatellite launch history (from *[60]*).

Over the last 50 years, more than 38 picosatellites (0.1–1 kg), 680 nanosatellites (1–10 kg), and 860 microsatellites (10–100 kg), have been launched worldwide [30]. CubeSats represent a considerable percentage of launches in the nanosatellite category, in fact, 471 CubeSats with a size of 1U and larger have been launched until August 2016 with several different missions [30]. Based on *Figure 2.3*, the 3U spacecrafts represent the largest fraction of all launches (57% share), while the 1U vehicles represent about 29% of all launches [30]. The 3U spacecrafts represent the largest fraction of all launches (57% share), while the 1U vehicles represent about 29% of all launches.

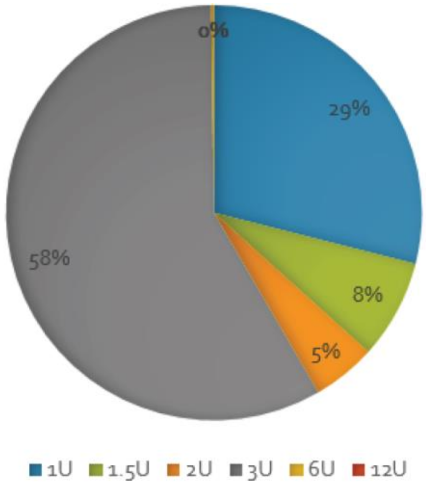

Figure 2.3: Launch Percentage of each CubeSat Size (from *[37]*).

2.2 CubeSat

The CubeSat concept and program started in 1999 as a collaboration between Prof. Jordi Puig-Suari from California Polytechnic State University and Prof. Bob Twiggs from Stanford University, [31], with the idea of meeting an educational need of a meaningful satellite mission that could be developed within a timeframe of a year or two. This way, CubeSat concept can be considered a very low cost alternative, because of its very low mass for reduced launch costs. These space program are not only used to inspire young students to realize the value in STEM (Science, Technology, Engineering and Math), but also providing hands-on training and learning dealing with aerospace technologies and space weather issues [28].

Due to the fact that the CubeSats can be launched as the secondary payloads, along with the low cost of launch called the interest universities, academies, industry and space agencies such as European Space Agency (ESA), the National Aeronautics and Space Administration (NASA), among others [32]. In addition, the use of these nanosatellites allows commercial companies to enter the space market more easily, planning a mission that best fits their requirements [32, 33]. Based on the success demonstrated by space operations using CubeSats, one can understand the transition from just making things work in space to doing real scientific missions with high potential value in terms of scientific return and commercial revenue [32, 33].

CubeSats are a standard for small spacecraft that weigh only a few kilograms and are based on a form factor of a 100 × 100 × 100 mm cube and a mass of up to 1,33 kg. CubeSats can be composed of a single cube (a “1U” CubeSat) or several cubes combined forming, for instance, 3U, 6U or even 18 units.

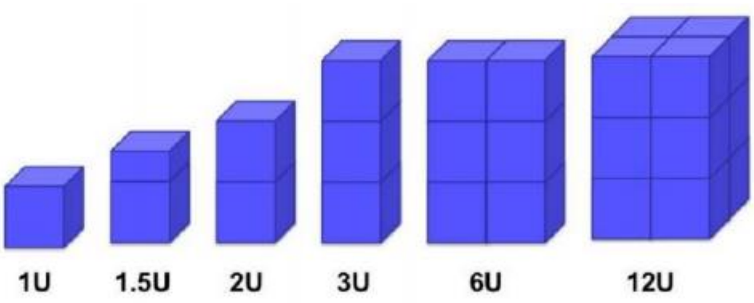

Figure 2.4: Classification of standard CubeSat Form Factor *[72]*.

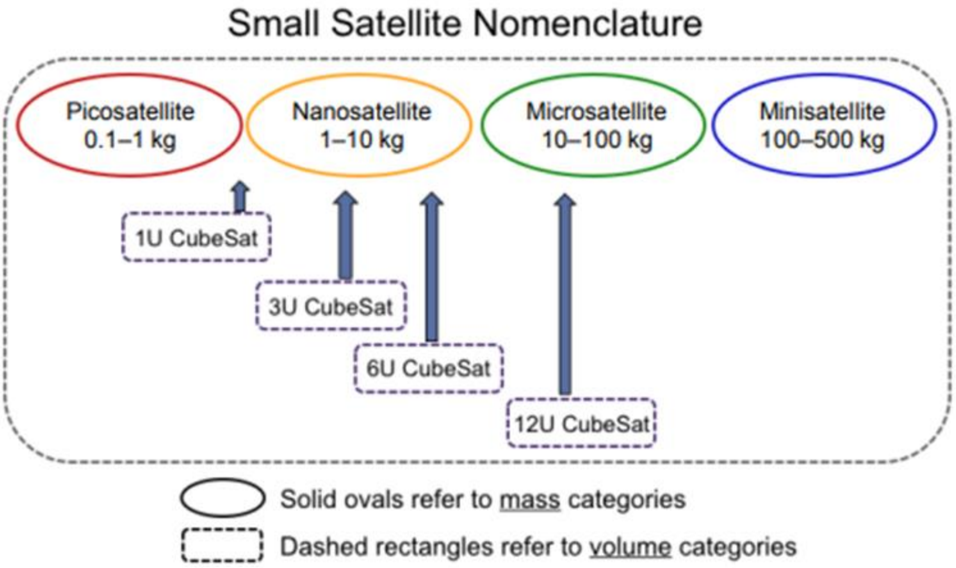

Figure 2.5 Small satellite nomenclature according to mass and volume categories *[32]*

Initially, the CubeSat missions consisted primarily in checking the behavior and viability of nanosatellites. The advancement of technology has allowed increasingly complex missions. Nowadays, it's possible to carry out CubeSat experiments from study of the space environment to telecommunications analysis.

In *Table 2.2* are presented several satellites, whose objective of mission are based on the study and measurements realized in terrestrial atmospheric environment. This balance is essential in a conceptual design phase, in order to understand the processes behind these types of missions.

Table 2.2: Atmospheric CubeSat missions *[28, 34]*.

Name	Type	Organization	Mission	Launch Year
Aerocube 2	1U	Aerospace Corporation	Education and Technology Testing	2002
CUTE-1	1U	Tokyo Institute of Technology	Education, Separation System Demonstration, Technology Testing and Amateur Radio	2003
UWE-1	1U	University of Wurzburg	Technology Demonstration	2005
COMPASS-1	1U	University of Applied Science at Aachen	Technology Demonstration	2008
NANOSAIL-D	3U	NASA	Technology Demonstration	2008
SwisseCube-1	1U	Ecole Polytechnique Fédérale de Lausanne	Upper Atmospheric Science Research	2009
RAX-1	3U	University of Michigan, Ann Arbor, MI, SRI International, Menlo Park and CA	Bi-static Radar Measurement of Plasma Formation in Earth's Ionosphere	2010
DICE-2	1.5U	Space Dynamics Laboratory	Ionospheric Research	2011
CSSWE	3U	University of Colorado Boulder / LASP	Space Weather Research	2012
ZACUBE-1	1U	French South African Institute of Technology at the Cape Peninsula University of Technology	Space Weather, Technology Demonstration, Education and Human Capital Development	2013
CubeSTAR	2U	University of Oslo/Space and Plasma Physics Research Group/ Electronics Department	Technology Demonstration	2014
GRIFEX	3U	University of Michigan / NASA JPL	Atmospheric Studies Technology	2015
FIREBIRD II	1.5Ux2	Montana State University / University of New Hampshire/ Los Alamos National Laboratory / Aerospace Corp	Space Weather Research	2015
EXOCube	3U	California Polytechnic State University / PolySat	Space Weather Research	2015
MinXSS	3U	University of Colorado Boulder / Laboratory for Atmospheric and Space Physics	Solar soft X-Ray Studies	2016
Aalto-2	2U	Aalto University, Finland	Atmospheric Research	2017

2.3 MECSE CubeSat Project

2.3.1 Overview

The MECSE (Magnetohydrodynamics / Electrohydrodynamic CubeSat Experiment) is a nanosatellite under development based on a standardized modular platform CubeSat (3U). The project has been proposed in the University of Beira Interior as a way of captivating students willing to be active members of an increasingly expanding space science community, as well as inspiring them to pursue careers in aerospace engineering.

C-MAST, the Center for Mechanical and Aerospace Science and Technologies of the University of Beira Interior (UBI), is developing and validating a Magnetohydrodynamics (MHD) numerical model for assisting in the design of re-entry objects with emphasis on radio blackout mitigation mechanisms and plasma layer manipulation [11, 12]. When validated, the numerical framework should assist in the development of efficient MagnetoHydroDynamics / ElectroHydroDynamics (MHD/EHD) approaches for manipulating the plasma flow.

With support of CEiiA, Centre of Engineering and Product Development, based in Matosinhos, the MESCE project emerged. CEiiA has the vision of establishing Portugal as a reference in the research, development and engineering fields by creating the conditions for a world-class innovation ecosystem. In such way, CEiiA was challenged by the innovative nature and complexity of the MECSE project, partnering with UBI to promote such a unique endeavor. CEiiA has the fundamental role of materializing the mission by creating the bridge between the scientific knowledge and the design of the space system.

MECSE aims to find the solution for a fundamental concern arising, during hypersonic re-entry flights. The project main purpose is to investigate the mitigation of the communication blackout during the atmospheric re-entry phase using an electromagnetic field. The MECSE mission reveals considerable scientific value, since it seeks to create a benchmark for the future validation of the theory that a magnetic field can mitigate the layer of plasma surrounding a spacecraft and, therefore, allowing communications during the so-called atmospheric re-entry radio frequency blackout phase [11, 12]. Radio frequency blackout is of high priority concern because continuous contact with ground stations and GPS satellites is required for communication and navigation.

In the first instance, it is relevant to corelate the MECSE project to previous CubeSat missions, whose scientific objectives are in the areas related to the structure of different atmospheric layers, telecommunication, interaction between magnetic field and plasma, as well as Ionosphere chemical composition are presented in *Table 2.3*.This process promotes greater knowledge about the most correct approach to take, as well as the collection of important data for the project.

Table 2.3: Description of spacecraft missions related with plasma, magnetosphere, and ionosphere studies *[28, 34]*.

Name	Type	Organization	Science Objectives	Launch Year
SJ-2A	Minisatellite	CAST (Chinese Academy of Space Technology)	Study the Distribution of Ionospheric Electron Density	1981
SAC-C	Minisatellite	CONAE (Argentinian Space Agency), NASA	To Study the Structure and Dynamics of the Earth's Surface, Atmosphere, Ionosphere and Geomagnetic field	2000
COMPASS-2	Microsatellite	Russian Academy of Sciences, Science Ministry	To Study the Dynamix Coupling of the Atmosphere, Ionosphere and Magnetosphere Systems	2006
Meteor-M-1	Large Satellite	NTs OMZ (Research Center for Earth Operative Monitorising), Roskmos/Roshydromet /Planeta	Analyse and Predict the Space Weather (Solar Win, Ionosphere, Earth's Magnetic Field, etc)	2011
DICE	Nanosatellite	Space Dynamics Laboratory	To Measure Ionospheric Plasma Density	2011
RAX-2	Nanosatellite	University of Michigan, SRI International, Michigan Exploration Laboratory, NSF (National Science Foundation)	Provide a Wealth of new Knowledge relating to the Upper Ionosphere and Plasma Properties	2012
EcoCube	Nanosatellite	California Polytechnic State University, NSF (National Science Foundation)	Measure the Density of Hydrogen, Oxygen, Helium, and Nitrogen in the Earth's lower Exosphere and Upper Ionosphere	2015
MinXSS	Nanosatellite	CU (University of Colorado)	Understand the Energy Distribution of Solar Emissions and its impact on the Earth's ITM (Ionosphere, Thermosphere and Mesosphere	2015
Galassia	Nanosatellite	NUS (National University of Singapore)	To measure the TEC (Total Electron Count) in the ionosphere	2016
LAICE	Nanosatellite	University of Illinois at Urbana Campaign, IL, Virginia Polytechnic Institute, State University, Blacksburg, VA (Virginia Tech)	To Measure Ion and Neutral Density Fluctuation at Lower F-Region	2016
PICASSO	Nanosatellite	ESA, Belgian Institute for Space Aeronomy, VTT Technical Research Center of Finland Ltd, Clyde Space Ltd. (UK), CSL (Centre Spacial de Liége)	Determine and Characterize Electronic Plasma in the Ionosphere	2016
ICON	Nanosatellite	NASA, Heliophysics Explorer Program	To Study Earth's Ionosphere and Thermosphere	2017

2.3.2 Scientific Case

In order to interpret the mission objectives of MECSE CubeSat, it is essential to specify the scientific case. For this, it is important to assume that during atmospheric reentry a highly dense plasma layer is formed around the vehicle, which cause's the radio frequency blackout. Considering the reentry altitudes and the vehicle velocity a shock wave is created in front of the vehicle and provides optimal conditions for the plasma formation. In fact, in Low Earth Orbit (LEO) the plasma formation still happens in all Ionospheric layers. In this way, the electron density and the plasma density are less than during the reentry phase.

Furthermore, the considered type of plasma flow regime, interferes with the plasma formation conditions. In this thesis, the type of plasma found during free-molecular flow and continuum flow are assumed as the same.

Investigations executed by several researchers, including C-MAST team, have already concluded that the distance of shock wave to the vehicle and the plasma layer are influenced by the use of a sufficiently strong magnetic field **[12]**. By a literature research, is demonstrated that the use of an electromagnetic field can decrease the electron density, and consequently, decrease the thickness of the plasma layer.

Hence, it is necessary to find a way to measure the plasma layer density. Based on previous missions ***Table 2.3***, the spacecraft instruments capable of measuring electron density in Ionosphere such as Langmuir probes **[4]**. From a conservative perspective, the use of this type of measurement instrument is assumed for the MECSE project.

Hereupon, the Langmuir probes are supposed to record the electron density throughout the MECSE lifetime. A magnetic field generator is to be implemented, with the particularity of operating in both active and non-active mode. The process is simple, when recording the electron density present at a given moment of the MECSE orbit, the magnetic field generator device is activated and then the value of the electron density is again recorded. This process is supposed to be execute cyclically, as is presented in ***Figure 2.6***.

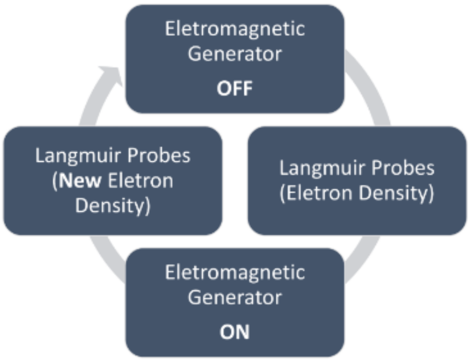

Figure 2.6:Process of electron density measurements and electromagnetic mitigation.

In this way, it is possible to create a model capable of describing the effect of the magnetic field on the plasma layer. This study can be performed during reentry or in Ionosphere, because the plasma formation is observed in both phases.

In the reentry conditions, in order to mitigate the radio frequency blackout, the value of plasma density should be lower than the value of critical plasma density around the spacecraft. For this case, the magnetic field strength shall be high enough to induce a high electron density reduction, near the communication antenna of the vehicle.

The use of a magnetic field in order to manipulate plasma, is an active approach applicable for small spacecraft, such as a CubeSat. Thus, the study, construction and experimental validation of a model capable of generating the electromagnetic field necessary for the manipulation of plasma, in the re-entry phase, is the major scientific case and requirement of this project.

2.3.3 Mission Objectives

The objectives of MECSE are presented in *Table 2.4* [36]. The main educational objective of the MECSE mission, common to other CubeSat university projects [33], is to provide tangible experience to university students in space projects. The base line here is that the learning factor is much greater when one actually design a space mission [35]. Thus, the first objective is educational and, for the students participating in it, the mission will already be considered a success when the spacecraft have been built and launched.

Table 2.4: MECSE mission objectives.

Primary Mission Objectives		
Education	M01	Provide hands-on experience to university students on space projects
Science	M02	Study the formation of plasma surrounding the S/C when traveling in LED
	M03	Assess the effects of the S/C attitude motion on the plasma layer
	M04	Study the effects of an electromagnetic field on the plasma layer
Secondary Mission Objectives		
Technology	SM01	Develop an MHD/EHD device for plasma layer manipulation
	SM02	Develop a modular structure for a CubeSat to be used in future space missions

Together with the educational objectives, the scientific objectives are part of the main objectives of the MECSE mission. Likewise, the scientific objectives of MECSE CubeSat project must be interpreted from the scientific case present in section 152.3.2 Scientific Case. To clarify it, they were divided in 3 groups of scientific studies to be performed in space environment. These studies are listed in *Table 2.5* in the form of scientific objectives [36].

Table 2.5: Description of scientific studies and objectives of MECSE.

Scientific Study	Scientific Objective	Description
Plasma Dynamics Study (PDS)	S01	Study the formation of the plasma layer in LEO by collecting data for different altitudes
	S02	Assess the effects of the spacecraft attitude motion on the plasma layer
Plasma Layer Mitigation Experiment (PLME)	S03	Study the effects of an electromagnetic field on the plasma layer
Re-entry	S04	Study the formation of the plasma layer surrounding the spacecraft during re-entry

The development of a device for plasma layer manipulation is a secondary objective of the mission. This technological objective is a MHD/EHD control device used to generate a sufficient magnetic field in order to reduce the plasma density surrounding the MECSE CubeSat structure. The author of this M.Sc. thesis assumes to perform the SM01 by adding numerical analysis and experimental test of the magnetic generator device.

One of the mission goals (SMO2) is to develop a CubeSat modular structure in-house and validate it in space. The ambition is to design a 3U structure capable of being used in the future for other missions. At this point, the preliminary design of the structure is already done assuming 1U as empty space for the payload. Furthermore, preliminary static linear analysis for the launch loads has been performed and the work on this subsystem is being optimized in parallel to this research and therefore it is not going to be detailed in this thesis.

Any payload embedded in the system must be connected with a specific scientific need or requirement of the MECSE mission.*Figure 2.7*, summarize and shows how the scientific studies and requirements are integrated with the mission subjects and the payload.

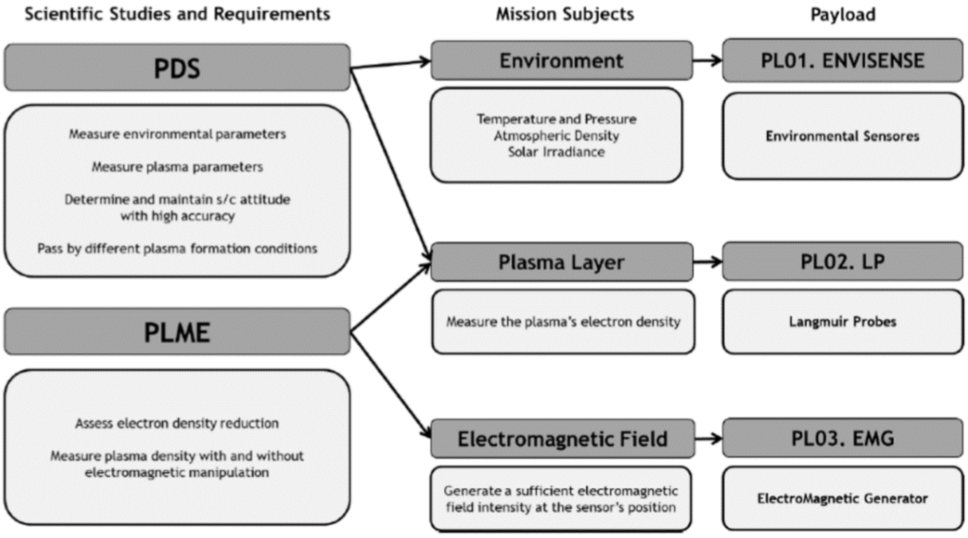

Figure 2.7: Traceability tree from scientific needs to MECSE payloads *[36]*.

2.3.4 MECSE Payload Module

Payloads are the main reason missions fly, and what drives the mission size, cost and risk. Hence, a critical part of mission analysis and design is to understand and identify what drives a particular set of space payloads so that those elements can become an integral part of the overall system trade process designed to meet mission objectives at minimum cost and risk [28].

Concerning the space segment equipment carried aboard the MECSE satellite [36], it can be divided into two modules: the payload that is required to accomplish the mission objectives, and the service module (or BUS) that provides the infrastructure required for the payload operation.

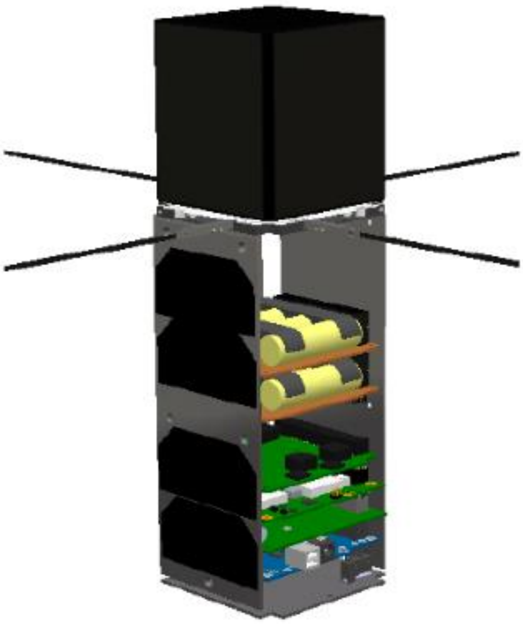

Figure 2.8: MECSE COTS electronics and "black box" payload *[37]*.

The payload definition and sizing determine many of the capabilities, along with the limitations of the mission. Previous studies, based on cost/benefit philosophy, have defined the MECSE CubeSat as a 3U structure. Two of these units are assigned to components necessary for the navigability of the spacecraft, and a unit is left for payload (1U). Based on mission requirements the upper CubeSat's unit has been reserved for the payload and defined as “black box”, as presented in *Figure 2.8* during the concept design phase [37].

In order to accomplish the objectives of the mission, the MECSE payload is divided in three different and interconnected groups: PL01-ENVISENSE, PL02-LP and PL03-EMG. *Table 2.6* shows the payload objectives based on the required mission parameters as well as the description of needed components for each payload objective.

Table 2.6: Mission subjects and respective payloads *[36]*.

Subject	Parameters	Payload	ID	Description
Environment	T, p, ρ, Solar Irradiance	PL01	ENVISENSE	Environmental Sensors
Plasma Layer	Electron Density	PL02	LP	Langmuir Probes
Electromagnetic Field	Magnetic Field Intensity	PL03	EMG	Electromagnetic Generator

2.3.4.1 PL01-ENVISENSE (Environmental Sensors)

PL01-ENVISENSE comprises the construction of a low atmosphere model, based on the analysis of parameters such as temperature, pressure, density, and solar irradiance, registered by environmental sensors.

Temperatures in satellite orbit can range from very lows during eclipses to extreme highs during sunlight period. Therefore, the sensor choice is influenced by the range of temperatures measured during the MECSE flight. Type K thermocouples [38], already used in QARMAN mission [39], are identified as a reasonable choice for measuring temperatures in low Ionosphere. However, it has been recently found that the use of thermocouples is not advisable in MECSE mission because of its susceptibility to the effects of electromagnetic fields [40].

On the upper layers of the atmosphere, air pressure would be much lower than closer to the Earth surface. As a result, the pressure sensor selected for MECSE must be able to measure pressures close to 0 kPa. The NPC-1220 [41], manufactured by Amphenol, is an appropriate choice as it fulfills all the competences mentioned, in addition to being used in QARMAN mission [39].

No solution could be found which directly measures air density. However, it would be possible to estimate it using temperature and pressure measurements or through the altitude.

Solar irradiance can be measured by sunlight power contacting with a particular area in $W/m2$ (SI units). The AvaSpec-Mini, manufactured by Avantes [42], is a spectrometer typically employed to measure this parameter. Although it was originally designed to fit within 1U, its high mass (175 g) and power consumption (3,75 W) are the main handicaps for the use of this device in MECSE project. Another option would be to use the solar arrays to also measure solar irradiance.

In conclusion, the scientific prerequisite of measuring all the described parameters should be reviewed. Firstly, because all the parameters can be estimated with reasonable accuracy using indirect techniques. For instance, by determining the temperature, pressure, air density and altitude can be presupposed using atmospheric models. Also, there is the possibility of estimating solar irradiance with solar array, because they are not critical for the fulfillment of the mission objectives which are focused on the plasma layer.

2.3.4.2 PL02-LP (Langmuir Probe)

The second payload, PL02-LP, intends to measure the electron density surrounding the MECSE CubeSat, and aims to create an approximate model between the position of the spacecraft and the plasma density, determining how it changes with the generation of a magnetic field.

For this purpose, it is required to measure the electron density reduction of the plasma layer. The device capable of measuring this parameter is called Langmuir probe. These sensors are able to measure the plasma density at various distances from the spacecraft surface within the plasma sheath.

Several types of Langmuir probes have been analyzed [43, 44, 45, 34]. It is concluded that, in previous missions, these probes are always attached to long deployable booms. This is useful to reduce the errors in measurements caused by the spacecraft floating potential, which is the voltage on the surface of the CubeSat as it moves through plasma. For MECSE case, this is an issue to be solved since it is required that the sensors are installed the closest possible to the CubeSat upper unit because their location will affect the design of the electromagnetic generator. The mNLP is the selected instrument (*Figure 2.10* [44]). It is a technology recently developed at the University of Oslo [44] and it has been successfully used in several QB50 missions [46] and sounding rockets [47, 48].

The mNLP consists of four cylindrical probes set at a positive fixed-bias and covers a plasma density range from 10^9 to 10^{12} m^{-3} [49]. The system comprises four cylindrical probes with a diameter of 0,51 mm and a length of 25 mm, as shown in *Figure 2.9*.

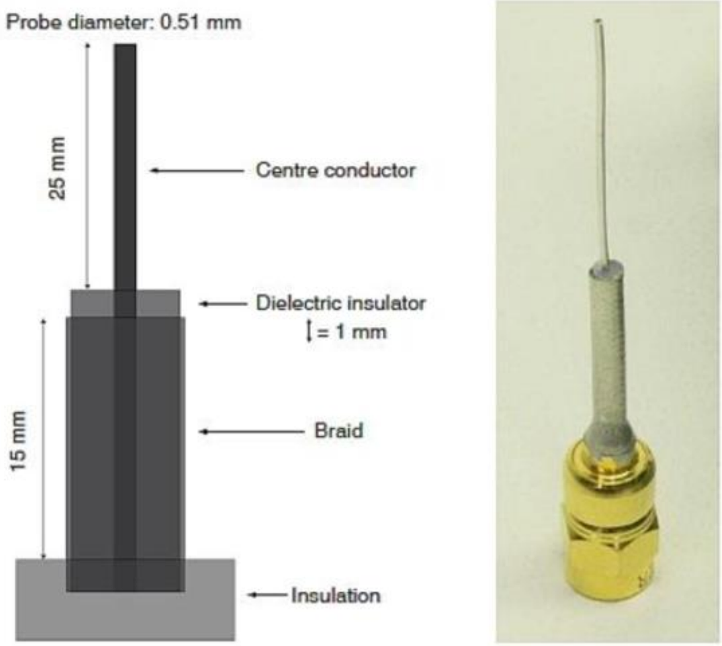

Figure 2.9: Technical drawing of mNLP of CubeStar probe *[45]*

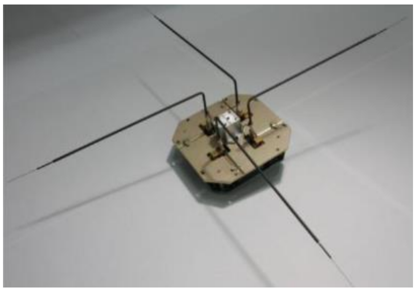

Figure 2.10: Type of Langmuir Probe used in CubeStar (mNLP) *[45]*.

In conclusion, this new Langmuir probe approach has the capability of measuring absolute electron density at a sufficient resolution to resolve the finest conceivable structure in an ionospheric plasma [47]. In fact, it has already proven to be able to measure structures down to the scale of one electron gyro radius [48] which provides high-quality measurements of electron density at any desired resolution [47]. The mNLP seems to be the most suitable instrument for highly-quality ionospheric plasma measurements. However, having the probes biased to a high enough voltage relative to the CubeSat floating potential should be sufficient to mitigate this effect. For future work, experiments must be conducted to confirm this hypothesis.

2.3.4.3 PL03-EMG (Electromagnetic Field Generator)

The PL03-EMG is defined as the most critical payload of the project, which is associated with a higher risk of failure due to its high complexity. This third group purposes a device capable of generate a robust magnetic field, in order to manipulate the plasma layer around the spacecraft. Hence, an experimental validation of the physical model is crucial, before being placed in a space environment.

Firstly, the main goal of the EMG is to generate a sufficient magnetic field in order to modify the plasma electron density within reentry condition plus 5% of safety margin. The magnetic field intensity value of 0.0375 tesla is assumed as a payload requirement and it is investigated in detail in section 2.5.1.

Secondly, it is assumed that the mNLP could be used without booms and its dimensions, length (25 mm) and diameter (0,51 mm) are taken into account. The magnetic field intensity required to manipulate the plasma layer must reach the farthest probe position, which is 25 mm from the MECSE CubeSat surface.

Thirdly, the electromagnet should be able to fit in a 1U *Figure 2.11*and the mass is constrained to a maximum of 1,2 kg. For safety reasons, is diameter was constrained to a maximum of 90 mm.

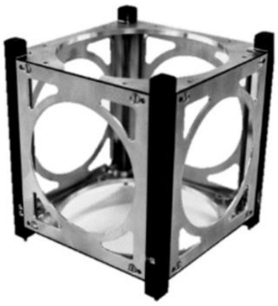

Figure 2.11: 1U format *[37]*.

Finally, based on studies performed in [12] a horizontal dipole configuration is chosen in order to maximize the effect of the magnetic field in the plasma layer. Having defined the payload objectives and subjects, the project one can move forward to the payload requirements.

2.3.5 Payload Requirements

MECSE has three scientific payloads capable of performing the research on plasma layer manipulation in low Ionosphere through electromagnetic control. For this reason, it is required to collect data about the environment and the plasma layer with and without the electromagnetic influence and determine the electron density reduction. Hereupon, based on the payload objectives and mission subjects the payload requirements are specified in *Table 2.7* [36].

In order to interpret *Table 2.7*, at the same time as the spacecraft collect environmental data, the Langmuir probe must be able to measure the density of the plasma layer, from the electron density existent amount, before, during and after the operation of the EMG. At the Langmuir probe position, a magnetic field with an intensity of 0,0365 tesla shall be generated. The system responsible for this magnitude must be fitted on a 1U and shall have a switch on/off capability in order to recognize the magnetic influence on the plasma layer created arround the MECSE CubeSat.

Table 2.7: Payload Requirements *[36]*.

# ID	Payload Requirements	Rationale
PL-01	The payload shall fit on a 1U	Design Constraint
PL-02	The S/C shall be able to collect environmental data	MR-02, MR-03
PL-03	The LP shall be able to measure the density of the plasma layer before, during and after the operation of the EMG	MR-03, MR-06
PL-04	The EMG shall have switch on/off capability	Functional
PL-05	An electromagnetic field shall be generated with a magnetic field intensity of 0.0375 T [TBC] at the LP position [TBD]	EMG Design Assumptions

To conclude, the performance of the payload and the different subsystems has been profoundly explored which has allowed developing an innovative concept of operations mainly remarkable by the use of a device capable to manipulate the plasma layer generating a powerful magnetic field. Henceforward, this thesis focuses on minimizing power consumption and mass of the EMG system. It is concluded that the mission seems feasible under certain assumptions that still require a further analyze.

In the next subsection, the mission profile of the MECSE is presented in order to understand how and when the payload performs its functions as well as the mission phases throughout the spacecraft lifetime.

2.3.6 Mission Profile

Having described the MECSE mission objectives and its different payloads, one can start designing the mission profile of the MECSE CubeSat project. In first instance, comparable missions are investigated in order to better interpret the MECSE trajectory. As a result, QARMAN, which is a triple unit (3U) CubeSat full-blown by Von Karman Institute, in Belgium [39, 49], has considered as a similar to MECSE. The QARMAN mission is designed to collect aerothermodynamic scientific data during reentry phase trying to demonstrate that CubeSat platforms could be used at during atmospheric reentry. The mission is intrinsically essential to understand its mission profile (*Figure 2.12*) which serve as a baseline for MECSE.

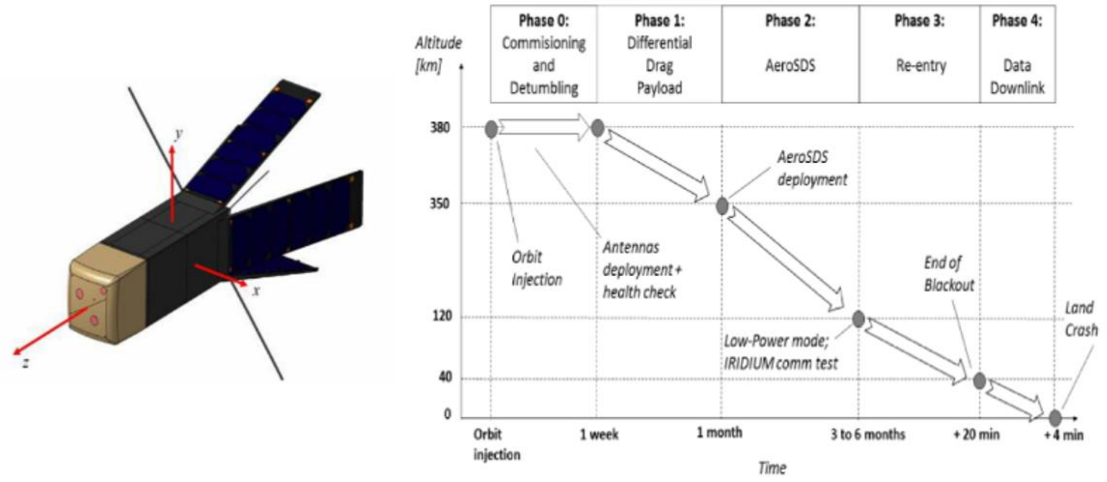

Figure 2.12: QARMAN design and mission profile *[50]*.

As can be observed in *Figure 2.12*, QARMAN has experienced a communications blackout [50] during atmospheric reentry demonstrated in phase 3. Consequently, once the blackout ends and before crashing, the data collected during the reentry phase have been hoarded on a flash memory and transmitted towards the Iridium constellation [39, 49].

Hereupon, based on previous studies performed in [36], MECSE trajectory is divided into 5 mission phase. The mission profile of MECSE CubeSat starts from the launch to the end of its life covered by different periods, as summarized in ***Figure 2.13*** [36].

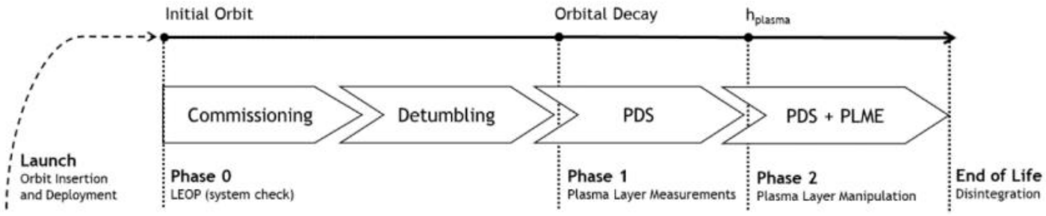

Figure 2.13: MECSE mission profile *[36]*.

Initially, the typical launch phase of CubeSat integrates the launch sequence which includes several separation stages of the diverse rocket structures as well as the deployment CubeSat from the orbital deployer (P-POD) into the initial LEO orbit. The P-POD (Poly Picosatellite Orbital Deployer) is capable of carrying three standard CubeSat units and serves as the interface between the CubeSat and launch vehicle.

After CubeSat injection executed by P-POD, the Early Orbit Phase (LEOP) starts. In this phase, the system's condition is checked, the vital systems are restored and the antennas are set up, which will allow the contact with the ground station. Consequently, the attitude of the satellite shall be maintained aligned with the velocity vector.

Hereafter, the scientific case studies can be implemented which are represented by phases 1 and 2 of the MECSE mission profile (*Figure 2.13*). Firstly in phase 1, the spacecraft will collect environmental data as well as plasma layer properties, focusing on plasma density measurements, in order to perform the plasma dynamics scientific study (PDS). The main goal of this study is create a database of the atmosphere properties with a peculiar interest in Ionosphere layer to better understand the behavior of the plasma fluctuation at specific altitudes.

At orbital altitude (defined by the primary payload on the space vehicle), the frequent collisions of gas molecules with the satellite cause atmospheric drag. This phenomenon is the major source of orbital decay for satellites in Low Earth Orbit (LEO) which, in practice, results in the reduction of the MECSE's altitude orbit.

Consequently, the spacecraft will decay to an altitude (h_{plasma}) where the plasma density is high enough to perform the plasma layer manipulation studies (PLME). From this altitude, the magnetic field generator device will act to cause the reduction of the electron density present in the plasma layer around the MECSE CubeSat. In this phase (Phase 2), both scientific studies (PDS and PLME) will be performed together until the end of vehicle's life which coincide to the disintegration of the MECSE in the Earth's atmosphere.

2.4 Radio Blackout Problem

2.4.1 Plasma Formation Conditions

2.4.1.1 Ionosphere Environment

The atmosphere surrounds Earth and it is responsible for protecting us by blocking out dangerous rays from the Sun. The Earth's atmosphere is usually divided vertically into concentric layers, defined by its temperature and pressure characteristics. These layers can be seen in *Figure 2.14*.

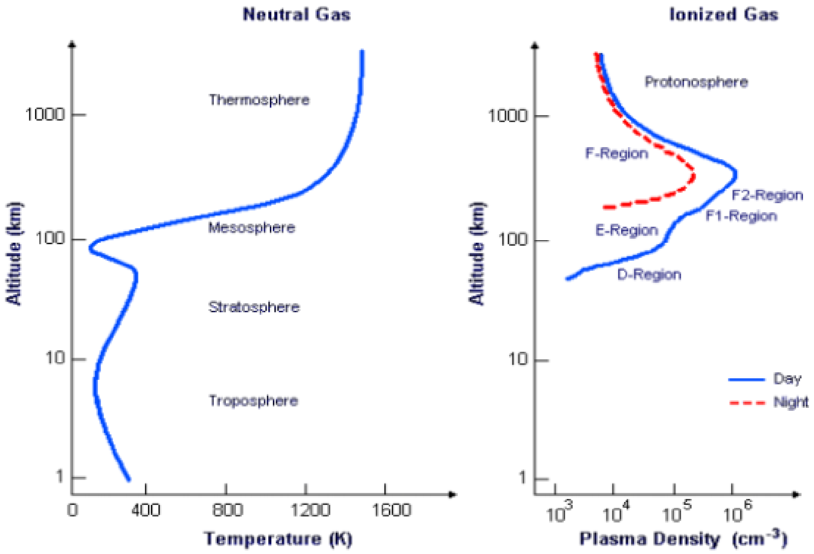

Figure 2.14: Ionosphere layers according to its temperature, plasma density and altitude *[53]*.

In the figure above, it is possible to see that the atmosphere is divided in five recognizable layers: troposphere, stratosphere, mesosphere, thermosphere and exosphere. Between each layer of the atmosphere is a boundary. Above the troposphere is the tropopause, above the stratosphere is the stratopause, above the mesosphere is the mesopause, and above the thermosphere is the thermopause.

The mesosphere, thermosphere and exosphere are coupled with a fascinating layer, the ionosphere. From about 50 km to 1000 km above the Earth's surface, the solar X-ray, EUV, and FUV photons, have the capability to strip electrons from neutral species [28]. At this range of altitudes, the density of neutral particles is low enough that free electrons, which are created through the ionization process, can remain an appreciable amount of time before recombining with ions. Ionization is a process by, through the interaction of radiation from the Sun or after collisions between particles, an atom or molecule acquires a positive or negative charge by adding or stripping away one or more electrons [51]. The result of these changes is a plasma, that is created on the dayside of the planet and disappears during the night (when the Sun goes behind the Earth) [28].

Hence, plasma can be defined as an ionized gas, electrically neutral and exhibit collective effects, which means that as the charge transfer is made, an electric current is generated, followed by a magnetic field, and as a consequence, each one is affected by the fields of the others [52]. Although the population of particles in the ionosphere is mostly composed of electrons and ions, in constant interaction, it can be defined as an electrically balanced medium [51, 53], due to the fact, that the total charge of the plasma environment is approximately zero [28]. In the same way that, the layers of the atmosphere are defined according to their temperature and pressure, the layers of ionosphere are characterized by their plasma density.

Ionosphere is divided into three main regions: D, E and F. The F regions is a special case because it splits into the F1 and F2 during de dayside. The state of ionization and dynamics of the ionosphere is mainly influenced by the Sun [51]. During the night, as the supply of radiation from the sun is not significant, the production of ions and electrons, through the ionization process, becomes impossible. However, recombination continues to occur, causing the gradual reduction of plasma density in layers D, E and F1. As for layer F2, it continues to exist after sunset, and its plasma density decreases slowly at night [53]. At altitudes of about 300 km there is a peak in the number of free ions and electrons, in other words, the maximum plasma density. *Figure 2.14* shows a representative profile of the plasma density of the different regions of the ionosphere, as well as the relationship between the temperature at different altitudes of the atmosphere.

Considering the movement of translation and rotation, geometry and the Axial tilt of the Earth, the time of day, season and geographical location (polar zones, equatorial regions, medium latitudes, auroras) have significance effects in the ionization process. Example of this, as in the winter hemisphere is far from the sun, the solar flow is smaller when compared to the summer hemisphere. The ionosphere contains some of the most complex chemical processes in the atmosphere, which makes for interesting, useful and exciting science [28, 53]. In order to describe concretely the regions of ionosphere, the *Table 2.8* shows the altitude range of different regions of plasma.

Table 2.8: Estimation of altitude of Ionosphere layers *[28]*.

Region	Altitude Range (km)
D	50-80
E	85-140
F1	140-250
F2	250-500

2.4.1.2 Electron Density

The term “plasma density” by itself generally refers to the “electron density”, which is defined as the number of free electrons per unit volume.

As illustrated in the *Figure 2.15* [54], the electron densities are greater during the day than at night time of the Earth. The diurnal variation of the ionosphere is primarily due to the fact that as the Sun rises and moves across the sky, solar radiation produces ionized particles and the number of electron concentration increases. When the Sun sets recombination and other electron-loss processes are dominant, and thus the number of ionized particles decreases.

The D and F1 regions disappear at night while E and F2 regions remain [52]. As the level of ionization in the D region is the lowest of the different regions in the ionosphere, it is in this region that the lowest value of electron density is presented. The E region, lies above D region, the peak of electron density is over a hundred times greater than the peak density in D region, and may sometimes disappear at night [51].

The densest region of the ionosphere is the F region. The ionization of F region decreases at night, but not as much as the E and D region. This region is divided into two layers during the day, F1 and F2. F1 electron density’s varies from $2 \times 10^5\ to\ 6 \times 10^5\ cm^{-3}$ and has its maximum at 220 km altitude. The most ionized and most variable region of the ionospheric layers is the F2 region. The peak daytime electron density, in the F2 region for mid-latitude locations, is usually reached around 300 km and typically decreases after sunset [28]. The maximum electron density can reach up to $10^7\ cm^{-3}$ [55].

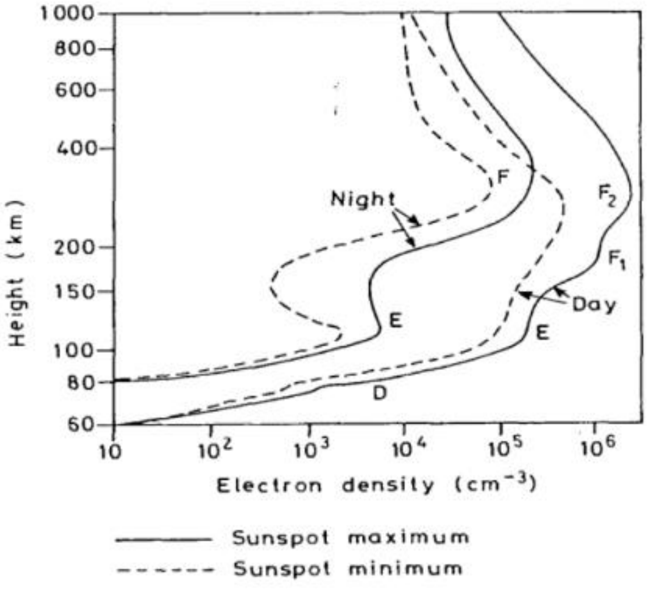

Figure 2.15: Typical vertical profiles of electron density in Ionosphere regions

Table 2.9: Estimation of the maximum electron density to different layers of Ionosphere

Region	**Altitude Range [km]**	**Maximum Electron Density [cm^{-3}]**
D	50-80	10^4
E	85-140	2,1x10^5
F1	140-250	6x10^6
F2	250-500	10^7

2.4.2 Causes of Radio Blackout

Several space vehicles flights, at certain moment, will descend into planetary or terrestrial atmosphere. During this descend phase through the atmosphere, at a velocity that significantly exceed the speed of sound, the air is compressed and heated by a shock wave which is formed in front of the vehicle. As far as the vehicle descends, the sheath of ionized particles becomes increasingly more compressed and heated by the shock and generates a plasma layer [56]. This layer consists of ions and free electrons [6, 4].

The density of plasma is defined by the density of electrons present per unit volume, as stated earlier. When the electron density gets sufficiently high, such that it exceeds the critical plasma density of the link frequency, it can cause a communication problem that is called “radio frequency blackout”. When this phenomenon occurs, the radio waves are reflected or attenuated by the plasma layer created surround the vehicle, and communications between the vehicle and the ground station or Global Positioning System (GPS) satellite are disrupted [4, 13, 27, 56].

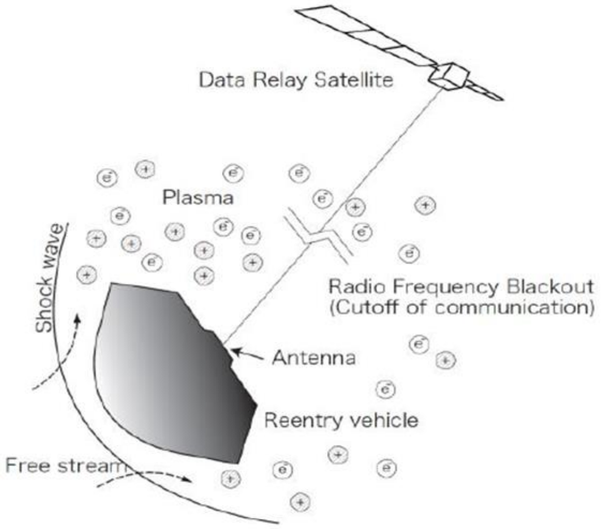

Figure 2.16: Illustrative example of RF Blackout during atmospheric reentry *[10]*.

Typically Radio blackout during Earth's atmosphere reentry lasts several minutes, usually between 4 and 16 minutes, depending on the shape of the vehicle, the angle of reentry, the properties of the atmosphere, and the particular trajectory [5, 6, 13]. When a hypersonic vehicle is crossing through an atmosphere of a larger celestial body, such as Jupiter, the blackout period may reach about 30 minutes [8].

The radio waveband is just a small fragment of the entire spectrum of radio communication frequencies. The commonly used radio bands for communication include VHF (Very High Frequency), UHF (Ultra High Frequency), L-band, S-band, X-band, and Ka-band. *Table 2.10* shows the most frequently used radio wave band frequencies and their applications [57, 58, 59].

Table 2.10: Usual radio wave frequencies and their applications *[7]*.

Band Name	Frequency [GHz]	Examples
VHF	0,03 ~ 0,3	Voice Communication
UHF	0,3 ~ 3,0	Data telemetry, Voice Communication
L-band	1,0 ~ 2,0	GPS, Military telemetry
S-band	2,0 ~ 4,0	Data telemetry, TDRS
X-band	8 ~ 12	Data telemetry, Satellite communications
K_a-band	27 ~ 40	Radar and experimental communications

The created plasma layer usually has an electron number density of $10^{15}\ to\ 10^{19}\ m^{-3}$, which has direct and negative influence on the communication signal transmitted [60]. The relationship between the signal frequency, in Hz, and the plasma density, in m^{-3}, is expressed as follow:

$$f_p = 8.985\,\eta^{1/2}\ (Hz), \tag{2.1}$$

where, the plasma frequency fp exceeds the transmission radio frequency, $fradio$, the communication between the vehicle and the receiving station is completely interrupted [5]:

$$f_p > f_{radio}. \tag{2.2}$$

Hence, in order to transmit a radio wave signal through the plasma layer, the radio wave frequency should be greater than the plasma frequency. This requirement regulates the radio wave signal capable to cross the plasma sheath, leading to determine the maximum plasma density surrounding the hypersonic vehicle [5]:

$$\eta_{critical} = \left(\frac{f_{radio}}{8.985}\right)^2. \tag{2.3}$$

Table 2.11: Usual radio wave frequencies and their respective critical plasma density *[7, 56]*

Frequency [GHz]	Critical Plasma Density [m^{-3}]	Designation
0,30	1.12×10^{15}	Voice communication
1,55	2.99×10^{16}	GNSS
1,68	3.52×10^{16}	L-band
8,20	8.75×10^{17}	X-band
32,0	1.27×10^{19}	K$_a$-band

Table 2.11 exhibits the critical plasma densities for different radio wave frequencies [4, 16].However, even when the electron density is less than the critical density, the plasma layer may attenuate the radio wave. Nonetheless, even when the electron density is less than the critical one, the radio wave can be attenuated by the plasma layer. Regarding this specific case, parameters such as the frequency of transmission, the electron collision frequency and the plasma density are able to cause the communication disruption [6]. However in this thesis, this topic is not taken into account.

The literature provides an extensive amount of data about the plasma layer formed by solar radiation in the ionosphere or by the extreme temperatures generated on the outer surface of the vehicle in the re-entry phase [4, 6, 8, 11, 15, 52]. In addition, different plasma density profiles during reentry are available, and generally depend on variables such as elapsed time, altitude, and vehicle velocity [4, 12].

While in low atmosphere the plasma density varies from 10^9 to 10^{13} m^{-3} (*Table 2.9*), during the reentry phase these values are higher, varying from 10^{17} to 10^{20} m^{-3} causing the communication blackout [4, 8, 10, 13, 14]. As a final conclusion, the plasma frequency largely exceeds the range of S, C and X band communication signals which range from 1 GHz to 12 GHz [8].

2.4.3 Importance of Solving the Radio Blackout

Since the beginning of the manned space program, the blackout period during atmospheric reentry phase has been a problem common to all hypersonic vehicles [56]. This fact represents a technological barrier to the development of hypersonic vehicles as well as to the advancement of interplanetary missions [4, 6, 11, 16].

It is important to understand the main reasons why the blackout problem should be solved in order to recognize the scientific value of the MECSE mission. During hypersonic flight and reentry missions, the communication disruption is observed, leading to a significant attenuation and, in most cases, a total communication blackout [6, 16].

In first instance, hypersonic vehicles could be traveling at velocities up to 26 times the speed of sound, about of 8 km/s [6]. Considering only a single minute of radio frequency blackout, this velocity corresponds to approximately 480 km of vehicle's incapability to transmit data telemetry. The inability to communicate can induce problems related to the accuracy of the vehicle's positioning. The position tracking error can range from several meters to tens of meters, even with little attenuations [60].

During atmospheric re-entry of hypersonic vehicles, real-time telemetry monitoring becomes particularly important in order to safeguard the safety of the vehicle. In blackout scenario, the vehicle loses the capacity of precise guidance and maneuvering, which can compromise the mission success and, in special cases, the human lives on board [4, 16]. Thus, permanent contact between the vehicle and the signal receiving station becomes crucial in order to make quick decisions on when to abort a flight [16].

Secondly, future manned and unmanned missions to explore planets, such as Mars, would greatly benefit from a solution to communication blackout [4, 8, 10, 14]. For this type of missions, scientifically interesting sites surrounded by dangerous terrain, demand high accuracy in entry navigation and precise landing control of the vehicle, in order to avoid catastrophes. During reentry missions on Mars, 12 seconds of radio frequencies blackout are experienced, thus solving the communication problem is a motivation for future space missions and technological advances [17].

Thirdly, the solution to the blackout problem can be very useful for understanding and preventing accidents during the renting phase. Data collected milliseconds before a catastrophe, are crucial in order to determine the cause of the disaster. Thus, during a hypersonic flight, onboard recorders would probably be destroyed in case of an incident, due to the velocities and altitudes involved [4, 6]. In the military defense context, the radio frequency mitigation technology will be beneficial to critical functions of anti-missile defense systems, such as radar tracking and identification, mission abort and missile electronic countermeasures [4, 6, 8].

In conclusion, the advancement of space exploration greatly depends on the ability of a hypersonic vehicle transmit data in real time. Therefore, the plasma manipulation technology will have to be implemented, presenting scientific and technological advances, such as the safety of the mission and spacecraft, the easiness of position and maneuvering control in exploration of new planets, the radar tracking in anti-missile defense functions, among others [6, 8]. Hence, considering a Mach 10 flight, it is possible to travel to any place on planet Earth in about 2 hours, then there is a greater concern to develop vehicles capable of reaching such velocities [6, 16].

As mentioned previously, the success of a hypersonic or re-entry mission can be compromised by the effect of radio frequencies blackout. Even though this topic has been continuously investigated by the scientific community, the solution is unsatisfactory, and the problem has become a common obstacle to all aircraft under hypersonic flight conditions [4, 6, 8, 9].

The need for a robust methodology capable of manipulating the plasma layer, allowing subsequent communication during the reentry phase, is essential for advancements in hypersonic vehicle design [16]. In summary, the ability to communicate through a plasma layer during re-entry phase remains a critical area of research, thus is the urgency to find a solution.

2.4.4 Radio Frequency Blackout Manipulation

As have been discussed, several procedures are able to mitigate the plasma layer created surrounding the vehicle. In general, mitigation techniques to attenuate the communication blackout period have two approaches: passive and active (*Figure 2.17*) [8, 9].

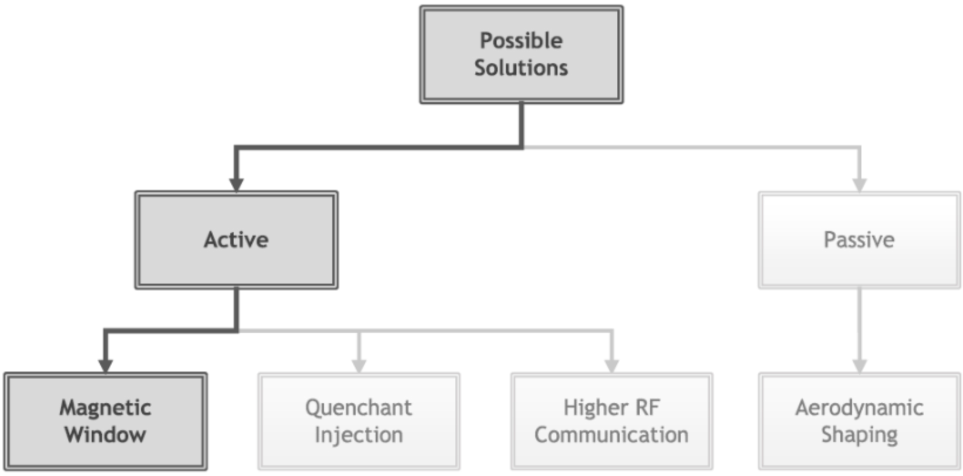

Figure 2.17: Possible solution for RF Blackout mitigation *[36]*.

Active plasma manipulation approaches includes techniques acting as high frequency transmission, quenchant injection, and electric or/and magnetic fields. This sub-section reviews previous approaches for radio frequency blackout mitigation and evaluates them in terms of realistic applications.

The applicability of any of these methods depends in part on its success in reducing or alleviating the communications blackout and in part on the geometry, velocity, and angle of attack of the re-entry vehicle in question. Some methods would be better for smaller vehicles while others are more adequate for larger manned re-entry vehicles.

2.4.4.1 Aerodynamic shaping and Remote Antenna Assemblies (RAA) method

Regarding the aerodynamic shaping method, it can be used to decrease the plasma density in order to allow data to be transmitted through the plasma layer [8]. Vehicles with a sharp geometry are surrounded by a much thinner plasma sheath than that surrounding the blunted vehicles. Reentry vehicles with this type of geometry have limitations presenting reduced load capacity and aerodynamic heating problems compared to a blunted vehicle [8, 13]. Generally speaking, this solution is not suitable for blunted vehicles of generic shape.

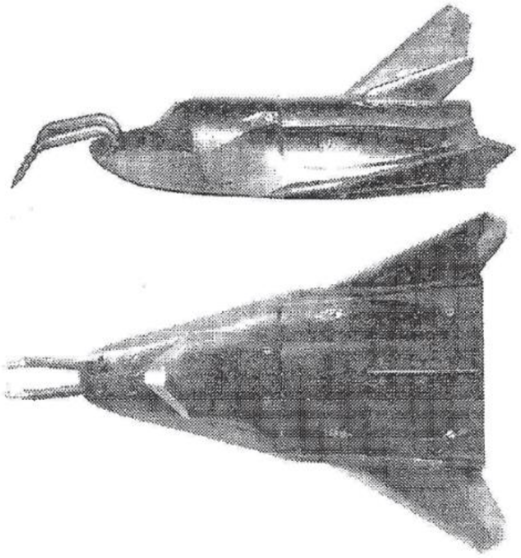

Figure 2.18: Schematic of the space vehicle with Remote Antenna Assemblies *[61]*.

In addition, Belov et al. [61] proposes the Remote Antenna Assemblies (RAA) method for hypersonic re-entry vehicle. The RAA consists of a hooked cylinder that contains an antenna and has a sharp tip. In *Figure 2.18* a blunted hypersonic vehicle with Remote Antenna Assemblies is presented [61]. In other words, during hypersonic flight the antenna is placed ahead of the shock wave of the vehicle being outside the plasma sheath allowing communication. In other words, during the hypersonic flight the antenna is placed in front of the shock wave of the vehicle getting out of the plasma sheath allowing communication. In this scenario, the main concerns are the maintenance of the sharp tip on the RAA, as well as the interaction between the flow field between different components of the RAA and also between the RAA and the vehicle [61]. In addition, one of the problems created by RAA is the relationship between the shock wave and the surface of the vehicle which requires the use of ablative materials for both the antenna and the front of the vehicle, in order to provide communication. The RAA heating problem also provides a technical limitation for realistic applications [4].

2.4.4.2 High-frequency transmission

Other leading candidate solution is the communication by high frequencies [4]. The explanation is simple: as the critical plasma density becomes higher the radio wave frequency is increased. Therefore, in order to reduce the signal attenuation the frequency is increased.

The main disadvantage is the tremendous attenuation in signal caused by any atmospheric phenomena, such as the rain. As a result, those frequencies are not currently used in radio communications.

2.4.4.3 Quenchants Injection

Spencer proposed a quenchant injection of electrophilic liquids or gases for blackout mitigation [62]. The quenchants are injected into the shock wave will modify the plasma properties in a specific location and provide communication [9, 62, 63, 64]. As can be seen in Figure 2.19, the injection orifice is placed near the communication antenna affecting the plasma layer density by cooling the temperature of the plasma around the vehicle and consuming free electrons.

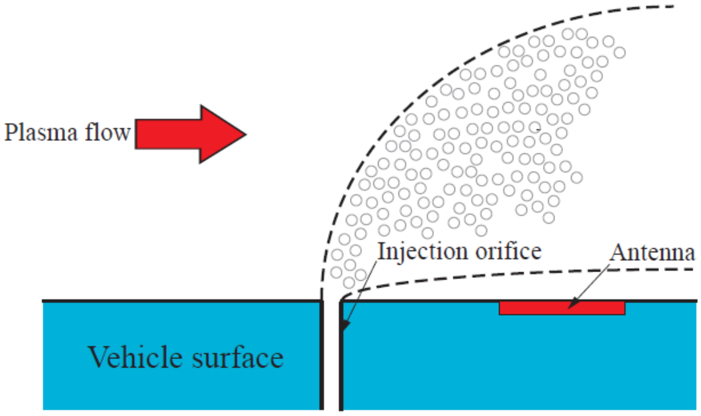

Figure 2.19: Schematic of the Quenchants Injection method *[4]*.

When the plasma temperature is cooled by the injected quenchants, the balance of the reaction is modified and the quenchant molecules themselves become part of the flow species consuming free electrons through electron attachment processes.

This method has experimentally shown to reestablish radio communication for re-entry conditions. However, the amount of quenchant mass needed for scale-up to large vehicles remains an issue [9, 15].

2.4.4.4 Magnetic Window

The magnetic window method suggests the use of a static magnetic field in order to open a communication window capable to mitigate the blackout [9, 65, 66, 67]. The static magnetic field created aims to reduce the plasma density which alters the electrons' motion in a localized region creating a "channel" for communications [6, 8].

By adding an electric field, the intensity of the generated magnetic field increases. The higher the intensity of the magnetic field, the greater the reduction of the density of the plasma created around the vehicle. As a result, the communication window is expanded, and the frequencies range of data transmitted is extended.

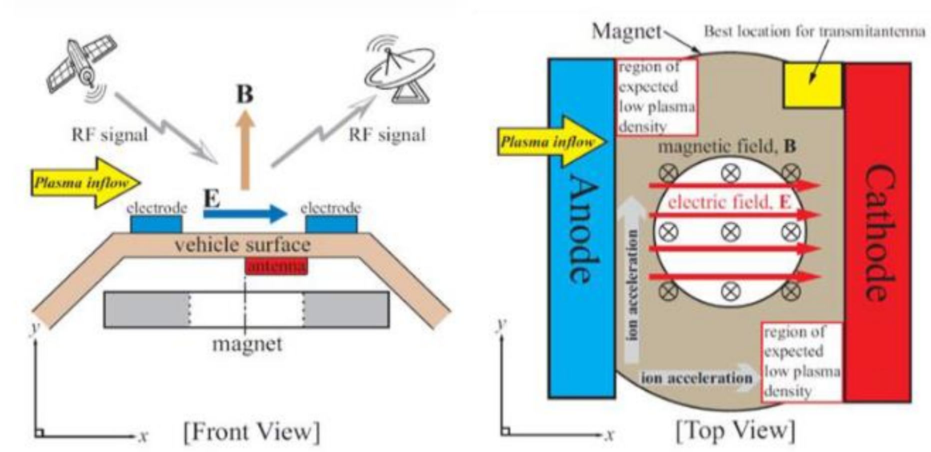

Figure 2.20: Schematic of the Magnetic Window method *[4]*.

As can be seen in *Figure 2.20*, the electromagnetic manipulation system is mainly composed of an embedded electromagnet which will create the magnetic field (B) together with electrodes (anode and cathode) which is responsible to generate the electric field (E) [4].

However, the biggest obstacles to implement the magnetic window method are the size and weight of the electromagnet, cooling systems and power supply. In addition, the size of the electromagnet represents a technical difficulty because the creation of a uniform magnetic field requires a very large coil radius.

Among the techniques of active plasma control that have been presented, the electromagnetic manipulation seems to be the most promising method for the possibility of mitigate the plasma layer [13]. In fact, recent numerical simulations and experimental tests have been performed and shown that the application of electromagnetic fields can reduce the plasma density significantly under reentry plasma conditions.

2.5 Literature Review

This subsection comprises a review of the most important theoretical and practical aspects focusing on the results of the plasma layer manipulation based on the magnetic window method, as well as the process of design of the static magnetic field generator. These concepts are essential to first understand the scientific theme of MECSE, which are associated with the radio frequency blackout mitigation, and secondly to better understand the scope of this dissertation.

2.5.1 Electromagnetic Manipulation of a Hypersonic Plasma Layer

Research based on the magnetic window method has been performed primarily via computational modeling [4, 5, 11, 12, 27, 68, 69], but also via experimental tests [5, 65]. These endeavors have been widely prosperous, demonstrating that the magnetic window technique is completely plausible and should be used to extensively test the mitigation.

Numerical and experimental analysis presented in [70] and the interaction between the applied static magnetic field and the plasma flow was examined, by using the expansion tube, as shown in the *Figure 2.21*.

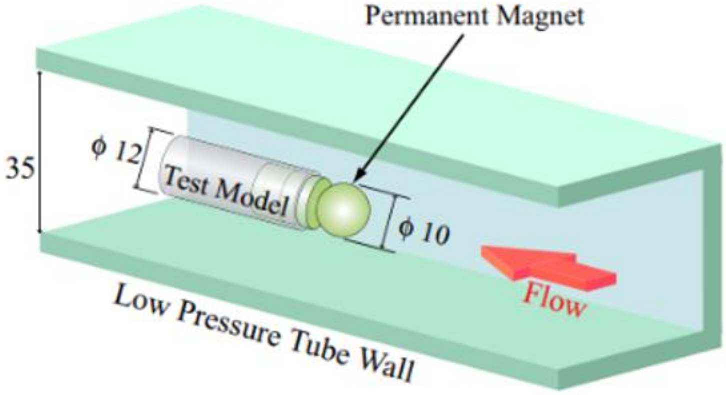

Figure 2.21: Model configuration and its environmental setup in the test tube *[70]*.

A numerical method to make use of the electromagnetic effect on the partially ionized plasma flow inherent to the reentry flight has been proposed. The test model was inserted into the measurement section and was placed at the center of the tube which is 35 mm x 35 mm in cross-section, as shown in *Figure 2.21*. For a spherical permanent magnet, with diameter is 10 mm, a magnetic field with a strength of 0,65 tesla was employed. The strength of the magnetic field decreases in all directions as it moves away from the surface of the model, as presented in *Figure 2.22* [70].

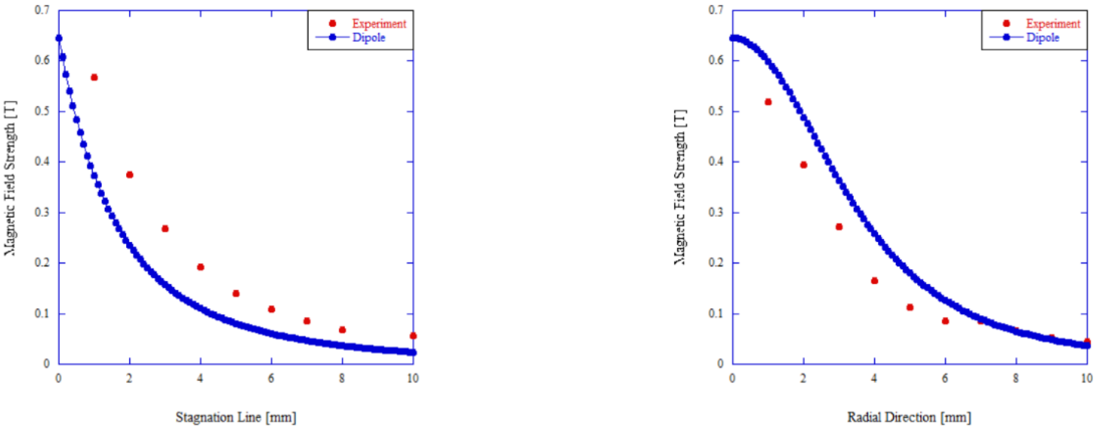

Figure 2.22: Magnetic field strength distribution along the stagnation line starting from its surface (Left) and along the line perpendicular to the stagnation line starting from the model surface (Right) *[70]*.

A demagnetized model with the same size was also tested in order to compare the behavior of the plasma flow with and without the influence of the magnetic field.

The experimental results of Tanifuji et al. [70] show a slight influence of the applied magnetic field on the plasma flow. On the other hand, the numerical simulation can not detect such influence. To resolve this discrepancy between the numerical and the experimental results, it is necessary to evaluate more precisely the flow condition at the test period.

In addition, Chernyshev et al. [71] have compared analytical plasma flow models with shock tube data to demonstrate the potential for using applied magnetic fields to improve the aerodynamic characteristics of supersonic and hypersonic vehicles. In order to intensify the influence of the magnetic field in the plasma flow, a case of both applied magnetic and electric fields was considered *Figure 2.24*. The results are prosperous, showing that the shock wave changes its position and shape providing high values of plasma velocity which cause the separation of the flow, as shown in *Figure 2.23*.

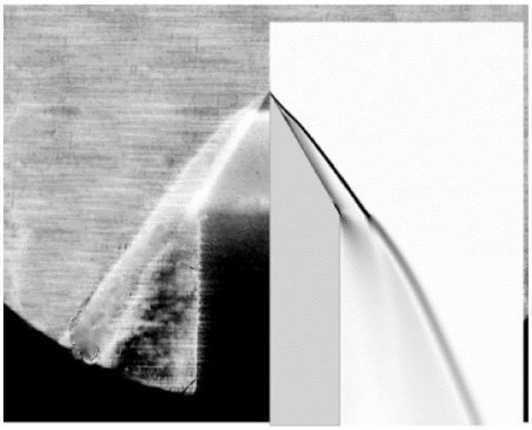

Figure 2.23: Comparison of simulated (Right) and experimental shadowgraphs of the flow under the applied magnetic and electric fields *[71]*.

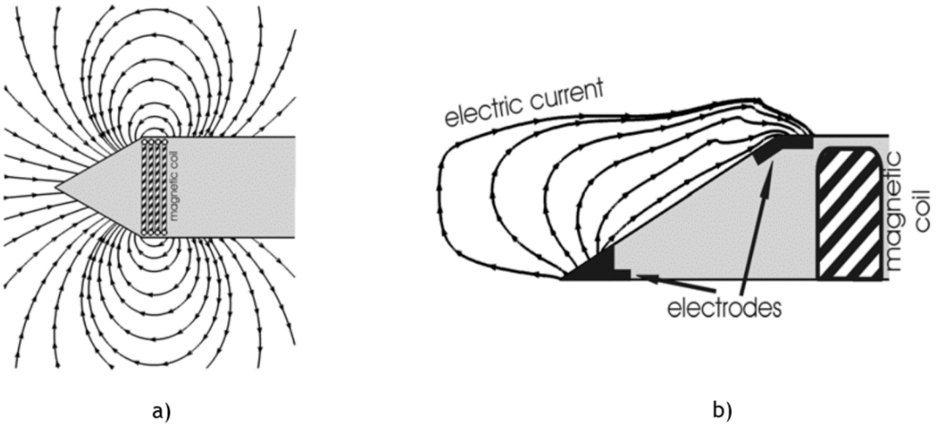

Figure 2.24: a) Configurations of the magnetic coils and corresponding magnetic induction streamlines; b) An electrode system and the electric current streamlines in case of both applied magnetic and electric fields *[71]*.

2.5.2 Telemetry, Tracking and Command (TTC)

The communications between the satellite and the ground station are executed by the telemetry, tracking and command system (TTC). This system has the particularity of providing the radio link allowing the spacecraft to downlink scientific and housekeeping data mission to the operation center. In addition, it allows to receive remote operator drivers (telecommand) sent from the ground station [72].

For the MECSE case, one condition required is the data collected by the payload sensors (environmental sensors and Langmuir Probes) during operation and the time it will be operating. Secondly, based on availability and capability of the ground station as well as the data rate required by mission, it is essential to choose the radio band frequency to use for the MECSE CubeSat. In previous studies [36], MECSE was compared to DICE [34] and QUARMAN [39] scientific missions which use UHF/VHF for the operation time of the payload given its low cost and power consumption. Notwithstanding, the author [36] suggests a further detailed analysis in S-band radio band in order to offer higher data rates to downlink the scientific data.

Having defined the radio frequencies, it is imperative to investigate the behavior of the radio band frequencies under blackout conditions in order to understand whether the use of a magnetic window is suitable for communications between the spacecraft and the ground station.

Several studies about blackout causes and plasma mitigation approaches are considered in [9], stating that a 1,3 tesla magnetic field intensity is required for transmitting an S-band signal under $10^{18}\ electrons/m^3$ plasma frequency. The window for communication would work only when the critical plasma frequency is in a given range around X-band, as shown in *Table 2.11*. Furthermore, in order to determine the radio band frequency for a spacecraft, a study on how the variations in plasma frequency, collision frequency, and magnetic field both along and normal to the axis would affect data transmission would be required. In conclusion, a magnetic field of this magnitude requires a very large coil radius which would almost certainly modify the flow of the plasma along the hypersonic vehicle's surface.

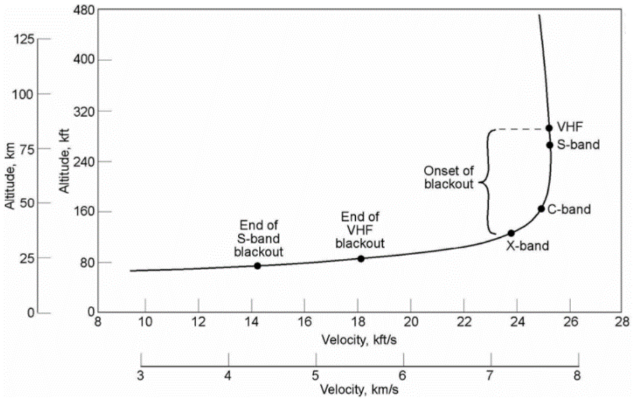

Figure 2.25: RAM C-II reentry trajectory
showing onset and end of RF signal blackout

Several spacecrafts with different shapes and geometries were analysed and their published flight data was reviewed and compared [73]. Considering this section, the results are focused on the RAM C-II data mission which reveals important information about the blackout of particular radio bands frequencies. The results are shown in *Figure 2.25*.

Firstly, at about 300 km of altitude the onset of Blackout starts with VHF and S-band radio signal which have the lowest frequency compared with X-band and C-band. As the space craft slows down, the communications begin to be established and at nearly to 80 km of altitude the end of Blackout of VHF and S-band arise respectively. X-band and C-band reacquisition were delayed because of tracking difficulties.

Finally, studies about OREX mission conducted by Kim [4], confirmed that the electron number density also depends on the altitude of the vehicle because the freestream conditions are different. *Figure 2.26* shows the calculated electron number densities for several altitude positions.

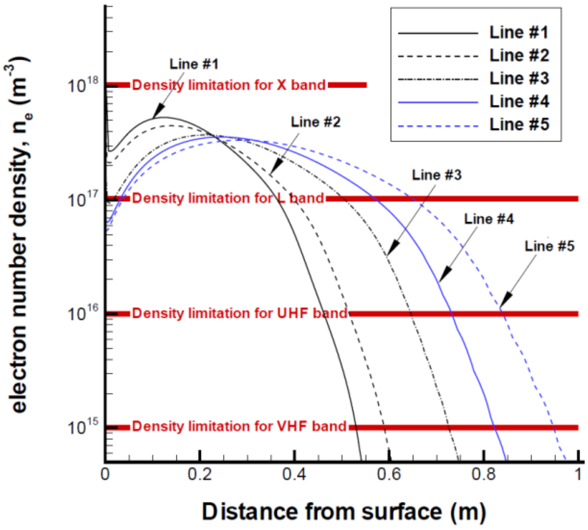

Figure 2.26: Electron number density at several location of the OREX *[4]*.

As described, the peak electron number density increases at low altitude, which exactly corresponds to the graduation of the radio frequencies blackout. During OREX reentry, firstly the vehicle loses low frequency radio band communication, such as VHF and UHF, fact which is in agreement with *Figure 2.25*. As the electron density number increases as the reentry hypersonic vehicle travels through the atmosphere, OREX will progressively lose higher frequency radio band communication.

In conclusion, the magnetic window method ensures the manipulation of the plasma layer at different plasma density conditions. This indicates that the configuration of the electromagnetic generator should be determined in terms of used radio wave band and altitude, which will be referenced in the next sub-section.

2.5.3 Electron Density Reduction (EDR)

The research about the magnetic field strength required to reduce the plasma layer density have been performed in several simulations [8, 56].

Based on the results of an analysis of transmission and reflection of radio waves at a plasma-air interface performed by Hodara in 1961 [74], it shows that the reentry radio blackout, where the highest electron concentration is conferred, can be eliminated when a static magnetic field of the order of 0,05 tesla is applied through the plasma sheath. Furthermore, the author considered an unbounded collisionless plasma with $10^{18}\, electrons/m^3$ concluding that it sustains wave propagation with no attenuation up to about 1 GHz when a static magnetic field of 0.0357 tesla is applied [74].

As investigated in section 2.4.1 Plasma Formation Conditions the plasma density can be characterized by its electron density. The adimensional parameter adopted to represent the plasma layer mitigation is the Electron Density Reduction (EDR), performed in [4]. When an electromagnetic field is applied to a plasma layer, this method calculates the amount of plasma density reduced taking into account the plasma density before and after the effect of the magnetic field, as expressed in the next equation (2.4):

$$EDR = \frac{\eta_e}{\eta_0}, \tag{2.4}$$

essentially, the EDR is represented by the ratio between the final electron density $,\eta e,$ and the initial one, $\eta 0$ [4]. This parameter was adopted by Kim [56] with the objective of to demonstrate the possibility of an electromagnetic layer mitigation scheme to solve radio blackout in the hypersonic flight condition. The author examines the OREX radio frequencies blackout under atmospheric reentry, and as expected, concludes that plasma density reduction depends on the intensity of the magnetic field applied (*Figure 2.27*).

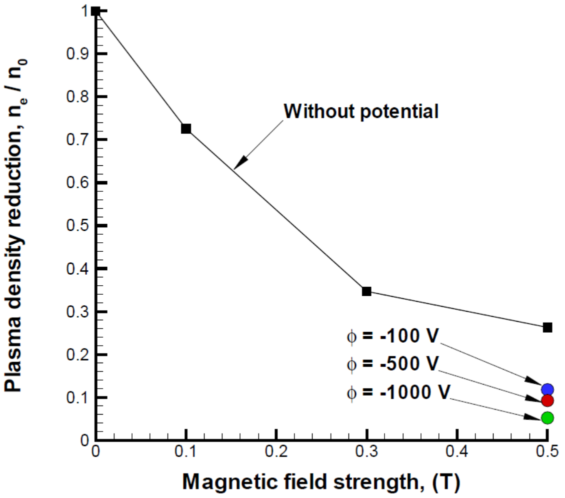

Figure 2.27: The maximum density reduction by an ExB layer in a hypersonic flight conditions *[13]*.

The numerical results presented in *Figure 2.27*, contemplate an initial plasma density of $10^{17}\ electrons/m^3$ showing the EDR decreases with the increase of the magnetic field strength. The maximum magnetic field intensity from *Figure 2.27* (0,5 T) without potential provides a EDR of 0,3, which means that the final plasma density would be of, approximately, $3 \times 10^{16}\ electrons/m^3$.

Considering the critical plasma densities presented in *Table 2.11*, a magnetic field strength of 0,5 T without potential allows the communication under Ka-band, X-band and, L-band radio frequencies. In contrast, this value is still higher than the critical plasma densities for voice communication and GNSS, so for these frequencies a higher EDR is necessary. In *Table 2.12* is tabulated the minimum plasma density reduction required for each radio frequency band for OREX under 79,9 km reentry condition [4].

Table 2.12: Commonly used radio wave frequencies and their applications *[4]*.

VHF 300 MHz	**UHF** 3000 MHz	**L-band** 2 GHz	**GPS** 1.4 GHz	**S-band** 4 GHz	**X-band** 12 GHz	**K_u-band** 18 GHz
0.004	0.3497	0.1486	0.0728	0.5945	No blackout	No blackout

In order to solve radio blackout for the S-band, which is used for the data telemetry of OREX, the author concludes that the plasma density reduction should be stronger than 0,6, which is in accordance with the data presented in *Table 2.11*. This density reduction can be achieved with a magnetic field intensity of 0,3 T which still provides a weak plasma density reduction for the L-band and GPS frequency.

The studies performed in [4] consider several reentry altitudes with distinct properties. At 81 km of altitude, which is a relatively rarefied plasma condition, the electromagnetic field applied can significantly reduce the plasma density. In this condition, a 0.5 T magnetic field gives a density reduction of about 0,05. Even for 0,15 T, which is the maximum magnetic field technically reasonable, the density reduction is almost 0,4, which is enough to solve the X-band radio blackout [4]. However, at 41 km of reentry altitude, even for 0,05 T condition the density reduction is very weak, concluding that the density reduction becomes less strong at lower altitude.

Considering a magnetic field strength of 0.0375 T, as specified in 22Payload Requirements according to literature, it will cause a plasma density reduction of, approximately, 0,9 (*Figure 2.27*). Thus, assuming the plasma density of $10^{17}\ electrons/m^3$, which is the most conservative value for atmospheric reentry [4, 8, 9, 10] under radio frequency blackout condition [13, 14], after the effect of the magnetic field imposed, the final plasma density will be $9 \times 10^{16}\ electrons/m^3$. In conclusion, based on *Table 2.11*, with 0.0375 T generated, makes possible Ka-band and X-band communication signal in MECSE atmospheric reentry.

Nevertheless, the properties of the atmosphere at different reentry altitudes are quite disparate (in terms of temperature, pressure, fellow velocity, etc…) which are related with the reentry plasma density of the MECSE flight. Thus, the electron density reduction can be influenced by it, which calls into question the performance of the magnetic field considered above on the plasma layer manipulation.

2.5.4 Magnetic Theoretical Principles

Based on the last sections, it is crucial to specify the method to generate the magnetic field strength required to manipulate the plasma layer. Firstly, some of the theoretical magnetic principles will be presented in order to understand which concepts are essential to the design of the electromagnetic generator. Secondly, the properties of magnetic materials, typically used in the construction of a magnetic device, will be clarified in order to ascertain which parameters influence the induction of the magnetic field. Finally, the MECSE payload requirements are taken into account in order to determine which method is adequate for the magnetic field generator model.

2.5.4.1 Density of Magnetic Flow

Density of magnetic flow or magnetic induction is represented by vector B and is expressed in tesla (T). When a magnetic field is applied in the vacuum, the number of lines of flow or density of flow is presented by the following relation:

$$\vec{B} = \overrightarrow{H}\mu_0, \tag{2.5}$$

where, μ_0 represents the vacuum's magnetic permeability and $\vec{H}$ represents the vector intensity of magnetic field, Ampere per metro *(A/m)*.

The magnetic induction is obtained by summing the applied field with the external field resulting in the magnetization and is represented by vector $\vec{M}$, measured in A/m.

$$\vec{B} = \left(\overrightarrow{H} + \overrightarrow{M}\right)\mu_0 \tag{2.6}$$

2.5.4.2 Relative Permeability

Permeability is the most important factor for magnetic materials, since it indicates the quantity of magnetic induction generated by a material when put under the action of a given magnetic field. Another useful parameter is the relative permeability, μr, expressed by the following equation (2.7):

$$\mu_r = \frac{\mu}{\mu_0} = \frac{\vec{B}}{\vec{H}\mu_0} \tag{2.7}$$

A large relative permeability means that the material amplifies the effect of the magnetic field. It is clear that the relative permeability is dimensionless.

2.5.4.3 Magnetic Susceptibility

A material's magnetization is proportional to the applied field. It is possible to define a factor of proportionality named magnetic susceptibility, being that:

$$x = \frac{\vec{M}}{\vec{H}}. \tag{2.8}$$

This parameter serves frequently to express material's weak magnetic responses and represents also the amplification of the magnetic field produced by the material. Relative permeability and magnetic susceptibility have the same meaning and are, therefore, related.

$$\mu_{relative} = 1 + x. \tag{2.9}$$

2.5.4.4 Magnetic Domains

Below the Curie temperature (the critical point where the intrinsic magnetic moment of the material changes direction), the magnetic dipole moments of the atoms of ferromagnetic materials tend to align in the same direction within small regions. These are called magnetic domains. When a magnetic material is demagnetized, the magnetic domains are randomly oriented, so there is no magnetic moment resulting from the overall sample. When an external magnetic field is applied to a demagnetized magnetic material, the magnetic domains grow thanks to the movement of the walls or borders of the domains.

2.5.4.5 Hysteresis

Hysteresis refers to the phenomenon in which the curve of B as a function of decreasing H does not coincide with the curve of B as a function of increasing H. One of the consequences of hysteresis is the production of heat inside the ferromagnetic substances, each time the excitation travels through the hysteresis cycle. This heat comes from a kind of internal friction that occurs when domains change direction.

In conclusion, as the permeability is not constant, once it is always defined by a maximum and minimum permeability, it is said that the relation between B and H is not linear and its representation is given by the hysteretic cycle. The next definitions concern the different behavior of the various magnetic materials, representing different types of magnetism.

2.5.5 Magnetic Materials

The first magnetic phenomenon was observed while using natural magnets. Those were iron fragments found in the ancient city of Magnesia (that is why they are called "magnets"). One of the properties of those magnets was being able of attracting demagnetized iron. This property is more accentuated in the material's poles. The materials have, ever since, been used in different kinds of applications such as transformers, motors, etc. In 1820, André-Marie Ampere discovered that the magnetic effects could also be produced by electric currents. Thereby, Ampere proposed a theory considering that the magnetic properties of a physical body are originated by a great number of minute circular currents inside that body.

In this way, the first idea of a solenoid was created and this was the first approach in the study of the materials. For the core, various types of magnetization behaviours that are associated with different materials will be considered.

2.5.5.1 Diamagnetism

Under the action of an external magnetic field, the atoms of an object undergo slight disturbances on the electrons in orbit that create small magnetic dipoles in the atoms, which oppose the applied “magnetic” field. This interaction produces a negative magnetic effect known as diamagnetism. The diamagnetic effect creates a low negative magnetic susceptibility and a relative permeability around 0.99995.

2.5.5.2 Paramagnetism

Paramagnetism results from the alignment of the individual magnetic dipoles of atoms or molecules in an applied field. Materials that have a small positive magnetic susceptibility in the presence of a magnetic field are referred to as paramagnetic. The paramagnetic effect in the materials disappears when the applied magnetic field is removed. Paramagnetism is very common in materials and gives susceptibilities between 10^{-6} and 10^{-2} and relative permeabilities between 1 and 1.01. Examples of paramagnetic materials are aluminium, magnesium, copper sulphate, titanium and platinum.

2.5.5.3 Ferromagnetism

In the previous types of magnetism, the magnetization only remains as long as the field is maintained. In ferromagnetism, when the applied field is removed, the material preserves much of the magnetization. Certain metallic materials have a permanent magnetic moment in the absence of an external field and show high and permanent magnetizations.

These are the distinguishing features of ferromagnetism. In ferromagnetic materials, the unpaired dipoles are easily aligned with the imposed magnetic field. High magnetizations are obtained, even for weak magnetic fields, and can reach relative permeabilities in the order of 10^{6}. Iron, nickel and cobalt are examples of ferromagnetic materials.

2.5.5.4 Antiferromagnetism

In the presence of a magnetic field, the magnetic dipoles of the atoms of the antiferromagnetic materials align in opposite directions, so that the overall magnetization is zero. Manganese and chromium, in their solid state and at room temperature, are antiferromagnetic.

2.5.5.5 Ferrimagnetism

A type of magnetism, present in some ceramic materials, in which the different ions have magnetic moments with different values and when aligned by a magnetic field in an antiparallel way create a global magnetic field. Ferrimagnetic materials, better known as ferrites, can provide high amplifications on the imposed field.

2.5.5.6 Copper Wire

American wire gauge (AWG), also known as the Brown & Sharpe wire gauge, is a standardized wire gauge system used since 1857 predominantly in North America for the diameters of round, solid, nonferrous, electrically conducting wire. Increasing gauge numbers denote decreasing wire diameters, which is like many other non-metric gauging systems such as SWG. This gauge system originated in the number of drawing operations used to produce a given gauge of wire. Very fine wire (for example, 30 gauge) required more passes through the drawing dies than 0-gauge wire did. The AWG tables are for a single, solid, round conductor. The AWG of a stranded wire is determined by the cross-sectional area of the equivalent solid conductor. *Figure*B.1 shows various data including both the resistance of several wire gauges and the maximum current based on a copper conductor with plastic insulation. The diameter information in the table applies to solid wires. Stranded wires are calculated by calculating the equivalent cross-sectional copper area.

2.5.6 Solenoid and Electromagnet Design

A solenoid is a simple electromagnetic device which consist of a coiled conductor wire, wrapped in a helix shape. When an electric current is passed through the wire, the solenoid operates as a magnet with north (N) and south (S) poles at the ends of the helix *Figure 2.29*. When a current is sent through the wire a uniform magnetic field is formed which is highly intense in the interior and weak in the exterior of the solenoid *Figure 2.29*. Like all magnets, the magnetic field of an activated solenoid has positive and negative poles that will attract or repel material sensitive to magnets. A typical solenoid design, is characterized by having a length (l) much larger than its radius (r) as shown in *Figure 2.28*.

Faced with this condition, in order to determine the behaviour of the magnetic field inside the coil, the radius of the solenoid can be neglected. Thus, the magnetic field strength B [T] for this uniform field can be given by the next equation (2.10):

$$B = \mu_0 \frac{N\,I}{l}, \tag{2.10}$$

where N is the number of turns in the coil, $I\,[A]$ is the current applied and $l\,[m]$ is the length of the solenoid. The special parameter, μ_0, is defined as the permeability of free space, given by $\mu_0 = 4\pi \times 10^{-7} m\,kg\,s^{-2}A^{-2}$.

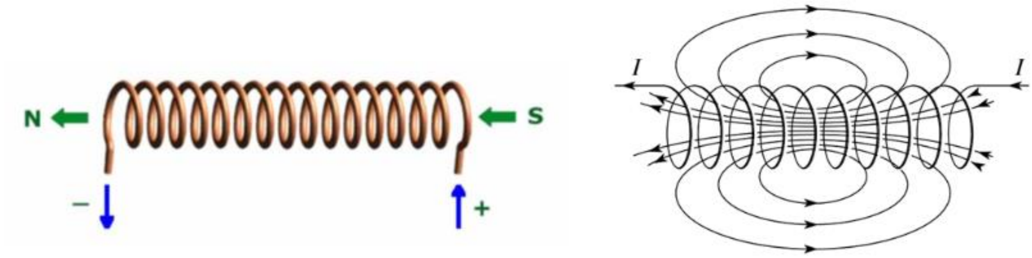

Figure 2.29: Geometric properties of an generic solenoid.

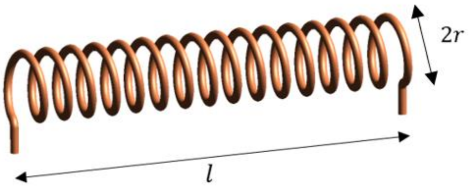

Figure 2.28:Solenoid generic design.

Based on the MECSE payload requirements as well as the EMG magnetic field intensity needed (0.0357 T), it is crucial to understand the usual magnetic strength provided by a solenoid. *Figure 2.30* presents different forms of generating a magnetic field as well as its corresponding magnetic field strength.

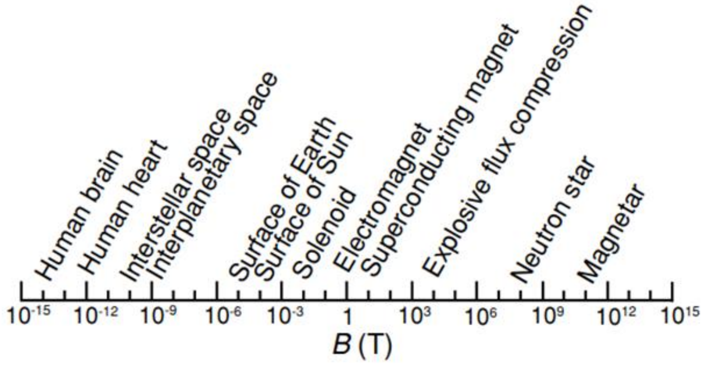

Figure 2.30: Magnitudes of some magnetic fields in tesla *[76]*.

An usual solenoid provides a magnetic field strength (B) around 10^{-2} T (*Figure 2.30*) which means it does not meet the payload requirements for the design of the magnetic field generator. Primarily, the magnetic field required to manipulate the plasma density during hypersonic reentry, leverages the $4 \times 10^{-2}\ tesla$, whereas the magnetic field generally created by a solenoid proves to be insufficient. And finally, since the decrease in magnetic field intensity is gradual with the distance to the coil winding end [75], as the magnetic field intensity required shall act in the Langmuir probe position at 25 mm from the CubeSat surface, it becomes necessary to use another tool. According to *Figure 2.30* an electromagnet, which provides a higher magnetic field intensity than a solenoid, seems to be the appropriate system for the MECSE payload design.

The simplest procedure to create an electromagnet is to make a solenoid, pass current through it and then place a piece of soft iron inside the solenoid (Figure 2.31). Due to the high relative permeability of soft iron, the magnetic field formed would be much stronger.

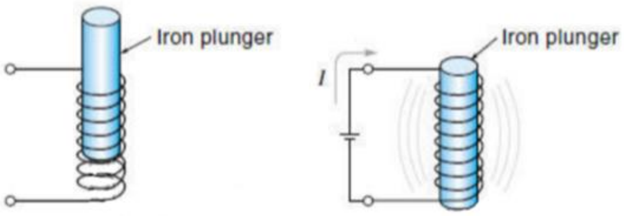

Figure 2.31: Generic electromagnet unenergized (Left) and an generic electromagnet energized (Right) [76] .

The rod of soft iron placed inside the solenoid would behave like an ordinary bar magnet when the current is switched on. The permeability of the core (μ), is the measure of the degree to which a material can be magnetized, thus, it is essential for the magnetic field intensity provided (B), which demonstrates a direct correlation between them. As the value of the permeability of free space is less than iron core permeability, thus, for an energized electromagnet the magnetic field strength equation (2.10) becomes:

$$B = \mu_0 \, \mu_r \frac{N \, I}{l}. \tag{2.11}$$

The relative permeability of the material is the comparison of the permeability concerning the air or vacuum. In fact, the relative permeability (μ_r), is the ratio of the permeability of a specific medium (μ) to the permeability of free space (μ_0). It is expressed as:

$$\mu_r = \frac{\mu}{\mu_0}, \tag{2.12}$$

being,

$$\mu = \mu_0 \, \mu_r. \tag{2.13}$$

Considering a solenoid, which its core is defined as free space, the relative permeability of air and the non-magnetic material is one ($\mu_0/\mu_0 = 1$).

One of the most substantial MECSE payload requirements is to assign the electromagnetic generator the function of switching on and off in order to better understand the effect of the magnetic field on the plasma layer (section 2.3.4 MECSE Payload Module). As in all electromagnets, a magnetic field is created when an electric current passes through the wire. Electromagnets have an advantage over permanent magnets in that they can be switched on and off by the application or removal of the electric current, which is what makes them useful for MECSE CubeSat objectives mission.

A summary of the different magnetic flux sources is provided in *Table 2.13*. Based on *Table 2.13*, the sum of the maximum magnetic fields produced by a solenoid and a permanent magnet is substantially the same as that generated by a single electromagnet. Firstly, this fact proves that coupling a permanent magnetic core with an electrically stimulated conductive winding around it, such as a solenoid, gives rise to an electromagnet. Secondly, the use of an electromagnet for the MECSE mission seems to be more adequate compared to a solenoid and a permanent magnet, because it has a maximum magnetic field strength that is in accordance with the payload requirements of the project. Finally, since an electromagnet produces a maximum of 2.5 tesla *Table 2.13*, it suggests to be sufficient to manipulate the plasma layer at the Langmuir Probe position, which is about 25 mm from the surface of the magnetic generator.

Table 2.13:A summary of different magnetic flux sources and their magnitudes *[76]*.

Method	Duration	Maximum Field [T]
Air-core solenoid	Steady	0.2
Permanent Magnet	Steady	0.1 – 2
Electromagnet	Steady	0.5 - 2.5
Superconducting solenoid	Steady	2 – 23
Bitter magnet	Steady	15 – 35
Hybrid magnet	Steady	40 – 45
Discharge coil	100 ms	25 – 80
Discharge coil	10 µs	50 – 100
Expendable coil	1 µs	> 100
Implosive flux compression	< 1 µs	1000

Chapter 3

3 Analytical Model

Analytical models can provide closed-form solutions giving physical insight for designers. They are useful tools for design optimization since continuous derivatives issued from the analytical solution are of great importance in most optimization methods.

3.1 Basic Magnetics Theory

Analytical models have been proposed since it takes a long time for computing the magnetic field distribution of ironless circular coils [77]. Although these methods give very accurate results, they are not suitable to study circular coils with iron-core structures. An alternative analytical method to compute the magnetic field of circular coils with iron parts is based on boundary value problems with Fourier analysis [78]. This method consists in solving directly the Maxwell's equations in the different regions, e.g., air-gap and coils by the separation of variables method [79, 80].

Maxwell's equations combine and complete the laws formerly established by Faraday, Oersted, Ampere, Gauss, Poisson, and others. Since Maxwell's equations are differential equations they do not account for any fields that are constant in space and time. Any such field can therefore be added to the fields. Therefore, the phenomena of electromagnetic wave propagation are governed by Maxwell's equations, in their differential form given as [81]:

$$\nabla \cdot D = \rho_{ch}, \tag{3.1}$$

$$\nabla \times B = 0 \; (Conservation\ Equation), \tag{3.2}$$

$$\nabla \cdot E = -\frac{\partial B}{\partial t} \; (Faraday - Lenz\ Law), \tag{3.3}$$

$$\nabla \times H = J + \frac{\partial D}{\partial t} \; (extended\ Amp\grave{e}re's\ law), \tag{3.4}$$

where, E [V/m] is the electric field strength vector, D [C/m^2] or [As/m^2] is the electric flux density vector, B [T] or [Vs/m^2] is the magnetic flux density vector, H [A/m] is the magnetic field strength vector, J [A/m^2] is the current density vector, ρ_{ch} [C/m^3] or [As/m^3] is the charge density.

The gradient operator will be represented by the nabla symbol (∇) and is defined as a Cartesian vector,

$$\nabla \equiv \begin{bmatrix} \partial/\partial x \\ \partial/\partial y \\ \partial/\partial z \end{bmatrix}, \tag{3.5}$$

which can be transformed to other coordinate systems in a straightforward way. Using ∇, the divergence operator (div) can be defined as $\nabla\cdot$. To illustrate this, let is operate with $\nabla\cdot$ on a vector F

$$\nabla \cdot F = \begin{bmatrix} \partial/\partial x \\ \partial/\partial y \\ \partial/\partial z \end{bmatrix} \cdot \begin{bmatrix} F_x \\ F_y \\ F_z \end{bmatrix} = \frac{\partial}{\partial x}F_x + \frac{\partial}{\partial y}F_y + \frac{\partial}{\partial z}F_z \tag{3.6}$$

Similarly, the rotation operator (rot) is expressed as $\nabla\times$ which, when applied to a vector F yields

$$\nabla \times F = \begin{bmatrix} \partial/\partial x \\ \partial/\partial y \\ \partial/\partial z \end{bmatrix} \cdot \begin{bmatrix} F_x \\ F_y \\ F_z \end{bmatrix} = \begin{bmatrix} \partial F_z/\partial y - \partial F_y/\partial z \\ \partial F_x/\partial z - \partial F_z/\partial x \\ \partial F_y/\partial x - \partial F_x/\partial y \end{bmatrix} \tag{3.7}$$

These mathematical concepts are deeply useful for all four Maxwell equations as well as for other physics problems. Gauss' Law is the first of Maxwell's equations which dictates how the electric field behaves around electric charges. Gauss' Law can be written in terms of the electric flux density and the electric charge density as shown in equation (3.1) [82]. Using the divergence operator, this equation becomes true at any point in space, which means that, if there exists electric charge somewhere, the divergence of electric flux density (D) at that point is nonzero, otherwise it is equal to zero [75].

The second of Maxwell's equations equation (3.2) is based on Gauss' Law for electric field. The Conservation Equation or Gauss' Magnetism Law states that the divergence of the magnetic flux density (B) is zero. Considering that magnets always have a positive and negative end, every magnetic object is a magnetic dipole, with a north and south pole [78]. Based on this physical foundation, no matter how many times the magnets is broken in half, it will just form more magnetic poles. Thus, the Gauss' Law for Magnetism affirms that magnetic monopoles do not exist, or at least nobody has found them yet [76]. In addition, since the divergence of B is always zero, the magnetic field circularly flow into and out of any volume equally, thus, away from magnetic dipoles, magnetic field flow in a closed loop [82].

In 1830, Faraday tested electrical circuits powered by a battery with a magnetic coil originating the third Maxwell equation (equation (3.3)). The Faraday-Lenz law shows that a changing magnetic field within a loop gives rise to an induced current, which is due to a force or voltage within that circuit, the Electromotive Force (EMF) [83]. The left side of this equation, using the rotation operator which is used to measure the tendency of the field lines to circulate around a point, illustrates a mathematical description of the rotation of the electric field. The right side represents the rate of change of the magnetic field over time.

The relationship established in Faraday' Law is very powerful as it shows the symmetry between electric and magnetic field [78]. Firstly, this equation states the magnetic field as a function of time and asked to find the rotation of the induced electric field [82]. Secondly, the expression results in the induced electric field vector and determines the time rate of change of the magnetic field [78]. This means that, if a current gives rise to a magnetic field then a magnetic field can give rise to an electric current [75]. Furthermore, a magnetic field changing in time domain gives rise to an electric field circulating in space around it in the same way that a moving electric field in time causes changes in the magnetic field in time domain [82].

At same that Faraday was working on Faraday's Law, Ampere was experimenting forces on wires carrying electric current [78]. Ampere's law relatesa steady electric current to a circulating magnetic field, however, Ampere's law was known to apply only to static situations involving steady currents [76]. It was Maxwell's addition of another source term, a changing electric flux, that extended the applicability of Ampere's law to time-dependent conditions.

The differential form of the extended Ampere' Law, declares that an electric current or a changing electric flux through a surface produces a circulating magnetic field around any path that bounds that surface [84]. The left side of this equation is a mathematical description of the rotation of the magnetic field while the two terms on the right side represent the electric current density and the time rate of change of the electric field [82]. In other words, a magnetic field is produced along a path if any current is enclosed by the path or if the electric flux through any surface bounded by the path changes over time [75].

Each of the four equations that have come to be known as Maxwell's Equations is powerful in its own right, for each one embodies an important aspect of electromagnetic field theory. However, in order to define the correlation between the different field vectors, the materials equations, constructive relations are associated [81]:

$$D = \varepsilon E = \varepsilon_0 \varepsilon_r E, \tag{3.8}$$

$$B = \mu H = \mu_0 \mu_r H = \frac{1}{\upsilon} H = \frac{1}{\upsilon_0 \upsilon_r} H, \tag{3.9}$$

$$J = \sigma E = \frac{1}{\rho_E} E \ (Ohm's\ law) \tag{3.10}$$

where, ε [F/m] or [A$_s$/m] is the electric permittivity, ε_0 [F/m] or [A$_s$/m] is the electric permittivity of vacuum ($= 8{,}85 \times 10^{-12}\ F/m$), ε_r is the relative electric permittivity, μ [H/m] or [V$_s$/A] is the permeability, μ_0 [H/m] or [V$_s$/A] is the permeability of vacuum ($= 4\pi \times 10^{-7}\ H/m$), μ_r is the relative permeability, υ [m/H] or [A/V$_s$] is the reluctivity tensor, υ_0 [m/H] or [A/V$_s$] is the reluctivity of vacuum ($= 1/\mu_0$), υ_r is the relative reluctivity, σ [S/m] or [A/V$_m$] is the electrical conductivity, ρ_E [Ω m] or [V$_m$/A] is the electrical resistivity.

Often the material parameters have a non-linear field and frequency dependency. The relative permeability and reluctivity of ferromagnetic materials is saturable and converges to unity for high magnetic fields [76]. Electric properties of semiconductors, such as conductivity and resistivity, are conditioned by the applied electric field [76]. The thermal field affects many material properties that influence the electromagnetic fields in a direct or indirect way. These thermal dependencies occur as part of nonlinear coefficients in the electromagnetic equations [84].

Maxwell’s achievement went beyond the synthesis of these laws or the addition of the materials equations and constructive relations. The combination of these equations made it possible to develop a comprehensive theory of electromagnetism. That theory elucidated the true nature of light itself and opened the eyes of the world to the full spectrum of electromagnetic radiation.

3.2 Case of Study

Since nearly all of the phenomena met with in electrical engineering in connection with the relations between electricity and magnetism are involved in the action of electromagnets [75], it is readily recognized that a careful study of this branch of design is necessary in order to predetermine any specific action of the analytical model.

Firstly, the main goal of analytical model is to clarify the behavior of the magnetic field applied to a classic electromagnetic model. As a convergent perspective, it has important choose the simplest magnetic generator models for analytical analysis. In this way, based on section 2.5 Literature Review, in order to create an analytical base model useful for the numerical and experimental simulations, a generic solenoid configuration was selected. This master thesis has endeavored to describe the evolution of the analytical model of a solenoid, by studying the magnetic flux density at the center and several arbitrary positions of the coil.

Secondly, the case study purposed should be integrated into the magnetostatics concepts, the classical physics of the magnetic fields, in which forces and energies are associated with distributions of magnetic material and steady electric currents. Magnetostatics refers to situations where there is no time dependence, which means a non-variation of the magnetic field generated in time domain [77, 84]. Thus, the choice of an electromagnetic model generator, matching different materials with a constant electric current through the winding, and without frequency interference, should be chosen as the case of study of the analytical model.

Thirdly, a FEMM 4.2 simulation of the electromagnetic configuration chosen (solenoid) is required in order to perform a reliable data comparison between the analytical and numerical results. The software considered to run the numerical study of the magnetic field generator model should consider geometrical properties and specific parameters, such as the number of turns (N) , the current (I), and the core permeability (μ). Based on these numerical results of a generic solenoid model, provided by the simulation of a trustworthy software, it will be possible to establish the relationship with the different analytical magnetic equations and to determine the relative error of each analytical approximation model.

In light of this matter, will be used the FEMM 4.2 magnetostatic tutorial [85], which uses Maxwell's equation, to numerically represent the aircored solenoid configuration in open space, which correlates different materials and circuit properties, as previously specified.

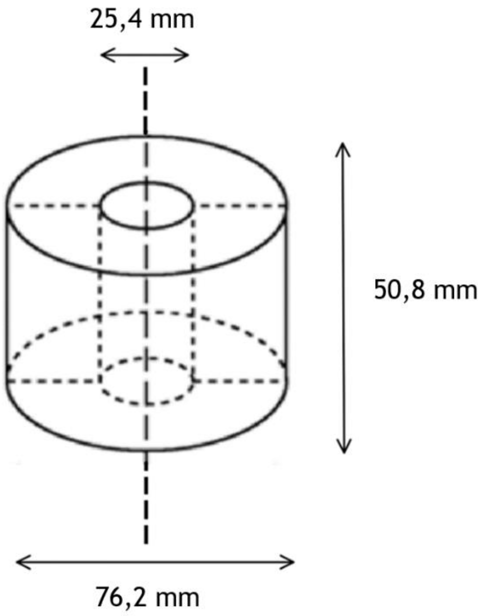

Figure 3.1: Geometric properties of the aircored solenoid used for the case study of Analytical model.

The solenoid to be examined is represented in Figure 3.1. The coil has an axial length of 0.0508 meters; an inner diameter of 0.0254 meters; and an outer diameter of 0.0762 meters. The solenoid is designed with 1000 turns of 18 AWG copper wire. All the materials are selected from Materials Library of the FEMM 4.2, and the air is added to the core of the current model. Furthermore, for the purposes of this solenoid model, a steady current of 1 Ampere flowing through the wire is considered and the frequency is set to zero.

This solenoid represents an axisymmetric model, which by convection means an axial rotation of the drawn section. At the beginning of the numerical analysis, several magnetic problem parameters and setup definitions, such as the boundary conditions, block labels, the mesh, among others parameters, are assumed in order to perform such model simulation. However, they will just be analyzed in detail on Chapter 4.

After modelling the coil and characterizing the magnetic problem regarding materials, number of turns, and current, the FEMM 4.2 tools allow to calculate the value of the magnetic flux density, as well as associated magnetic properties, at a specific location of the space under analysis. *Figure 3.2* shows the FEMM output window, which provide detailed information about the magnetic field at the selected point, allowing a more concrete comparation with the analytical equations.

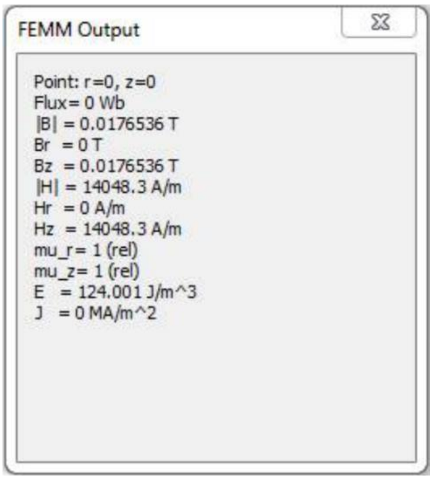

```
Point: r=0, z=0
Flux= 0 Wb
|B| = 0.0176536 T
Br  = 0 T
Bz  = 0.0176536 T
|H| = 14048.3 A/m
Hr  = 0 A/m
Hz  = 14048.3 A/m
mu_r= 1 (rel)
mu_z= 1 (rel)
E   = 124.001 J/m^3
J   = 0 MA/m^2
```

Figure 3.2: FEMM Output window of the case study solenoid model.

In summary, a generic aircored solenoid is numerically validated using finite element method magnetics software, which uses its package to assign explicit qualities to the coil. With these characteristics, the solenoid is simulated providing information about magnetic flux density at a located point. Considering several points of the numerical model, they will contribute for a magnetic flux density data base which will be correlated with various mathematical magnetic equations in order to clarify which one offers the least relative analytical error. This assumptions will be clearly described in the next section.

3.3 Analytical Validation

The magnetic field can be evaluated by analytical methods or by numerical techniques like finite elements. With a view to expanding the knowledge regarding the magnetic field distribution in a solenoid, the author of this master thesis will establish a relationship between magnetic flux density mathematical equations and FEMM 4.2 numerical results under distinct conditions. Based on the numerical validated results from FEMM 4.2, which consists in solving directly the Maxwell's equations in the different regions, the main objective of the this study is to determine which analytical magnetic flux density formula best represents the behaviour of the magnetic field of a generic solenoid model.

Based on a bibliographic research, a research of possible magnetic flux density equations that are able to represent the behaviour of the magnetic field. Firstly, the focus of the research was on equations which report the magnetic flux action at the centre of the solenoid. In this way, after an extensive literature analysis [75, 78, 76, 84, 86, 87, 88, 89, 90, 91], the selected equations that demonstrate the magnetic flux density behaviour at the geometric centre of a generic solenoid are as follows:

$$B = \frac{\mu_0\, N\, I}{2\, r} \quad (Equation\ 1), \tag{3.11}$$

$$B = \mu_0\, N\, I\ (Equation\ 2), \tag{3.12}$$

$$B = \frac{\mu_0\, N\, I}{L} \quad (Equation\ 3), \tag{3.13}$$

$$B = \frac{\mu_0\, N\, I}{\sqrt{L^2 + 4r^2}} \quad (Equation\ 4), \tag{3.14}$$

where, r [m] is the radius of the solenoid, L [m] is the length of the solenoid. In order to verify which analytical magnetic flux density formula best represents the behaviour of the magnetic field of a generic solenoid model, *Figure 3.3* exhibits the logical procedure to obtain analytical and numerical validated data. Based on the procedure presented in *Figure 3.3*, each equation will be used to calculate the magnetic flux density at the centre of the solenoid.

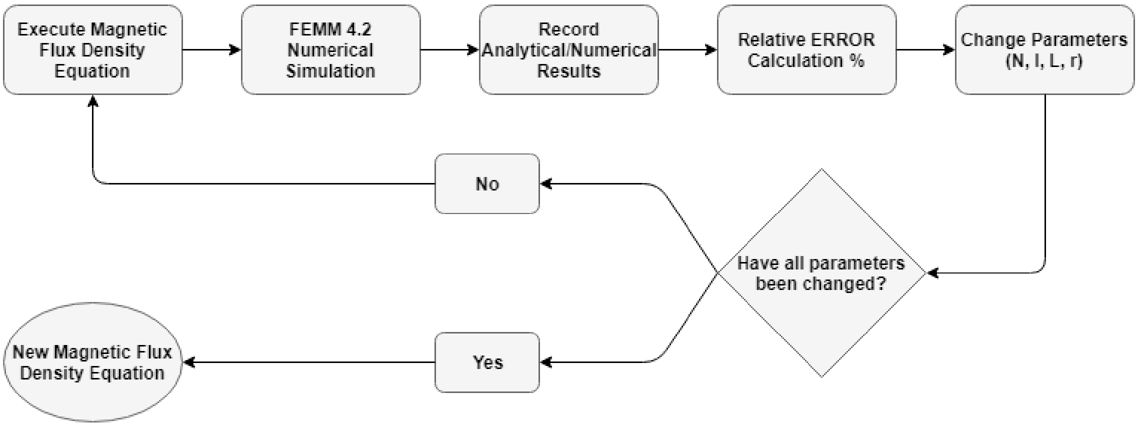

Figure 3.3: Validation of the analytical and numerical data.

Firstly, an equation is selected and executed according to the geometric properties of the general solenoid, conferred in scientific case study. Secondly, based on the tutorial step by step, the solenoid model is performed in FEMM 4.2 as a magnetostatic problem which, through the numerical simulation of the software, the value of the module of the magnetic flux density at the central location of the coil model is extracted from the post-processor window (*Figure 3.2*). Thirdly, after recording the data from the analytical and numerical results, the relative error is calculated as follows:

$$Relative\ ERROR\ (\%) = \frac{Analytical\ Result - FEMM\ 4.2\ Numerical\ Result}{Analytical\ Result} \times 100 \tag{3.15}$$

Fourthly, in order to contribute to a more detailed and comprehensive study about the analytical equations, several magnetic related parameters are changed. In *Table 3.1*, based on FEMM 4.2 Magnetostatic Tutorial, the properties of the case of study model are succinctly described.

Table 3.1: Properties of the tutorial model.

TUTORIAL Parameters		
Number of Turns		1000
Current	[A]	1
Core Radius	[m]	0.0127
Wire Radius	[m]	0.0254
Length	[m]	0.0508
Core Permeability	[H/m]	1.25664E-06
Total Radius	[m]	0.0381

Table 3.2: Properties of the analytical model considering the variation of current.

Variation of CURRENT [I]		
Number of Turns		1000
Current	[A]	3
Core Radius	[m]	0.0127
Wire Radius	[m]	0.0254
Length	[m]	0.0508
Core Permeability	[H/m]	1.25664E-06
Total Radius	[m]	0.0381

Table 3.3: Properties of the analytical model considering the variation of radius.

Variation of RADIUS [m]		
Number of Turns		1000
Current	[A]	1
Core Radius	[m]	0.014
Wire Radius	[m]	0.0254
Length	[m]	0.0508
Core Permeability	[H/m]	1.25664E-06
Total Radius	[m]	0.0394

Table 3.4: Properties of the analytical model considering the variation of length.

Variation of Length [m]		
Number of Turns		1000
Current	[A]	1
Core Radius	[m]	0.0255
Wire Radius	[m]	0.0126
Length	[m]	0.1024
Core Permeability	[H/m]	1.25664E-06
Total Radius	[m]	0.0381

Table 3.5: Properties of the analytical model considering the variation of Number of Turns.

Variation of the Number of Turns		
Number of Turns		1800
Current	[A]	1
Core Radius	[m]	0.0002
Wire Radius	[m]	0.0379
Length	[m]	0.0508
Core Permeability	[H/m]	1.25664E-06
Total Radius	[m]	0.0381

In this phase of the analytical model procedure, the number of turns (N), the current (I), the length (L) and, the total radius (r) of the tutorial solenoid are separately modified, which means that when a parameter is altered, the other parameters remain constant (*Table 3.2*, *Table 3.3*, *Table 3.4*, *Table 3.5*).

Each change suggests a new parameter value which is again performed as input into the magnetic flux density equation and the numerical simulation. Finally, after this operation, when all parameters are modified, the initial tutorial model characteristics are restored and the new magnetic flux density equation arises, repeating all the procedure once again.

Considering all the variations of the parameters mentioned in (*Table 3.2*, *Table 3.3*, *Table 3.4*, *Table 3.5*), all the analytical equations initially selected $Equation\ (1, 2, 3, 4)$. were executed, as well as the numerical simulations in FEMM 4.2 software. Therefore, Table 3.6, *Table 3.7*, *Table 3.8*, Table 3.9 show the results at the center of the generic solenoid model, regarding the different simulated magnetic flux density equations and numerical simulations, as well as the related relative error.

Table 3.6: Relative difference and magnetic flux density results of $equation\ 3.11$.

B [T] Calculation		
TUTORIAL	FEMM 402 Result	0.0176536
	Analytical Result	0.0164913
	ERROR	7.05%
Variation of CURRENT [I]	FEMM 402 Result	0.053153
	Analytical Result	0.0494739
	ERROR	7.44%
Variation of Number of Turns	FEMM 402 Result	0.360578
	Analytical Result	0.2968434
	ERROR	21.47%
Variation of Length [m]	FEMM 402 Result	0.0172709
	Analytical Result	0.015947171
	ERROR	8.30%
Average ERROR		11.06%

Considering the results of the relative difference of $equation\ 3.11$ (Table 3.6), it is possible to conclude that the variation of the number of turns is the one that produces a superior relative error when compared with the other variations. In addition, the tutorial analytical result of the $equation\ 3.11$, is the one that reveals the smallest associated relative error, however, the errors associated with the variation of the current and radius of the solenoid model are also relatively low, suggesting acceptable values of relative error for this analytical performance. Although this equation presents plausible results for all the parameter's variances, it does not have the possibility to vary the length of the solenoid, therefore this fact is seen as the main disadvantage of this analytical option.

Table 3.7: Relative difference and magnetic flux density results of *equation* 3.12.

B [T] Calculation		
TUTORIAL	FEMM 402 Result	0.0176536
	Analytical Result	0.0164913
	ERROR	28.63%
Variation of CURRENT [I]	FEMM 402 Result	0.0531531
	Analytical Result	0.0742109
	ERROR	28.38%
Variation of Number of Turns	FEMM 402 Result	0.0360578
	Analytical Result	0.0445265
	ERROR	19.02%
Variation of Length [m]	FEMM 402 Result	0.0104621
	Analytical Result	0.0122719
	ERROR	14.75%
Average ERROR		22.69%

Regarding *equation* 3.12 results (*Table 3.7*), the variation of the length is recognized as the parameter with the lowest relative error, about 14,85%. Moreover, this analytical equation demonstrates admissible values for the number of turns, contrary to the fact that it presents high values for the tutorial simulation and the variation of the current, when compared with the average of *equation* 3.12 relative error. This equation only allows three analytical variations of the four possible parameters, which are the current, the number of turns, and the length of the solenoid. Thus, the variation of the radius can not be performed, which is seen as a disadvantage of *equation* 3.12.

Table 3.8: Relative difference and magnetic flux density results of *equation* 3.13

B [T] Calculation		
TUTORIAL	FEMM 402 Result	0.0176536
	Analytical Result	0.001256637
	ERROR	1304.83%
Variation of CURRENT [I]	FEMM 402 Result	0.053153
	Analytical Result	0.003769911
	ERROR	1309.93%
Variation of Number of Turns	FEMM 402 Result	0.0360578
	Analytical Result	0.00261947
	ERROR	1494.10%
Average ERROR		1369.62%

Equation 3.13 represents the analytical option with the highest relative error associated. Since this equation presents excessively high values of relative error (*Table 3.8*), it is possible to conclude that it does not adequately represent the behavior of the magnetic flux density at the central location of the solenoid model, so it is automatically neglected.

Table 3.9: Relative difference and magnetic flux density results of equation 3.14.

B [T] Calculation		
TUTORIAL	FEMM 402 Result	0.0176536
	Analytical Result	0.013721591
	ERROR	25.66%
Variation of CURRENT [I]	FEMM 402 Result	0.53153
	Analytical Result	0.41164773
	ERROR	29.12%
Variation of Number of Turns	FEMM 402 Result	0.0360578
	Analytical Result	0.024698864
	ERROR	45.99%
Variation of LENGTH [m]	FEMM 402 Result	0.01772709
	Analytical Result	0.013403353
	ERROR	28.86%
Variation of RADIUS [m]	FEMM 402 Result	0.0104621
	Analytical Result	0.009845097
	ERROR	6.27%
Average ERROR		27.78%

Based on the results of *equation* 3.14 (Table 3.9), the parameter variation whose relative error value is smaller, is the length. All other results of the parameters variation are above the average of the global relative error of *equation* 3.14, showing the variation of the number of turns as the parameter with the highest relative error associated. Since *equation* 3.14 allows the analysis of the radius and the length of the solenoid, it is seen as the main advantage of this analytical equation. This characteristic is not exhibit by any other equation, distinguishing itself from the others essentially by offering a greater number of parameter variations.

Summarizing, based on the results of the average of the relative error for each magnetic flux density equation, *equation* 3.11 is the best solution, with a relevant margin compared to the other analytical equations. Furthermore, *equation* 3.11 provides accurate analysis of the tutorial as well as the variation of the electric current, radius, and length, presenting the lowest values of relative error for these parameters of all the equations. However, for the variation of the number of turns the analytical option that illustrates the lowest relative error value is *equation* 3.12, about 19,02%. Finally, the length variation of the solenoid model is the last missing parameter to be assigned to an analytical equation. Thus, the equation that is capable of performing the most effective analytical approximation of the variation of the length is *equation* 3.14, which has an associated relative error of about 6,27%.

In order to synthesize the work performed until now, analytical analysis of the magnetic flux density at the centre of a generic solenoid as performed, based on a validated numerical model. This investigation fulfilled the objective to better understand the behaviour of the magnetic field inside a solenoid, as well as to interpret which variables influence the most the value of the magnetic flux density in each analytical equation.

With a convergent perspective, in order to satisfy the MECSE mission requirements as well as its payload requirements, it is indispensable to study the value of the magnetic flux density at several positions away from the surface of the magnetic field generator. Therefore, to complete the analytical model, several analytical analysis in different axial positions is performed based on the specification of the same numerical validated model presented in section 3.2 Case of Study. In light of this matter, *Figure 3.4* shows how the analytical model for an arbitrary position of the solenoid generic model will be processed.

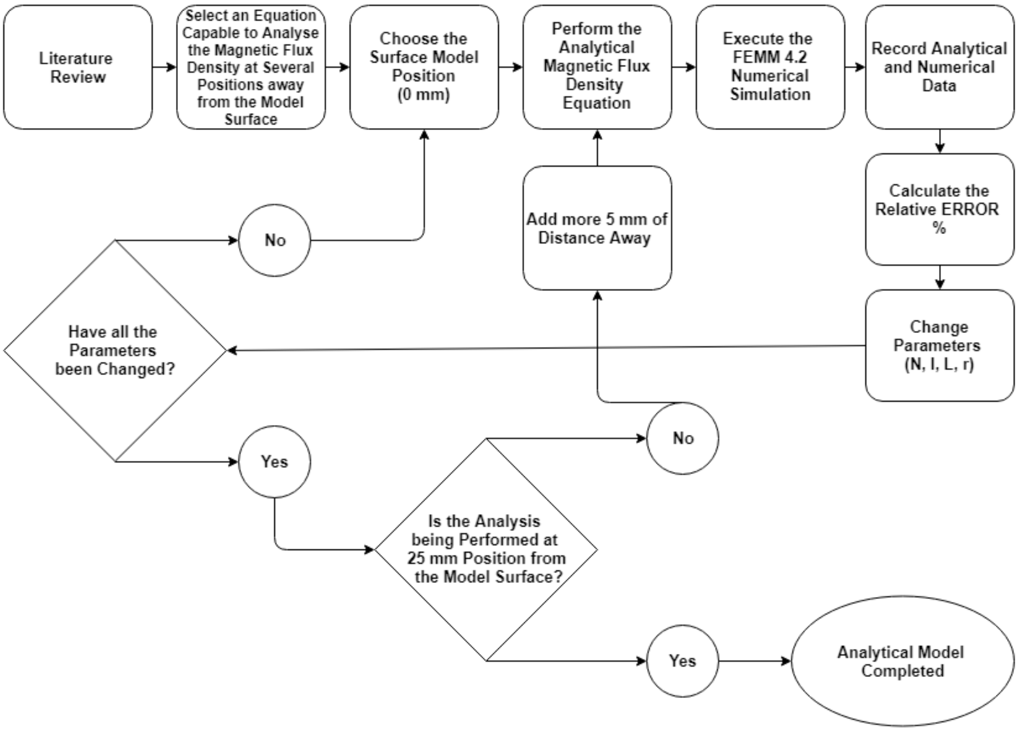

Figure 3.4: Analytical model procedure for an arbitrary position of the generic solenoid.

Firstly, a literature review process is required in order to determine which analytical equation best represents the behavior of the magnetic flux density at an arbitrary axial position. In [75, 77, 78, 76, 84, 86, 89, 91, 92], several investigations about the analytical result of the magnetic flux density at various positions were scrutinized. As a consequence, Maxwell's equations were taken into account to predict the behavior of the magnetic field in free space conditions [77, 78, 76, 84, 92]. However due to its complexity, they have been converted from differential and integral form to analytical mode, as presented in equation (3.16).

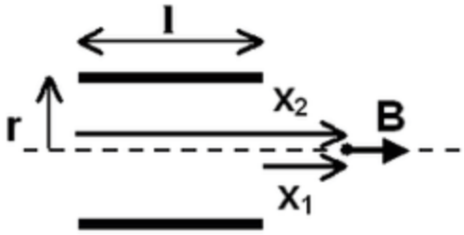

Figure 3.5: Schematic of the analytical analysis for an arbitrary position.

$$B = \frac{\mu_0 IN}{2L}\left[\frac{x_2}{\sqrt{{x_2}^2 + r^2}} - \frac{x_1}{\sqrt{{x_1}^2 + r^2}}\right] \ (Equation\ 5) \tag{3.16}$$

Based on equation 3.16, x_1 and x_2 factors are the distances, along the axial axis, from the ends of the solenoid to the magnetic field measurement point, in meters (*Figure 3.5*). The remaining parameters, proceed with the same designation previously assigned in $Equation\ (1, 2, 3, 4)$.

Secondly, after selecting an equation capable of examining the magnetic flux density data at several positions away from the model surface, it is imperative to start the simulation cycle. Thus, the surface of the solenoid is defined as the fundamental position of the analytical and numerical study, since it is from there that the simulation procedure will advance. Hereupon, at the surface model position the value of 0 mm is assigned, a condition that is considered for the entire analytical procedure.

Thirdly, the magnetic flux density at surface of the model surface will consider the value of x_1 parameter equal to zero, as follows:

$$\begin{gathered} x_2 = L + x_1 \\ x_1 = 0 \implies x_2 = L \end{gathered} \tag{3.17}$$

Considering the model surface as the measurement location, x_2 will be equal to the length of the solenoid (L), as represented in equation (3.17). Thus, the equation of the magnetic flux density $equation$ 3.16 will be presented as follows:

$$\begin{gathered} B = \frac{\mu_0 IN}{2L}\left[\frac{x_2}{\sqrt{{x_2}^2 + r^2}} - \frac{x_1}{\sqrt{{x_1}^2 + r^2}}\right] \\ B = \frac{\mu_0 IN}{2L}\left[\frac{L}{\sqrt{L^2 + r^2}}\right] \\ B = \frac{\mu_0 IN}{2\sqrt{L^2 + r^2}} \end{gathered} \tag{3.18}$$

Fourthly, the FEMM 4.2 numerical simulation is performed regarding the properties and specifications of the case study. After the design and simulation of the solenoid model, will be executed the axial numerical analysis at the surface model location (0 mm position), and the magnetic flux density data is carried out from the FEMM Output Window, as represented in *Figure 3.2*.

Fifthly, the analytical data taken from the equation $x_1 = 0\,;\ x_2 = L$ and the numerical data from FEMM 4.2 simulation results is recorded. Comparing the results of the two different methods, its relative error is calculated following the equation (3.15).

Sixthly, the number of turns (N), the current (I), the length (L), and the radius of the solenoid (r) is changed through the same procedure executed for the analytical analysis of the magnetic flux density at the centre of the solenoid, as previously described. The parameter variation for the surface position (0 mm from the surface model) is performed until all of them are individually changed (*Table 3.2*, *Table 3.3*, *Table 3.4*, *Table 3.5*), restating the previous analytical and numerical operation as well as the data recorded and relative error calculation, as presented in *Figure 3.5*.

When the parameters modification to the initial position (0 mm) is completed, 5 mm will be added to the point under analysis. This condition will act as a new input in the analytical magnetic flux density equation and the FEMM 4.2 numerical simulation, similarly executing the parameter variation procedure used for the initial position. As the simulation progresses, the addition of 5 mm is performed until the analytical and numerical analysis for the 25 mm position of the model surface are verified.

Table 3.10: Relative difference and magnetic flux density results at 0 mm relative position.

B [T] Calculation		
TUTORIAL	FEMM 402 Result	0.0111288
	Analytical Result	0.00989478
	ERROR	12.47%
Variation of CURRENT [I]	FEMM 402 Result	0.0833865
	Analytical Result	0.02968434
	ERROR	12.47%
Variation of Number of Turns	FEMM 402 Result	0.0206921
	Analytical Result	0.017810604
	ERROR	16.18%
Variation of LENGTH [m]	FEMM 402 Result	0.0109062
	Analytical Result	0.009773434
	ERROR	11.59%
Variation of RADIUS [m]	FEMM 402 Result	0.00580303
	Analytical Result	0.005750764
	ERROR	0.91
Average ERROR		10.72%

Considering the axial relative position of 25 mm from the model surface, at the end of recording the data of the analytical and numerical simulation, and after executing of the calculation of the relative error for all the parameter variations at this position, the analytical model is finally completed. In *Table 3.10*. *Table 3.11*, *Table 3.12*, *Table 3.13*, *Table 3.14*, *Table 3.15*, the results of the whole procedure are presented. For each relative position (0 to 25 mm from the model surface) under analysis, the information based on the analytical and numerical results of the magnetic flux density is provided, as well as the description of the relative percentage error for the tutorial case and for all the parameter variables of the analytical equation.

Table 3.11: Relative difference and magnetic flux density results at 5 mm relative position.

B [T] Calculation		
TUTORIAL	FEMM 402 Result	0.00860299
	Analytical Result	0.008605162
	ERROR	0.03%
Variation of CURRENT [I]	FEMM 402 Result	0.025809
	Analytical Result	0.025815487
	ERROR	0.03%
Variation of Number of Turns	FEMM 402 Result	0.0128188
	Analytical Result	0.015489292
	ERROR	17.24%
Variation of LENGTH [m]	FEMM 402 Result	0.00859403
	Analytical Result	0.008546528
	ERROR	0.53%
Variation of RADIUS [m]	FEMM 402 Result	0.00500363
	Analytical Result	0.004984435
	ERROR	0.39%
Average ERROR		3.65%

Table 3.12: Relative difference and magnetic flux density results at 10 mm relative position.

B [T] Calculation		
TUTORIAL	FEMM 402 Result	0.00659202
	Analytical Result	0.007340726
	ERROR	10.20%
Variation of CURRENT [I]	FEMM 402 Result	0.0197761
	Analytical Result	0.022022177
	ERROR	10.20%
Variation of Number of Turns	FEMM 402 Result	0.00927006
	Analytical Result	0.13213306
	ERROR	28.84%
Variation of LENGTH [m]	FEMM 402 Result	0.00701223
	Analytical Result	0.007336887
	ERROR	4.42%
Variation of RADIUS [m]	FEMM 402 Result	0.00415218
	Analytical Result	0.004253433
	ERROR	2.38%
Average ERROR		11.41%

Table 3.13: Relative difference and magnetic flux density results at 15 mm relative position.

B [T] Calculation		
TUTORIAL	FEMM 402 Result	0.00504018
	Analytical Result	0.00617266
	ERROR	18.35%
Variation of CURRENT [I]	FEMM 402 Result	0.0151206
	Analytical Result	0.01851798
	ERROR	18.35%
Variation of Number of Turns	FEMM 402 Result	0.00654962
	Analytical Result	0.011110788
	ERROR	41.05%
Variation of LENGTH [m]	FEMM 402 Result	0.0051902
	Analytical Result	0.006210888
	ERROR	16.43%
Variation of RADIUS [m]	FEMM 402 Result	0.00337613
	Analytical Result	0.003588488
	ERROR	5.92%
Average ERROR		20.02%

Table 3.14: Relative difference and magnetic flux density results at 20 mm relative position

B [T] Calculation		
TUTORIAL	FEMM 402 Result	0.00381145
	Analytical Result	0.005142843
	ERROR	25.89%
Variation of CURRENT [I]	FEMM 402 Result	0.0114344
	Analytical Result	0.01542853
	ERROR	25.89%
Variation of Number of Turns	FEMM 402 Result	0.00501145
	Analytical Result	0.009257118
	ERROR	45.68%
Variation of LENGTH [m]	FEMM 402 Result	0.00401669
	Analytical Result	0.00520924
	ERROR	22.89%
Variation of RADIUS [m]	FEMM 402 Result	0.0271495
	Analytical Result	0.003006751
	ERROR	9.70%
Average ERROR		26.05%

Based on the results presented in Table 3.23. Table 3.24, Table 3.25, Table 3.26, Table 3.27, Table 3.28, it is possible to conclude that the average relative error between the analytical and the numerical results increases with the distance from the model surface, which means that as the axial distance from the solenoid surface to the point under analysis increases, the associated average relative error will increase too. However, analysis performed at the initial point (0 mm from the model surface) do not follow this trend because the results of the relative error at this position have higher values than the results at 5 mm distance.

Table 3.15: Relative difference and magnetic flux density results at 25 mm relative position

B [T] Calculation		
TUTORIAL	FEMM 402 Result	0.00293317
	Analytical Result	0.004265562
	ERROR	31.24%
Variation of CURRENT [I]	FEMM 402 Result	0.00879952
	Analytical Result	0.012796685
	ERROR	31.24%
Variation of Number of Turns	FEMM 402 Result	0.0385518
	Analytical Result	0.007678011
	ERROR	49.79%
Variation of LENGTH [m]	FEMM 402 Result	0.00312309
	Analytical Result	0.004347862
	ERROR	28.17%
Variation of RADIUS [m]	FEMM 402 Result	0.00219231
	Analytical Result	0.002512451
	ERROR	18.74%
Average ERROR		30.63%

Furthermore, in all the simulations performed, the variation of the number of turns (N) is the parameter which presents the highest relative error. The longer the distance from the model surface to the point under study, the greater the relative error associated with the variation of the number of turns. On the other hand, comparing the analytical and the numerical results, the parameter with the lowest relative error associated is the variation of the solenoid length (L). However, simulations performed at 5 mm away from the solenoid surface show the best results for the tutorial case and, with the same value of relative error (about 0,03%), the variation of current (I).

Finally, based on MECSE payload requirements, the analytical results of the behaviour of the magnetic flux density (B) at 25 mm from the generic solenoid surface exhibit 30,63% of average relative error. Nevertheless, the analytical model for an electromagnetic generator (solenoid) has promising results for short distances, presenting its best approximation of the magnetic flux density performance to 5 mm of distance from the surface of the solenoid model (3,65%).

In order to progress in the design process of the magnetic field generator, it is essential to create a numerical model capable of providing results with lower associated errors, getting closer to the experimental results. In the next chapter, the method behind the numerical analysis as well as the FEMM 4.2 numerical results of the magnetic field generator applied to the MECSE CubeSat are explained. In Chapter 4, it is possible to investigate all the specifications of the FEMM 4.2 Magnetostatic in order to better understand the software characteristics and its constrains.

Chapter 4

4 Numerical Model

An accurate knowledge of the magnetic field distribution is necessary for the computation of useful quantities such as self and mutual inductances, stored energy and electromagnetic forces. The magnetic field can be evaluated by analytical methods or by numerical techniques as finite elements. Finite elements simulations give accurate results considering the nonlinearity of ferromagnetic materials for iron-cored coils.

In this Chapter the main characteristics and functions of the FEMM open source software are presented. In order to demonstrate its use and exhibit the aid it offers in the study of electromagnetics an illustrative example is given. Therefore, the aim of Chapter 4 is to demonstrate the method of the numerical model considering an electromagnet case study. As a conclusion of this chapter, based on an optimization process, the numerical results of the electromagnet model are presented, suggesting the final model to be tested through the experimental procedure.

4.1 FEMM – Open Source Finite Element Software

4.1.1 Overview

The finite element method (FEM) is a computational method which can be applied to acquire solutions to a variety of problems in engineering and science. Steady, transient, linear and nonlinear problems in electromagnetics, structural analysis, and fluid dynamics may be analysed and solved with it, [93]. This method incorporates geometrical adaptability and material properties definition for modelling arbitrary geometries without a need to reform the formulation of the computer code that implements it.

The theory of this method is to divide / discretize the problem domain into a large number of subdomains, called finite elements, each with a simple geometry resulting in the transformation of the initial problem from a small but difficult to solve into a big but an easy to solve [81]. In the electromagnetics a discretization scheme, such as the one that FEM implies, which implicitly associates most of the theoretical features of the problem under analysis is one of the best solutions to get accurate results in a variety of problems.

Software has been developed for this reason addressing some limiting cases of Maxwell's equations (section 3 Analytical Model) [94]. The software package is a suite of programs for solving low frequency electromagnetic problems on two dimensional planar and axisymmetric domains, in which displacement currents can be negligible. Displacement currents are typically relevant to magnetics problems specifically at radio frequencies domain [93].

Furthermore, the software currently addresses linear/nonlinear magnetostatic problems, linear/nonlinear time harmonic magnetic problems, linear electrostatic problems, and steady-state heat flow problems [93]. In order to provide results for these types of problems, the package is composed of an interactive shell encompassing graphical pre- and postprocessing; a mesh generator; and various solvers [95]. FEMM is divided into three sections [93, 94, 95]:

- Interactive shell (*femm.exe*). For the various types of problems solved by FEMM, this section represents a Multiple Document Interface pre-processor and a post-processor. Firstly, it contains a CAD interface for laying out the geometry of the problem to be solved as well as for defining material properties and boundary conditions. Secondly, Autocad DXF files can be imported to simplify the analysis of existing geometries. Field solutions can be displayed in the form of density plots and contours. Finally, the program also allows the user to examine the magnetic field behavior at arbitrary points, as well as to evaluate a number of different integrals used and to plot various quantities of interest along user-defined contours.

- Mesh generator (*triangle.exe*). Based on the finite element method, the formed mesh breaks down the solution region into a large number of or elements, contributing to a better approximate solution.

- Solvers (*fkern.exe* for magnetics; *belasolv* for electrostatics); *hsolv* for heat flow problems; and *csolv* for current flow problems. In order to obtain values for the desired field across the solution domain, each solver takes a set of data files describing the problem and solves the relevant Maxwell's partial differential equations.

FEMM is an open-source, easy-to-use, accurate and low-cost computer software with many applications in electromagnetism, materials science, industry, experimental and particle physics, robotics, astronomy, space engineering and education [85]. In this chapter, it will be shown that FEMM is a useful tool for an in-depth study of electromagnetics, more specifically in the area of magnetostatic problems, suitable for scientists and engineers.

4.2 Simulation Environment Setup

After presenting the FEMM software content and tools, it is crucial, for the construction and validation of the numerical model, to define the conditions and requirements of the electromagnetic field generator (EMG) applied to the MECSE CubeSat.

Considering the diagram presented in Figure 4.39, firstly, the numerical software FEMM will use the Maxwell's equation to simulate the magnetic flux density under several specific geometries, materials, boundary, and circuit conditions.

Secondly, based on the Maxwell's equations, the magnetic flux density has different behaviour for low or high frequencies. The frequency domain confers the oscillation range of the magnetic field, which is associated with the performance of harmonic analysis in FEMM [93, 95]. At low frequency terms, the reduction of the magnetic field oscillation magnitude is observed, when compared to the operation at high frequencies. Thus, considering a constant value of 0.0375 tesla as a MECSE mission and payload requirement (*Table 2.7*), the low frequency domain is adopted in order to perform the numerical model of the electromagnetic generator. The frequency used in the EMG numerical model simulation is zero because it provides a constant behavior of the magnetic flux density without oscillation.

Thirdly, the FEMM numerical software can provide special conditions for electrostatics and magnetics simulations, which are associated with the low frequency domain. As investigated in section 2.5 Literature Review, this master thesis is focused on the influence of the magnetic field in plasma layer. The study of electrostatics numerical performances considers the cases in which the frequency is neglected [93].

Fourthly, two distinct techniques are correlated with magnetic problems, which are the magnetostatics and magnetodynamics. In the magnetostatic domain, the system considers static currents which are not changing with time. The current is fixed in pre-processor properties, which will provide non-variation of the magnetic flux density at a specific point analysis, performed in the FEMM postprocessor [94]. On the other hand, the magnetodynamics numerical problem conditions, are analogue to electrodynamics in the study of the dynamics of magnetic systems, which implies the addition of current variation in time domain. These facts suggest a numerical model based on magnetostatics concepts, taking into account the non-variation of current as an EMG requirement.

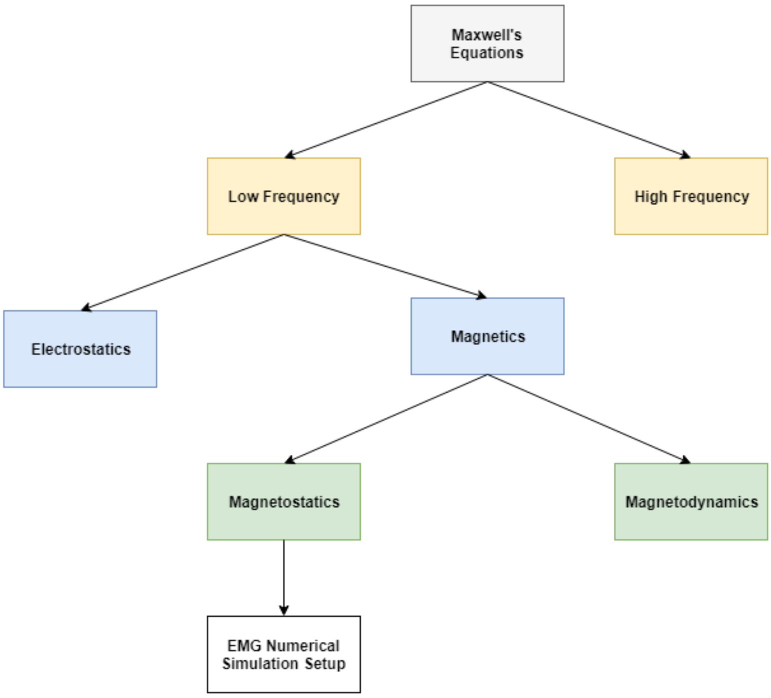

Figure 4.1: Logic process of EMG numerical simulation environment.

Finally, having defined the type of problem as well as the theoretical procedure of the initial conditions of the EMG numerical simulation model, it is necessary to specify how the EMG requirements will be numerically processed for its adaptability, magnetic flux density, mass, and power.

4.2.1 Adaptability

Considering the basic structure of the MECSE CubeSat (3U), as discussed in the section 2.5 Literature Review, the EMG is constrained to 1U (*Figure 2.8*), the remaining 2U are reserved for components necessary for the operation of the spacecraft.

Thus, the numerical simulations of the different models considered is performed in such a way that the EMG model is able to fit within 1U, as presented in *Figure 4.3*. For the performance of the numerical model, considering the MECSE mission and payload requirements, the height, width and length of the EMG model will be restricted to 9 cm. In addition, considering the objectives of the MECSE mission, one of the most innovative objectives is the study of the layer of plasma manipulated through a magnetic field, to allow communication during the re-entry phase. In order to establish communication between the vehicle and the ground station, it is essential that the magnetic field surrounds the MECSE communication antenna. Studies of the position of the antenna of the MECSE project are not being carried out, thus, the EMG model must be adaptable in order to reproduce the magnetic field in any desired direction. Hence, for the numerical model, geometries of magnetic field generating models capable of acting in any direction of the 1U destined to the MECSE CubeSat payload will be considered.

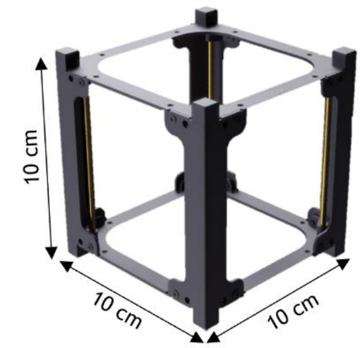

Figure 4.3: Geometric properties of standard CubeSat unit (1U)

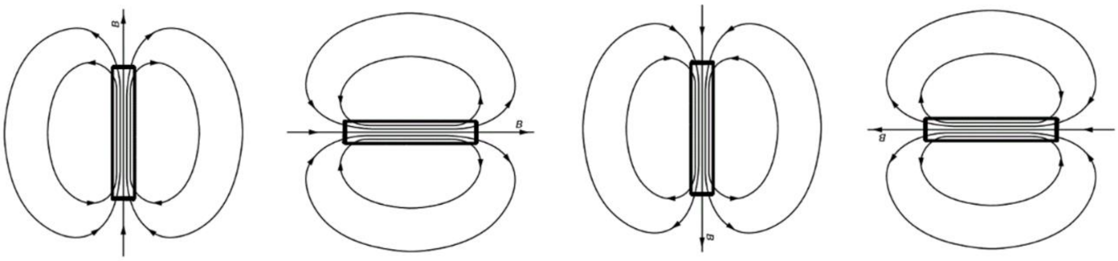

Figure 4.2: Schematic of EMG model considering the adaptability factor

4.2.2 Magnetic Flux Density

Considering the maximum length of the Langmuir Probe (LP) of 25 mm, the value considered necessary for the reduction of plasma density must act at that specific position. It means that, a magnetic field intensity value of 0.0375 T at the LP position was assumed as a numerical simulation requirement. A schematic scene is represented in Figure 4.42.

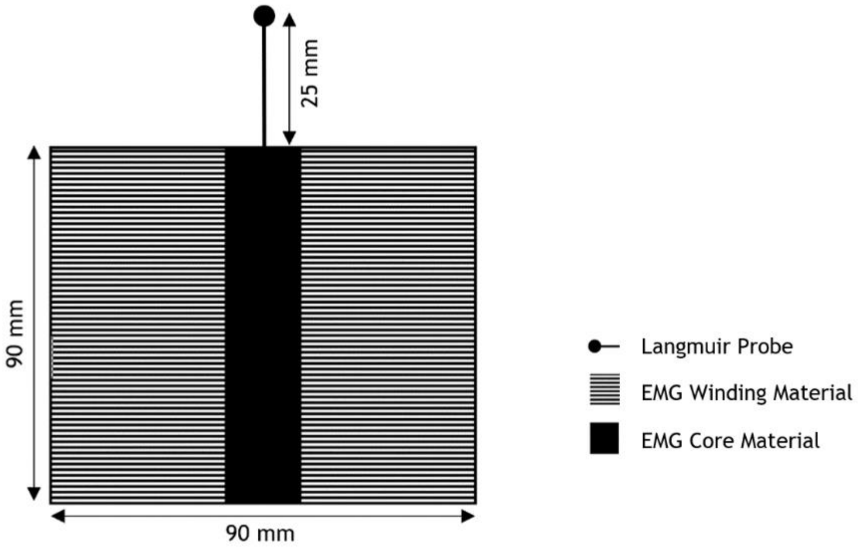

Figure 4.4:Schematics of the EMG model with the LP.

In addition, the performance of the EMG numerical model will consider the results of the magnetic flux density for several positions, from the surface to the LP position. Thus, 5 mm intervals were assumed from the 0 mm position (model surface) to 25 mm (LP position), analyzing a total of 6 axial positions in each simulated numerical EMG configuration(0, 5, 10, 15, 20, 25 mm from the model surface).

4.2.3 Mass

CubeSat 3U standard configuration constrains both the volume and the mass. Therefore, the EMG numerical model shall be designed and performed with respect to those specifications, according to ECSS (European Cooperation for Space Standardization) requirements.

Table 4.1: MECSE mass budget *[37]*.

Subsystem	ID	Mass [kg]
Structure	Side Frames	0.157
	Rib 1	0.009
	Rib 2	0.009
	Rib 3	0.009
	Rib 4	0.009
	Rib 5	0.009
	Rib 6	0.009
	Top Plate	0.097
	End Plate	0.044
	Endless Screw 1	0.004
	Endless Screw 2	0.004
	Endless Screw 3	0.004
	Endless Screw 4	0.004
	Support Antenna	6.5E-4
	Support Antenna	605E-4
	Support Switch	0.006
	Support Switch	0.006
Avionics	Payload	1.2
	Antenna	0.1
	Batteries	0.54
	EPM	0.2
	Transceiver	0.075
	AOCS Board	0.206
	OBC	0.077
	Deployment Switches	7.3E-4
MECSE Total Mass	2.78	

Previous mechanical studies performed in [37], define the MECSE payload mass to a maximum of 1.2 kg. In the numerical model simulation, the MECSE payload mass requirement will be considered, however, studies on the mechanical design optimization of the MECSE structure are ongoing in order to provide an increase in the available payload mass.

4.2.4 Power

Since the properties of the electric circuit of the EMG model are related to the power dissipated, it is essential to establish restrictions on the MECSE payload power budget operation. Studies performed in [36], define that the MECSE electrical power subsystem shall be able to supply at least 140 W for the Service module (2U BUS), however, no limitations were set to the payload module. Thus, in order to optimize the power of the EMG model, different configurations and materials will be considered. For this study, several numerical analysis will be performed to understand the impact of different EMG designs on the subsystem power consumption. Concluding, the simulation environment setup is defined regarding the adaptability, magnetic field, mass, and power requirements, as summarized in *Table 4.2*.

Table 4.2: Requirements and specifications of the Numerical Environment Setup.

Simulation Environment Setup	
Requirements	Specification
Adaptability	Fit in 1U CubeSat Be able to be applied in different positions, within 1U CubeSat
Magnetic Flux Density	Provide 0.0375 tesla at 25 mm from the model surface
Mass	< 1.2 kg
Power	No Constraints

4.3 Case Study: Electromagnet

Having defined the basic conditions for the use of FEMM 4.2 software in problems related to magnetostatic, as well as the numerical setup of the EMG model applied to MECSE, in this section the numerical procedure of a cylindrical electromagnet is presented, and the materials to be used for the numerical simulation of the EMG model and some auxiliary analytical formulas are defined, such as the calculation of the number of turns, the total length of copper wire, the total mass of the model, among others, will be examined in order to construct a more accurate numerical model.

4.3.1 Design

As specified in Chapter 2 and Chapter 3, a cylindrical electromagnetic configuration will be used to create the EMG numerical model applied in the MECSE CubeSat payload. In order to design a cylindrical electromagnet in FEMM 4.2 software, the axisymmetric problem shall be selected.

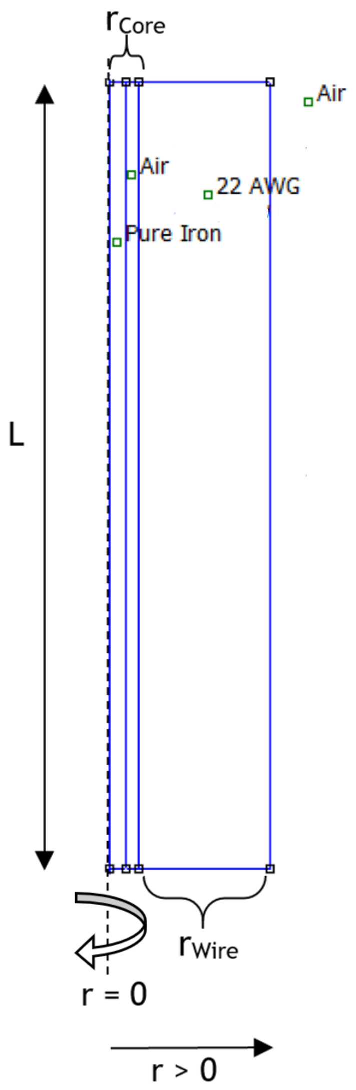

Figure 4.5: Design properties of the axisymmetric electromagnet model.

By convention, the $r = 0$ axis is understood to run vertically, and the problem domain is restricted to the region where $r \geq 0$, which means that half of the numerical EMG model will be constructed on $r \geq 0$ domain, and the other half will be considered symmetrical with respect to $r = 0$ axis. To better understand the axisymmetric problem characteristics, *Figure 4.5* represents an illustrative model of a generic cylindrical electromagnet.

In order to draw the geometry of a generic cylindrical electromagnet model, firstly, it is important to define the radius of the core and the winding, represented in the *Figure 4.5* by r_{core} and r_{wire} respectively. In this design phase, based on the EMG adaptability requirements, the following condition must be guaranteed:

$$0 \leq r_{core} + r_{wire} \leq 45\, mm. \tag{4.1}$$

In addition, unlike the radius (r), the length (L) of the electromagnet will not undergo rotation around $r = 0$, thus, based on the EMG adaptability requirements, this design parameter of the numerical model must be comprised between the following values:

$$0 \leq L \leq 90\,mm \tag{4.2}$$

The length (L) of the cylindrical electromagnet numerical model will be equal to the core and to the wire path, since the winding will be carried out over the entire length of the core.

Note that, in order to promote the simple physical construction of the numerically simulated model, the magnetic core will be surrounded by a plastic structure that will support the copper winding, as specified in Chapter 5. Thus, during the layout phase of the EMG numerical model, in all cases, the core radius will consist of two types of radius, the radius of the magnetic material and the radius of the plastic structure.

Since the plastic structure will not influence the magnetic flux density value generated by the EMG model, only the study of the relationship between the radius of the magnetic material and the radius of the winding has been performed. In order to determine the radius of the plastic structure, the production conditions of the plastic structure designed by CEiiA must be taken into account. Thus, for the numerical simulation performed by FEMM 4.2, the value of the radius of the plastic structure was fixed as:

$$r_{plastic\ struture} = r_{air} = 3{,}8\,mm \tag{4.3}$$

In the next section, the assignment of the air material to the plastic structure, presented in the previous condition is clarified, as well as the selection of the other materials performed in the EMG numerical model.

4.3.2 Materials Selection

The FEMM 4.2 Magnetic Problems has a materials library which allows selecting the most suitable materials according to the conditions of the magnetostatic problem. In this section, the selected core and winding materials as well as its magnetic properties performed in the numerical model simulation are clarified.

As already mentioned in section 4.1, several types of materials are capable of being implemented in a cylindrical electromagnet. Considering the electromagnet core, only four groups will be selected in the list provided by *Figure 4.6*: PM Materials (Paramagnetic Materials), Soft Magnetic Materials, and Air.

In the solenoid case, addressed in Chapter 3, the air is assigned to the core material, however, in the numerical analysis, the cylindrical electromagnet core requires a material with a higher relative permeability in order to provide an increase in the magnetic flux density generated. In light of this matter, Pure Iron is assumed as the most suitable for the construction of the cylindrical electromagnet model. Considering the B-H curve (*Figure 4.6*), of all types of materials considered, it is the one with the greatest magnetic flux density value. In addition, Pure Iron has a high relative permeability value, which, according to equation (3.18), is linearly dependent on the magnetic flux density [94].

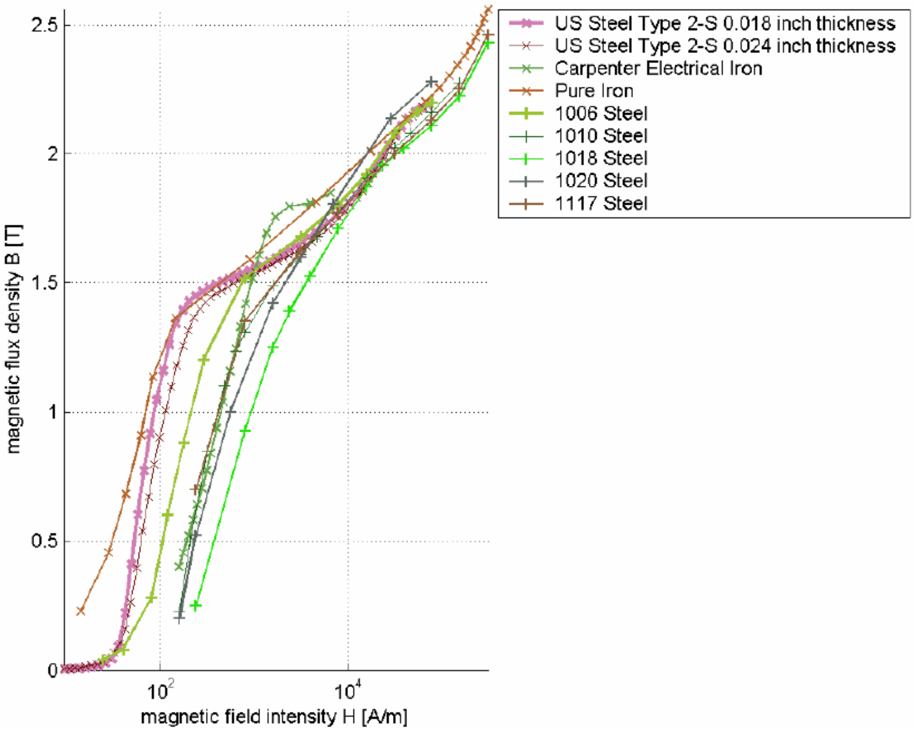

Figure 4.6: Magnetic performance of FEMM 4.2 Soft magnetic materials *[94]*.

Furthermore, as mentioned in the last section 4.3.1 Design, considering the simulation of the numerical model, the cylindrical electromagnet core consists of a magnetic material (Pure Iron) and a material that does not influence the magnetic field (Plastic). Since the plastic is not listed in the material library provided by FEMM 4.2, it is important to choose a material that does not influence the behavior of the magnetic field. Thus, for the EMG numerical model, air is assumed as the substitute element for the traditional plastic, because of all the materials presented by the FEMM library, it is the one with the lowest permeability value [94].

Consequently, the selection of the coil winding material will be subjected to the same process as the core material assignment. In the FEMM 4.2 materials library, only two extended groups were considered, Copper AWG Magnet Wire and Copper SWG Magnet Wire (*Figure 4.7* and *Figure 4.8*. These types of copper wire are seen as the most usual in building a coil.

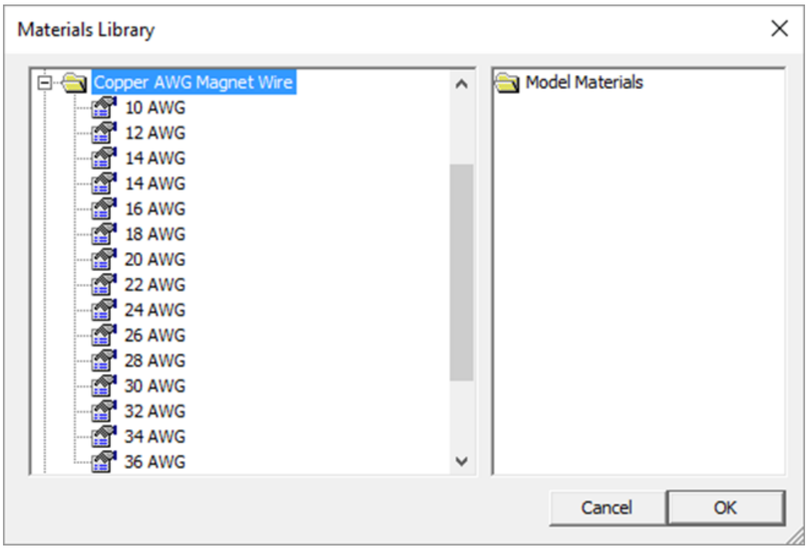

Figure 4.8: AWG Magnet Wire FEMM 4.2 list.

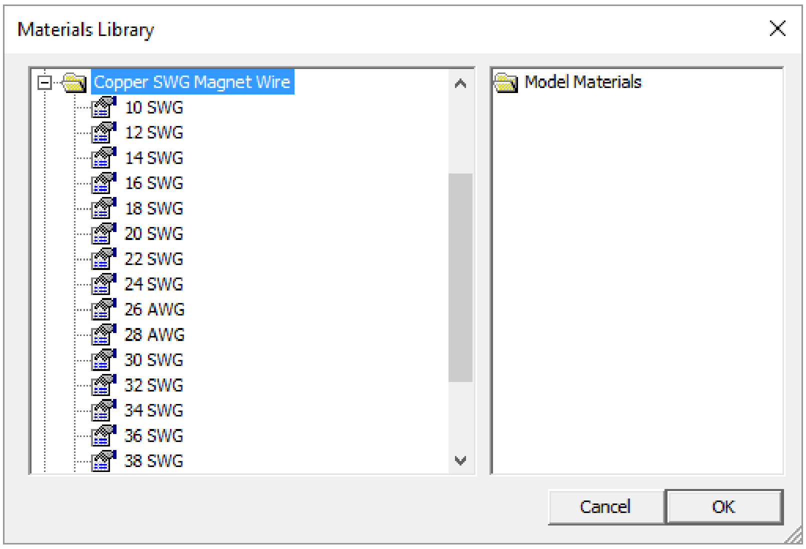

Figure 4.7: SWG Magnet Wire FEMM 4.2 list.

All the thirty materials shown in Figure and Figure, where the value of the diameter is the differentiating factor between them, in addition to the maximum current allowed. However, there is a tight relationship between AWG and SWG copper wire diameter. Hence, the type of AWG copper wire was selected for the numerical simulation of the EMG model.

Based on *Table 4.3*, the respective tabulated diameter ($D_{Theoretical}$) for this type of copper wire does not include a small layer of varnish which was assumed as about 5% of $D_{Theoretical}$. Thus, the real wire diameter will actually be larger than the tabulated value:

$$D_{real} = D_{Theoretical} \times 1{,}05, \qquad (4.4)$$

where, D_{real} is the actual diameter of copper wire used in numerical EMG simulation.

Another important property, to be considered for the implementation of the winding circuit, is the maximum current supported by copper wire. In *Table 4.3* is presented the theoretical diameter as well as the specifications of each copper wire.

Table 4.3: Real diameter and maximum current of AWG copper wire.

AWG	Theoretical Diameter [mm]	Real Diameter [mm]	Maximum Current [A]
8	3.264	3.4272	25.1
10	2.588	2.7174	15.8
12	2.053	2.15565	9.90
14	1.628	1.7094	6.27
16	1.291	1.35555	3.90
18	1.024	1.0752	2.45
20	0.08118	0.85239	1.71
22	0.6438	0.67599	0.965
24	0.5106	0.53613	0.612
26	0.4049	0.425145	0.378
28	0.3211	0.337155	0.242
30	0.2546	0.26733	0.147
32	0.0219	0.211995	0.094
34	0.1601	0.168105	0.060
36	0.1270	0.13335	0.039

In order to summarize all the winding information used for the numerical EMG model, *Table 4.3* shows the relationship between the real and theoretical diameter and the maximum current in the different types of copper wire available by the FEMM 4.2 software.

4.3.3 Number of Turns and MMF

Based on *Figure 4.9*, it is possible to identify which design region is destined to the winding of copper wire, being its area translated by the following expression:

$$A_{wire} = r_{wire} \times L \tag{4.5}$$

Considering the area intended for the copper wire, the most appropriate technique to determine the maximum number of turns is given by two iterative calculations. Firstly, it is required to calculate how many times the real diameter of the chosen copper wire *Table 4.3* fits on each of the horizontal (r_{wire}) and vertical (L) geometric model axes *Figure 4.9*. On each geometric model axis, the result of the arithmetic calculation, is the greatest integer number that is less than or equal to the number of turns value.

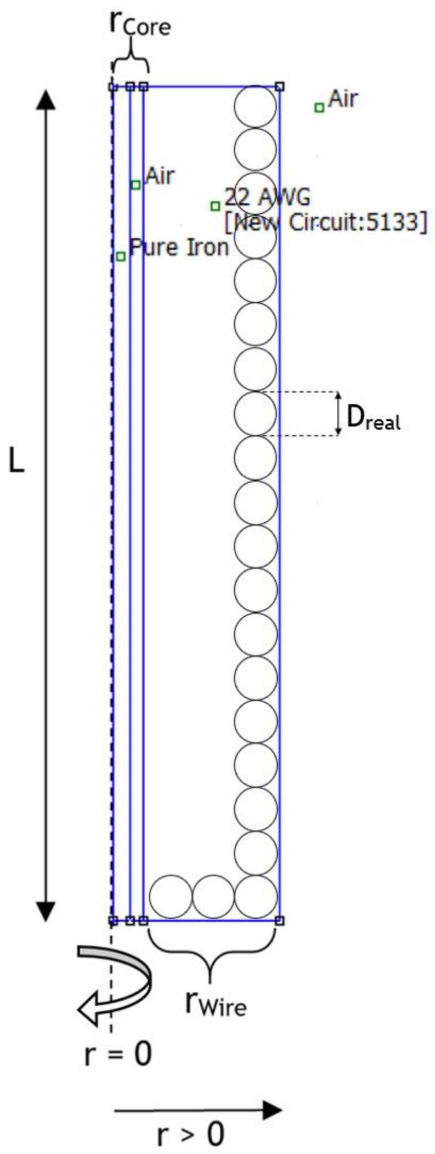

Figure 4.9: Real diameter of the copper wire in the design of the axisymmetric electromagnet model.

In order to verify the maximum number of turns for an arbitrary EMG numerical design, the second step is to perform the product between the number of turns given in each direction of the design axis (r_{turns} and z_{turns}). Hence, the calculation of the number of turns, considering the area destined to the winding of copper wire, can be translated in the following system of equations:

$$\begin{cases} r_{turns} = \left\lfloor \frac{r_{Wire}}{D_{real}} \right\rfloor \\ z_{turns} = \left\lfloor \frac{L}{D_{real}} \right\rfloor \\ N = r_{turns} \times z_{turns} \end{cases} \tag{4.6}$$

As examined in the Analytical Model (Chapter 3), the magnetic flux density is influenced by the number of turns and the current imposed on the winding of the cylindrical electromagnet model. These parameters can be related by magnetomotive force (MMF). In fact, the MMF produced by the cylindrical electromagnet case study is:

$$MMF = N \times I, \tag{4.7}$$

where, N represents the maximum number of turns of the coil winding travelled by the current (I).

Disregarding in the analysis of the devices the magnetic nonlinearity and the losses in the core, introduces simplifications that facilitate the study of this type of electromagnetic models. Therefore, the assumption is that the magnetic flux density in the magnetic circuit and the MMF produced by the cylindrical electromagnet are directly proportional.

4.3.4 Mass Calculation

In this section, will be reviewed step by step all of the processes required to determine the total mass of the EMG. Several parameters are considered, such as the density of the materials used, the total length of the copper wire, the diameter of the copper wire, among others.

For the calculation of the mass of the core, it is important to define the materials selected for the numerical simulation. Based on section 4.3.2 Materials Selection, Pure Iron and Air were chosen as the core materials of the cylindrical electromagnet.

After characterizing the core materials of the case study model, the two dimensional FEMM numerical simulations will be converted to a three dimensional model, in order to determine the total mass of the cylindrical electromagnet model. Thus, the total volume of the core (V_{core}) is equal to the sum between the air volume (V_{air}) and the Pure Iron volume $(V_{pure\ iron})$, as represented in equation 4.8.

$$\begin{gathered} V_{core} = V_{air} + V_{pure\ iron} \\ r_{core} = r_{air} + r_{pure\ iron} \end{gathered} \tag{4.8}$$

Since the case study considered has a cylinder geometric shape, the total volume of the core has been restructured by equation 4.9.

$$V_{core} = L \times \pi \times (r_{air} + r_{pure\ iron})^2, \tag{4.9}$$

where, r_{air}, air's radius $[mm]$ $(r_{air} = 3{,}8\ mm)$, $r_{pure\ iron}$, core's radius [mm]. Then, by implementing the density of pure iron and air, it is possible to estimate the total mass of the cylindrical electromagnet core.

$$\rho_{Pure\ Iron} = 7{,}874 \times 10^{-3}\ [g/mm^3]$$
$$\rho_{air} = 1{,}225 \times 10^{-6}\ [g/mm^3]$$

Following the identical interpretation of the volume of the core, the total mass of the case study core (m_{core}) will be formed by the mass of air (m_{air}) with the mass of pure iron ($m_{pure\ iron}$), as shown by the final expression:

$$\begin{gathered} m_{core} = m_{air} + m_{pure\ iron} \\ m_{core} = L \times \left[5{,}557 \times 10^{-5} + {r_{pure\ iron}}^2 \times 2{,}46 \times 10^{-2}\right] \end{gathered} \tag{4.10}$$

As can be seen in the final equation, the design parameters L and $r_{pure\ iron}$ are directly proportional to the total mass of the core of the cylindrical electromagnet. Note that the magnitude of the total mass of the core is given in grams [g].

Having determined the mass of the EMG core, in order to estimate the value of the total mass of the cylindrical electromagnet model, it is imperative to calculate the mass of the copper wire used. Therefore, for the calculation of the mass of the copper wire, the type of copper wire, the diameter of the copper wire, the maximum number of turns, the length of the copper wire and their density must be taken into account, as well as the design parameters. Converting again the FEMM two-dimensional model to a three-dimensional cylindrical problem approximation, the volume of the copper wire is given by the following expression:

$$\begin{gathered} V_{Wire} = V_{Coil} - V_{Core} \\ <=> V_{Wire} = \left(A_{base\ (coil)} \times L_{coil}\right) - \left(A_{base\ (core)} \times L_{core}\right) \\ <=> V_{Wire} = L \times \pi({r_{Coil}}^2 - {r_{Core}}^2), \end{gathered} \tag{4.11}$$

where, $L_{Wire} = L_{Core} = L_{Coil} = L\ [mm]$ and $r_{Coil} = r_{core} + r_{wire}\ [mm]$ is the total radius of the coil, including the core and wire radius.

The first step of winding total mass is to choose the class of the copper wire material (*Table 4.3*), with different strength, maximum current supported, diameter, among other parameters. For the calculation of the copper wire's total mass, the actual diameter of the copper wire was assumed, which are designated as D_{real} (*Table 4.3*).

In order to better understand the calculation of the number of turns presented previously, the area of the FEMM 2-D model for copper wire and the representation of its turns is shown by *Figure 4.9*. Based on these assumptions, for the calculation of the total length of the wire, a circular surface area for the copper wire will be considered. Thus, the perimeter of copper wire surface is represented by the following expression:

$$P_{circle} = 2 \times \pi \times r \tag{4.12}$$

$$P_{wire\,surface} = 2 \times \pi \times \left(\frac{D_{real}}{2}\right) \tag{4.13}$$

As an example, consider only a single turn around the core of the cylindrical electromagnet model, the perimeter of the circle equation is applied to describe the total length of copper wire used to perform the operation, represented by the equation 4.14.

$$Total_{Length\,(1\,turn)} = 2 \times \pi \times (r_{Core} + D_{real}), \tag{4.14}$$

where, $Total_{Length\,(1\,turn)}$ $[mm]$ represents the maximum length of copper wire used to realize one turn around the cylindrical core. Then, when considering a second turn in the direction of the geometric axis r (*Figure 4.9*), the total length of copper wire will consider the real wire diameter as well as its relative position to the core radius. Thus the total length will take a new form as represented in the following equation:

$$\begin{gathered} Total_{Length\,(2\,turns)} = P_{circle\,(1st\,turn)} + P_{circle\,(2nd\,turn)} \\ <=> Total_{Length\,(2\,turns)} = 2 \times \pi \times (r_{Core} + D_{real}) + \; 2 \times \pi \times (r_{Core} + D_{real} + D_{real}), \end{gathered} \tag{4.15}$$

where, $P_{circle\,(1st\,turn)}$ [mm] is the perimeter of the first turn, $P_{circle\,(2nd\,turn)}$ [mm] is the perimeter of the second turn in r geometric axis direction, $Total_{Length\,(2\,turns)}$ [mm] is the maximum length of copper wire used to realize two turns around the cylindrical core in the horizontal geometric axis direction.

If the winding are performed in this order, superimposed on the horizontal geometric axis direction, the wire radius (r_{wire}) (*Figure 4.9*) will be the limiting factor of this process. In fact, r_{turns}, will be the maximum number of perimeters added in the previous equation, which means that if $r_{turns} = 3$, the relative equation $\text{Total}_{\text{Length}}$ will make the sum of 3 perimeters around the cylindrical core ($P_{circle\,(1st\,turn)} + P_{circle\,(2nd\,turn)} + P_{circle\,(3rd\,turn)}$). Thus the maximum length of copper wire only for overlapping turns in horizontal geometrical axis, is given by the equation:

$$Total_{Length\,(r\,axis)} = 2 \times \pi \times \left(\sum_{i=1}^{r_{turns}} r_i\right) \tag{4.16}$$

$$r_i = r_{i-1} + D_{real}, \tag{4.17}$$

being,

$$r_1 = r_{Core} + D_{real}, \tag{4.18}$$

where, r_1 [mm], represents the first radius considered in the winding procedure. To complete the calculation of the total length of the copper wire, the formula above shall be considered and be applied to the length (L) of the cylindrical electromagnet.

Theoretically, the first turn made by the winding around the core is along the coil's length (L), only r_1 is counted, consequently, overlapping turns to r_1 are also made along the length (L), and so on. Thus, the factor that limits the maximum number of turns over the vertical geometrical axis (z) is the z_{turns} parameter. This procedure is translated into the following formula:

$$Total_{Length\ (winding)} = 2 \times \pi \times z_{turns} \times \left(\sum_{i=1}^{r_{turns}} r_i \right) \tag{4.19}$$

Following the specification of equation (4.17) and equation (4.18), In order to determine the final mass of the copper winding of the cylindrical electromagnet, and considering the total length of copper wire used to perform turns around the core (equation (4.19)), it is required to consider the grams per each meter of the winding material chosen. *Figure 4.10* presents the grams per meter, for several AWG copper wires considered in the material selection phase (2.5.5 Magnetic Materials).

AWG	8	10	12	14	16	18	20	22	24	26	28	30	32	34	36
Sm [g/m]	74,6	46,7	29,4	18,5	11,6	7,31	4,59	2,89	1,82	1,15	0,72	0,45	0,28	0,18	0,11

Figure 4.10: Grams per meter of the AWG copper wire.

In *Figure 4.10* the grams per meter (S_m) is associated with each AWG copper wire. As the number of the AWG copper wire number class increases, the diameter of the wire decreases and consequently the grams per meter reduces. The grams per meter of the material aggregated to the total length of the copper winding, gives rise to the following equation, which is used to calculate the final mass of the copper wire:

$$m_{wire} = \frac{1}{10^3} \times \mathrm{S_m} \times Total_{Length\ \mathrm{(winding)}} \tag{4.20}$$

where, m_{wire} $[g]$ represents the total mass of copper wire used in the winding process, $\frac{1}{10^3}$, is the conversion of $[g/m]$ to $[g/mm]$ of the grams per meter of the winding material.

Finally, throughout this section, the procedure for calculating the total mass of the electromagnetic cylindrical model is exposed. The total mass of the electromagnet model is determined by summing the mass of the core with the mass of the copper winding, thus having defined the method for calculating both masses, the following equation summarizes all the parameters considered during this section:

$$m_{TOTAL} = m_{Core} + m_{Wire}$$

$$m_{TOTAL} = \left[L \times \left[8{,}659 \times 10^{-6} + r_{pure\,iron}{}^{2} \times 2{,}46 \times 10^{-2} \right] \right] \left[\frac{2\pi}{10^{3}} \times \mathrm{S_m} \times z_{turns} \times \left(\sum_{i=1}^{r_{turns}} r_i \right) \right] \tag{4.21}$$

4.4 Optimization Process

The main purpose of this section is to optimize the numerical model procedure in order to produce more accurate results. The optimization of the magnetomotive force (MMF) and a study of the convergence of the mesh will be performed in order to promote a more efficient numerical approximation of the magnetic density. Furthermore, the balance of all simulated results is assigned, taking into account the parameters of adaptability, magnitude of the magnetic flux density, mass and power. At the end of applying the referred approaches, the numerical cylindrical electromagnet model with the best results will be presented, where all its geometrical components, as well as parameters related to its electrical circuit, and magnitude of the magnetic field generated will be described.

4.4.1 MMF Optimization

In section 4.2 Simulation Environment Setup, the adaptability requirements of the EMG cylindrical model were defined. Based on these conditions, several numerical tests on the relationship between the magnitude of the magnetic flux density and the dimensions of the iron core were performed.

Magnetic saturation is a material characteristic which is expressed through the surface area of the iron core, thus the results of FEMM 4.2 simulations suggest that the value of 0.0375 tesla at a distance of 25 mm from the surface of the electromagnetic model is generated only for the minimum pure iron radius of 12 mm and a maximum length of 80 mm. Furthermore, due to the magnetic saturation of the material, from 15 mm of pure iron radius, the properties of the magnetic core will no longer have a considerable effect on the generation of magnetic field required at 25 mm.

Thus, with a convergence perspective, since the plastic radius is constant ($r_{plastic} = r_{air} = 3{,}8\,mm$) and the minimum value of pure iron radius is 12 mm, in order to optimize the MMF, the following equation shows that the radius for copper wire (r_{wire}) can take the following range of values:

$$\begin{gathered} r_{pure\,iron} + r_{plastic} + r_{wire} \leq 45\,mm \\ 12 + 3{,}8 + r_{wire} \leq 45 \\ r_{wire} \leq 29{,}2\,mm \end{gathered} \tag{4.22}$$

However, in order to simplify the performance of the MMF optimization procedure, it is considered the minimum EMG winding radius of 1 mm and a maximum of 30 mm, as represented in the following equation:

$$1\,mm \leq r_{wire} \leq 30\,mm \tag{4.23}$$

Since the core and winding length are the same, $L = 80\,mm$ is defined as the minimum value of the winding length considered for the optimization of the magnetomotive force (MMF). In addition, according to EMG adaptability requirements, the maximum length (L) of the cylindrical electromagnet considers values less than 90 mm $(L \leq 90\,mm)$. In order to optimize the MMF value, the procedure will consider the length variation between the following values:

$$80\,mm \leq L \leq 90\,mm \tag{4.24}$$

The geometric parameters of the EMG winding $(r_{wire}\ and\ L)$, influence the total number of turns depending on the copper wire chosen. Thus, through equation (4.7), the number of turns and the maximum current supported by the copper wire are the parameters dependent on the magnetomotive force (MMF).

As mentioned before, the magnetic flux density magnitude and the magnetomotive force (MMF) produced by the cylindrical electromagnet are directly proportional. Several numerical simulations were performed and, based on the magnetic flux density requirements in section , defined $MMF_{minimum} = 4800\ [A\ turn]$ as the minimum value to generate the magnitude of magnetic flux density of 0.0375 tesla at the position of 25 mm of the surface of the cylindrical electromagnetic model. In order to summarize all the information discussed, *Table 4.4* shows the requirements of MMF optimization.

Table 4.4: MMF optimization setup.

MMF Optimization Setup
Real Diameter AWG Copper Wire
Minimum Pure Iron Radius = 12 mm
1 mm ≤ Wire Radius ≤ 32 mm
80 mm ≤ Wire Length≤ 90 mm
MMF Minimum = 3800 ampere-turn

Thus, the MMF optimization setup is ready to run. Under these conditions, a procedure is required to simplify the data acquisition process as well as to promote the iteration of the parameters mentioned in *Table 4.4*. In light of this matter, *Figure 4.11* the procedure considered for optimization of MMF is demonstrated.

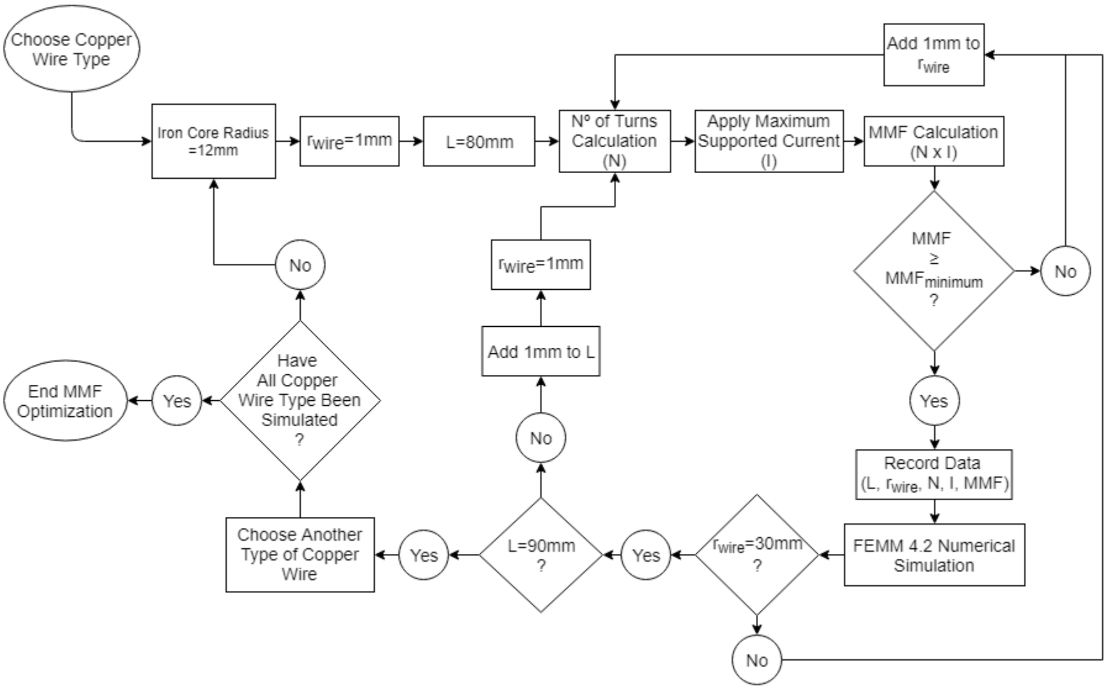

Figure 4.11: MMF optimization procedure.

After executing the diagram, shown in Figure 4.11, all AWG copper wires (section 4.3.2 Materials Selection) were performed considering its real diameter (D_{real}) as well as the geometric winding specifications (r_{wire} and L). At the end of the MMF optimization, the FEMM 4.2 numerical results will be presented, providing several cylindrical electromagnet models, with different properties, capable of generating a minimum magnetic flux density of 0.0375 tesla at a distance of 25 mm from the surface of the EMG model. Furthermore, the pure iron radius will be performed according to the magnetic saturation conditions [$12\ mm \leq r_{pure\ iron} \leq 15\ mm$] in order to optimize the magnitude of the magnetic flux density.

In addition, considering the MMF minimum value, the recorded data of the geometric variables (r_{wire} and L), number of turns (N), maximum current supported by the copper wire (I), and the MMF value generated, will improve the results of the total mass of the model. In other words, considering the same AWG copper wire and a constant EMG length (L), the models which present MMF closest to the MMF minimum, will be the configurations that suggest the least number of turns and consequently a lower mass.

4.4.2 Mesh Convergence

Based on the literature review 4.2.2 Magnetic Flux Density, the magnetic flux density magnitude of 0.0357 tesla seems to be sufficient to manipulate the plasma density under re-entry conditions. In this master thesis, a margin of 5% was established by the bibliography, thus, for all numerical simulations the value of 0.0375 tesla was considered in order to preserve certain associated errors.

Mesh convergence is an important issue that needs to be addressed. Additionally, in nonlinear problems, convergence in the iteration procedure also needs to be considered. Therefore, in the mesh convergence phase, the results of the magnetic flux density value are estimated to have 0.0001 tesla of accuracy, which means that in the worst case, the value of 0.0374 tesla is assured, which is sufficient to reduce the plasma layer, as previously mentioned.

In order to perform the optimization of the mesh, firstly, a generic model shall be used, whose its properties will not change during the convergence study. The characteristics of the solenoid model with air core are described in *Table 4.5*.

Table 4.5: Properties of the aircored generic electromagnet model.

TUTORIAL Parameters		
Number of Turns		1000
Current	[A]	1
Core Radius	[m]	0.0127
Wire Radius	[m]	0.0254
Length	[m]	0.0508
Core Permeability	[H/m]	1.25664E-06
Total Radius	[m]	0.0381

Thus, the method used for the mesh refinement was based on the principle of a constant model configuration in terms of its dimensions, number of turns, materials and current applied in the circuit. In addition, along with model attributes, shown in *Table 4.5*, the boundary conditions were constant throughout the mesh optimization. Considering the properties of the fixed solenoid model as well as its boundary conditions, only the parameters related to the mesh generated by the FEMM 4.2 software will be changed.

The lower the value considered for the mesh size, the greater the number of nodes generated by the mesh, and consequently the more accurate the magnetic flux density results presented by the FEMM 4.2 post-processor. Based on these foundations, the mesh optimization procedure consists in the following steps:

1. Create a mesh using the fewest, reasonable number of elements and analyse the magnetic flux density magnitude in different relative positions of the model;
2. Record information about the time spent on the mesh formation and the number of element/nodes created;
3. Recreate the mesh with a denser element distribution, re-analyse it, and compare the results to those of the previous mesh;
4. Record information about the time spent on the new mesh formation and the number of element/nodes created;
5. Keep increasing the mesh density and re-analysing the model until the results converge to 0.0001 tesla of accuracy.

In finite element modelling, a finer mesh typically results in a more accurate solution. However, as a mesh is made finer, the computation time increases. This type of mesh convergence study can help obtain an accurate solution with a mesh that is sufficiently dense and not overly demanding of computing resources. Thus, based on the procedure described, in each refinement process, considering the generic solenoid model, the magnetic flux density data was collected from its surface up to 25 mm away, with intervals of 5 mm.

The trend lines represents the mesh ideal point, which comprise the computational time spent by FEMM 4.2 numerical simulations, in seconds [s], with the number of nodes created and the deflection of the magnetic flux density value, in tesla [T].

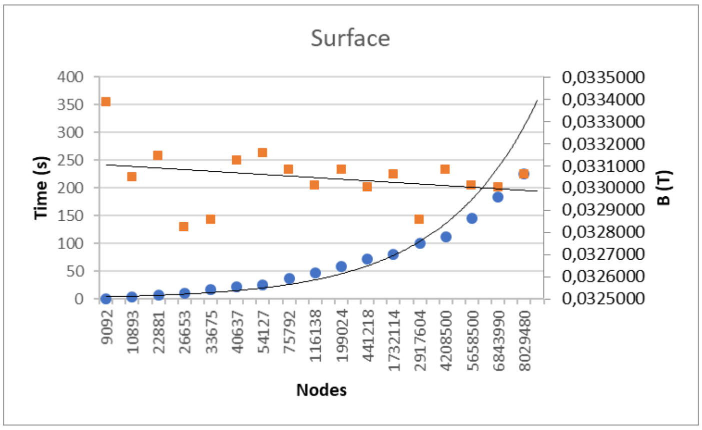

Figure 4.12: Results of mesh convergence at the surface of the generic model.

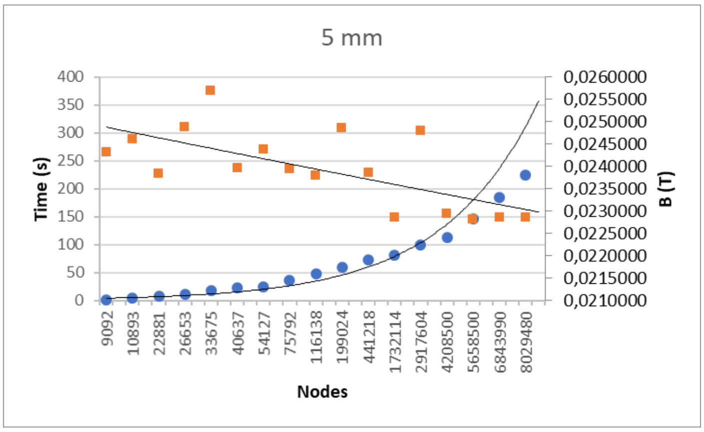

Figure 4.14: Results of mesh convergence at 5 mm of the generic model.

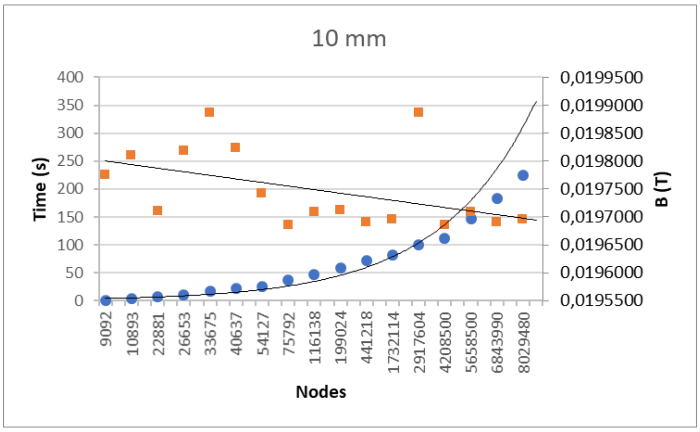

Figure 4.13: Results of mesh convergence at 10 mm of the generic model.

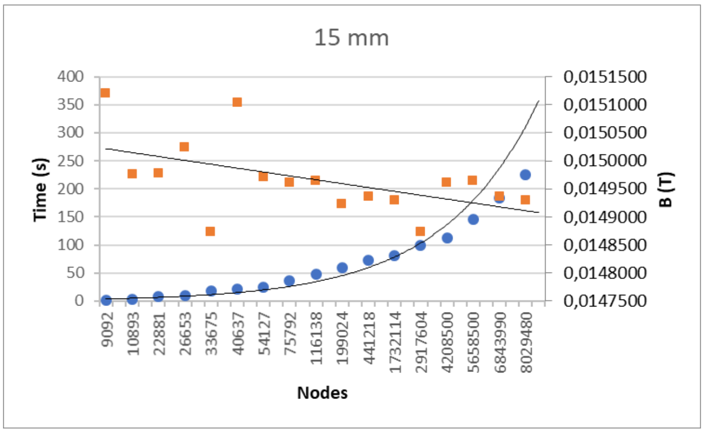

Figure 4.15: Results of mesh convergence at 15 mm of the generic model.

Analysing the mesh convergence results of all relative positions, shown graphically by Figures Figure 4.12, Figure 4.13, Figure 4.14, Figure 4.15, Figure 4.16, Figure 4.17, from approximately 5 658 500 nodes, which correspond to 0.07 mm mesh size, the magnetic flux density results start to be precisely requiring a reasonable simulation computational time of 146 seconds.

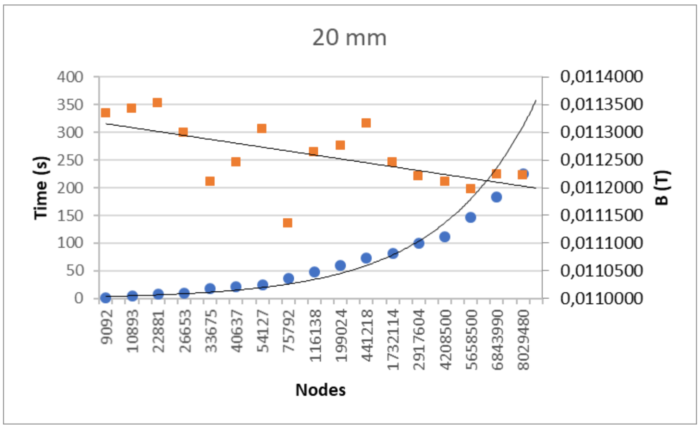

Figure 4.16: Results of mesh convergence at 20 mm of the generic model.

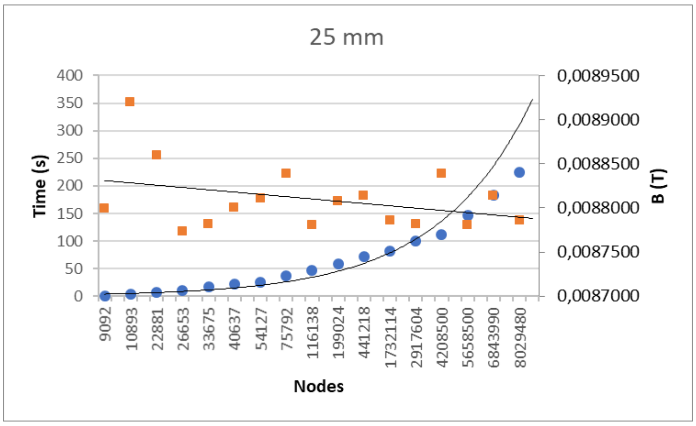

Figure 4.17: Results of mesh convergence at 25 mm of the generic model.

In conclusion, for the numerical simulation of the cylindrical electromagnet models, the characteristics of the mesh mentioned will be performed in order to provide an accuracy of 0.0001 T to all the results of the magnetic flux density.

4.5 EMG Numerical Balance

Considering the processes of the MMF optimization as well as mesh refinement, after 160 numerically simulated models in FEMM 4.2 software, to select the optimized model that fulfils the requirements of the MECSE payload, becomes crucial to the project. Thus, based on the payload and MECSE requirements (*Table 2.7*), three optimizations of EMG models numerically simulated by FEMM 4.2 were performed. In each model optimization, the model characteristics of adaptability, magnetic flux density, mass, and power were evaluated.

Before starting the EMG numerical balance process, it is essential to assign the percentage and the rate of importance to the parameters considered. In order to fulfil the requirements of the MECSE mission, a sufficiently robust magnetic flux density is required in order to manipulate the plasma layer. Thus, of all four parameters, the magnetic flux density, is given greater importance, and consequently the largest percentage (40%).

Secondly, the mass of the electromagnetic cylindrical model is the parameter with second rate of importance (30%), since it represents a structural constrain of the MECSE project. Furthermore, it is important to emphasize that if the EMG model exhibit an excessively large mass, it implies the change to a higher CubeSat class, which leads to an increase in launch costs, undermining the performance of the MECSE mission.

Thirdly, related to the performance of the MECSE payload, the adaptability is the parameter with the third highest rate of importance (20%). Compared with the mass of the model, this parameter presents a smaller percentage because, if it is not possible to adapt the EMG model for future studies related with the position of the communication antenna, the performance of the MECSE mission remains viable.

Finally, power is the parameter with the lowest rate of importance (10%) since no constraints on this parameter exist according to the MECSE payload requirements, as referenced in section 2.3.4 MECSE Payload Module. Thus, after analysis of each model, according to the conditions of the mentioned parameters, the following equation translates the final score of each EMG configuration.

$$\begin{aligned} Final\ Score = {} & 0{,}4 \times (Magnetic\ Flux\ Density \text{ Performance Level}) \\ & + 0{,}3 \times (Mass \text{ Performance Level}) \\ & + 0{,}2 \times (Adaptability \text{ Performance Level}) \\ & + 0{,}1 \times (Power \text{ Performance Level}) \end{aligned} \tag{4.25}$$

At the end of the final evaluation, the models that present a higher score will be those selected for the next optimization phase, only one of them being selected for the subsequent experimental test. In the first optimization, the models were classified from 0 to 5, while in the second and third optimization were evaluated in the range from 1 to 10, as a more detailed evaluation of the properties of the models is required. Each of the four variables was assigned various levels of performance, which represent the results of the model according to each parameter.

Table 4.6: Range of the first numerical balance.

Performance Levels	Power [W]	Mass [g]	Magnetic Flux Density [T]	Adaptability [mm]	
1	> 120	> 4000	5	L > 100	W > 100
2	90 – 120	3000 – 4000	10	L > 100	W < 100
3	60 – 90	2000 – 4000	15	L > 100	W < 90
4	30 – 60	1000 – 2000	20	90 < L < 100	W < 90
5	0 - 30	0 - 1000	25	L < 90	W < 90

Firstly, considering the parameter of adaptability, models that have small mass have a higher quotation. However, in all 3 optimizations, all models received a similar performance levels in the adaptability assessment, since most of them met the requirements of maximum adaptability, i.e., length (L) and width (W) less than 90 mm. The following Table 4.6 represents the several performance levels of the adaptability variable.

Secondly, considering the magnetic flux density variation, since the main objective of this parameter is to generate 0.0375 tesla at the position of 25 mm from the surface, the models were evaluated for the decay of the magnetic field. For the evaluation of this parameter, the maximum distance where the value of 0.0375 tesla is guaranteed, is analyzed. In the first optimization, the maximum score was considered for models that had a flow density value equal to or greater than 0.0375 tesla at the 25 mm surface position, as shown in *Table 4.6*.

Thirdly, the mass of each simulated model is evaluated. In this process, the objective is to promote the models with lower mass. *Table 4.6* describe the performance levels of the first optimization of the mass variable, which consider values between 0 and 4000 grams.

Finally, after 160 models numerically performed, the power of the winding circuit is considered. In the first optimization, the worst case is given for values higher than 120 Watt, and the best case for circuits with values between 0 and 30 Watt of dissipated power, as represented in *Table 4.6*.

At the end of the first optimization, 26 models were selected based on their final score. Therefore, it is imperative to reformulate the parameters evaluation, in order to implement more precise analysis, to select the most appropriate model for the payload of the MECSE CubeSat. In light of this matter *Table 4.7* presents the new evaluation of the parameters and respective levels of performance. As previously mentioned, the second optimization considers the evaluation from 1 to 10 of the 26 models resulting from the first optimization. In addition, this new screening does not consider the assessment of adaptability since all 26 models have maximum adaptability performance.

Table 4.7: Range of the second EMG numerical balance.

Performance Levels	Power [W]	Mass [g]	Magnetic Flux Density [T]
1	> 51.5416	> 3132.46	< 0.031588
2	50.05924 – 50.16021	3052.032 – 3132.461	0.031588 – 0.032328
3	48.57689 - 50.05924	2971.604 – 3052.032	0.032328 – 0.033069
4	47.09453 – 48.57689	2891.177 – 2971.604	0.033069 – 0.033809
5	45.61218 – 47.09453	2810.749 – 2891.177	0.033809 – 0.064549
6	44.12982 – 45.61216	2730.321 – 2810.749	0.064549 – 0.035291
7	42.06474 – 44.12982	2649.893 – 2730.321	0.035291 – 0.036032
8	41.16511 – 42.64747	2569.466 – 2649.893	0.036031 - 0.367722
9	39.16511 – 41.16511	2489.038 – 2569.466	0.036771 – 0.038251
10	38.20014 – 39.68276	2408.611 – 2489.038	0.037511 – 0.038531

Since all the models selected from the first optimization provide a magnitude of magnetic flux density equal to or greater than 0.0375 tesla at the position of 25 mm of the surface, in second optimization, the magnitude of the magnetic field is analyzed only at this specific position (25 mm), as shown in *Table 4.7*.

Since no model has a mass below 1.2 kg, the minimum and the maximum mass of the 26 models was considered, and consequently, the final mass of the EMG models will be evaluated between 2408.61 g and 3132.46 g, as shown in the *Table 4.7*.

The power of the circuit is reduced, as expected. Since all 26 models have a dissipated power value less than 46,5416 W, this is considered to be the worst case of the second EMG balance. *Table 4.7* shows the different performance levels associated with the power variation between 38.2004 and 51.5416 W.

After performing in the second balance of the EMG configurations, the models with the best evaluation, according to equation (4.26), will be selected. 8 of the 26 models present similar final score, thus, will be re-evaluated according to the conditions presented in *Table 4.7*.

Table 4.8: Range of the third EMG numerical balance.

Performance Levels	Power [W]	Mass [g]	Magnetic Flux Density [T]
1	> 51.3501	> 2938.221	< 0.0372938
2	51.1969 – 51.3501	2931.862 - 2938.221	0.0372938 – 0.0374009
3	51.0438 - 51.1969	2925.503 - 2931.862	0.0374009 - 0.0375080
4	50.8906 - 51.0438	2919.144 - 2925.503	0.0375080 - 0.0376151
5	50.7374 - 50.8906	2912.785 - 2919.144	0.0376151 - 0.0377222
6	50.5842 - 50.7374	2906.426 - 2912.785	0.0377222 - 0.0378294
7	50.4311 - 50.5842	2900.067 - 2906.426	0.0378294 - 0.0379365
8	50.2779 - 50.4311	2893.708 - 2900.067	0.0379365 - 0.0380436
9	50.1248 - 50.2779	2887.349 - 2893.708	0.0380436 - 0.0381507
10	49.9716 - 50.1248	2880.999 - 2887.349	0.0381507 - 0.038257

Based on the evaluation method used in the second optimization, the third optimization consists of the detailed analysis of the magnetic field value at the 25 mm position of the model surface. The maximum performance level (10 values) refers to the model with the highest magnetic flux density, and the minimum (1 value) represents the lowest magnetic flux density, as shown in *Table 4.8*.

Considering the mass of the 8 models selected, the mass range is decreased, giving rise to more accurate evaluation results. Thus, the mass of the model is analysed considering the range of 2880.99 g to 2938.221 g. *Table 4.8* presents the mass evaluation levels as well as the range of each level.

Finally, for the third balance of the power dissipated by the electric circuit of the EMG models, considers a range of 49.9716 to 51.3501 watt, as presented in *Table 4.8*. As the intervals of the analysis are decreased, the power evaluation results of the 8 models are more accurate, compared to the second optimization. At the end of the third balance, considering the results according to equation (4.26), the EMG model most appropriate to the MECSE CubeSat payload was selected. The design, circuit, and magnetic flux density properties of the optimized electromagnet cylindrical model, are presented in *Table 4.9*, *Table 4.10*, *Table 4.11* respectively.

In conclusion, after performing the MMF optimization, the convergence of the mesh conditions as well as the execution of the balance of the 160 EMG models, the cylindrical electromagnet configuration will have a length of 90 mm and a total diameter of 82 mm. In addition, 2835 turns will be used with an electric current of 1.71 A applied to the 20 AWG copper wire, providing a magnetomotive force equal to 4847.85 A times turns and a dissipated power of 50.9787 W . Considering the analytical mass calculation, the optimized EMG model will have a total mass of 2880.99 g, generating a magnetic flux density of 0.0382431 T at 25 mm from the model surface. Taking into account these characteristics, the EMG numerical model meets the requirements of adaptability, magnetic flux density and power, not presenting satisfactory results in terms of its total mass, exceeding the maximum of 1,2 kg.

Table 4.9: Design properties of the cylindrical EMG optimized model.

FEMM 4.2 Model Construction		
Pure Iron	Radius [mm]	14
Wire		23.2
Air/Plastic		3.8
Length	L [mm]	90
Wire		
20 AWG		
Turns		
2835		
Current [A]		
1.71		
Mass [g]		
2880.99		
MMF [N x I]		
4847.85		

Table 4.10: Circuit properties of the cylindrical EMG optimized model.

FEMM 4.2 Circuit Results	
Total current [A]	1.71
Voltage Drop [V]	29.8121
Flux Linkage [Webers]	1.1175
Flux/Current [Henries]	0.653508
Voltage/Current [Ohm]	17.434
Power [W]	50.9787

Table 4.11: Magnetic flux density properties of the cylindrical EMG optimized model.

FEMM 4.2 Magnetic Results	
Positive Relative Position [mm]	Magnetic Flux Density [T]
0	0.123484
5	0.110638
10	0.0865807
15	0.0652488
20	0.0505469
25	0.0382431

4.6 Numerical Results (EMG Optimized Model)

In this section, the numerical results of the optimized electromagnet cylindrical model suggested by the EMG model balance process are introduced and analysed. After all the considerations previously established about the features of the FEMM open source software, firstly, it is essential to understand how the EMG model will be constructed.

Based on the properties of the EMG model, since it is an electromagnetic cylindrical model, it is assumed as an axisymmetric problem. In addition, as discussed in the section, this type of model is part of problems related to the magnetostatic, which means that constant current is assumed in the winding. In addition, initially zero frequency is established as a condition of the problem ($Fr = 0\,Hz$).

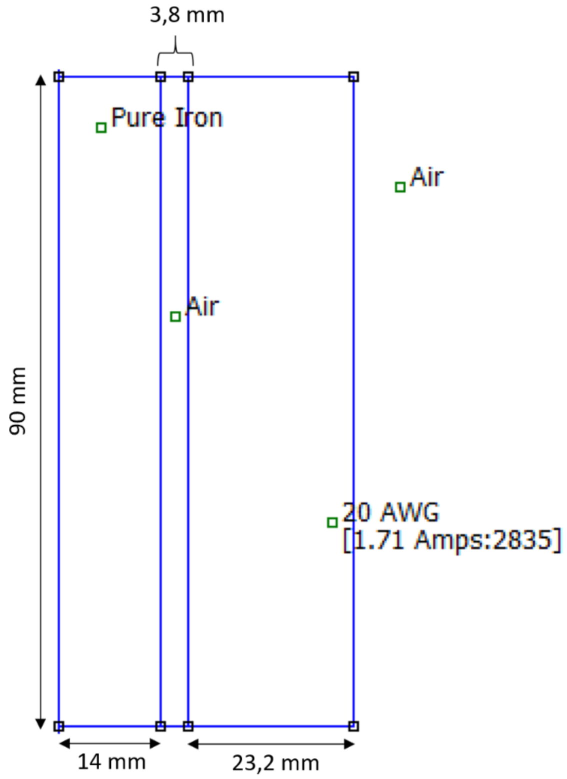

Figure 4.18: Schematic of the axisymmetric EMG optimized model.

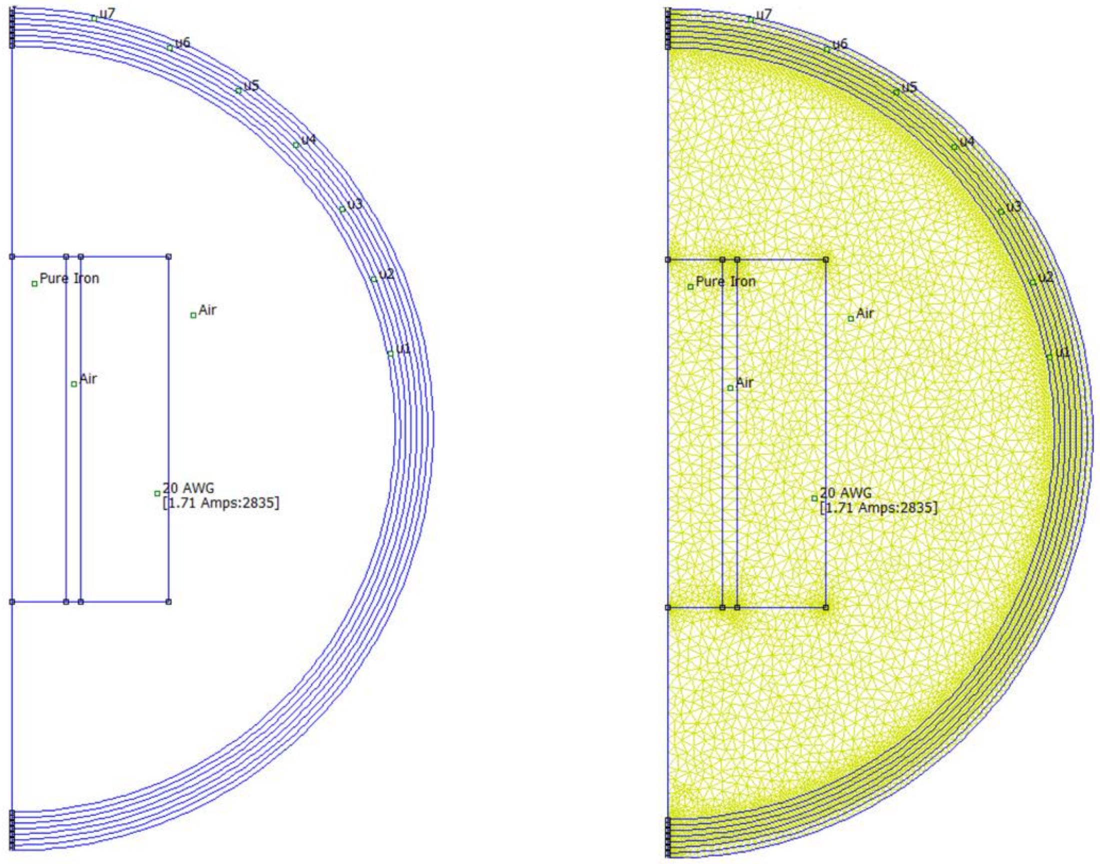

Figure 4.19: Schematic of boundary (Left) and mesh (Right) creation, with the axisymmetric EMG optimized model.

Given the initial conditions of the problem, using the FEMM software design tools, the EMG model optimized according to the properties is presented in ***Figure 4.18***.

Analyzing ***Figure 4.18***, it is possible to see the plastic/air radius ($r_{air} = 3.8\,mm$), the radius of the pure iron ($r_{pure\ iron} = 14\,mm$), the radius of the copper wire ($r_{wire} = 23.2\,mm$) as well as the length of the cylindrical electromagnet ($L = 90\,mm$). In addition, properties related to material selection (20 AWG, Pure Iron, Air), electrical circuit properties ($N = 2835\ and\ I = 1.71\ A$) are also recognized.

Thus, after the design phase of the cylindrical electromagnet model, the next stage is the creation of the boundary conditions. A set of 7 layers, with origin at the center of the model ($r\ =\ 0\ and\ z\ =\ 0$) and with a radius of 100 mm, sufficient to analyze the magnetic flux density at 25 mm from its surface, are the boundary conditions considered, which are represented by Figure *4*.19.

Then, considering the specifications established in the mesh convergence study, a total of 5658500 nodes is generated for a mesh size of 0.07 mm. Figure *4*.19 shows the mesh aspect after executed according to the conditions presented. As specified in section 4.4.2 Mesh Convergence, an accuracy of 0.0001 T is given by these mesh conditions. Established the pre-processor environment of FEMM 4.2 numerical simulation, after the creation of the mesh is suggested the post-processor analysis of the magnetostatic axisymmetric problem.

Considering the characteristics of the circuit of the numerical model (*Table 4.10*), optimized by the balance process of the EMG models, *Figure 4.20* represents mainly the proof that the results provided by the FEMM 4.2 simulation are validated.

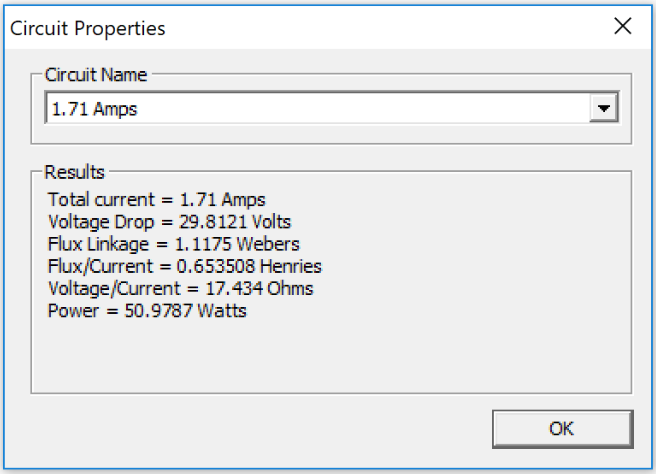

```
Total current = 1.71 Amps
Voltage Drop = 29.8121 Volts
Flux Linkage = 1.1175 Webers
Flux/Current = 0.653508 Henries
Voltage/Current = 17.434 Ohms
Power = 50.9787 Watts
```

Figure 4.20: Circuit properties of the axisymmetric EMG optimized

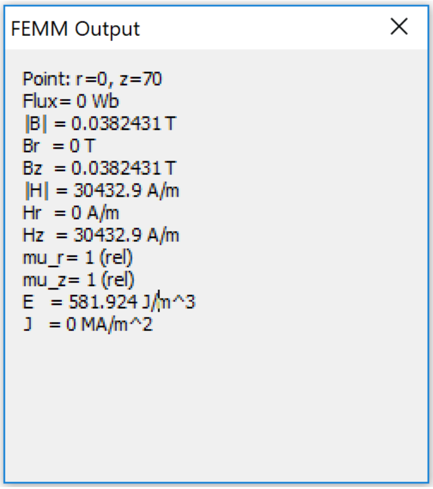

```
Point: r=0, z=70
Flux= 0 Wb
|B| = 0.0382431 T
Br  = 0 T
Bz  = 0.0382431 T
|H| = 30432.9 A/m
Hr  = 0 A/m
Hz  = 30432.9 A/m
mu_r= 1 (rel)
mu_z= 1 (rel)
E   = 581.924 J/m^3
J   = 0 MA/m^2
```

Figure 4.21: FEMM 4.2 magnetic properties
of the axisymmetric EMG optimized model.

Through the localized analysis of points, the investigation of the magnetic field density is the next stage of the numerical results analysis process. The entire numerical study of the magnetic flux density is established in the acquisition of data in different positions relative to the surface of the model. Thus, considering the length of the 90 mm electromagnetic cylindrical model, since the cylindrical electromagnet configuration is constructed centred at the point $r = 0 \; and \; z = 0$, in order to obtain results about the magnetic flux density at the axial position of 25 mm of the model surface, the analysis will be performed at point $r = 0 \; and \; z = 70$. *Figure 4.21* represents the specific point analysis of 25 mm of the surface of the optimized model.

Finally, the magnetic flux density is an important factor in the study of the decay of the magnetic field as it assigns a shape to the magnetic field generated by the model. The left side of Figure 4.22 represents schematically the behaviour of the magnetic field along the entire area under consideration. As it can be observed, the field manifests more strongly in the axial positions of the model, losing intensity as it moves away from its surface. In addition, the right side of Figure 4.22, represents the scale considered for the representation of the numerical results of the magnetic flux density.

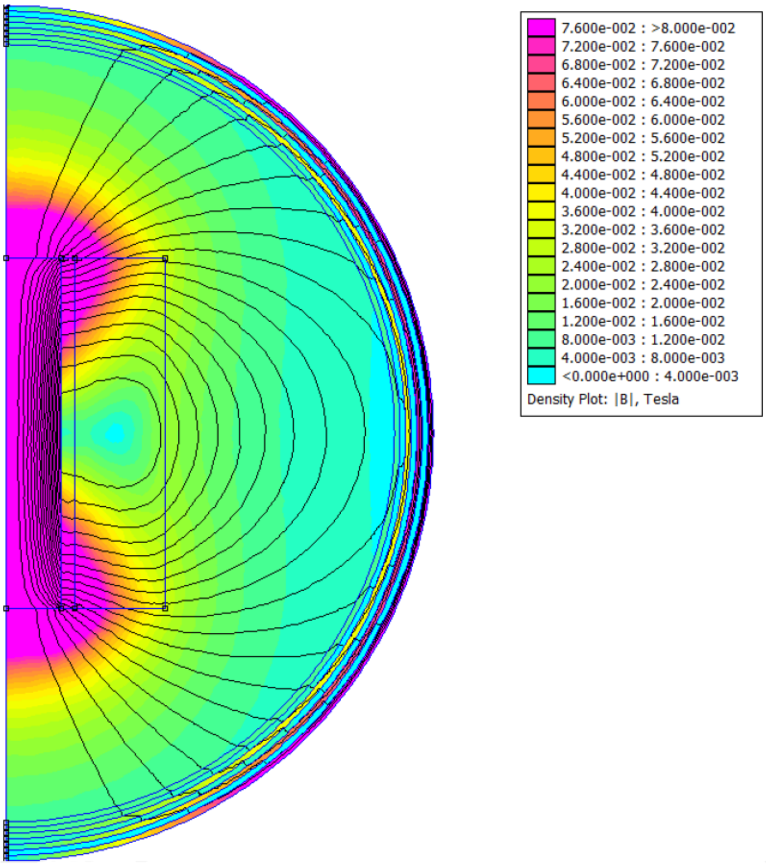

Figure 4.22: Magnetic flux density behaviour of the optimized numerical EMG model (0.08 T upper range).

Performing the scaling refinement operation, the analysis of the magnetic field behaviour of the EMG optimized model is more detailed. In *Figure 4.22* has presented the graphical results about the magnetic flux density of the optimized EMG model, considering a more refined scale than the one used in Figure 4.22. Therefore, the remanence of the field become more visible, promoting the detailed analysis mainly along the vertical axis (z), where it is possible to observe the connection of the field lines outside the electromagnetic cylindrical configuration.

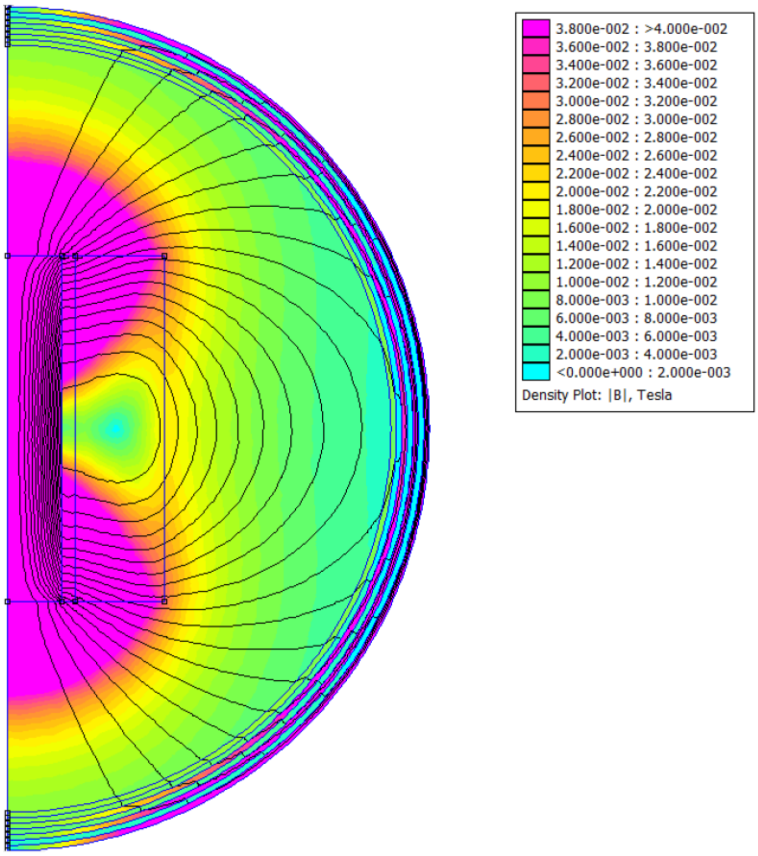

Figure 4.23: Magnetic flux density of the numerical EMG model with several relative model surface positions.

In Figure 4.24 the magnetic flux density behaviour in relation to the surface distance of the optimized EMG model is plotted. By analysing the graphical data, the behaviour of the magnetic field is in accordance with the expected results.

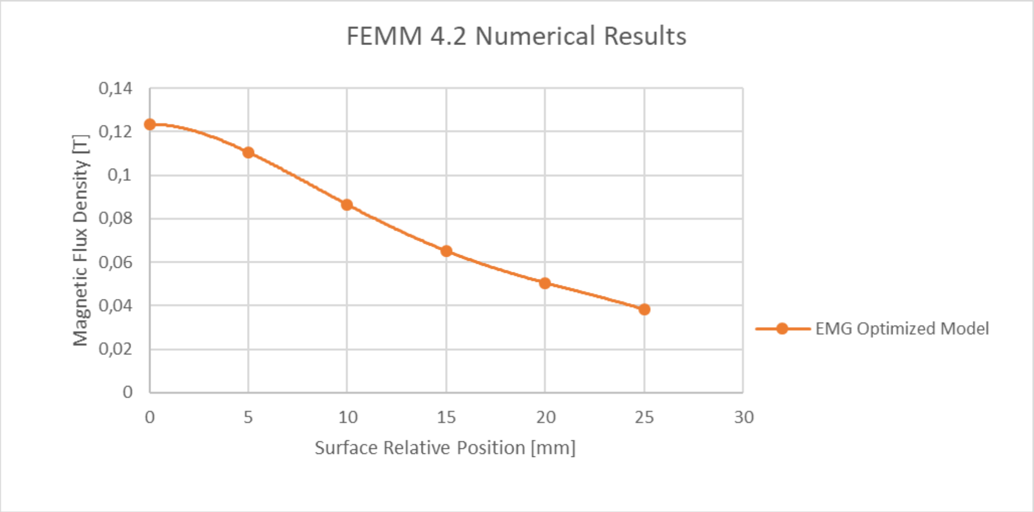

Figure 4.24: Magnetic flux density behaviour of the optimized numerical EMG model (0.04 T upper range).

Chapter 5

5 Experimental Study

Considering the MECSE CubeSat project, the creation of a device capable to generate a robust magnetic field is essential for the accomplishment of its mission. Since the implementation of the EMG model in the MECSE payload is a value-added product with impact in the aerospace industry, an experimental validation of the cylindrical electromagnetic numerical model is required.

Spacecraft DC magnetic field emission requirements shall be verified by a combination of analysis and tests according to [96]. As the costs associated with launching a spacecraft are considerably high, prior controlled environment verification of EMG device attributes is a way to avoid possible failures when performing the MECSE CubeSat mission in the space environment.

Thus, in this section the experimental environmental setup, the method of construction of the EMG cylindrical model, the procedure of data collection as well as the analysis of the experimental results are presented.

5.1 Objectives

In this section, the objectives to perform the experimental activity of the EMG optimized model are presented. Firstly, the main objective of the experimental analysis is the validation of the magnetic and electrical properties of the optimized numerical cylindrical electromagnet model. The study of the influence of the magnetic core on the generated magnetic flux density is a fundamental factor in order to complement the numerical and analytical foundations described in this master's thesis.

Secondly, the performance of the MECSE payload mission requires short periods of EMG operation. For the cylindrical electromagnet model presented in section 4.3 Case Study: Electromagnet, the minimum operating current is considered, so as not to exceed the maximum temperature supported by the copper wire. According to the minimum magnetomotive force (MMF) to generate the magnetic flux density required to manipulate the plasma layer, increasing the current applied to the electric circuit will decrease the required number of turns of the copper winding. Thus, this process has the main objective of minimizing the total mass of the EMG model. For the experimental study, several current values exceeding the maximum current supported by the 20 AWG copper wire shall be applied, considering the maximum permissible temperature.

Thirdly, the optimized EMG model presented in section 4.4 Optimization Process consists of a 20 AWG copper wire component that is associated with a plastic structure in order to support its winding. In this way, the experimental validation of the numerical model of the EMG winding is essential to better understand the relation between the number of turns and the applied current with the magnetic flux density generated.

5.2 Experimental Environment Setup

Considering the numerical properties presented in Figure 4.19, this section presents the methods and considerations to be taken into account, in order to represent them in experimental environment. Thus, there are several factors that should be included.

Firstly, the materials selected for the numerical simulation of the optimized EMG model must be the same for the experimental activity. According to *Figure 5.1*, the 20 AWG is the copper wire that provides better magnetic flux density results for the diameter and maximum current supported. Consequently, for the practical winding of the model, the 20 AWG copper wire was selected (*Figure 5.1*), presenting the properties presented in *Table 5.1*.

Figure 5.1: 20 AWG copper wire roll [107].

Table 5.1: Properties of the enamelled 20 AWG copper wire [108].

Wire Enamelled Copper 20 AWG	
External Diameter [mm]	0.8
Diameter Tolerance [mm]	0.008
Reel Length [m]	125
Cut through	2min ≥ 230ºC

Analyzing *Table 5.1*, each 20 AWG unit presents 125 meters, thus, according to the analytical calculations of the total length of copper wire needed to perform the maximum number of turns (2835) around the core diameter of 35,6 mm, are required for at least 5 units of the model shown in *Figure 5.1*.

Secondly, having defined the material of the experimental winding, the same philosophy to the core materials is applied. The material of the magnetic core is pure iron, but due to the high cost and changes in the degree of purity of this element, it is necessary to choose an iron alloy with similar magnetic properties. Thus, *Table 5.2* presents the properties of the core of Iron opted for the experiment.

Table 5.2: Properties of the F10 Iron Alloy with percentage chemical composition *[97]*.

F10 Iron Alloy	
Diameter [mm]	28
Length [mm]	90
Section [mm^2]	616
Relative Weight [kg/m]	4.834
Chemical Composition [%]	
Manganese (Mn)	0.65
Carbon (C)	0.45
Silicon (Si)	≤ 0.40
Chromium + Molybdenum+ Nickel (Cr+Mo+Nk)	≤ 0.63

Since low-alloyed materials are the most permeable, according to the manufacturer's process, the closest element to pure iron is F10 Iron Alloy. Materials with high alloy content represent a lower amount of iron, which leads to the reduction of the desired permeability properties for the validation of the numerical model.

Thirdly, the material of the winding support structure requires no influence on the magnetic field, as specified throughout Chapter 4. Thus, based on the cost-benefit philosophy, ABS is the element chosen for this component. *Figure 5.2* shows the dimensions of the ABS material of the winding structure provided by 2D drawings of CATIA V5 R24, which will be used in the experimental environment.

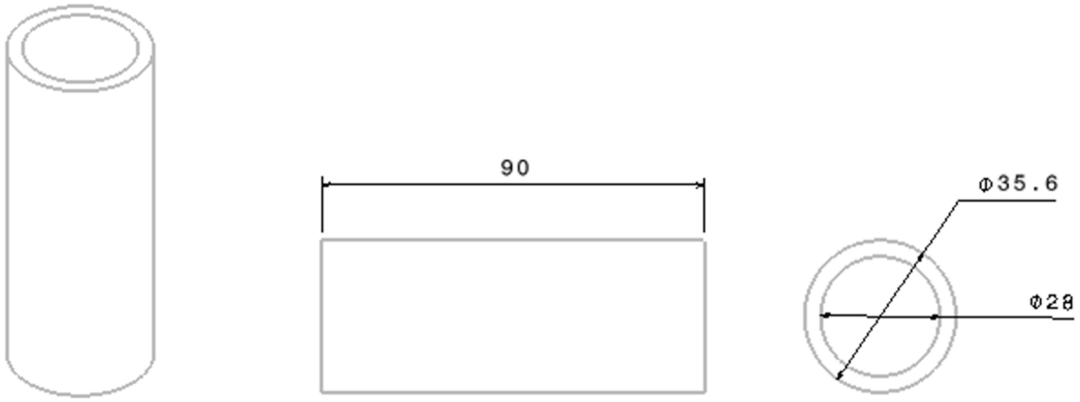

Figure 5.2: Schematic of geometric properties of the ABS winding structure.

Fourthly, based on the geometric attributes previously presented, it is necessary to establish the operating conditions of the electric circuit applied during the experimental test of the EMG model. Thus, considering *Table 5.2* relative to the properties of the numerical circuit, for 2835 turns performed by 20 AWG copper wire, 17.434 Ω is required.

One of the objectives of the experimental experiment is the study of mass reduction by increasing the current applied to the cylindrical electromagnet model. Thus, in order to not exceed the maximum temperature supported by copper wire (*Table 5.2*), the maximum current of 4 A is assumed. Based on the desired current, the required voltage to be supplied to the model is calculated, according to the following equation:

$$\begin{gathered} V = R \times I \\ V = 17.434\ [\Omega] \times 4\ [A] \\ V = 69.736\ Volt \end{gathered} \tag{5.1}$$

Based on UBI laboratory materials, 40 V power supply is the one capable of providing the highest voltage value. A series association will be made when a power source has a positive pole connected to a negative pole from another source. This combination will result in a sum of the voltage of the power sources. Thus, when two 40 V power supplies are connected in series it is equivalent to a voltage of 80 V, sufficient to provide the necessary voltage magnitude (equation (5.1)). Therefore, the electric circuit implemented in the experimental test of the EMG model will have the configuration shown in *Figure 5.3*.

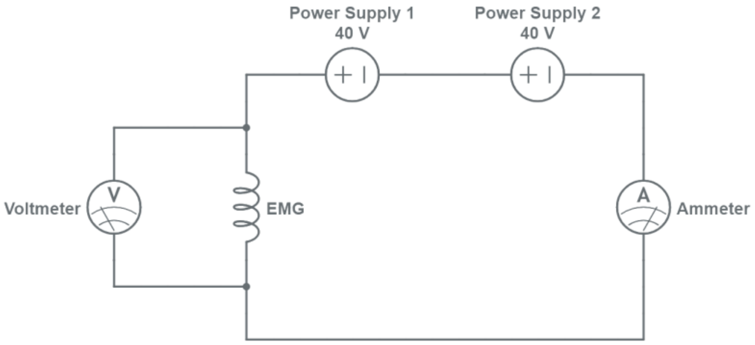

Figure 5.3: Architecture of the electric circuit implemented in the experimental tests.

Based on *Figure 5.3*, 80 Volt will be provided to the EMG model by two power supplies (Power Supply 1 and Power Supply 2). In order to examine the direct current through the winding circuit of the electromagnet, an ammeter is added in series. In addition, the voltmeter is inserted in parallel to record the voltage difference between two points of the electric circuit, obtaining the desired voltage.

Fifthly, according to the objectives of the experimental study section, the magnetic flux density analysis of the optimized EMG model is essential. Considering the results presented in *Figure 4.23*, the software simulations were performed at several axial positions relative to the surface of the cylindrical electromagnetic configuration. The experimental setup environment must be clarified in order to perform the needed measurements for the validation of the numerical simulations.

Therefore, since the FEMM 4.2 analysis of the magnetic flux density was performed from the model surface to 25 mm away, with intervals of 5 mm, in laboratory activity the same measurements must be presented in order to guarantee the concrete validation of the numerical model . The FH 54 Gaussmeter [98] is a handheld, portable device which displays an extremely high degree of measuring accuracy of AC and DC magnetic fields using hall sensors.

Figure 5.4: FH 54 Teslameter *[98]*

Figure 5.4 schematically shows how the experimental validation of the magnetic flux density will be performed at several relative axial positions of the EMG model. After placing the cylindrical electromagnet in the test position, the 6 positions relative to the surface of the EMG considered (0, 5, 10, 15, 20, 25 mm) will be marked through the millimetric scale paper. Before performing magnetic flux density measurements by the FH 54 Gaussmeter, the EMG model must be connected to the power supply. Finally, the magnetic probe will be placed in the selected position and, subsequently, the value of the corresponding magnetic flux density will be consulted in the Gaussmeter. In the magnetic flux density data collection phase, the test station must be controlled in order not to allow any magnetic material to interfere with the magnetic flux density generated by the EMG model.

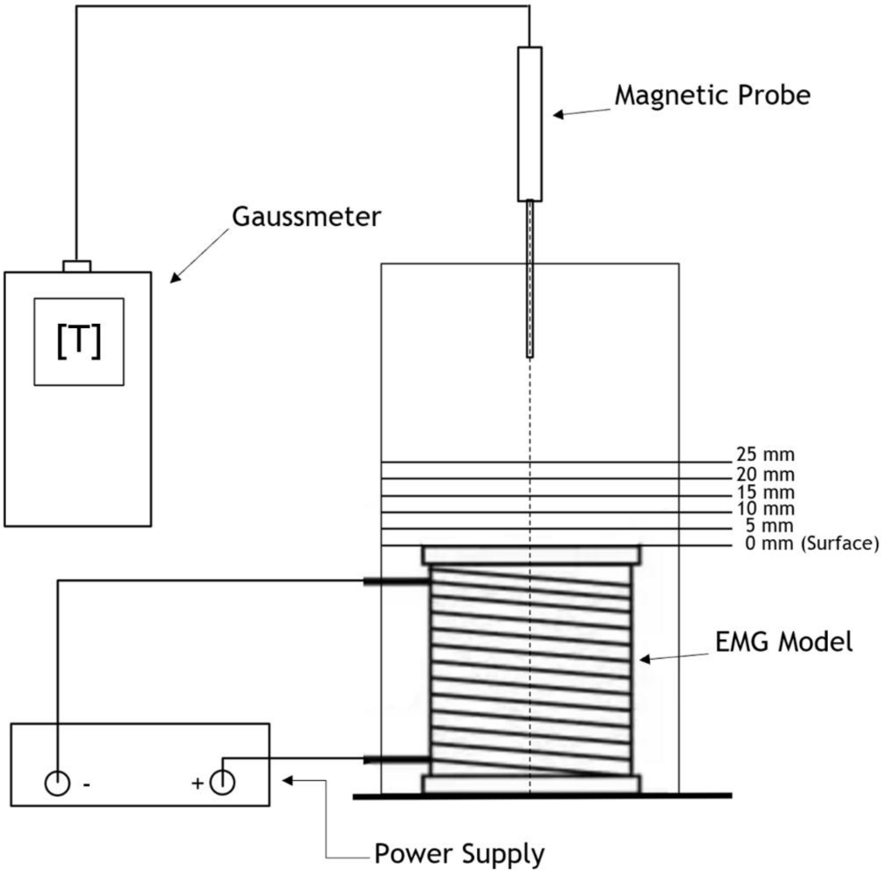

Figure 5.5: Experimental setup of the EMG magnetic flux density

Therefore, according to the numerical simulation of magnetic flux density of the EMG optimized model (*Figure 4.23*), in order to provide experimental measurements with a high degree of accuracy, the full-scale range of the FH 54 Gaussmeter which best adjusts the magnitude of the magnetic field must be selected. Considering the 7 full-scale range offered by the FH 54 Gaussmeter (30 μT, 300 μT, 3 mT, 30 mT, 300 mT, 3 T, 30 T), the 30 mT, 300 mT and 3 T mode scales will be chosen for magnetic flux density experimental measurements.

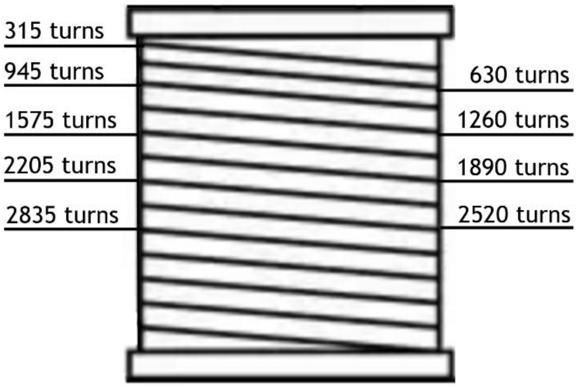

Figure 5.6: Schematic of the number of turns periods with EMG model.

Lastly, considering the third objective of the experimental operation, it is necessary to define the winding validation procedure of the EMG optimized model. The validation of the winding of the cylindrical electromagnetic model consists in examining the relation between the current applied in the electric circuit and the number of turns. So far, 2835 turns have been considered in the EMG model, in order to study the influence of MMF on the magnitude of magnetic flux density, 315 turns will be considered.

In light of this matter, a total of 9 intervals of 315 turns will be rolled up to 2835 turns. *Figure 5.6*, schematically shows the appearance of the EMG model after the described procedure. For each winding period, a range of 0.5 to 4 A of electric current will be applied, in order to validate the EMG winding for different MMF values. At the end, considering 9 winding periods and 8 current intensities, 72 measurements of different MMF values will be performed.

Since the conditions of the experimental environment setup were defined, the next stage is to describe the EMG model construction procedure. In the next section, the manufacture requirements of the cylindrical electromagnet model will be taken into account according to the numerical specifications and based on the experimental setup.

5.3 Model Construction

In this section, the procedures of the model’s design and fundamental considerations adopted until its manufacturing are presented. Besides the design of the EMG model, helpful tools were also designed to adapt to the experiments.

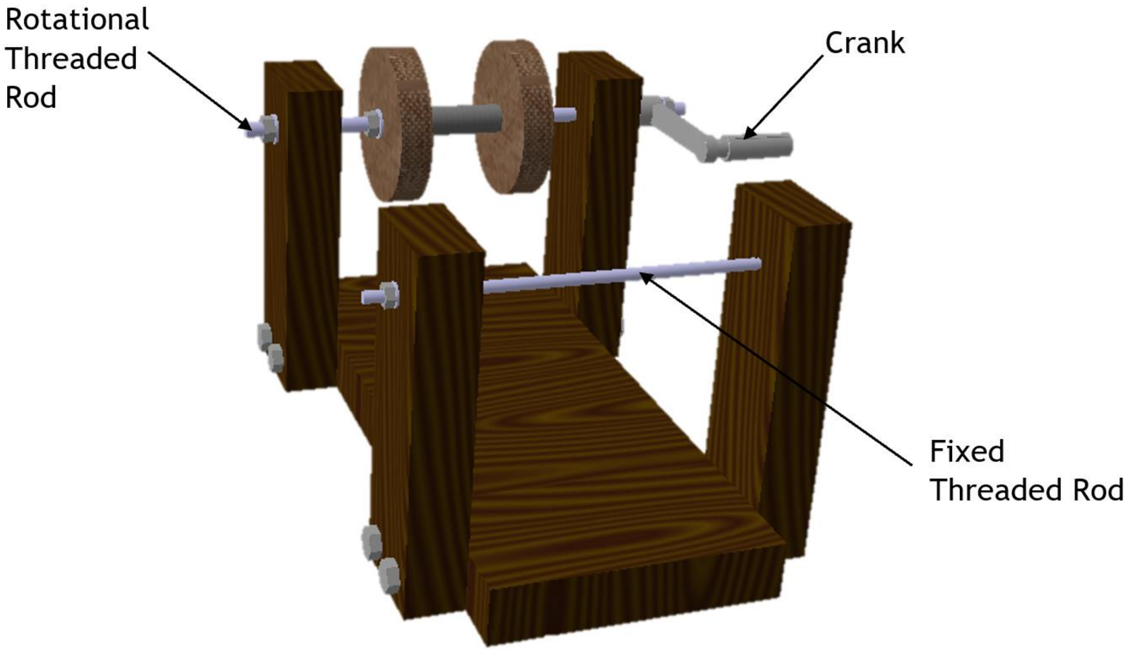

Figure 5.7: Schematic of the winding structure used in the EMG model construction.

In order to manufacture the EMG model according to the dimensions of its components, it is necessary to implement the design of a structure capable of performing the cylindrical winding. Thus, the software used to design this experimental procedure was CATIA V5R24 by Dassault Systèmes [99]. CEiiA provided the use of this commercial software. In *Figure 5.7*, the structure responsible for the winding of the cylindrical electromagnet model is represented.

Based on a cost-benefit perspective, the base of the structure as well as the 4 support columns are made of Medium Density Fiberboard material (MDF). The winding assistance cylinders have 150 mm of diameter, higher than the maximum diameter of the EMG (82 mm), in order to provide the continuous winding of the copper wire. The 20 AWG copper wire roll (*Figure 5.1*) will be attached to the fixed threaded rod. To perform the winding in the ABS support structure, the crank will provide rotary movement to the movable threaded rod and all of its associated parts.

In addition, the support structure of the ABS winding, with a maximum length of 90 mm, is placed between the two winding assistance rollers. The association of the three components is executed by applying a kinetic friction force between them, in order to fix the structure shown in *Figure 5.8*.

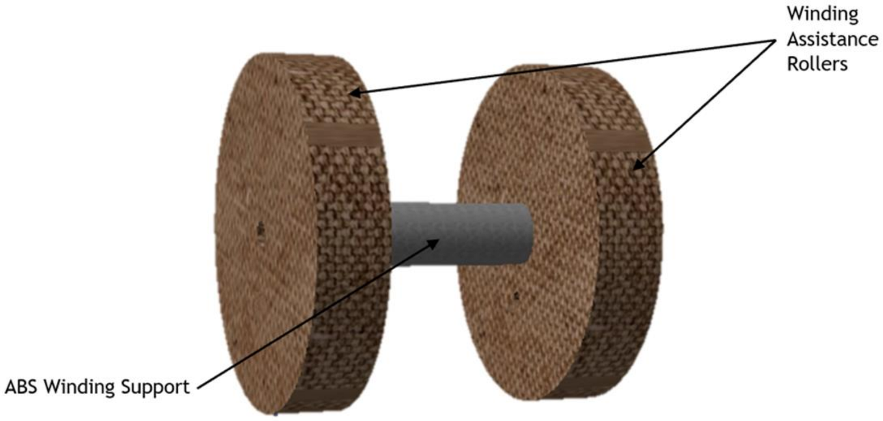

Figure 5.8: Schematic of the winding assistance structure.

Firstly, the winding begins with a loose end of the copper wire to be used. The copper wire passes through the hole in one of the winding assist rollers, and it is fixed in order to provide continuous winding. As the crank applies rotational movement, to achieve a stable winding of the copper wire, a considerable tension is required on the copper wire between the fixed threaded rod and the *Figure 5.8* system.

Secondly, in order to perform the winding described in *Figure 5.6*, it is necessary to specify how the 9 periods of turns will be manufactured. The winding will be performed until 315 turns are given. At this specific moment, a sample of copper wire is cut and, through the welding process, is connected to the same roll of copper wire (Copper Roll 1 '). For all intervals of 315 turns, this process will be performed until 2835 turns are completed around the ABS component. *Figure 5.9* represents the description of this procedure.

Also, the welding method will be used for the exchange of copper wire rolls, since the continuity of the winding is a requirement of the construction of the EMG model. In this case, the loose end of copper wire is not shown, as it does not represent the end of the 315-turns period.

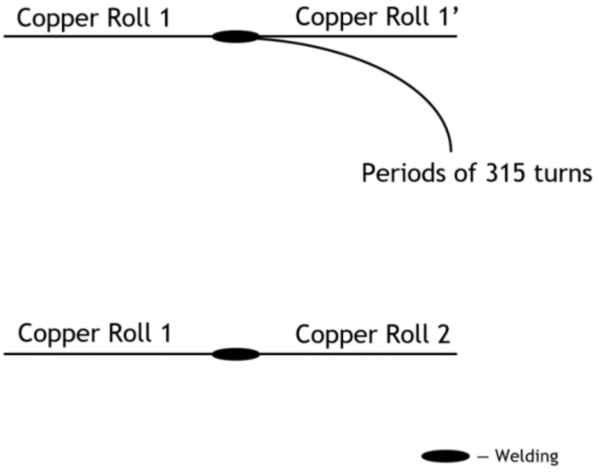

Figure 5.9: Welding experimental procedure.

In both welding processes, described in *Figure 5.9*, the test of the electrical continuity of the system is performed in order to guarantee the operation of the current throughout the complete winding. Consequently, the weld location will be isolated through paper tape.

Thirdly, after performing the procedure described for the 2815 turns, paper tape is added to the entire winding in order to maintain its shape (*Figure 5.10*). If the adhesive tape was not applied, the winding would disperse and its length would be more than 90 mm. Then the magnetic core will be inserted into the ABS plastic structure and the EMG model construction process is completed.

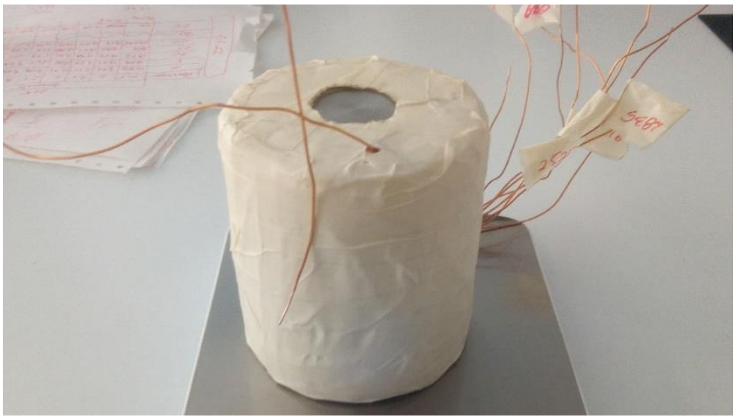

Figure 5.10: Final experimental EMG with magnetic core.

Thus, the conditions and manufacturing processes of the EMG cylindrical model are defined. In the next section, the procedure of data collection as well as the number of measurements required for the validation of the electromagnet model with and without the magnetic core will be analyzed, in addition to other specifications.

5.4 Data Collection

In this section, the parameters under analysis as well as the data collection method of laboratory experiment are described. At the end of the experimental simulation, 432 analyzes of different cases for the winding will be carried out for 72 samples of the EMG model, considering the magnetic core.

Figure 5.11: Final EMG winding (without magnetic core) mass with paper tape.

After the construction phase of the EMG model, the winding is weighed separately from the electromagnetic model (with inserted magnetic core). Using the digital scale with a precision of 1g and with 4 significant figures, the model is weighted according to *Figure 5.11*. The weighing of the complete EMG model, coupled with the magnetic core, is described in Appendix D-Experimental study.

Table 5.3: Mass of each component and total mass of the EMG model with and without isolation tape.

	Copper Wire	Magnetic Core	ABS Structure	TOTAL [g]
With Paper Tape (75 g)	2440	374	40	2854
Without Paper Tape	2365	374	40	2779

Secondly, in order to expose all the considerations of construction, electrical circuit and data analysis discussed throughout this chapter, *Figure 5.12* sums up the experimental setup of the EMG model. In *Figure 5.12* it is possible to observe two power supplies connected in series, an ammeter to measure the current applied in the circuit, a multimeter that will measure the cold and hot resistance and the electric voltage, and a gaussmeter and its respective magnetic probe in order to measure the magnetic flux density at several positions regulated by millimeter scale paper. In addition, the EMG model is connected through the initial winding tip to one of the 9 periods of turns.

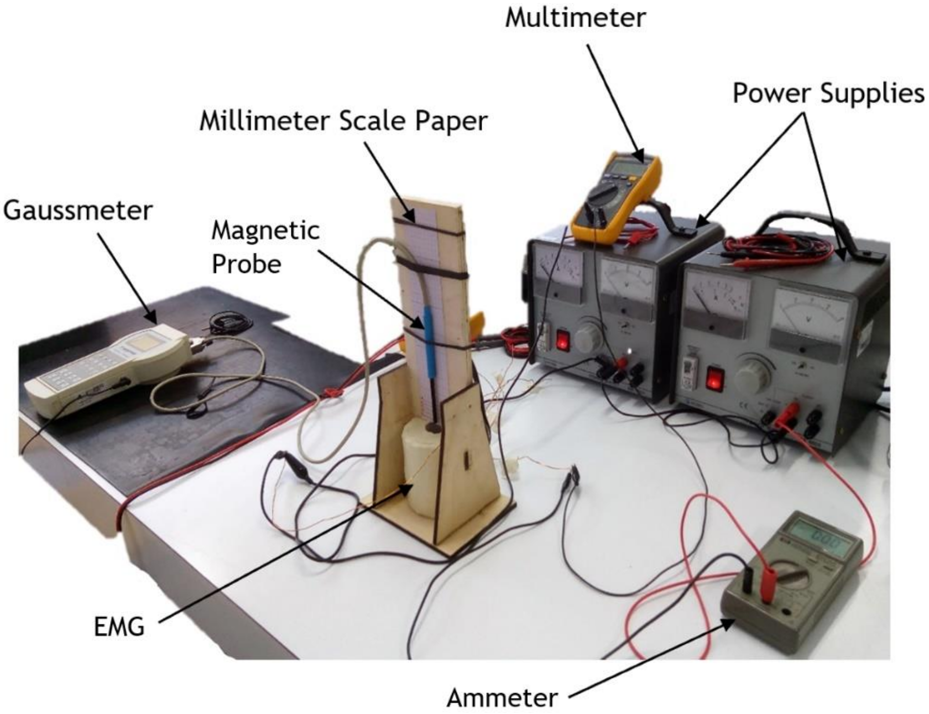

Figure 5.12: Experimental environment setup.

Thirdly, considering the experimental environment setup, it is necessary to experimentally validate the different values of MMF. Thus, according to the EMG copper wire winding construction process, the first phase of data analysis consists of leaving outside the magnetic core of the winding structure (*Figure 5.10*). Thus, since the winding of the EMG model considers several numbers of turns intervals for different current values at 6 distinct relative positions, the diagram shown in *Figure 5.5*, describes the EMG winding data collection method of the cylindrical electromagnet model.

Examining the procedure presented in *Figure 5.14*, considering the maximum current of 4 A, the magnetic flux density analysis of 315 turns on the winding surface of the EMG model is performed. Then, the current is decreased in 0.5 A intervals, until the minimum current considered is obtained (0.5 A) for the same number of turns and at the same position. After running the current variation, the position of the magnetic probe is changed to a further 5 mm away from the surface model, and the maximum current of 4 A is applied again, repeating the current decay process. Finally, for the number of turns considered, after repeating the process of variation of the current and the position of the magnetic probe, when the magnetic flux density is being examined at the position of 25 mm from the surface of the winding under 0.5 ampere, both power supplies are turned off and the hot resistance is examined.

Subsequently, maintaining the connection of the initial winding tip to the electrical supply system, the copper wire end corresponding to the next number of turns (630 turns) is connected. The entire process previously described must be applied to the new number of turns implemented. After performing the variation of current and magnetic flux density at different positions relative to the surface of the EMG model for the 9 periods of turns, the results are recorded and experimental data on winding of the EMG cylindrical model reaches the end.

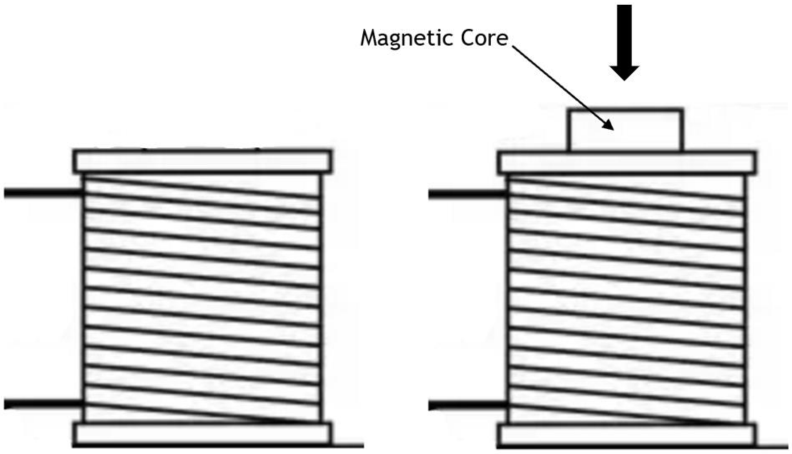

Figure 5.13: Schematic of the transition from EMG winding to EMG with magnetic core.

After performing the experimental study of the winding of the EMG model, it is necessary to add the magnetic core in order to validate an electromagnetic cylindrical model. *Figure 5.13* shows on the left side the beveling of the previously tested model. On the right side, the magnetic core is inserted to validate the EMG numerical model shown in *Figure 4.23*.

Considering the complete EMG model (magnetic core + copper wire winding), the data collection procedure will be performed according to the diagram described in *Figure 5.14*. Since the main objective of this dissertation is to construct and test a magnetic device capable of generating a magnetic flux density of 0.0375 T at 25 mm from the model surface, with a conservative perspective, all analyzes of several values of MMF will be performed at the fixed position of 25 mm away from the surface of the complete EMG model.

After performing the procedure described in *Figure 5.14*, all measurements of the mass, resistance, current, number of turns of the different axial positions relative to the EMG model are completed. In the next section the data collected from the experimental experiment will be analyzed in Chapter 6.

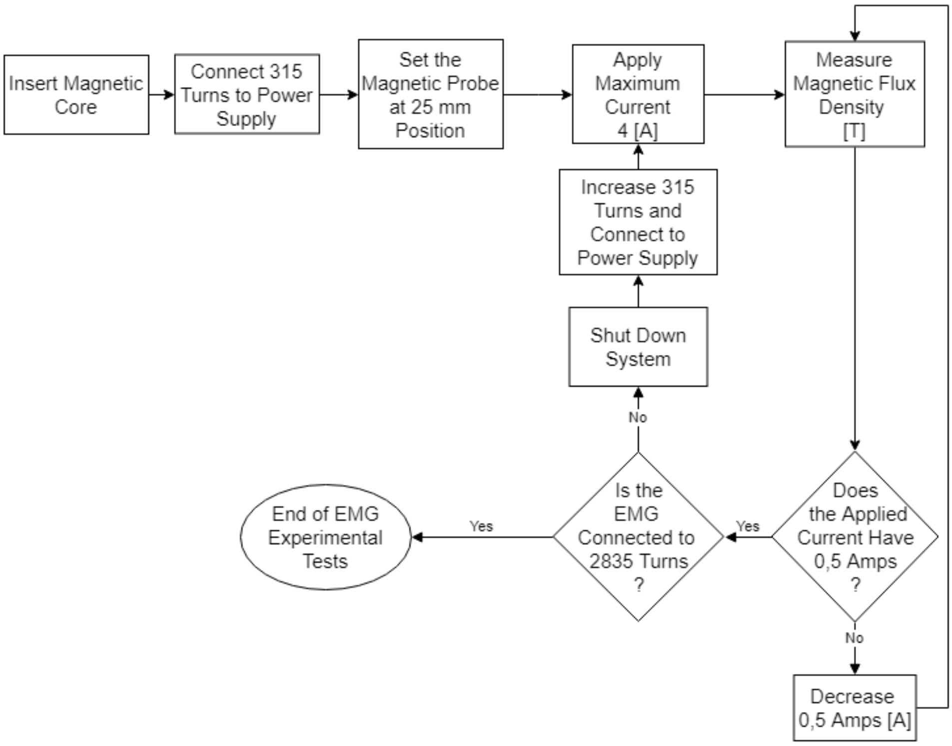

Figure 5.14: Experimental procedure of EMG (with magnetic core) data collection.

5.5 Experimental Results

Having defined the construction method and data collection procedure during the laboratory activity, in this section, the experimental results of the EMG model will be analyzed. In addition, considering the parameters mentioned above, considerations about the current, number of turns, MMF, magnetic flux density and power dissipated by the system will be established. Firstly, the relationship between the magnetic flux density with the number of turns will be clarified. *Figure 5.15* shows the interrelation between magnetic field behavior and the number of turns for various positions relative to the EMG winding surface, considering a current of 4 A.

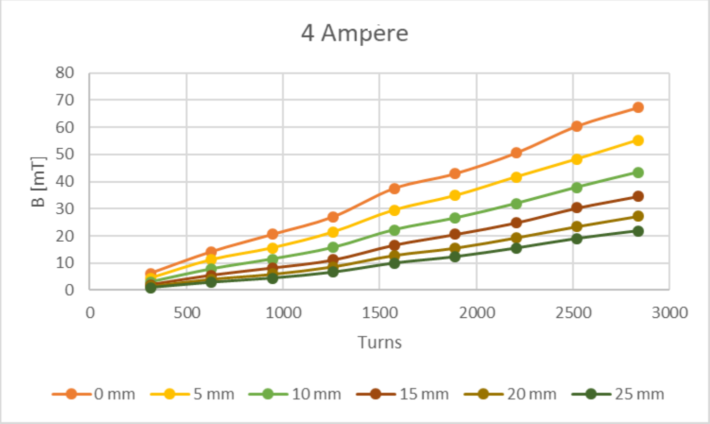

Figure 5.15: Results of the magnetic flux density of the EMG winding (without magnetic core), with a current of 4 A.

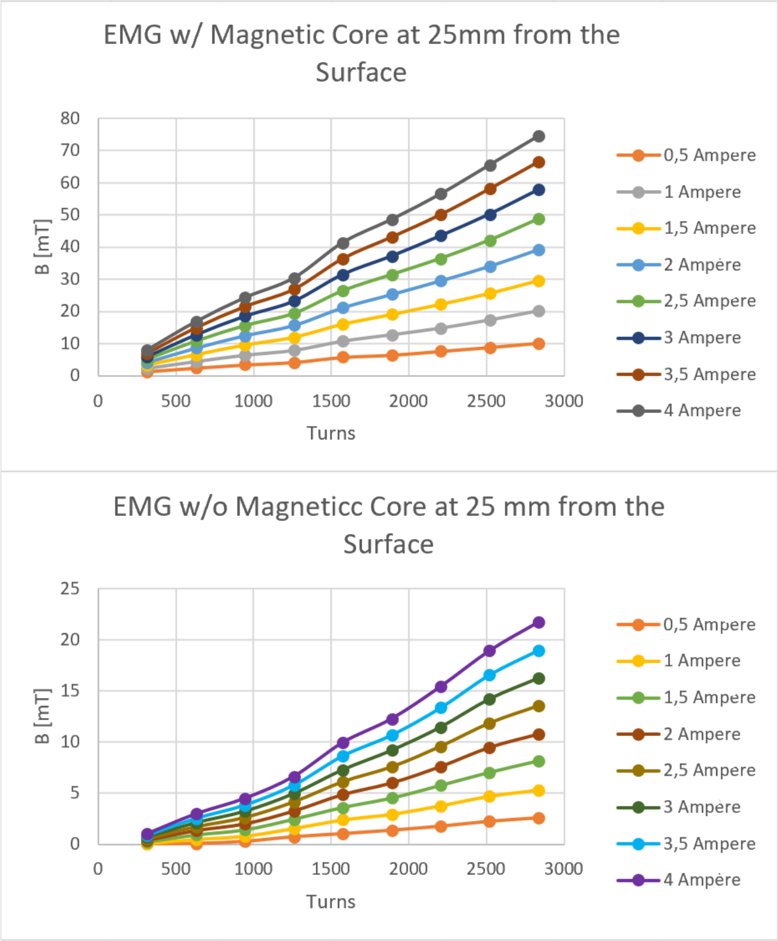

Figure 5.16: Magnetic flux density of the EMG with and without the magnetic core at 25 mm, considering different values of current.

According to the measurements performed on the magnetic flux density for a fixed position of the magnetic probe, the value of B [T] varies linearly with the number of turns as idealized by the analytical and numerical models, presented in Chapter 3 and Chapter 4 respectively. In addition, the magnetic flux density gradually decreases with the distance to the surface of the EMG winding. Without the addition of the magnetic core, the experimental results of the magnetic flux density are insufficient to the value needed to manipulate the plasma density at 25 mm away from the cylindrical winding model (0.0375 T). The results of the magnetic flux density for the remaining current values are similar to those suggested in *Figure 5.15*, which are presented in the Appendix D-Experimental Study.

Secondly, it is essential to clarify how the magnetic field of a cylindrical electromagnet model behaves with the addition of a magnetic core comparatively to that generated only by the copper wire winding. Thus, *Figure 5.16* presents the magnetic flux density experimental data of the EMG model, with and without magnetic core, to the permanent position 25 mm from the surface of the EMG model, considering the 8 current values considered.

Based on the results of *Figure 5.16*, the addition of the magnetic core represents an increase in the value of the magnetic flux density B [T], as expected. Inserting the magnetic core in the winding model, according to the results shown in *Figure 5.16*, causes approximately an 80% increase of the magnetic flux density value. Furthermore, considering the magnetic core model, the empirical data of the magnetic flux density is sufficient to manipulate the plasma density to the 25 mm position of the EMG model surface. In fact, there are 15 possible cases of generating at least 0.0375 T according to the first top graph of *Figure 5.16*, which will be examined in more detail in the next chapter.

Since the electric resistance is altered by the length of the conductor, the study of the relationship between this parameter and the number of turns of the model is important to better understand the concept of power dissipated by the EMG model. First, as mentioned earlier, the power of the system is influenced by the resistance of the conductor and the current applied. Thus, *Figure 5.17* clarifies the operation of the power of the cold and hot EMG model, considering several turns of copper wire, for different values of current.

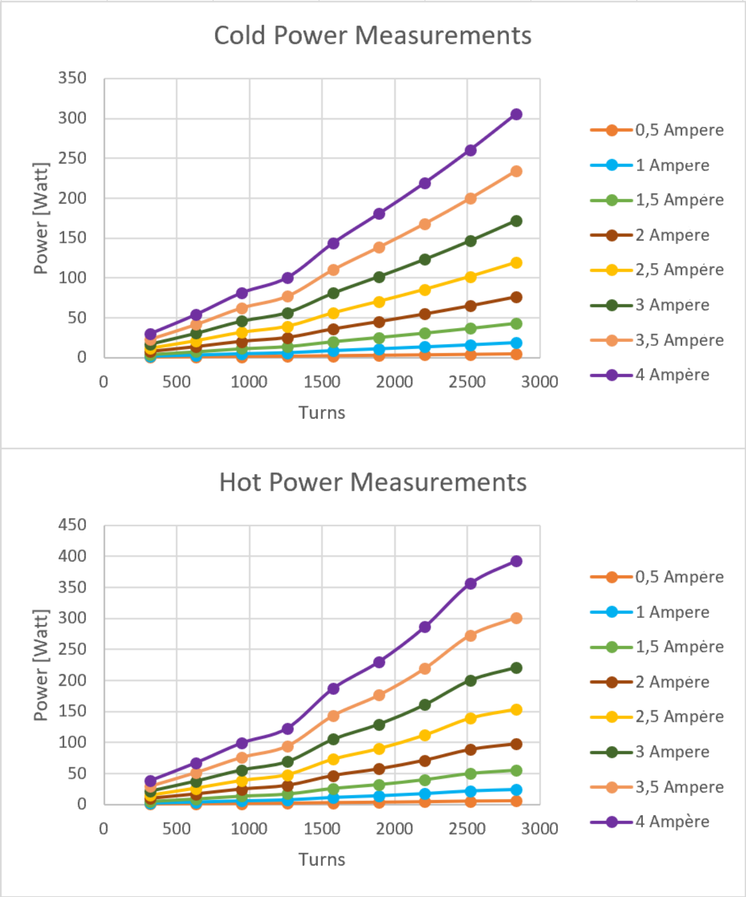

Figure 5.17: Cold and hot power experimental measurements, with different values of current.

Selecting a particular example, *Figure 5.17* represents the analysis of the cold and hot power of the EMG model, considering 2835 turns of copper wire (full EMG winding). According to *Figure 5.17*, the relation between the dissipated power and the current that crosses the 2835 turns of the winding is graphically validated by *Figure 5.18*.

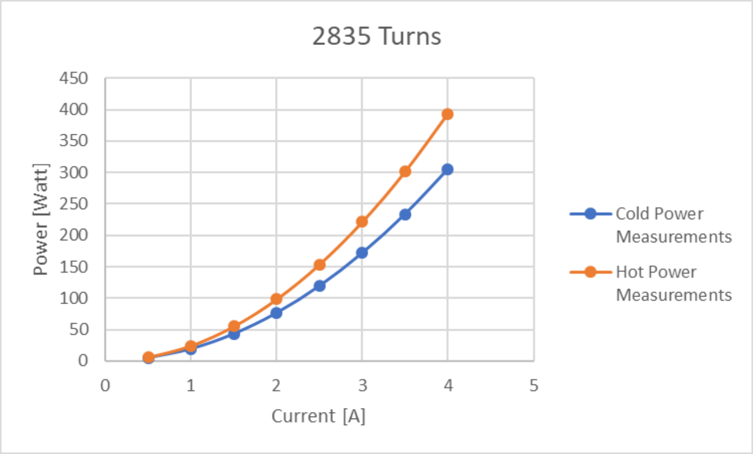

Figure 5.18: EMG experimental cold and hot power measurements, with 2835 turns.

The results of *Figure 5.18* suggest that the resistance measured while the model is not connected to the power supply (cold power measurements) is lower than when it is under the electric power effect (hot power measurements), regardless of the current value that crosses the electrical circuit. In fact, by providing electric current in the conductive copper wire, its temperature will increase. Consequently, with increasing temperature the degree of agitation of the molecules causing the increase of the resistance value will increase, as suggested graphically by *Figure 5.18*.

Considering the magnetic core, the electrical behavior of the system is not influenced by its properties, thus, the increase of the current applied in the electric circuit of the EMG winding implies the increase of the power dissipated. In this case, 2835 turns are considered, however, for all periods of turns considered, the power behavior follows the same trend, as presented by figures in Appendix D-Experimental Study.

Based on the experimental results presented, it is necessary to understand the relation between the data coming from the analytical and numerical models previously investigated. Thus, in the next chapter, all parameters mentioned throughout this dissertation will be taken into account in order to suggest the final conclusions of the EMG cylindrical model, considering errors and deviations associated with the analytical, numerical and experimental analyzes.

Chapter 6

6 Results and Discussion

In this section, the following results are addressed: comparisons between the analytical, numerical and experimental models, trends of the different models as well as the relative error of each magnetic flux density measurement and electric circuit, and two different designs of the EMG model in order to reduce its mass.

6.1 Data Analysis

In this subsection, the processing of data from analytical, numerical and experimental analyzes is investigated. Firstly, considering the comparison between the EMG winding validation results, the analytical and numerical model follow the same trend. In most cases, the analytical results of the magnetic flux density are more optimistic than the numerical results, it means that, under the same conditions, the analytical investigation presents a higher magnetic flux density than the numerical simulation. A special case for the position of the model surface (0 mm), which has a lower analytical magnetic flux density value than the numerical value.

This fact, may be justified by the behavior of the magnetic flux lines being the same along the total length of the solenoid. *Figure 6.2* represents the experimental and numerical analyzes of the magnetic flux density at positions relative to the surface of the EMG winding configuration, considering an applied current of 1.5 A and 2835 turns. The graphics regarding the comparison between the experimental and numerical model of the remaining values of electric current have exactly the same trend, presented in Appendix E-Data Treatment.

Based on *Figure 6.2* results, considering relative associated error between the experimental and numerical performances, a maximum of 27.5% and a minimum of 4.4% is attributed to the 0 mm and 25 mm of the surface relative positions, respectively.

Secondly, considering only the winding of the EMG model, it is important to examine the comparison between numerical and analytical data. Figure 6.2 represents the analytical and numerical results of the magnetic flux density considering 6 relative positions and an applied current of 1.5 A.

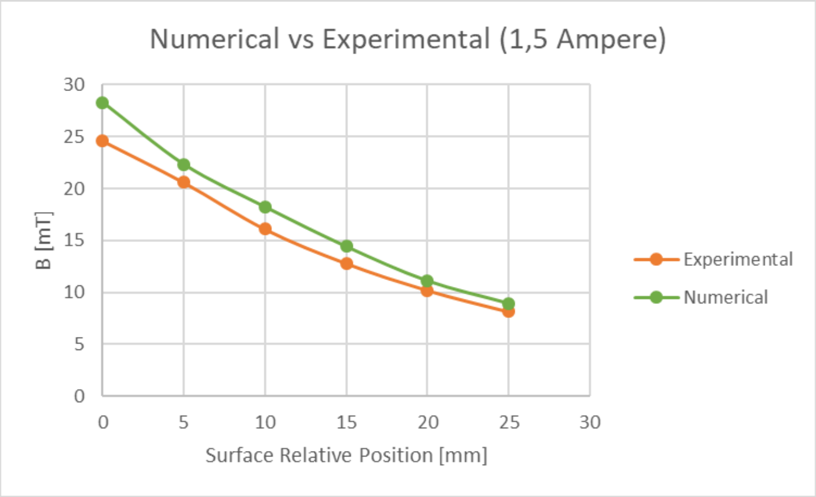

Figure 6.2: Comparation between the numerical and experimental results of the EMG winding, with 1.5 A.

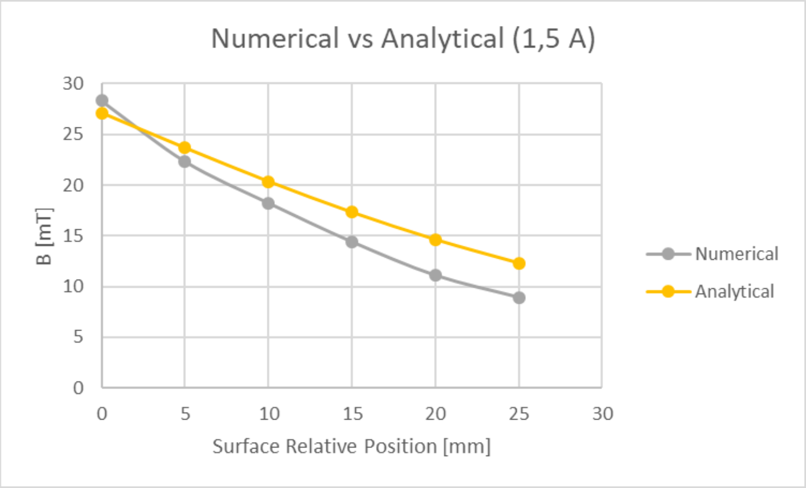

Figure 6.1: Comparation between the analytical and numerical magnetic flux density results of the EMG winding, with 1.5 A.

According to *Figure 6.1*, the analytical results of the magnetic flux density are, in all cases considered, superior to the numerical tests, as previously suggested. In addition, considering the results for several relative positions of the model, the maximum of 12.7% and the minimum of 7.7% are assigned to the positions of 0 mm and 5 mm respectively. At 25 mm distance from the surface of the EMG model, the results of the magnetic flux density present 9.6% of relative error associated between the numerical and analytical data. Considering the current applied in the winding system, increasing the value of the electric current gradually decreases the associated relative error. In this way, a maximum of 12.2% and a minimum of 9.3% associated relative error are assigned to 0.5 A and 4 A respectively. The graphs of the several currents considered are presented in Appendix E-Data Treatment.

Thirdly, in order to summarize the results of the analytical, numerical, and experimental analysis, *Figure 6.3* represents the comparison of the three models considering 2835 turns of EMG winding and an applied current of 1.5 A.

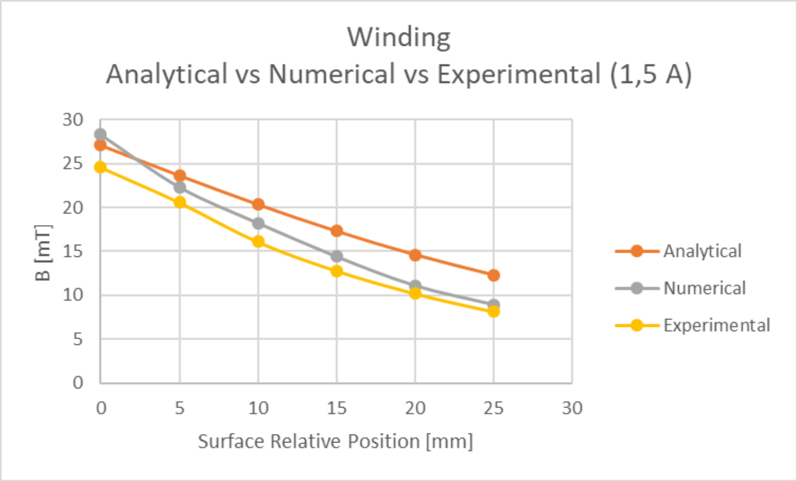

Figure 6.3: Comparation between analytical, numerical and experimental results of the EMG winding, with 1.5 A.

As previously suggested, the analytical model is the most optimistic of all models, generally offering higher magnetic flux density values at all relative positions considered except at the surface location (0 mm). In Appendix E-Data Treatment the figures referring to the simulation of different applied currents are presented, which in all cases follows the trend presented by *Figure 6.3*.

In order to assign the respective relative errors associated with the comparison between the analytical and numerical models with the experimental tests, *Figure 6.4* is presented. According to *Figure 6.4* for the complete winding of 2835 turns, while the error of the comparison between the analytical model and the results of the experimental measurements, the associated relative error increases with the increase of the model surface distance, as opposed to the error of the numerical model which does not present any trend.

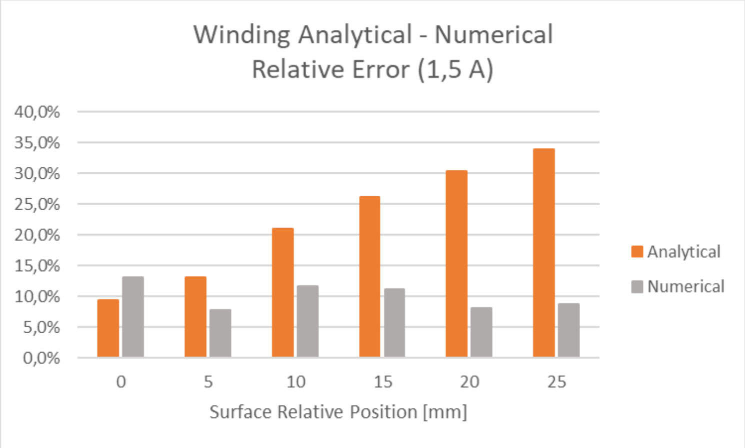

Figure 6.4: Comparation between analytical and numerical EMG winding relative ERROR, considering 1.5 A.

Considering the comparison between the analytical and experimental model, the conclusion about the associated relative error study shows a minimum of 7.1% and a maximum of 36.4%, and an average of 22%. On the other hand, considering the comparison between the numerical model and the experimental activity measurements, the results show a minimum of 7.1% and a maximum of 16.3%, with an average value of 10% associated relative error.

Fourthly, the analysis of the EMG model under the influence of the magnetic core should be considered. According to the results presented in section 5.5 Experimental Results, the value of the magnetic flux density required to manipulate the plasma layer during hypersonic reentry is only generated by the implementation of a magnetic core. Thus, *Figure 6.5* compares the numerical results with the experimental measurements of the complete EMG model (with the magnetic core) under the influence of an electric current of 2 A. In Appendix E-Data Treatment the graphs referring to the numerical and experimental comparison of the different values of current are presented, showing the same trend of *Figure 6.5*. As suggested by the numerical and experimental data analysis on the EMG winding, the numerical values are, in all cases, higher than the results of the experimental measurements.

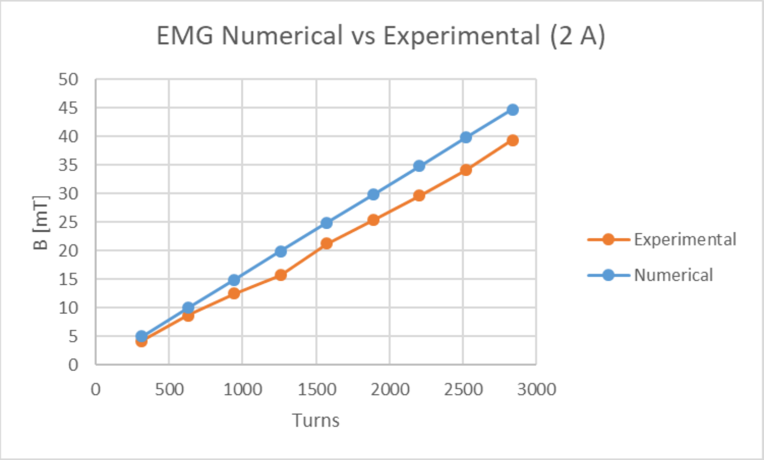

Figure 6.5: Comparation between numerical and experimental magnetic flux density results of the EMG model (with magnetic core), considering 2 A.

In addition, the investigation of the relative error is important, in order to investigate the accuracy of the numerical simulations with the experimental results of the EMG model. Hence, *Figure 6.6* demonstrates the relative error between the numerical analysis and the experimental test, considering the influence of the magnetic core, different number of turns, and several values of electric current. Based on the results shown in *Figure 6.6*, in most cases, the relative error increases under high current values, which means, that considering the same geometric conditions, the relative error for the maximum current (4 A) is higher than for the minimum current applied (0.5 A). Considering the variation of the number of turns, the behavior of the relative error shows no pattern or trend. According to *Figure 6.6*, the numerical results of the EMG have an average relative error of 15% compared to the experimental tests.

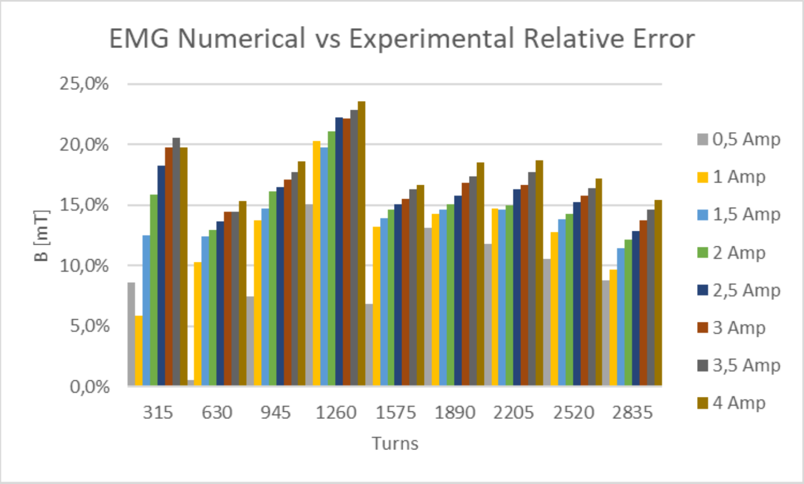

Figure 6.6: Comparation between numerical and experimental relative ERROR of the EMG model (with magnetic core), at 25 mm of relative position.

Fifthly, having determined the behavior of the magnetic flux density according to the numerical and experimental results, it is essential to examine the performance of the power dissipated by the EMG model. *Figure 6.7* shows the trend of the experimental results of the power measured in hot and cold condition comparing to the numerical results of the electric circuit.

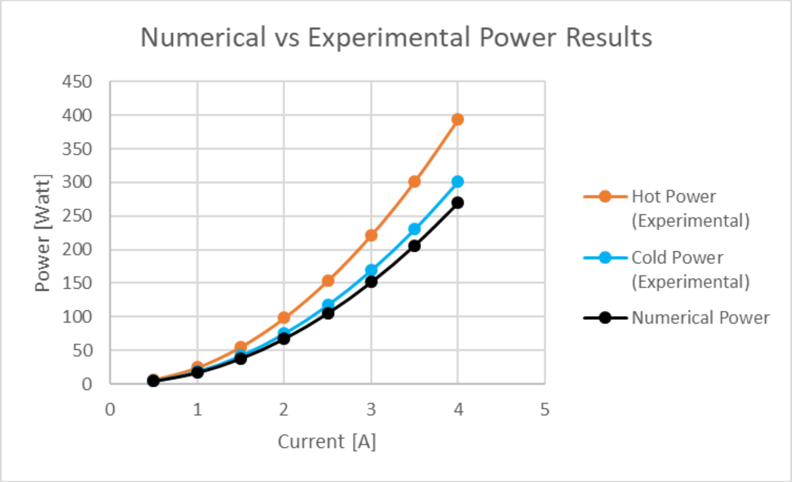

Figure 6.7: Numerical vs experimental (cold and hot) power results.

Analyzing *Figure 6.7* considering the same electrical properties, the numerical power results represent the same trend as the experimental results. In addition, it is possible to conclude that the numerical results provided by FEMM 4.2 software consider cold dissipated power measurements, since it suggests a smaller relative error than the measurements of the hot dissipated power. In fact, the percentage of relative error of the cold dissipated power measurements, compared to the numerical results, is 12%, while the error of the hot dissipated power output is almost 4 times higher (46%).

6.2 EMG Design Optimization

Based on the analytical, numerical and experimental validation of a generic cylindrical electromagnet model, it is possible to apply the same procedure to electromagnetic models that are governed by the same conditions. According to *Table 5.3* the total mass of the EMG experimental model is 2779 g. Considering the mass requirements of the MECSE CubeSat payload, only 1200 g are available. In this way it is necessary to optimize the design of the EMG model in order to decrease the total mass of the magnetic field generating system.

Thus, considering the MECSE CubeSat payload requirements, Figure 6.8 shows two configurations of the EMG model capable of providing magnetic flux density values in order to manipulate the plasma layer 25 mm from its surface.

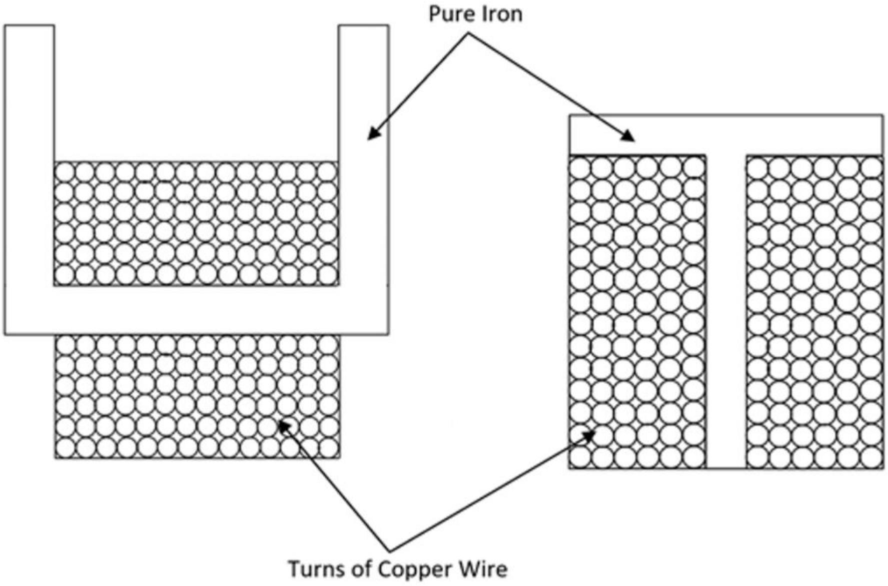

Figure 6.8: Preliminary design of "U" and "T" planar configurations.

In addition, the new geometries proposed in Figure 6.8, provide a better ratio of magnetic flux density and mass, which means, they are able to generate the minimum value of 0.0375 tesla at 25 mm distance from the model surface, offering lower mass than the EMG configuration experimentally tested.

In order to investigate the magnetic behaviour and mass properties, several numerical simulations have been performed by FEMM 4.2 software. Since the suggested 2D configurations do not have a rotational axis of symmetry (*Figure 6.9*), the "Planar" mode of the FEMM 4.2 problem definition dialog must be selected, as opposed to the numerical simulations of the cylindrical EMG axisymmetric model. Consequently, it is possible for the user to enter the value of the desired depth to the electromagnet model. Next, the entire model construction procedure (Appendix A) is performed.

In addition, the simulation of the suggested models will take into account the properties of the materials and the circuit mentioned in Chapter 4. The selected materials will be the Pure Iron for the core and the AWG Copper Wire for the winding (*Figure 6.9*89).

Firstly, the construction of the "T" configuration considers five geometric variables (x, x', y, y', z) as shown in *Figure 6.9*.

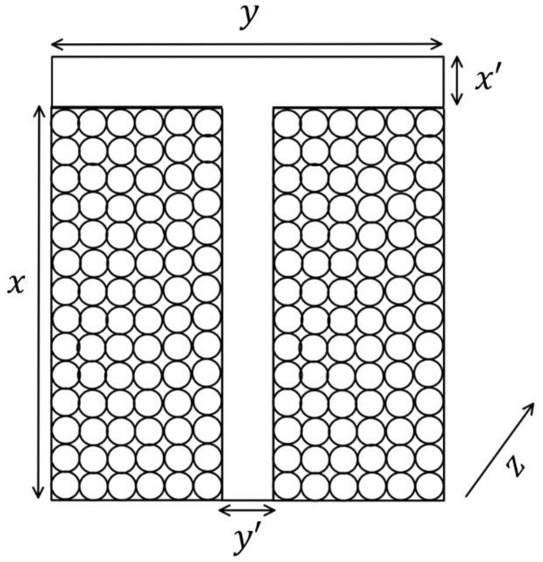

Figure 6.9: Geometric variables of the "T" planar configuration.

Based on the design parameters of the "T" configuration, conditions of the geometry, the maximum number of turns, the total wire length, and the total mass of the model are specified by:

$$Geometric\colon \begin{cases} y \leq 90\ mm \\ x + x' \leq 90\ mm \\ z \leq 90\ mm \end{cases} \tag{6.1}$$

$$M\acute{A}X_{turns}\colon \left\lfloor \frac{y - y'}{2D_{real}} \right\rfloor \times \left\lfloor \frac{x}{D_{real}} \right\rfloor \tag{6.2}$$

$$Total_{Length\ (Copper\ Wire)}\colon \left\lfloor \frac{x}{D_{real}} \right\rfloor \times \sum_{k=1}^{\left\lfloor \frac{y-y\prime}{2D_{real}} \right\rfloor} \left(2 \times (y' + z + (2 \times k \times D_{real}))\right) [mm] \tag{6.3}$$

$$m_{TOTAL}\colon 7{,}874 \times 10^{-3} \times \left((x' \times y \times z) + (x \times y' \times z)\right) + \left(Total_{Length} \times 10^{-3} \times S_m\right) [g] \tag{6.4}$$

Considering the above conditions, it is possible to perform several numerical simulations of the "T" configuration using FEMM 4.2 software. The model that present the best results in terms of mass is described in *Table 6.1*.

Table 6.1: Geometric properties of the "T" planar optimized configuration.

FEMM 402 Model Construction (Planar)		
Core/Wire	Up Height (x’) [mm]	5
	Down Height (x) [mm]	69
	Up Length (y) [mm]	74
	Down Length (y’) [mm]	5
Depth	(z) [mm]	1
Wire		
22 AWG		
Turns		
5202		
Current [A]		
0.965		
Mass [g]		
1242.95		
MMF [N x I]		
5020		

Implementing the model shown in *Table 6.1* it is possible to generate at least 0.0375 T at a distance of 25 mm from its surface. The behavior of the magnetic field is characterized by *Figure 6.10*, where it is possible to observe the highest magnetic flux density at the base of the "T" configuration considered. Thus, the collection of magnetic flux density data at 25 mm will be performed from that surface.

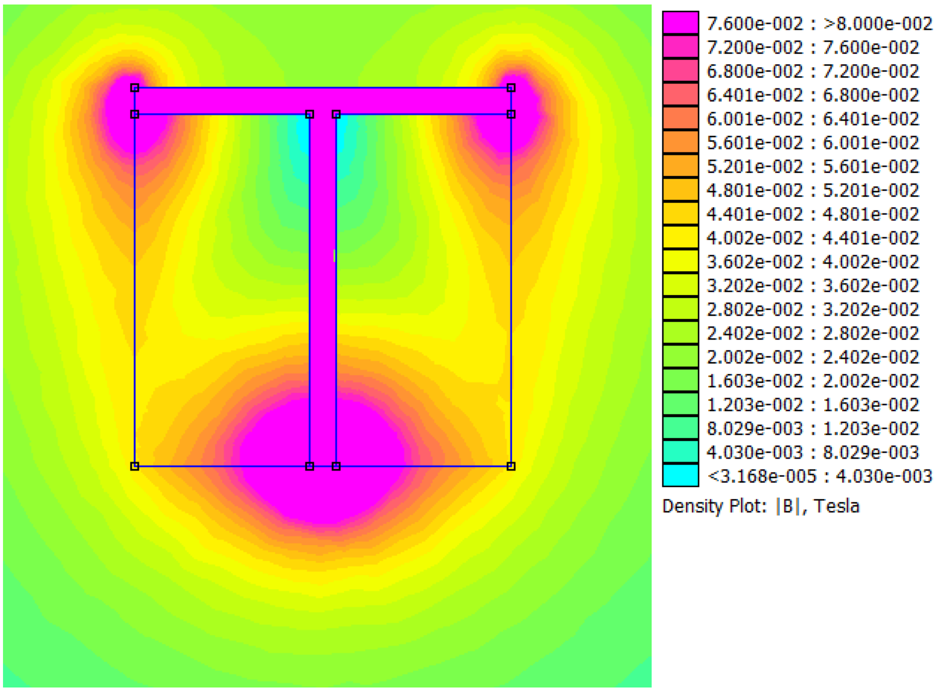

Figure 6.10: Schematic of the magnetic field behaviour of the "T" planar optimized configuration.

Secondly, the procedure performed for the "T" configuration is adopted for the "U" configuration. Thus, six geometric variables of the "U" configuration are considered in order to specify the design of the core and winding, as shown in *Figure 6.11*2.

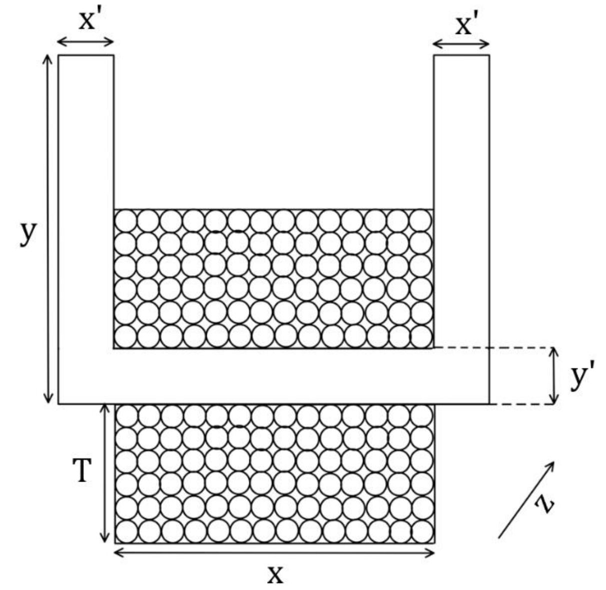

Figure 6.11: Geometric variables of the "U" planar configuration.

Since the "U" configuration has a different shape from the "T" configuration, a different environment setup for the numerical simulation of the "U" configuration is considered, ruled by the following conditions:

$$Geometric\colon \begin{cases} y + T \leq 90\ mm \\ x + 2x' \leq 90\ mm \\ z \leq 90\ mm \end{cases} \tag{7.5}$$

$$M\acute{A}X_{turns}\colon \left\lfloor \frac{x - 2x'}{D_{real}} \right\rfloor \times \left\lfloor \frac{T}{D_{real}} \right\rfloor \tag{7.6}$$

$$Total_{Length\ (Copper\ Wire)}\colon \left\lfloor \frac{x - 2x'}{D_{real}} \right\rfloor \times \sum_{k=1}^{\left\lfloor \frac{T}{D_{real}} \right\rfloor} \left(2 \times (y' + z + (2 \times k \times D_{real}))\right)\ [mm] \tag{7.7}$$

$$\begin{aligned} m_{TOTAL}\colon 7{,}874 \times 10^{-3} \times \Big((2 \times x' \times y \times z) + \big((x - 2x') \times y' \times z\big)\Big) \\ + \left(Total_{Length} \times 10^{-3} \times S_m\right)\ [g] \end{aligned} \tag{7.8}$$

Based on the assumptions considered, the setup environment is ready to perform the software analysis according to the numerical model shown in Chapter 4. Based on the geometric variables of the “U” configuration, the design properties of the optimized model are presented in *Table 6.2*. According to the characteristics of the model, shown in *Table 6.2*, its magnetic flux density results, provided by FEMM 4.2 software, are presented in *Figure 6.12*.

Table 6.2: Geometric properties of the "T" planar optimized configuration.

FEMM 402 Model Construction (Planar)		
Core	Horizontal Height (x') [mm]	75
	Vertical Height (x) [mm]	50
	Horizontal Length (y) [mm]	15
	Horizontal Length (y') [mm]	5
Depth	(z) [mm]	1
Wire	Vertical Height (T) [mm]	40
Wire		
20 AWG		
Turns		
2392		
Current [A]		
1.54		
Mass [g]		
1025.05		
MMF [N x I]		
3684		

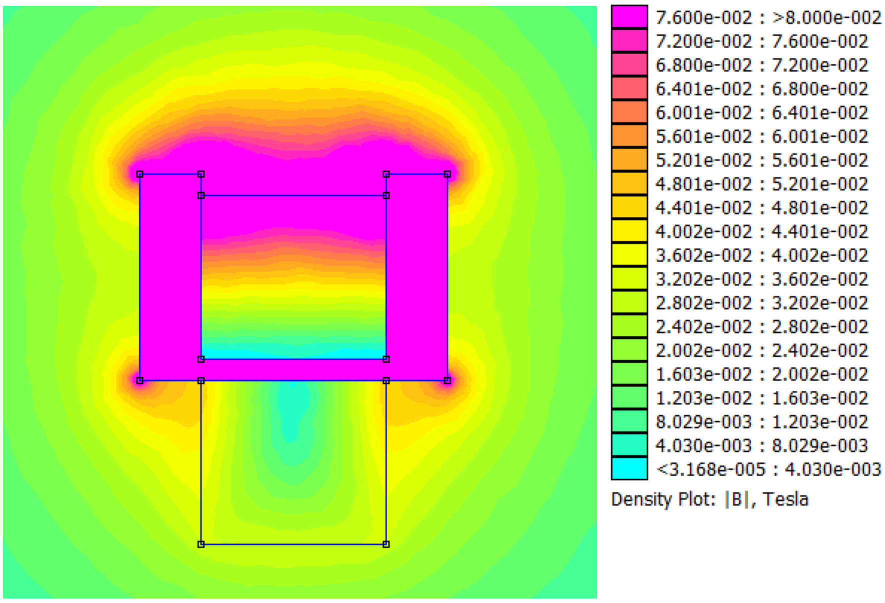

Figure 6.12: Schematic of the magnetic field behaviour of the "T" planar optimized configuration.

According to the results of the magnetic flux density provided by the FEMM 4.2 analyzes, the "T" and "U" configurations are capable of generating at least 0.0375 T at 25 mm from its own surface. Considering the configurations suggested in this section, according to their specific premises mentioned, they present a lower mass than the generic cylindrical EMG model optimized by numerical simulation (4 Numerical Model). As expected, this fact proves that switching to more efficient configurations will reduce the minimum MMF value. Finally, comparing the results of the total mass of the two configurations presented, the mass of the "U" model is smaller than the "T" model.

Chapter 7

7 Conclusion and Future Work

In this section the final conclusions of this dissertation are formulated with respect to considering the MECSE CubeSat payload requirements. In addition, according to the objectives of the MECSE mission, future improvements on the study of the EMG model are proposed. Lastly, the conferences and publications associated with the work developed throughout this dissertation are listed.

7.1 Conclusions

Firstly, considering the adaptability requirements, the cylindrical EMG model, experimentally tested and validated, is capable to fit into a standard CubeSat unit (1U). In addition, since two of the three units of the MECSE CubeSat structure are occupied by electronic equipment, the payload plate in contact with the Service module (2 BUS), should be excluded from the adaptability results. Therefore, considering 6 geometrically identical faces of the CubeSat unit, the cylindrical EMG model, as well as the two numerically optimized configurations, is able to manipulate the plasma density at 25 mm from its surface at least in 5 different positions.

Secondly, according to the magnetic flux density requirements, the EMG model experimentally validated, with influence of the magnetic core, demonstrate the ability to generate the minimum value of 0.0375 T at 25 mm from its surface. In fact, 15 new configurations are suggested by the experimental results. As investigated in the section 2.5, the value of magnetic flux density has 5% of safety margin. In light of this matter, according to section 6.1, 15% error should be imposed on the numerical analyzes of the magnetic flux density. Therefore, 0.0411 tesla should be considered for FEMM 4.2 software performance, in order to reduce the relative errors associated with the experimental validation of the EMG model.

Thirdly, in order to minimize the power demanded by the magnetic field generating system, the minimum current, capable of generating the sufficient magnetic flux density to reduce the plasma layer, must operate between 1.5 A and 2 A, as suggested by numerical and experimental results of the EMG model. According to the information presented in the section 4.1.1, based on experimental measurements of the hot and cold power of the electrical circuit, and considering the worst case possible, 98 W is required for EMG operation. Since the power dissipated is low which suggests lighter batteries. However, considering the MMF assumptions, the use of low current values will increase the number of turns of the winding, which consequently will increase the overall mass of the MECSE payload.

Fourthly, during the experimental study, the winding of the EMG cylindrical model was tested under currents higher than those considered for the numerical model performance. Depending on the mode of payload's operation during the MECSE CubeSat mission, it is possible for the magnetic field generator to operate through high current spikes, without changing the characteristics of the conductive material. Thus, according to the MMF definition, the current increment will decrease the winding mass, and consequently the total mass of the EMG.

Finally, according to the mass requirements of the EMG model, the lighter experimental configuration that is able to meet the requirements of adaptability, magnetic flux density and power, considers 1575 turns operating under 4 A. Considering these properties, the numerical model suggests a total mass of the EMG cylindrical model of 1560.90 g. Since the relative error of the numerical model is 4%, according to the conclusions of this dissertation, the estimated value of the total mass of the physical EMG model is 1500.87 g. Ongoing studies on the optimization of the 3U structure of the MECSE CubeSat [100], defined the maximum mass for the payload of 1.315 kg. Thus for the same value of MMF, it is possible to reduce the EMG model's mass, decreasing the winding turns and increasing the electric current value to over 4 ampere. However, an experimental validation of the EMG model will be necessary in order to verify its operation under higher currents than those used in the experimental activity.

7.2 Future Work

In this sub-section, the difficulties encountered during the work performed in this dissertation are considered. Therefore, future tasks are suggested in order to contribute to a more detailed study of the EMG model applied to the payload of MECSE CubeSat Experiment.

7.2.1 Analytical Model

As presented in Chapter 6, the analytical model presents a maximum error associated with experimental validation of 27.5%. Thus, the analytical study must be refined by considering Maxwell's equations under a more elaborated environment. Inputing more complexity to the Maxwell equations, in order to construct a more accurate analytical model, the analysis of different configurations of the EMG model is suggested as future work.

7.2.2 Software

Regarding the method of construction performed by FEMM 4.2, the numerical model has configurations with a high design error associated. As a result, in order to contribute for a more reliable numerical results, since FEMM 4.2 provide a CAD mode only considering two spatial dimensions, implementation of a three dimensional EMG model configuration is suggested as a future work of the MECSE CubeSat payload. In order to contribute for a more trustworthy numerical magnetic flux density results, the design and the numerical analysis shall be performed by a 3D magnetic finite element method software.

7.2.3 Losses

During the analytical, numerical, and experimental validation performed throughout this dissertation, no losses were considered. In this way, the investigation of the energetic and magnetic losses of the EMG model is suggested as future work. Considering the objectives of the MECSE CubeSat mission, this study is essential to provide more accurate magnetic flux density results.

7.2.4 Aluminum Layer

The main structural components of the MESCE CubeSat consists of aluminum material. Based on the research performed in section 2.5.5, analytical, numerical and experimental electromagnetic tests should be applied for future work, considering aluminum plates of 2 mm of thickness at the EMG surface. Consequently, it will be possible to predict the effect of the aluminum plate of the standard CubeSat unit on the magnetic flux density generated.

7.2.5 Magnetic Field Isolator

Considering the electronic components required for the MECSE CubeSat mission, EMG performance will interfere in its operation. Thus, in order to prevent the failure of the electronics systems, the study of magnetic field isolators is essential to verify the viability of the MECSE mission. Two schemes of insolation are suggested as future work, by Active Gel materials or by a Faraday cage structure.

7.2.6 Communication Antenna and Sensors

Since most of the work depends on the payload’s design, there are two main studies to be done regarding the EMG model performance. The EMG must be experimentally tested assuming the location of the communication antenna. This study will allow to proof its feasibility and provide a preliminary value of the radio frequency. Meanwhile, a study about the relationship between the size of booms and probe bias is required to determine the final location of the sensors with respect to the satellite surface.

7.2.7 Materials

In this dissertation, a detailed study of EMG core and winding materials has been performed, however, it is necessary to continue the research of new elements. In this way, one should focus on investigating materials with high magnetic permeability and low density, in order to generate a more intense magnetic field and to minimize the mass of the EMG model. In addition, the replacement of copper in the EMG winding material is a factor to be taken into account as it may decrease the overall mass of the magnetic generator model.

7.2.8 Plasma Chamber

In order to examine the effects of the magnetic field on the plasma layer, an experiment inside a plasma chamber is suggested as future work. Considering different plasma environments, and associating the magnetic properties of the EMG model, through the Langmuir Probe the measurements of the plasma density variation will provide an investigation of the interference of the magnetic flux density in different plasma layer conditions, before and during hypersonic reentry. The verification of the Magnetohydrodynamic/Electrohydrodynamic model requires an experimental ground test in order to avoid possible failures during the execution of the MECSE mission.

7.3 Publications and Conferences

The work developed in this dissertation, regarding the design, construction, and validation of the EMG model, has already been presented at the 11th International Workshop and Advanced School, "Spaceflight Dynamics and Control" held at the Universidade da Beira Interior on September 26-28, 2018 [101].

Furthermore, the abstract of this work has been submitted and will be published at the III IAA Latin American CubeSat Workshop" on "CubeSats future payloads and experiments" topic, in Ubatuba, Brazil, December 2018 [102].

Bibliography

[1] NASA, “Investigation of Invisible Magnetic Bubbles in Outer Solar System”, [Online]. Available: https://www.nasa.gov/feature/goddard/2017/nasa-investigates-invisible-magnetic-bubbles-in-outer-solar-system. [Accessed in 12 July 2018].

[2] NASA, “Magnetospheres”, [Online]. Available: https://science.nasa.gov/heliophysics/focus-areas/magnetosphere-ionosphere. [Accessed in 10 August 2018].

[3] S. E. O. Resources, “MMS Constellation”, [Online]. Available: https://directory.eoportal.org/web/eoportal/satellite-missions/m/mms-observatory. [Accessed in 13 August 2018].

[4] M. Kim et al, “Electromagnetic Manipulation of Plasma Layer for Re-entry Blackout Mitigation, dissertation”, The University of Michigan, 2009.

[5] A. Gulhan et al, “Plasma Manipulation using a MHD-based Device for a Communication Blackout in Hypersonic Flights”, em *Proceedings of 5th International Conference on Recent Advances in Space Technologies*, RAST , 2011.

[6] P. Starkey et al, “Plasma Field Telemetry for Hypersonic Flight”, 2003.

[7] M. Kim et al, Analysis of an Electromagnetic Mitigation Scheme for Reentry Telemetry Through Plasma, J. Spacecr. Rockets, 2008.

[8] B. D. Gillman et al, Review of Leading Approaches for Mitigating Hypersonic Vehicle Communications Blackout and a Method of Ceramic Particulate Injection Via Cathode Spot Arcs for Blackout Mitigation, 2010.

[9] A. Hartunian et al, Causes and Mitigation of Radio Frequency Blackout (RF) during Reentry of Reusable Launch Vehicles, Cambridge, 2007.

[10] Y. Takahashi et al, “Analysis of Radio Frequency Blackout for a Blunt-Body Capsule in Atmospheric Reentry Missions”, *Aerospace,* vol. 3, no. 1, p. 2, 2016.

[11] J. Páscoa and F. Dias, “Numerical Computations of MHD Flow on Hypersonic and Re-Entry Vehicles”, *ASME 2016 International Mechanical Engineering Congress and Exposition,* p. 1-9, 2016.

[12] F. Dias, “Modelação numérica de escoamento MHD em veículos de reentrada na atmosfera”, Universidade da Beira Interior, 2016.

[13] M. Keidar et el, “Electromagnetic Reduction of Plasma Density During Atmospheric Reentry and Hypersonic Flights”, *J. Spacecr. Rockets,* vol. 45, no.3, p. 445-453, 2008.

[14] D. D. Morabito, “The Spacecraft Communications Blackout Problem Encountered during Passage or Entry of Planetary Atmospheres”, 2002.

[15] A. E. Cross et al, “Electrostatic-Probe Measurements of Plasma Parameters For Two Reentry Flight Experiments at 25000 Feet per Second”, Washington, D.C. , 1972.

[16] R. P. Starkey, “Hypersonic Vehicle Telemetry Blackout Analysis”, *J. Spacecr. Rockets,* vol. 522015, no. 28, p. 426–43, 2015.

[17] Y. Xia et al, “Navigation Strategy with the Spacecraft Communications Blackout for Mars Entry”, *Adv. Sp. Res.,* vol. 55, no. 4, p. 1264–1277, 2004.

[18] I. Telecommunications, “PROJECT / INFANTE”, [Online]. Available: https://www.it.pt/Projects/Index/4523. [Accessed in 30 August 2018].

[19] I. M. Applications, “About INFANTE”, [Online]. Available: http://infante.space/about-us/. [Accessed in 30 August 2018].

[20] I. M. Applications, 30 August 2018. [Online]. Available: http://infante.space/about-us/.

[21] ClusterDEM, “Multiphysics Flow Research”, [Online]. Available: [http://wordpress.ubi.pt/clusterdem/. [Accessed in 28 August 2018].

[22] V. Richard Leifer et al, Radical Innovation: How Mature Companies Can Outsmart Upstarts, Harvard Business Press, 2003.

[23] G. Facchinetti, Small Satellites: Economic Trends, dissertation, Universita' Commerciale Luigi Bocconi, Milano, 2016.

[24] B. Battrick et al, "The Impact of Space Activities Upon Society", *The European Space Agency, The International Academy of Astronautics,* no. 237, ESA Publications Division - ESTEC, 2005.

[25] N. D. Tyson, "The Case for Space: Why we should keep reaching for the stars", *Foreign Aff,* vol. 91, no. 2, p. 22–33, 2012.

[26] E. Tubbal et al, "A Survey and Study of Planar Antennas for Pico-Satellites", *IEEE Access,* 2015.

[27] M. Kim et al, "Analysis of an Electromagnetic Mitigation Scheme for Reentry Telemetry Through Plasma", *J. Spacecr. Rockets,* vol. 45, no. 6, p. 1223–1229, 2008.

[28] J. R.Wertz et al, "Space Missions Engineering: The New SMAD", *Space Technology Library,* 2015.

[29] M. N. Sweeting, "Modern Small Satellites-Changing the Economics of Space", *IEEE, Proceedings of the IEEE,* vol. 106, p. 343-361, 2018.

[30] J. H. Helvajian, "Anti-Satellite Weapons, Countermeasures, and Arms Control", *Aerospace Press,* 2008.

[31] A. Toorian et al, "The CubeSat Approach to Space Access", *IEEE Aerospace Conference,* vol. 1, p. 1-9, 2008.

[32] C. P. S. University, "CubeSat Design Specification", *Rev.13,* 2014.

[33] A. Golkar et al, "CubeSat evolution: analyzing CubeSat capabilities for conducting science missions", *Progress in Aerospace Sciences,* 2016.

[34] e. Directory, "DICE (Dynamic Ionosphere CubeSat Experiment)", [Online]. Available: https://directory.eoportal.org/web/eoportal/satellite-missions/d/dice. [Accessed in 4 August 2018].

[35] C. V. McDonald, "STEM Education : A review of the contribution of the disciplines of science, technology, engineering and mathematics", *Sci. Educ. Int,* vol. 27, no. 4, p. 530–569, 2016.

[36] J. T. Monteiro, "Mission Analysis and Design of MECSE Nanosatellite", Universidade da Beira Interior, Covilhã, 2017.

[37] A. Azevedo, "Design of MECSE Nanosatellite Mechanical", Universidade da Beira Interior, Covilhã, 2017.

[38] Thermometrics, "Type K Thermocouple", [Online]. Available: http://www.thermometricscorp.com/. [Accessed in 20 July 2018]

[39] H. I. Sakraker et al, "QARMAN: An Atmospheric Enty Experiment On CubeSat Platform", *LPI Contrib,* 2014.

[40] OMEGA, "Temperature Measurement in Electromagnetic Environments.", [Online]. Available: http://www.omega.com/technical-learning/temperature-measurement-in-electromagnetic-environments.html. [Accessed in 19 July 2018].

[41] Amphenol, "NPC-1220 Specifications", [Online]. Available: http://pt.mouser.com/search/ProductDetail.aspx?R=0virtualkey0virtualkeyNPC-1220-100G-3N. [Accessed in 20 July 2018].

[42] Avantes, "AvaSpec-Mini: Small and powerful OEM spectrometer", [Online]. Available: https://www.avantes.com. [Accessed in 19 July 2017].

[43] W. Linwood Jones et al, "Electrostatic-Probe Measurements of Plasma", *National Aeronautics and Space Administration, Washington, D.C.,* 1972.

[44] E. S. Helgeby, "Active Spacecraft Potential Control of the CubeSTAR Nano-satellite", University of Oslo, 2013.

[45] "CubeSTAR", University of Oslo, 2017. [Online]. Available: http://www.cubestar.no/index.php. [Accessed in 5 August 2018].

[46] V. K. Institute, "QB50 Project", [Online]. Available: https://www.qb50.eu/index.php/community [Accessed in 5 August 2018].

[47] K. S. Jacobsen et al, “A new Langmuir probe concept for rapid sampling of space plasma electron density”, *Meas. Sci. Technol,* vol. 21, no. 8, p. 85902, 2010.

[48] T. A. Bekkeng et al, “Payload charging events in the mesosphere and their impact on Langmuir type electric probes”, *Ann. Geophys,* vol. 31, no. 2, p. 187–196, 2013.

[49] R. T. Nadal, “Design And Testing Of The Pressure Payloads And Data Acquisition of QARMAN CubeSat”, *Université de Liège,* 2013.

[50] ESA, “Reentry Test of QARMAN CubeSat”, [Online]. Available: https://www.esa.int/spaceinimages/Images/2018/06/Reentry_test_of_QARMAN_CubeSat. [Accessed in 14 August 2018].

[51] M. Moldwin, An Introduction to Space Weather, Cambridge University Press, 2008.

[52] J. K. Hargreaves, The Solar-Terrestrial Environment, Cambridge University Press, 1992.

[53] M. M. Amin, Influence of lightning on electron density variation in the ionosphere using WWLLN lightning data and GPS data, University of Cape Town, 2015.

[54] Z. T. Katamzi, “Statistical Analysis of Ionospheric Total Electron Content”, University of Bath, 2011.

[55] H. T. Gerzen et al, “Reconstruction of F2 Layer Peak Electron density based on Operational Vertical Total Electron Content Maps”, *German Aerospace Center (DLR), Institute of Communications and Navigation, Kalkhorstweg 53, 17235 Neustrelitz, Germany,* 2013.

[56] M. Kim, M. Keidar, I. D. Boyd e D. Morris, “Plasma Density Reduction Using Electromagnetic E x B Field during Reentry Flight, Published in International Telemetering Conference Proceedings”, *International Foundation for Telemetering Journal,* 2017.

[57] R. A. Wood et al, “Mars Pathfinder Entry, Decent, and Landing Communicstions”, *Jet Propulsion Laboratory, Pasadena, CA, The Telecommunications and Data Acquisition Progress Report,* 1997.

[58] N. Tecnologies, I. Administration, “Manual of Regulations and Procedures for Federal Radio Frequency Management”, Washington, D.C, 2007.

[59] N. Technologies, I. A. The Radio Spectrum, United States Frequency Allocations, Washington, D.C, 2003.

[60] L. Y. Du et al, “Plasma Sheath Multipath Analysis and Its Effect on GNSS Navigation”, *Appl. Phys. A,* vol.121, no. 3, p. 1081–1085, 2015.

[61] A. S. Belov et al, “Investigation of Remote Antenna Assembly for Radio Communication with Reentry Vehicle”, *Journal of Spacecraft and Rockets,* vol. 38, no. 2, p. 249–256, 2001.

[62] D. F. Spencer, “An Evaluation of the Communication Blackout Problem for a Blunt Mars-Entry Capsule and a Potential Method for the Elimination of Blackout”, Technical Report 32-594, Jet Propulsion Laboratory, Pasadena, Califonia, 1964.

[63] L. G. Hunter et al, “Low Energy Electron Attachment to SF6 in N2, Ar, and Xe buffer gases”, *Journal of Chemical Physics,* vol.90, no. 9, p. 4879–4891, 1989.

[64] B. D. Kowari et al, “The Coupling of Electron Thermalization and Electron Attachment in CCl4/Ar and CCl4/Ne Mixtures”, *Journal of Chemical Physics,* vol. 108, no. 4, p. 1587–1600, 1998.

[65] J. K. Russo et al, “Measurements of The Effects of Static Magnetic Fields on VHF Transmission in Ionized Flow Fields”, *TM X-907, NASA,* 1964.

[66] R. Rawhouser, “Overview of the AF Avionics Laboratory Re-entry Electromagnetics Program”, *The Rntry Plasma Sheath and its Effects on Space Vehicle Electromagnetic Systems,* vol. 1, NASA Langley Research Center , nº NASA SP-252, p. 3–17, 1964.

[67] J. C. Starkey et al, “Electromagnetic Wave/Magnetoactive Plasma Sheath Interaction for Hypersonic Vehicle Telemetry Blackout Analysis”, em *34th AIAA Plasmadynamics and Lasers Conference*, 2003.

[68] M. Fujino et al, “Numerical simulation of Control of Plasma Flow With Magnetic Field for Thermal Protection in Earth Reentry Flight”, *IEEE Transactions on Plasma Science,* vol. 34, no. 2, p. 409-420., 2006.

[69] K. D. Otsu et al, “Feasibility Study on the Flight Demonstration for a reentry vehicle with Magnetic Flow Control System”, em *37th AIAA Plasmadynamics and Laser Conference*, San Fanscisco, 2006.

[70] A. Tetsuya Tanifuji et al, “Expansion tube experiment of applied magnetic field effect on reentry plasma”, em *46th AIAA Aerospace Sciences Meeting and Exhibit*, Reno, Nevada, 2008.

[71] A. Alexander, S.Chernyshev et al, “Effect of an Applied Magnetic Field on Blunt Body Plasma Flow”, em *44th AIAA Aerospace Sciences Meeting and Exhibit*, Reno, Nevada, 2006.

[72] A. Golkar et al, “CubeSat evolution: Analyzing CubeSat capabilities for conducting science missions”, *Prog. Aerosp. Sci.*, no. 1, p. 1–25, 2016.

[73] W. S. Richard, A. Hartunian et al, “Implications and Mitigation of Radio Frequency Blackout during Reentry of Reusable Launch Vehicles”, em *AIAA Atmospheric Flight Mechanics Conference and Exhibit*, Hilton Head, South Carolina, 2007.

[74] H. Hodara, “The Use of Magnetic Fields in the Elimination of the Re-Entry Radio Blackout, Illinois Institute of Technology, Chicago, Ill.”, 28 August 1961.

[75] C. R. Underhill, Solenoids Electromagnets and Electromagnetic Windings, New York: D. Van Nostrand Company, 1910.

[76] J. M. D. Coey, Magnetism and Magnetic Materials, Cambridge University Press, 2010.

[77] R. Thierry Lubin et al, “Inductance and Force Calculation for Axisymmetric Coil Systems Including an Iron Core of Finite Length”, *Progress In Electromagnetics Research B,* vol. 41, p. 377–396, 2012.

[78] D. Fleisch, A Student's Guide to Maxwell's Equations, Cambridge University Press, 2008.

[79] R. Thierry Lubin et al, “Exact Analytical Method for Magnetic Field Computation in the Air Gap of Cylindrical Electrical Machines Considering Slotting Effects”, *IEEE Transactions on Magnetics,* vol. 46, no. 4, p. 1092-1099, 2010.

[80] L. J. Gysen et al, “General Formulation of the Electromagnetic Field Distribution in Machines and Devices Using Fourier Analysis”, *IEEE Transaction on Magnetics* , vol. 3, no. 1, p. 39-52, 2010.

[81] G. Meunier, The Finite Element Method for Electromagnetic Modeling, ISTE Ltd, 2008.

[82] P. Monk, Finite element methods for Maxwell's equations, Numerical mathematics and scientific computation, Oxford University Press: Clarendon Press, 2003.

[83] T. K. Kenji Kawano, Introduction to optical waveguide analysis: solving Maxwell's equations and the Schrodinger equation, J. Wiley, 2001.

[84] B. Thidé, Electromagnetic Field Theory, Swedish Institute of Space Physics and Department of Astronomy and Space Physics Uppsala University, Sweden and School of Mathematics and Systems Engineering Växjö University, Sweden, 2004.

[85] 4.2 FEMM, “Finite Element Method Magnetics: MagneticsTutorial”, [Online]. Available: http://www.femm.info/wiki/MagneticsTutorial. [Accessed in 4 August 2018].

[86] G. Bernhardt, “Formula of Solenoid Magnetic B-field at Ending, Middle and Outside”, [Online]. Available: https://www.physicsforums.com/threads/formula-of-solenoid-magnetic-b-field-at-ending-middle-and-outside.828426/. [Accessed in 4 August 2018].

[87] Farside, “Magnetic Field of a Solenoid”, [Online]. Available: http://farside.ph.utexas.edu/teaching/302l/lectures/node76.html. [Accessed in 4 August 2018].

[88] AspenCore, “The Electromagnet”, [Online]. Available: https://www.electronics-tutorials.ws/electromagnetism/electromagnets.html. [Accessed in 4 August 2018].

[89] P. S. P. Spring, “Magnetic field of a solenoid”, [Online]. Available: https://web.pa.msu.edu/courses/2000fall/phy232/lectures/ampereslaw/solenoid.html. [Accessed in 5 August 2018].

[90] Department of Physics Education, “Magnetic Field inside a Solenoid”, [Online]. Available: http://physicstasks.eu/1785/magnetic-field-inside-a-solenoid. [Accessed in 5 August 2018].

[91] D. Hoult, “Flux Density inside a Long Coil (Solenoid)”, [Online]. Available: http://www.saburchill.com/physics/chapters/0052.html. [Accessed in 6 August 2018].

[92] B. Dias, “Mitigação da Exposição Pública a Campos Magnéticos Gerados por Transformadores de Distribuição de Energia”, Instituto Superior Técnico, Universidade Técnica de Lisboa, 2011.

[93] K. B. Baltzis, “The Finite Element Method Magnetics (FEMM) Freeware Package: May it Serve as an Educational Tool in Teaching Electromagnetics?”, *Education and Information Technologies,* 22 Mach 2010.

[94] D. Meeker, Finite Element Method Magnetics, Version 4.2, User’s Manual, 2015.

[95] T. Stokes Rees, “FEMM 4.2 Magnetostatic Tutorial, Introduction to FEA with FEMM”, 2006.

[96] S. Division et al, “Space engineering: Electromagnetic compatibility”, em *European Cooperation for Space Standardization*, Noordwijk, The Netherlands, 2012.

[97] Ramada Indústria, “Ramada Aços, Special Steel Solutions”, [Online]. Available: http://www.ramada.pt/pt/. [Accessed in 5 October 2018].

[98] M. P. D. S. GmbH, “Magnetic Field Strength Meter Gauss-/Teslameter FH 51 and GH 54”, Köln, 2008.

[99] Dassault Systèmes. [Online]. Available: http://www.3ds.com/products-services/catia/. [Accessed in 25 July 2018].

[100] M. Esteves, “Design Optimization for AM of MECSE CubeSat's Mechanical System”, 2018.

[101] C-MAST and SPACEWAY, “11th International Workshop and Advanced School "Spaceflight Dynamics and Control"“, 26-28 September 2018. [Online]. Available: http://www.ubi.pt/entidade/workshop_spaceflight. [Accessed in 5 October 2018].

[102] O. Committee, “III IAA Latin American CubeSat Workshop”, International Academy of Astronautics, 3 to 7 December 2018. [Online]. Available: http://iaalacw.org/. [Accessed in 5 October 2018].

[103] L. T. Bekkeng et al, “Design of a multi-needle Langmuir probe system”, University of Oslo, 0316 Oslo, Norway and ESA/ESTEC, Noordwijk, The Netherlands, 2010.

[104] J. C. Starkey et al, “Active FlowField Modification For Plasma Telemetry”, *International Test & Evaluation Association Workshop, Lancaster, CA,* 2002.

[105] Farside, “Magnetic Field of a Solenoid”, [Online]. Available: http://farside.ph.utexas.edu/teaching/302l/lectures/node76.html. [Accessed in 4 August 2018].

[106] C. R. Nave, “Magnetic Field Concepts”, [Online]. Available: http://hyperphysics.phy-astr.gsu.edu/hbase/magnetic/solenoid.html. [Accessed in 7 August 2018].

[107] Farnell, “Enamelled Copper Wire, 20 AWG”, [Online]. Available: http://www.farnell.com/datasheets/2353651.pdf?_ga=2.124637197.689819890.1537484499-119663737.1534929768. [Accessed in 27 July 2018].

[108] Farnell, “ECW0.80 - Wire, Solid, Solderable PU Enamelled Copper, Unjacketed, 20 AWG, 0.515 mm^2, 410.1 ft, 125 m”, [Online]. Available: https://pt.farnell.com/pro-power/ecw0-80/wire-0-8mm-copper-enamelled-125m/dp/1230984?st=Wire,%20Solid,%20Solderable%20PU%20Enamelled%20Copper,%20Unjacketed,%2012%20AWG. [Accessed in 27 July 2018].

[109] N. Technologies, I. Administration, “United States Frequency Allocations: The Radio Spectrum”, Washington, D.C, 2003.

[110] Electrical Engineering articles and tutorial. [Online]. Available: http://eblogbd.com/wht-is-solenoid-and-its-basic-working-principle/.

Appendix A

A FEMM 4.2

A.1 Interfaces

To demonstrate the characteristics and capabilities of FEMM a series of illustrative examples are presented here. The first example is described in detail in order to make clear the characteristics of the software. The steps followed in each case are:

I. Physical problem description;
II. Model design;
III. Materials description;
IV. Boundary conditions application;
V. Mess generation;
VI. Finite Element Method application;
VII. Results extraction and analysis.

A.1.1 Magnetic Pre-processor

The pre-processor is used for select the problem type, drawing the problems geometry, defining materials and its properties, and defining boundary conditions. Firstly a new model can be created by selecting File|New off of the main menu and then choosing "Magnetics Problem" from the list of problem types which then appears (Figure A.1).

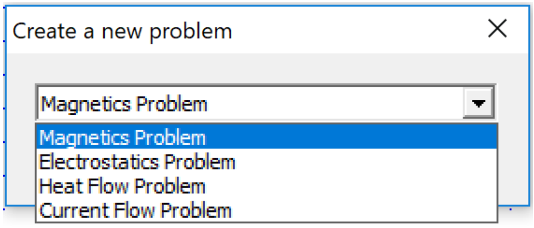

Figure A.1: List of problem types of FEMM 4.2.

Consequently, in order to draw a valid geometry, four sequential tasks must be followed:

- Drawing the endpoints of the lines and arc segments that make up a drawing;
- Connecting the endpoints with either line segments or arc segments;
- Adding "Block Label" markers into each section of the model to define material properties and mesh sizing for each section;
- Specifying boundary conditions on the outer edges of the geometry drawn.

In order to realize the pre-processor phase, firstly, it is fundamental to define the characteristics of the geometry. The user uses nodes, or points, to define all corners in the solution geometry, line segments and arc segments to connect the nodes which form interfaces and block labels which denote what material properties and mesh size are associated with each solution region. The fifth mode, the group mode, is meant to glue different objects together into parts so that entire parts can be manipulated more easily. One can switch between drawing modes by clicking the appropriate button on the Drawing Mode potion of the toolbar. This section of the toolbar is represented in *Figure A.2*. The buttons correspond to Point, Line Segment, Arc Segment, Block Label, and Group modes respectively. The selected drawing mode (*Figure A.2*) is the Point mode.

Figure A.2: Drawing model toolbar buttons.

After the design of the geometry, the definition of the problem is specified by choosing the Problem selection off of the main menu. Selecting this option, brings up the Problem Definition dialog, shown in *Figure A.3*.

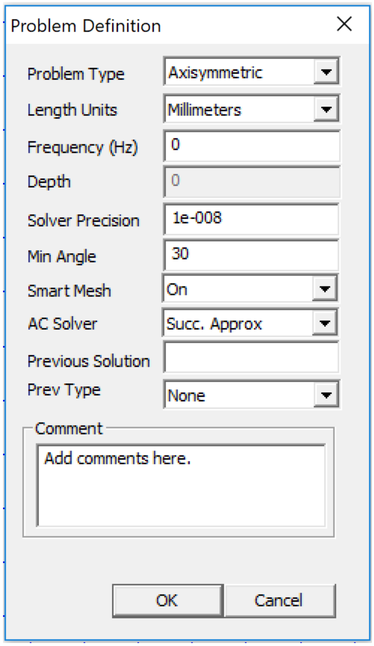

Problem Definition
Problem Type: Axisymmetric
Length Units: Millimeters
Frequency (Hz): 0
Depth: 0
Solver Precision: 1e-008
Min Angle: 30
Smart Mesh: On
AC Solver: Succ. Approx
Previous Solution:
Prev Type: None
Comment: Add comments here.

Figure A.3: Problem definition FEMM 4.2 dialog.

The first option, presented in *Figure A.3*, is the Problem Type drop list, which allows the user to choose from a two dimensional planar problem (the Planar selection), or an axisymmetric problem (the Axisymmetric selection).

The next option category is the Length Units drop list. This drop box determines which unit is associated with the dimensions established in the model's geometry. The selecting options are inches, millimeters, centimeters, meters, miles, and micrometers.

The first edit box of the problem definition dialog is the Frequency (Hz). For a magnetostatic problem selected, the frequency is set to zero. If the frequency is non-zero, the software will perform harmonic analysis, where all field quantities are oscillating at this prescribed frequency.

The second edit box is the Depth specification, which becomes activated just if a Planar problem is selected. This value is the length of the geometry in the "into the page" direction which is used for scaling integral results in the post processor to the appropriate length. The units in the Depth selection are the same as the selected Length Units.

The third edit box is named Solver Precision. In this box, the value specifies the stopping criteria for the linear solver. The linear algebra of the problem could be represented by:

$$M\,x = b \tag{A.1}$$

Where M is a square matrix, b is the vector and x is the vector of unknown variables. The solver precision number determines the maximum allowable value for $\|b - M\,x\|/\|b\|$, which by default is 10^{-8}.

The fourth edit box is the Min Angle. The input in this box is used as a constraint in the Triangle meshing program. The edit box will accept values between 1 and 33,8 degrees, which for highly refined meshes, it may be necessary to reduce the minimum angle to well below 20 to avoid problems associated with insufficient floating-point precision.

Lastly, there is an optional Comment edit box. In this box, it is possible enter in a few lines of text a brief description of the problem that is being solved. The comment can be used to identify the relevant features for a particular geometry.

In order to specify the properties associated with the block labels disposed in geometry, the Block Property dialog box is employed. Here is possible to select the material's specific properties as well as attributes related with its composition. The Block Property dialog is revealed when a new material property is added or an existing property modified, as represented in *Figure A.4*.

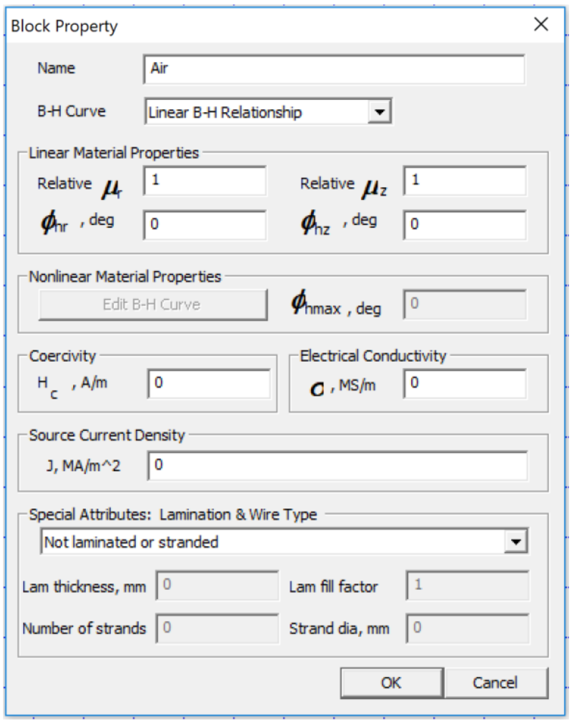
Block Property

Name: Air

B-H Curve: Linear B-H Relationship

Linear Material Properties

Relative μ_r: 1

Relative μ_z: 1

ϕ_{hr}, deg: 0

ϕ_{hz}, deg: 0

Nonlinear Material Properties

ϕ_{hmax}, deg: 0

Coercivity

H_c, A/m: 0

Electrical Conductivity

σ, MS/m: 0

Source Current Density

J, MA/m^2: 0

Special Attributes: Lamination & Wire Type

Not laminated or stranded

Lam thickness, mm: 0

Lam fill factor: 1

Number of strands: 0

Strand dia, mm: 0

Figure A.4: Material properties of Block Property FEMM 4.2 dialog.

In Block Property dialog is introduced material characteristics such as the behaviour of the B-H Curve, the Relative Permeability (μ), the Relative Hysteresis Lag ($ø_h$), the Coervcivity (Ac), the Electrical Conductivity (α), The Source Current Density (J), and Special Attributes related with lamination or the wire type.

In pre-processor phase, different types of material might be needed in several particular models, thus it is important built an library of block property definitions. In this sense, FEMM allows the access and maintain this library by selecting the Materials Library option. When this option is selected, the Materials Library dialog, pictured in Figure A.5 emerge.

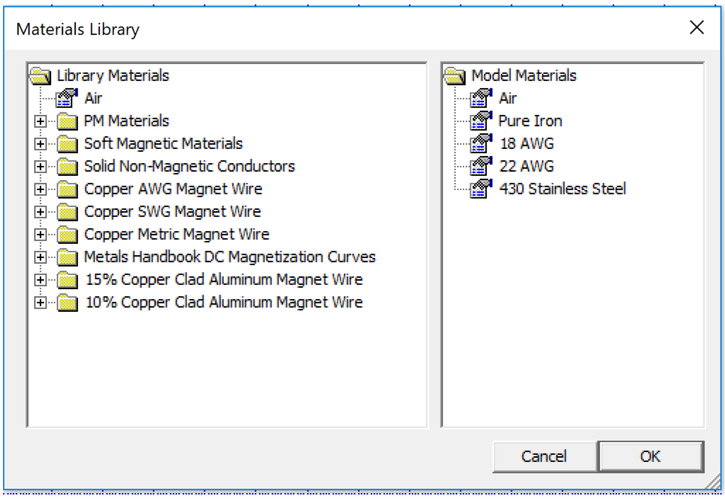
Materials Library

Library Materials
- Air
- PM Materials
- Soft Magnetic Materials
- Solid Non-Magnetic Conductors
- Copper AWG Magnet Wire
- Copper SWG Magnet Wire
- Copper Metric Magnet Wire
- Metals Handbook DC Magnetization Curves
- 15% Copper Clad Aluminum Magnet Wire
- 10% Copper Clad Aluminum Magnet Wire

Model Materials
- Air
- Pure Iron
- 18 AWG
- 22 AWG
- 430 Stainless Steel

Figure A.5: Materials Library dialog of FEMM 4.2.

This dialog allows the user to exchange Block Property definitions between the current model and the materials. The Materials Library dialog features are available of choosing the desired material as well as edit its block properties. Furthermore, material from other material libraries or models can be imported by selecting Import Materials

The purpose of the Circuit Properties is to allow the application of the constraints on the current flowing in one or more blocks. Circuits can be defined as either ”parallel” or ”series” connected. In Parallel selection, the current is split between all regions marked such that the voltage drop is the same across all sections connected in parallel. If Series is selected, the specified current is applied to each block named with that circuit property. The two option mentioned as well as the value of the Circuit Current selecting mode are represented in *Figure A.6*.

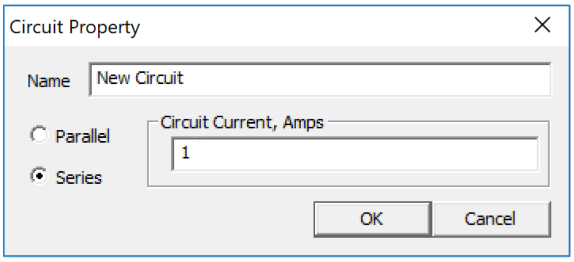

Name: New Circuit
○ Parallel
● Series
Circuit Current, Amps: 1

Figure A.6: Circuit Property dialog of FEMM 4.2.

In addition, blocks which are associated with a series circuit property can also be assigned a number of turns, such that the region is treated as a stranded conductor in which the total current is the series circuit current times the number of turns in the region, as presented in *Figure A.7*.

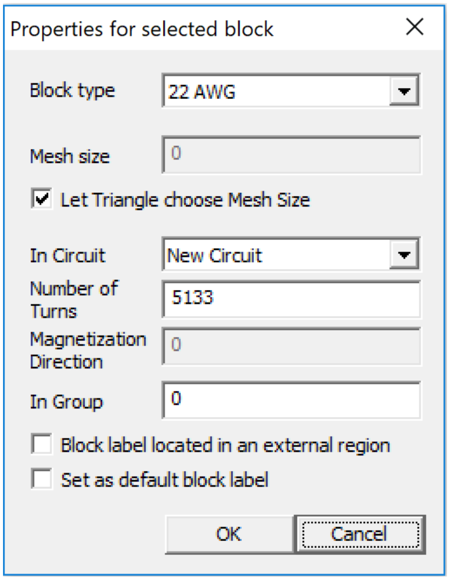

Block type: 22 AWG
Mesh size: 0
☑ Let Triangle choose Mesh Size
In Circuit: New Circuit
Number of Turns: 5133
Magnetization Direction: 0
In Group: 0
☐ Block label located in an external region
☐ Set as default block label

Figure A.7: Specific properties of the Block selected (FEMM dialog).

The Properties for Selected Block dialog for the region of interesting prescribes a number of turns. All stranded coils must be defined as series-connected, which means each turn is connected together with the other turns in series. Note that the number of turns assigned to a block label can be either a positive or a negative number. The sign on the number of turns indicated the direction of current flow.

The Open Boundary Builder dialog box is used to specify the properties and the conditions of line segments or arc segments that are to be boundaries of the solution domain. It is strictly necessary to create a boundary condition so that the FEMM can proceed to the data analysis. *Figure A.8* shows the Open Boundary Builder dialog.

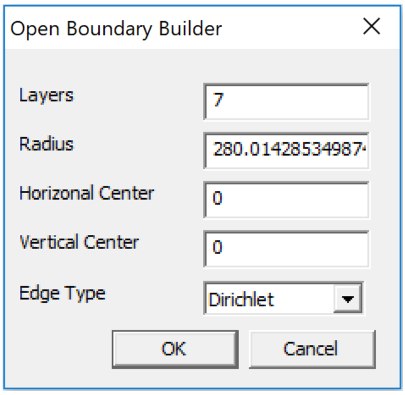

Layers: 7
Radius: 280.01428534987
Horizonal Center: 0
Vertical Center: 0
Edge Type: Dirichlet

Figure A.8: Boundary builder dialog of FEMM 4.2.

The first edit box in the dialog is the Layers of the boundary, which is related to the number of layers that are associated with the mesh simulation. The FEMM analysis becomes more detailed the greater the number of layers of the boundary.

The second edit box in the dialog is the Radius of the boundary. This parameter will restrict the size of the boundary, which means that the number of results consulted, after FEMM simulation, depends linearly of the value presented in the Radius selection.

The Horizontal Center and Vertical Center edit boxes, determine the centre of the boundary creation. Usually in the numerical simulation, the geometry model design was predefined in order to assign the central boundary point at (0,0), respectively.

Lastly, the Edge Type selection allows the user to choose between different boundary conditions. In Dirichlet type of boundary condition, the value of potential A or V is explicitly defined on the boundary, e.g. A = 0. The most common use of Dirichlet type boundary conditions in magnetic problems is to define A = 0 along a boundary to keep magnetic flux from crossing the boundary. On the other hand, Neumann boundary condition specifies the normal derivative of potential along the boundary. In magnetic problems, the homogeneous Neumann boundary condition is defined along a boundary to force flux to pass the boundary at exactly a 90o angle to the boundary.

Considering the FEMM specifications discussed before, meshing the model, analyzing the model, and viewing the results are most easily performed by the toolbar exhibited in *Figure A.9*.

Figure A.9: Toolbar buttons for starting analysis task.

The first of these buttons (with the “yellow mesh” icon) runs the Mesh Generator. The solver automatically invocate the mesh generator, which considering the boundary properties, will to make sure that the mesh is up to date. After the geometry is triangulated, the finite element mesh is loaded into memory and displayed underneath the defined nodes, segments, and block labels as a set of yellow lines.

The second button (with the “hand-crank” icon) executes the solver, fkern.exe. Before fkern is actually run, the Triangle is called to make sure the mesh is up to date. Then, fkern is invoked. The time that fkern requires is highly dependent on the problem being solved. Solution times can range from less than a second to several hours, depending upon the size of the mesh and complexity of the problem.

Once the analysis is finished, the “big magnifying glass” icon is used to Display the Results in a postprocessing window. This button makes the bridge between the magnetic pre-processor to postprocessor. A detailed description of the magnetics postprocessor is addressed in the next section.

A.1.2 Magnetic Postprocessor

The magnetics postprocessing use the fkern solver to visualize FEMM solutions. Similar to the pre-processor, the postprocessor always operate in one of three modes, depending upon the task to be performed. These modes are:

- Point Values Mode

In this mode, it is possible to consult various points in the solution region, where local field values are listed in the FEMM Output window.

- Contour Mode

With this mode allows, a solution region can be defined by arbitrary contours . Defining the contour, plots of field quantities can be produced, and various line integrals can be evaluated along the contour.

- Block Mode

This mode define a subdomain in the solution region, which a variety of area and volume integrals can be taken over the defined subdomain. Integrals include stored energy (inductance), various kinds of losses, total current in the block, and so on.

The Analysis Mode toolbar buttons (*Figure A.10*) can transduce the current postprocessor mode. The buttons denote, respectively, Point Values mode, Contour Mode, and Block Mode.

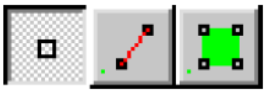

Figure A.10: Analysis mode toolbar buttons.

After defining the mode of analysis, the FEMM offers different methods of analysis of several parameters. Thus, FEMM provides three useful tools to get a subjective approximations for a magnetics finite elements solution. The three methods are Contour Plot, Density Plot and Vector Plot, presented in *Figure A.11*.

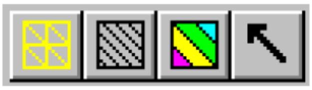

Figure A.11: Graphic mode toolbar buttons.

The Contour Plot provides information about the streamlines along which flux flows in the finite element geometry. Where flux lines are close together, the flux density is high.

The Density Plot (colored central bottom in *Figure A.11*) is used to visualize the magnetic flux density in several parts as well as in specific points. Depending on the problem type under analysis, this method has the particularity of choosing to plot flux density, field intensity, or current density. Furthermore, the magnitude range of the parameters can be altered, in order to understand better the behavior of the magnetic field in special locations. Thus the flux density at each point is classified into one of twenty contours distributed evenly between either the minimum and maximum flux densities or user-specified bounds.

The last analysis method of the postprocessor mode, is the Vector Plot. This type of plot indicates the direction and the magnitude of the field analyzed. The presence and appearance of this type of plot can be controlled by pressing the “arrows” icon pictured in *Figure A.11*.

Finally, in *Figure A.12* are represented the Line Plot, Integration, and Circuit Results toolbar buttons.

Figure A.12: Line Plot, Integration, and
Circuit results toolbar buttons.

All the option are useful to get important results as Cartesians graphics by Line Plot, the Integrals operation during the simulation phase, and Circuit Properties.

The Circuit Properties dialog confer results about Total current, the Voltage Drop, the Flux Linkage, the Flux/Current, the Resistance, and the Power set in the simulation analysis. *Figure A.13* shows the results of the Circuit Properties dialog window, as mentioned before.

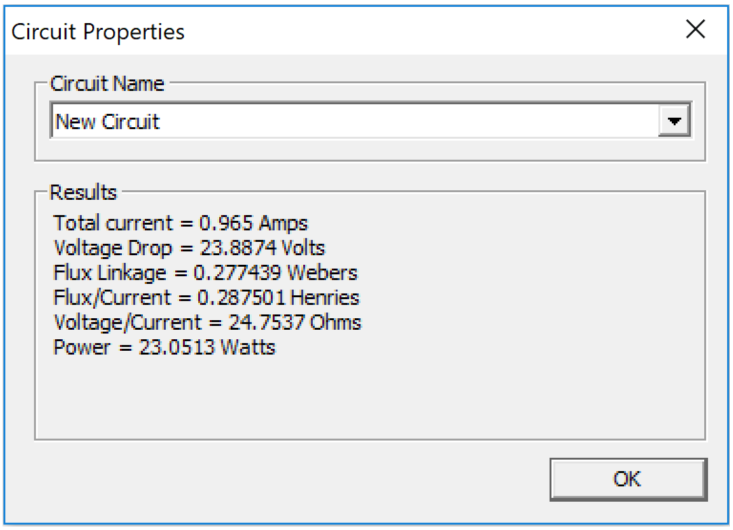

Total current = 0.965 Amps
Voltage Drop = 23.8874 Volts
Flux Linkage = 0.277439 Webers
Flux/Current = 0.287501 Henries
Voltage/Current = 24.7537 Ohms
Power = 23.0513 Watts

Figure A.13: Example of FEMM 4.2 Circuit properties

Appendix B

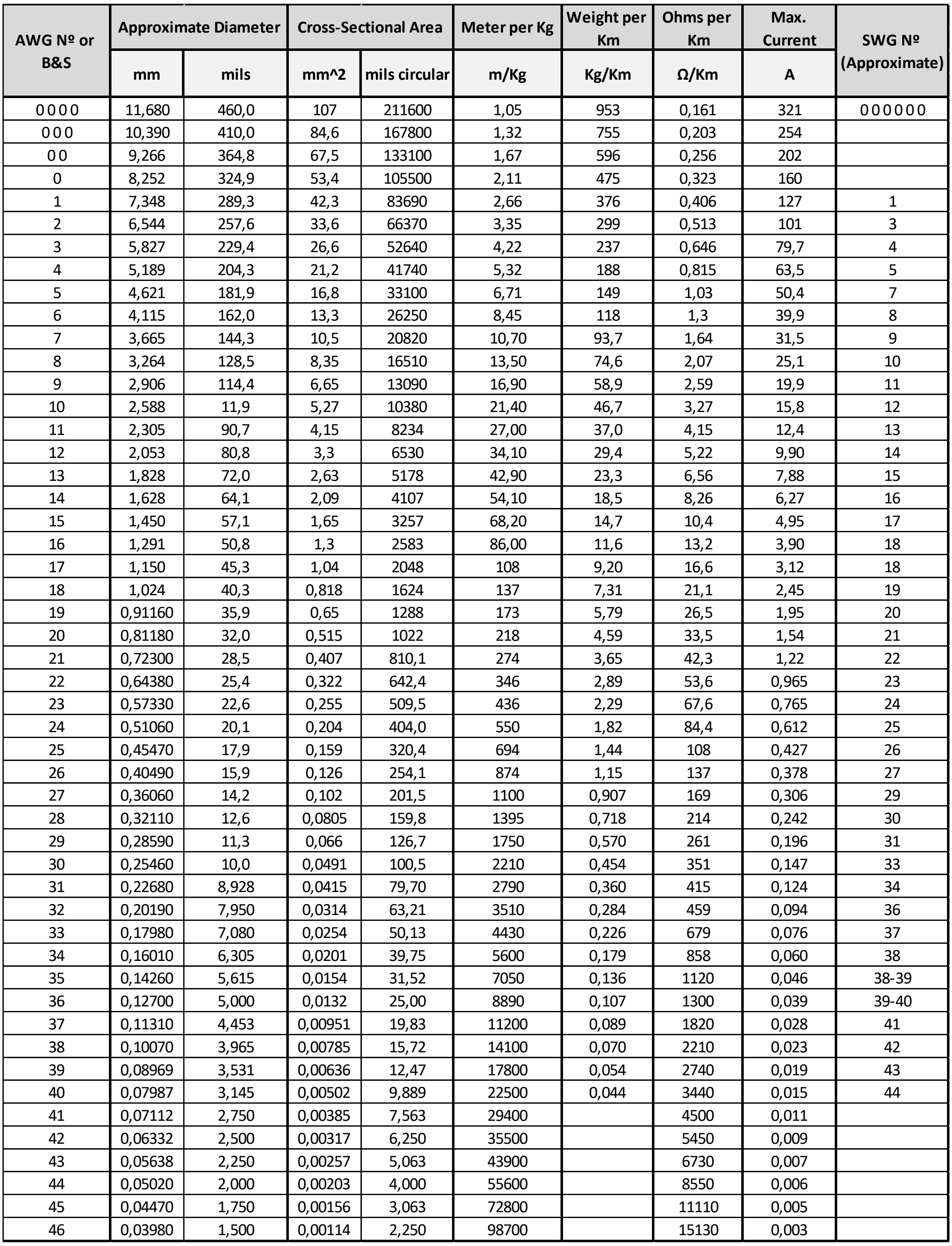

AWG Nº or B&S	Approximate Diameter		Cross-Sectional Area		Meter per Kg	Weight per Km	Ohms per Km	Max. Current	SWG Nº (Approximate)
	mm	mils	mm^2	mils circular	m/Kg	Kg/Km	Ω/Km	A	
0 0 0 0	11,680	460,0	107	211600	1,05	953	0,161	321	0 0 0 0 0 0
0 0 0	10,390	410,0	84,6	167800	1,32	755	0,203	254	
0 0	9,266	364,8	67,5	133100	1,67	596	0,256	202	
0	8,252	324,9	53,4	105500	2,11	475	0,323	160	
1	7,348	289,3	42,3	83690	2,66	376	0,406	127	1
2	6,544	257,6	33,6	66370	3,35	299	0,513	101	3
3	5,827	229,4	26,6	52640	4,22	237	0,646	79,7	4
4	5,189	204,3	21,2	41740	5,32	188	0,815	63,5	5
5	4,621	181,9	16,8	33100	6,71	149	1,03	50,4	7
6	4,115	162,0	13,3	26250	8,45	118	1,3	39,9	8
7	3,665	144,3	10,5	20820	10,70	93,7	1,64	31,5	9
8	3,264	128,5	8,35	16510	13,50	74,6	2,07	25,1	10
9	2,906	114,4	6,65	13090	16,90	58,9	2,59	19,9	11
10	2,588	11,9	5,27	10380	21,40	46,7	3,27	15,8	12
11	2,305	90,7	4,15	8234	27,00	37,0	4,15	12,4	13
12	2,053	80,8	3,3	6530	34,10	29,4	5,22	9,90	14
13	1,828	72,0	2,63	5178	42,90	23,3	6,56	7,88	15
14	1,628	64,1	2,09	4107	54,10	18,5	8,26	6,27	16
15	1,450	57,1	1,65	3257	68,20	14,7	10,4	4,95	17
16	1,291	50,8	1,3	2583	86,00	11,6	13,2	3,90	18
17	1,150	45,3	1,04	2048	108	9,20	16,6	3,12	18
18	1,024	40,3	0,818	1624	137	7,31	21,1	2,45	19
19	0,91160	35,9	0,65	1288	173	5,79	26,5	1,95	20
20	0,81180	32,0	0,515	1022	218	4,59	33,5	1,54	21
21	0,72300	28,5	0,407	810,1	274	3,65	42,3	1,22	22
22	0,64380	25,4	0,322	642,4	346	2,89	53,6	0,965	23
23	0,57330	22,6	0,255	509,5	436	2,29	67,6	0,765	24
24	0,51060	20,1	0,204	404,0	550	1,82	84,4	0,612	25
25	0,45470	17,9	0,159	320,4	694	1,44	108	0,427	26
26	0,40490	15,9	0,126	254,1	874	1,15	137	0,378	27
27	0,36060	14,2	0,102	201,5	1100	0,907	169	0,306	29
28	0,32110	12,6	0,0805	159,8	1395	0,718	214	0,242	30
29	0,28590	11,3	0,066	126,7	1750	0,570	261	0,196	31
30	0,25460	10,0	0,0491	100,5	2210	0,454	351	0,147	33
31	0,22680	8,928	0,0415	79,70	2790	0,360	415	0,124	34
32	0,20190	7,950	0,0314	63,21	3510	0,284	459	0,094	36
33	0,17980	7,080	0,0254	50,13	4430	0,226	679	0,076	37
34	0,16010	6,305	0,0201	39,75	5600	0,179	858	0,060	38
35	0,14260	5,615	0,0154	31,52	7050	0,136	1120	0,046	38-39
36	0,12700	5,000	0,0132	25,00	8890	0,107	1300	0,039	39-40
37	0,11310	4,453	0,00951	19,83	11200	0,089	1820	0,028	41
38	0,10070	3,965	0,00785	15,72	14100	0,070	2210	0,023	42
39	0,08969	3,531	0,00636	12,47	17800	0,054	2740	0,019	43
40	0,07987	3,145	0,00502	9,889	22500	0,044	3440	0,015	44
41	0,07112	2,750	0,00385	7,563	29400		4500	0,011	
42	0,06332	2,500	0,00317	6,250	35500		5450	0,009	
43	0,05638	2,250	0,00257	5,063	43900		6730	0,007	
44	0,05020	2,000	0,00203	4,000	55600		8550	0,006	
45	0,04470	1,750	0,00156	3,063	72800		11110	0,005	
46	0,03980	1,500	0,00114	2,250	98700		15130	0,003	

Figure B.1: AWG global properties.

Appendix C

C.1 Materials Permeability

Soft Magnetic Materials	
Material	Relative Permeability (μ) [H/m]
US Steel Type 2-S 0.018 inch thickness	9400
US Steel Type 2-S 0.024 inch thickness	7400
Carpenter Electrical Iron	2065
Pure Iron	14872
1006 Steel	1404
1010 Steel	902,6
1018 Steel	529
1020 Steel	760
1117 Steel	1777
416 Stainless Steel	440
430 Stainless Steel	409
455 Stainless Steel	470
Silicon Core Iron	7000
M-19 Steel	4416
M-27 Steel	12138
M-36 Steel	1616
M-45 Steel	4689
Hiperco-50	3520
Vanadium Permedur	6856
Supermalloy	529095
Mu Metal	82910

Figure C.1: Soft magnetic materials of FEMM 4.2.

PM Materials	
Material	Relative Permeability (μ) [H/m]
Alnico 5	1,5
Alnico 6	3,3
Alnico 8	6,678
NdFeB 32 MGOe	1,045
NdFeB 37 MGOe	1,048
NdFeB 40 MGOe	1,049
NdFeB 10 MGOe (Bonded)	1,223
Ceramic 5	1,886
Ceramic 8	1,438
SmCo 20 MGOe	1,034
SmCo 24 MGOe	1,110
SmCo 27 MGOe	1,103

Figure C.2: PM Materials of FEMM 4.2.

Appendix D

D.1 Images of Experimental Simulation

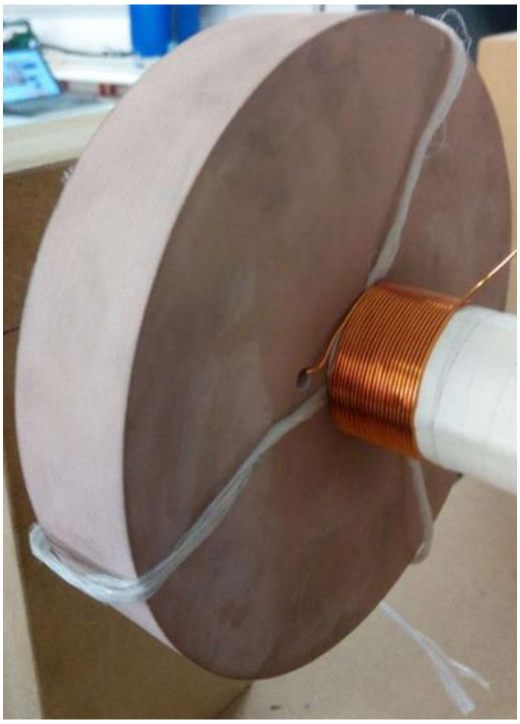

Figure D.1: Winding assistance structure.

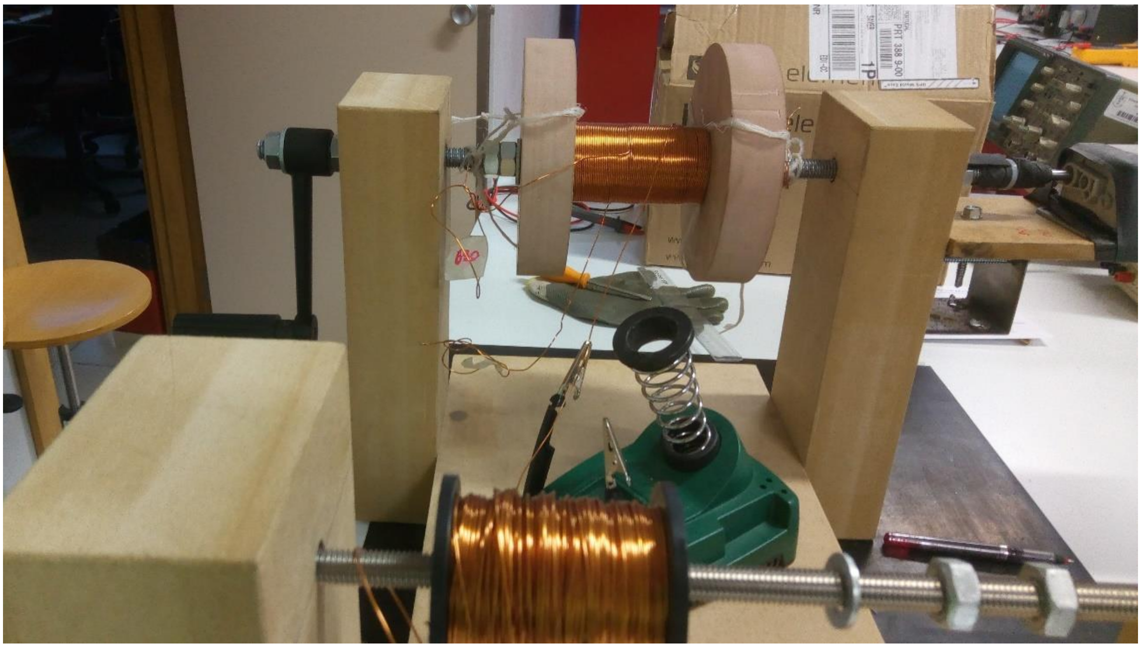

Figure D.2: Schematic of the welding process.

Figure D.3: Magnetic core weighing.

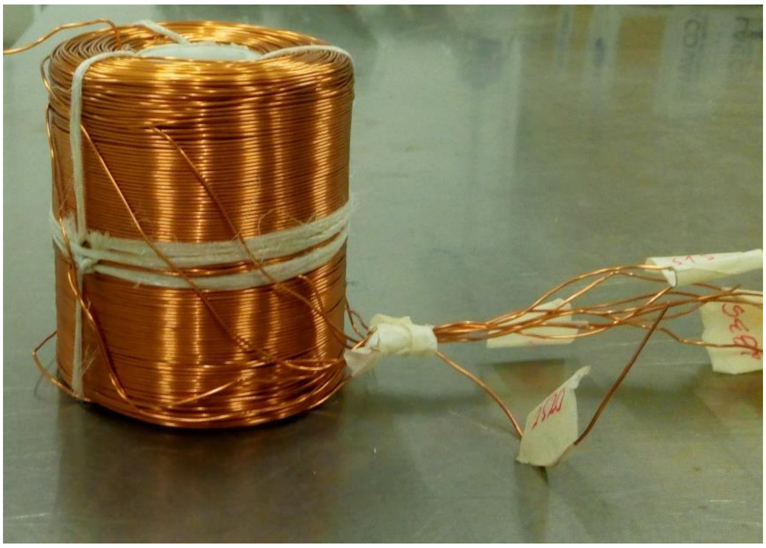

Figure D.4: Experimental EMG winding.

D.2 Experimental Winding Results

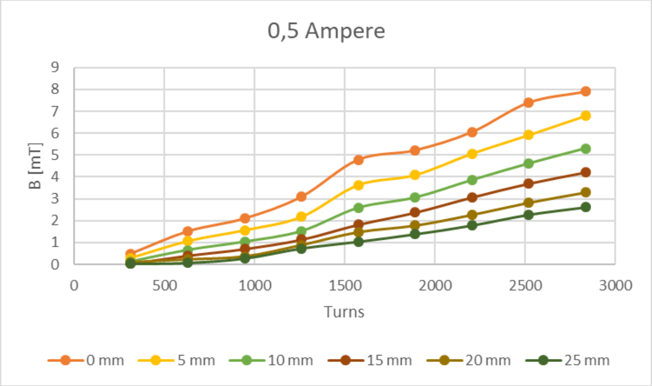

Figure D.5: Results of the magnetic flux density of the EMG winding, with a current of 0.5 A.

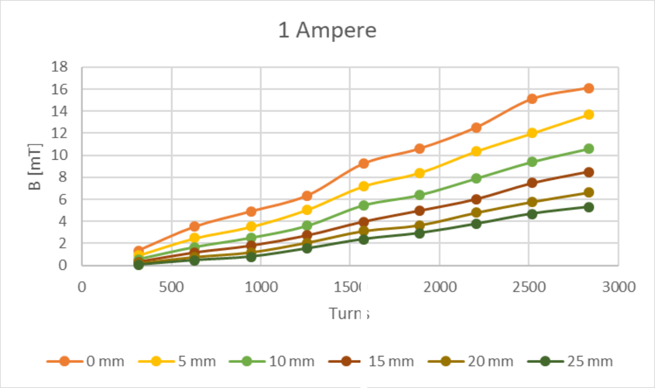

Figure D.6: Results of the magnetic flux density of the EMG winding, with a current of 1 A.

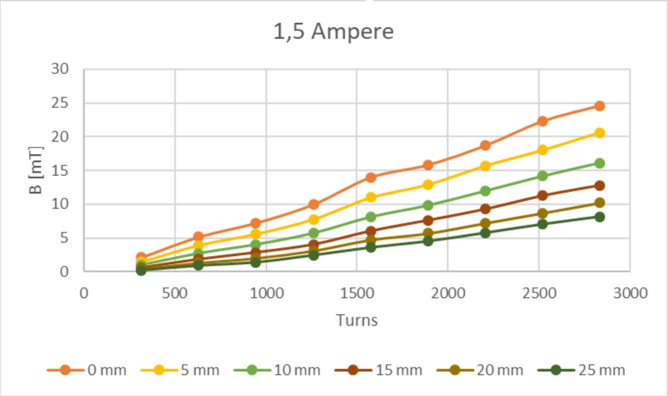

Figure D.7: Results of the magnetic flux density of the EMG winding, with a current of 1.5 A.

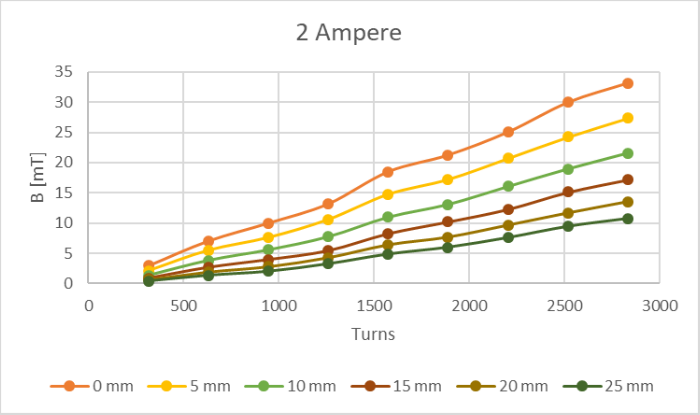

Figure D.8: Results of the magnetic flux density of the EMG winding, with a current of 2 A.

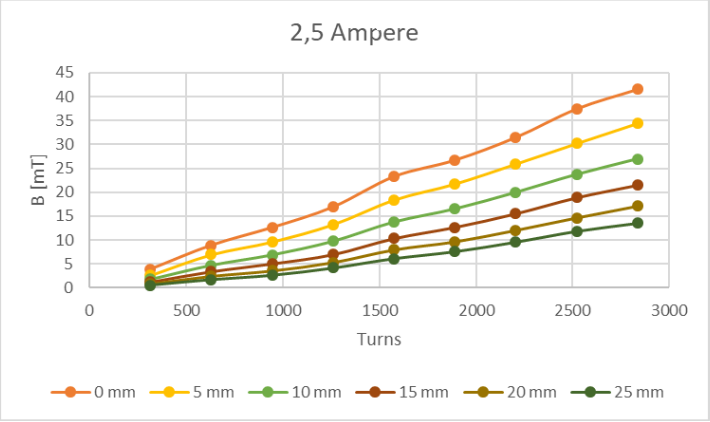

Figure D.9: Results of the magnetic flux density of the EMG winding, with a current of 2.5 A.

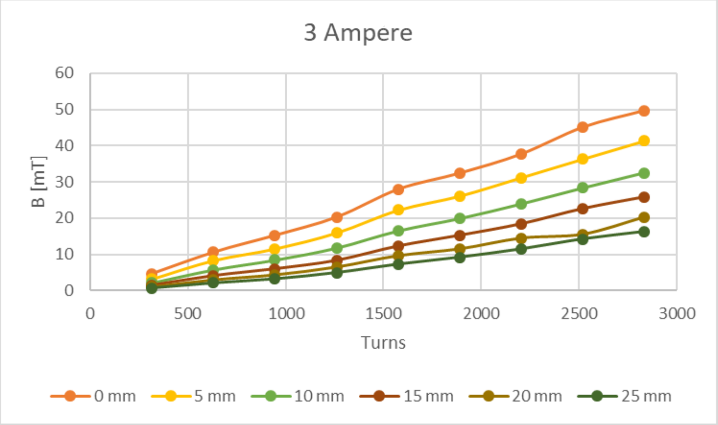

Figure D.10: Results of the magnetic flux density of the EMG winding, with a current of 3 A.

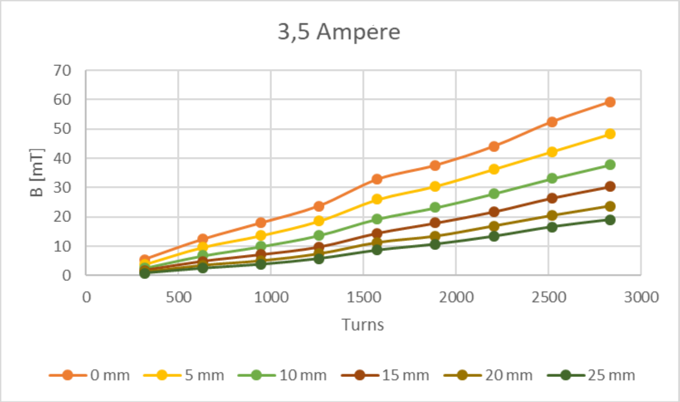

Figure D.11: Results of the magnetic flux density of the EMG winding, with a current of 3.5 A.

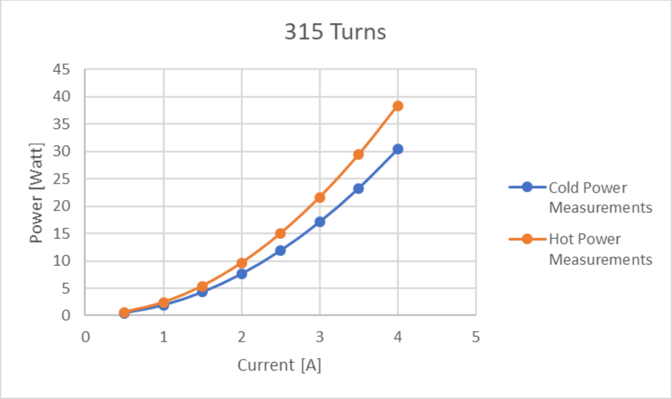

Figure D.12: EMG experimental cold and hot power measurements, with 315 turns.

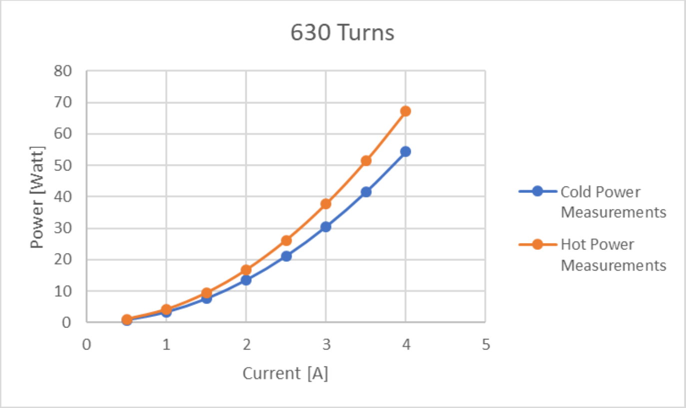

Figure D.13: EMG experimental cold and hot power measurements, with 630 turns.

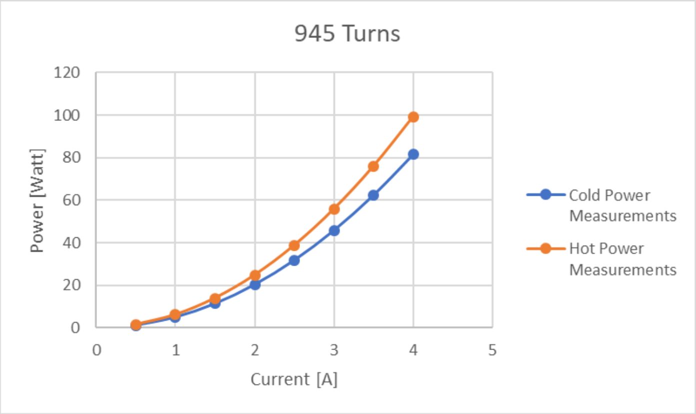

Figure D.14: EMG experimental cold and hot power measurements, with 945 turns.

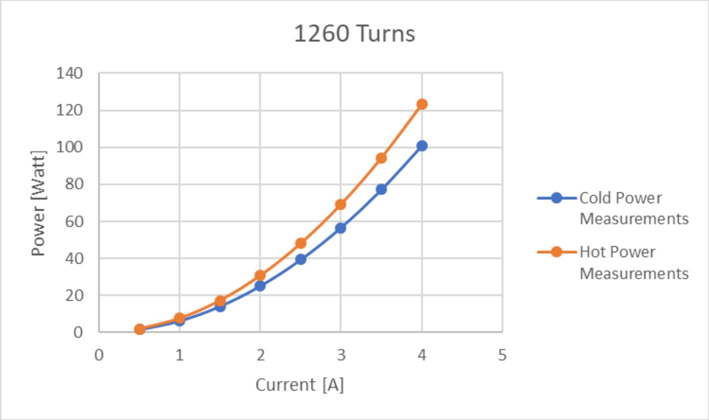

Figure D.15: EMG experimental cold and hot power measurements, with 1260 turns.

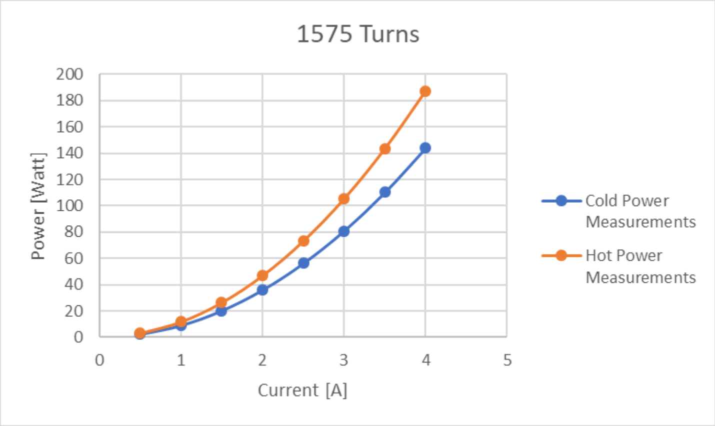

Figure D.16: EMG experimental cold and hot power measurements, with 1575 turns.

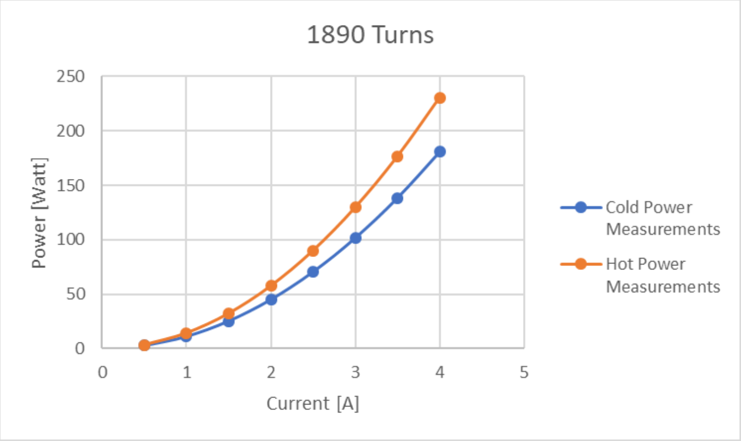

Figure D.17: EMG experimental cold and hot power measurements, with 1890 turns.

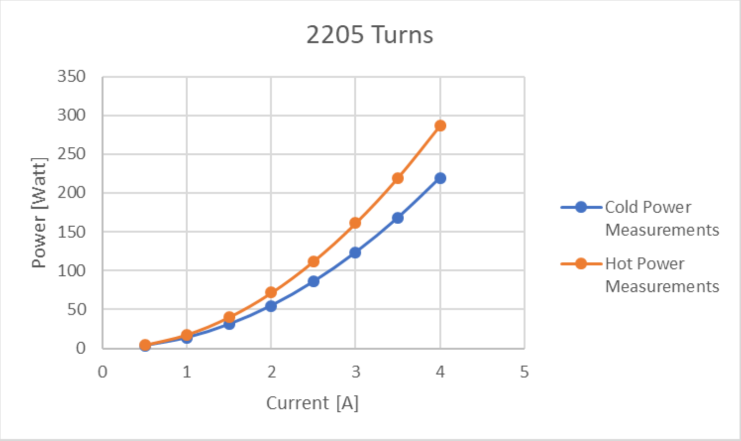

Figure D.18: EMG experimental cold and hot power measurements, with 2205 turns.

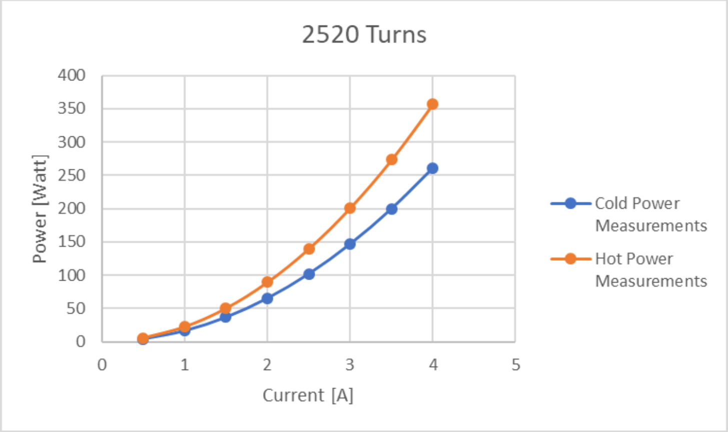

Figure D.19: EMG experimental cold and hot power measurements, with 2520 turns.

Appendix E

E.1 Winding Numerical vs Analytical Results

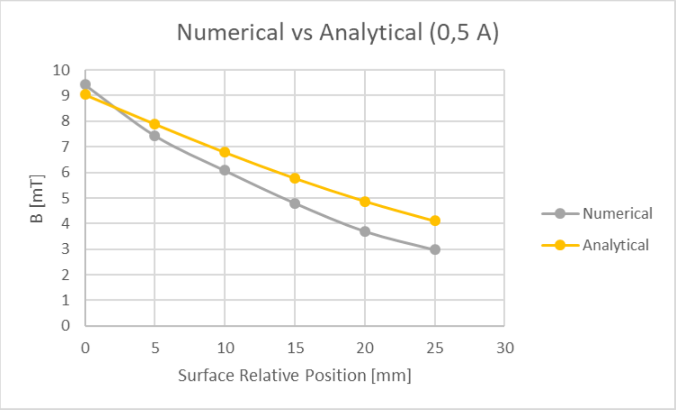

Figure E.1: Comparation between the analytical and numerical magnetic flux density results of the EMG winding, with 0.5 A.

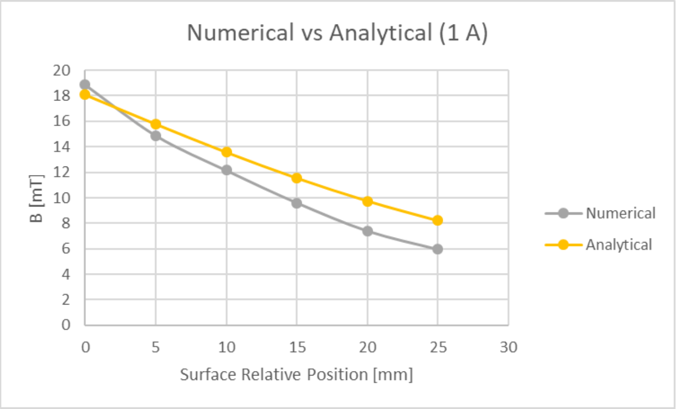

Figure E.2: Comparation between the analytical and numerical magnetic flux density results of the EMG winding, with 1 A.

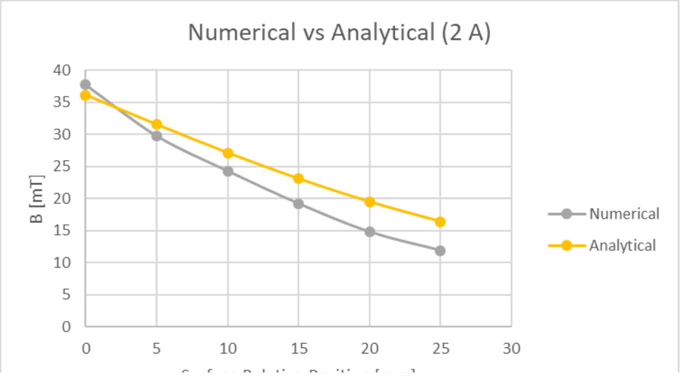

Figure E.3: Comparation between the analytical and numerical magnetic flux density results of the EMG winding, with 2 A.

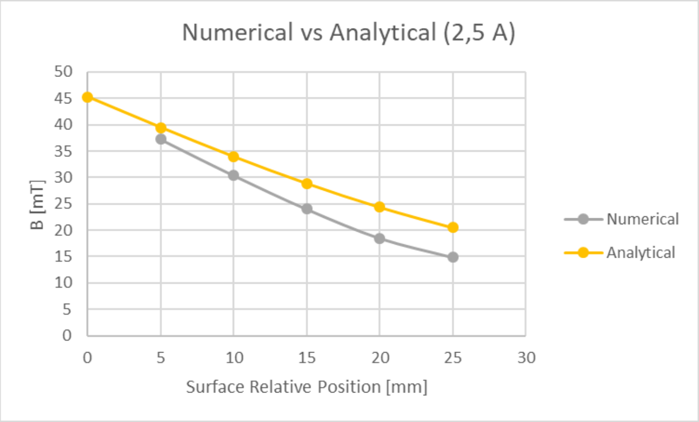

Figure E.4: Comparation between the analytical and numerical magnetic flux density results of the EMG winding, with 2.5 A.

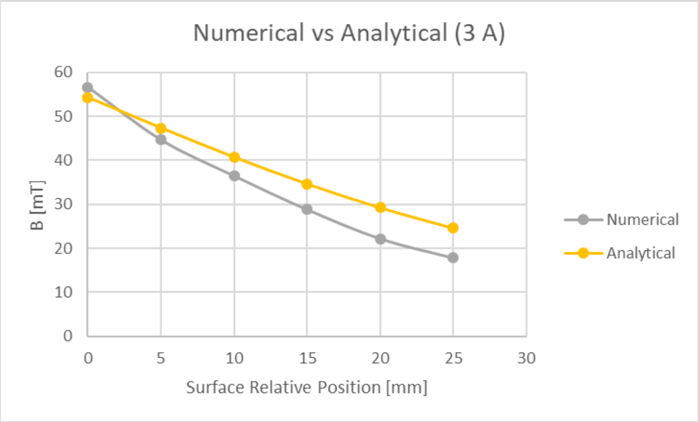

Figure E.5: Comparation between the analytical and numerical magnetic flux density results of the EMG winding, with 3 A.

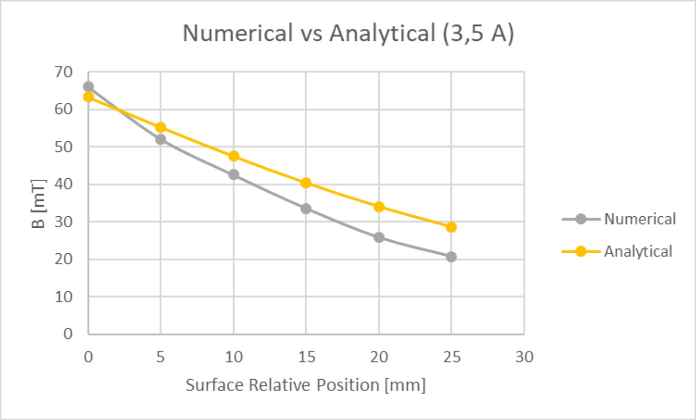

Figure E.6: Comparation between the analytical and numerical magnetic flux density results of the EMG winding, with 3.5 A.

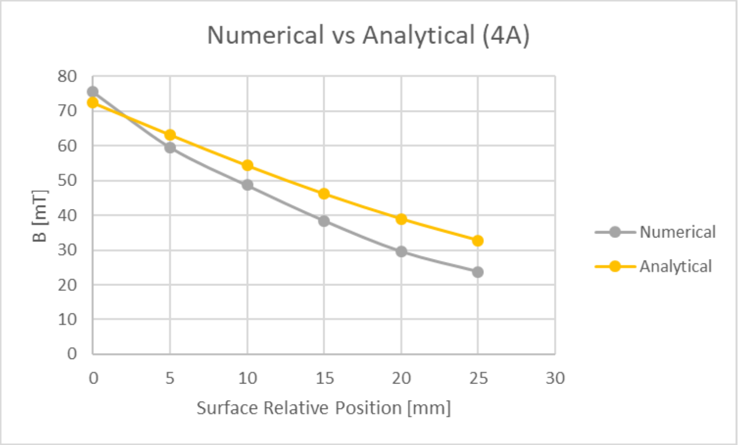

Figure E.7: Comparation between the analytical and numerical magnetic flux density results of the EMG winding, with 4 A.

E.2 Winding Numerical vs Experimental Results

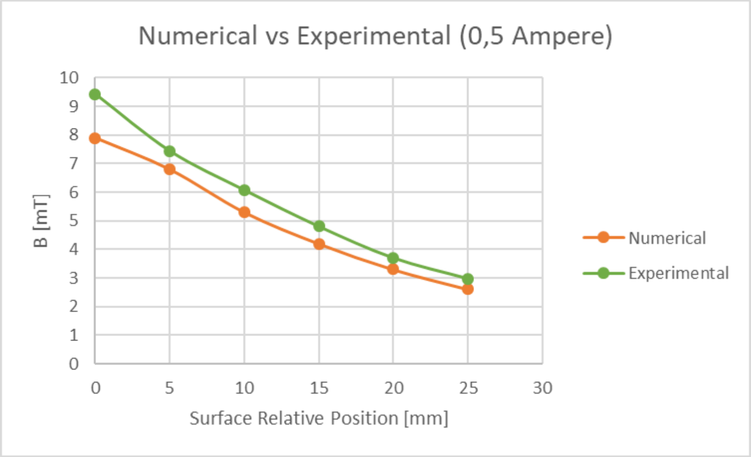

Figure E.8: Comparation between the numerical and experimental results of the EMG winding, with 0.5 A.

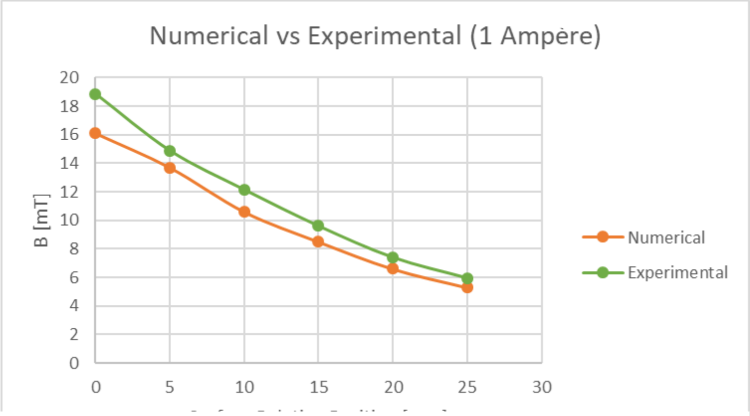

Figure E.9: Comparation between the numerical and experimental results of the EMG winding, with 1 A.

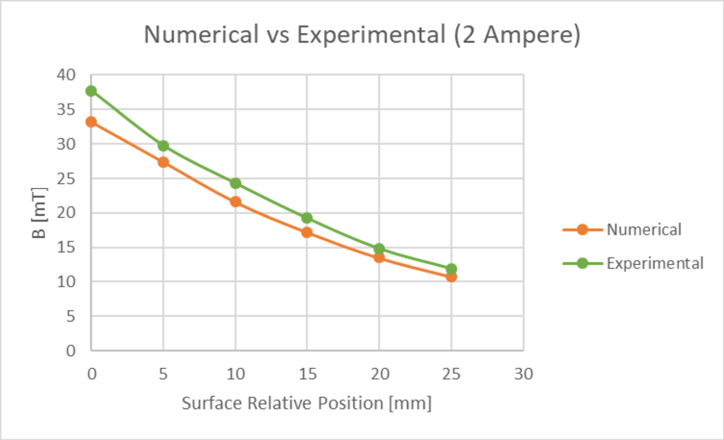

Figure E.10: Comparation between the numerical and experimental results of the EMG winding, with 2 A.

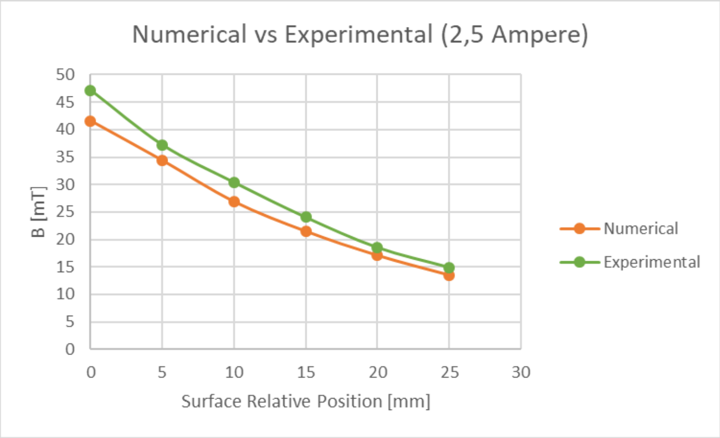

Figure E.11: Comparation between the numerical and experimental results of the EMG winding, with 2.5 A.

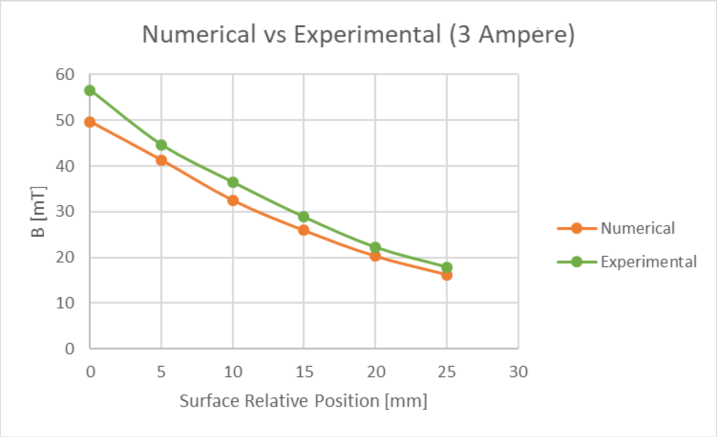

Figure E.12: Comparation between the numerical and experimental results of the EMG winding, with 3 A.

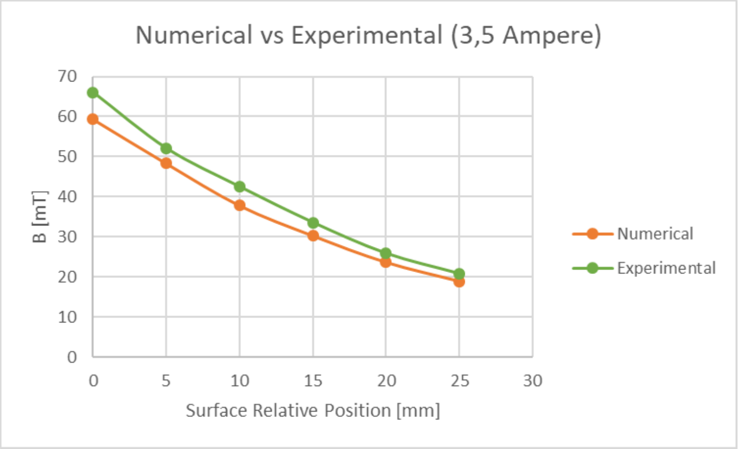

Figure E.13: Comparation between the numerical and experimental results of the EMG winding, with 3.5 A.

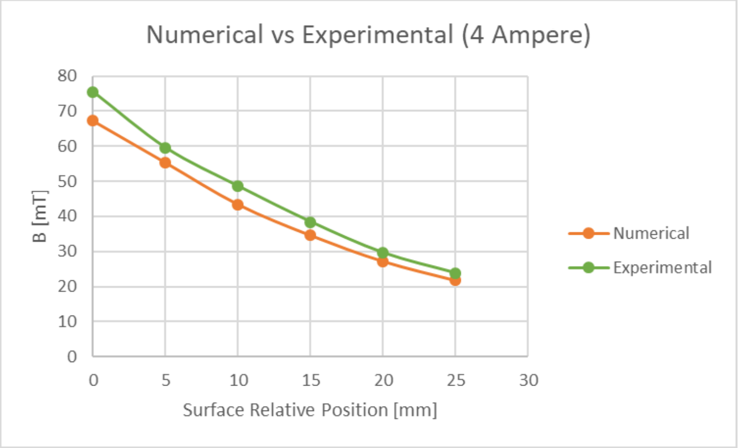

Figure E.14: Comparation between the numerical and experimental results of the EMG winding, with 4 A.

E.3 Winding Analytical vs Numerical vs Experimental Results

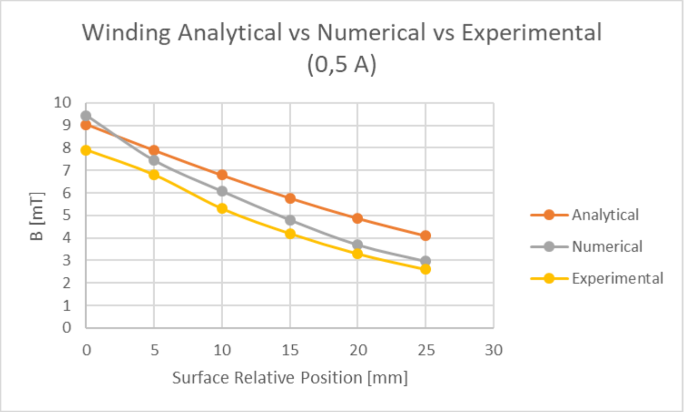

Figure E.15: Comparation between analytical, numerical and experimental results of the EMG winding, with 0.5 A.

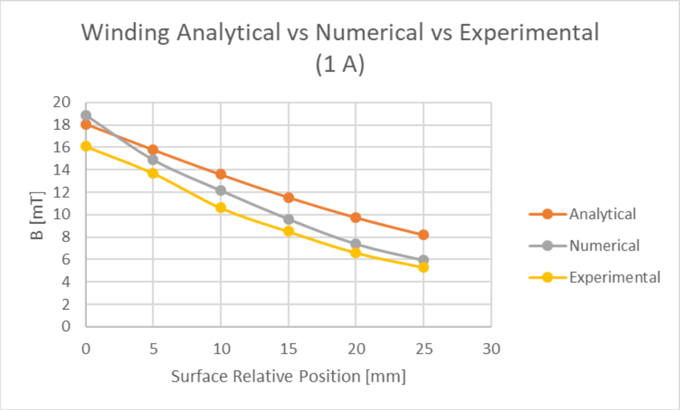

Figure E.16: Comparation between analytical, numerical and experimental results of the EMG winding, with 1 A.

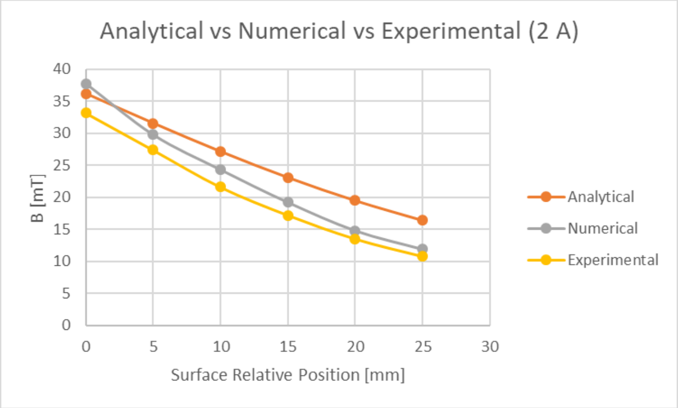

Figure E.17: Comparation between analytical, numerical and experimental results of the EMG winding, with 2 A.

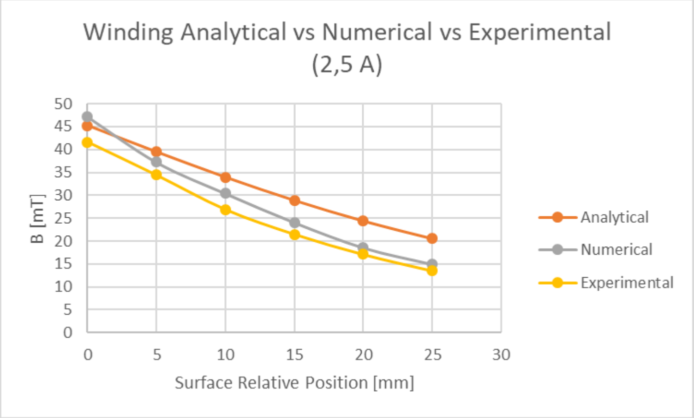

Figure E.18: Comparation between analytical, numerical and experimental results of the EMG winding, with 2.5 A.

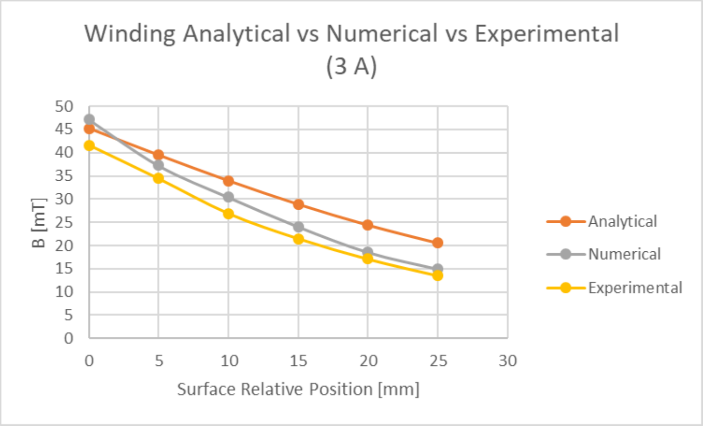

Figure E.19: Comparation between analytical, numerical and experimental results of the EMG winding, with 3 A.

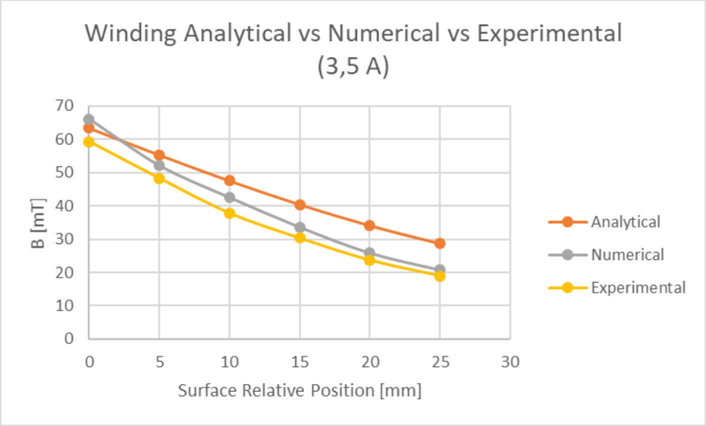

Figure E.20: Comparation between analytical, numerical and experimental results of the EMG winding, with 3.5 A.

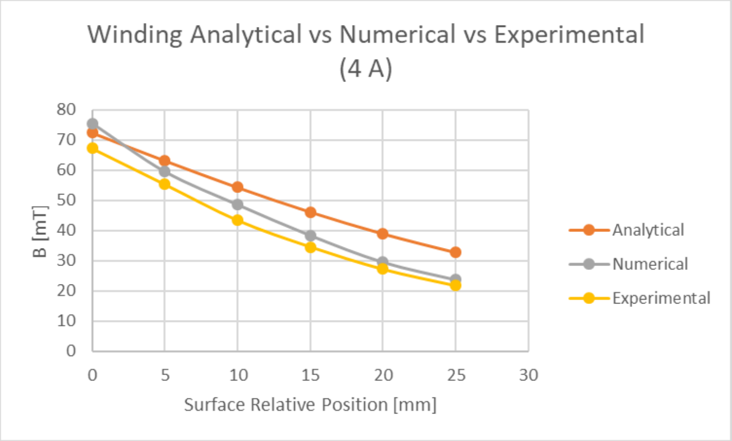

Figure E.21: Comparation between analytical, numerical and experimental results of the EMG winding, with 4 A.

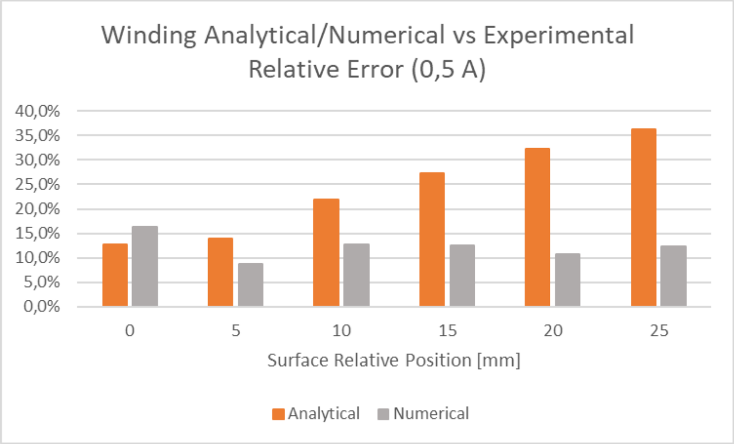

Figure E.22: Comparation between analytical and numerical EMG winding relative ERROR, considering 0.5 A.

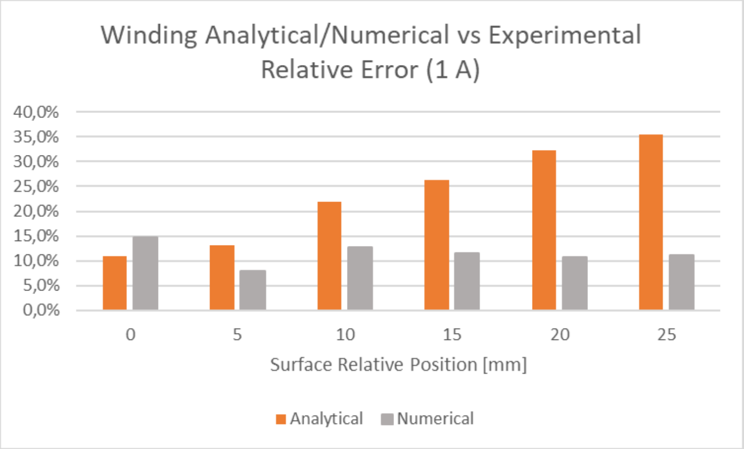

Figure E.23: Comparation between analytical and numerical EMG winding relative ERROR, considering 1 A.

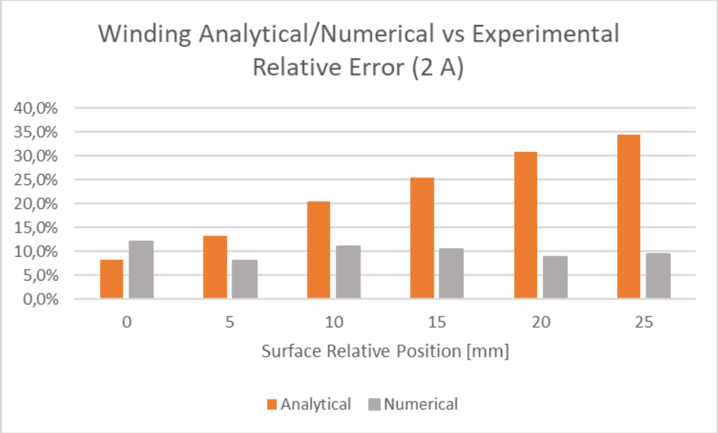

Figure E.24: Comparation between analytical and numerical EMG winding relative ERROR, considering 2 A.

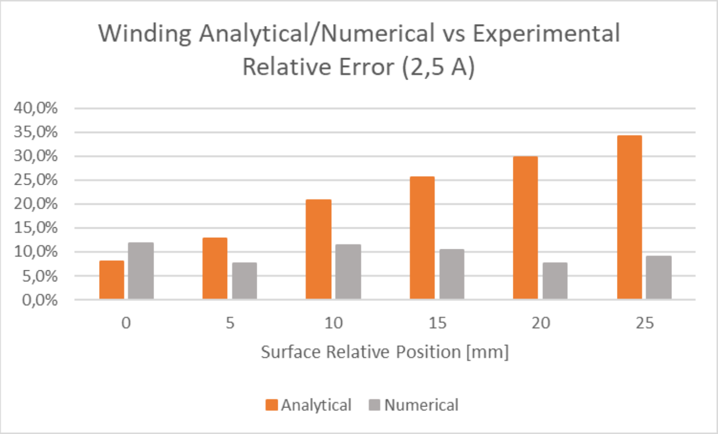

Figure E.25: Comparation between analytical and numerical EMG winding relative ERROR, considering 2.5 A.

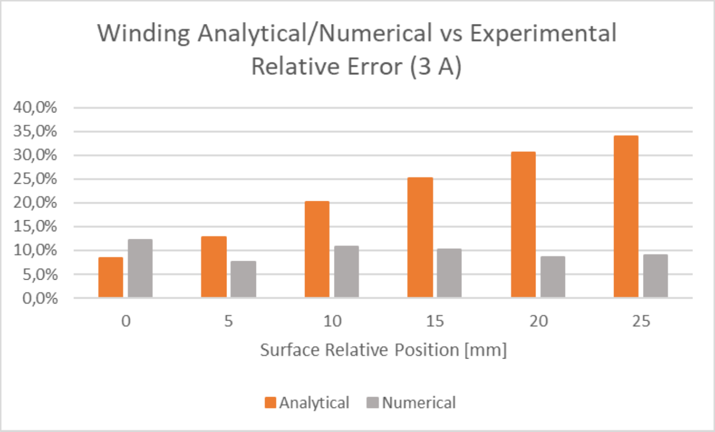

Figure E.26: Comparation between analytical and numerical EMG winding relative ERROR, considering 3 A.

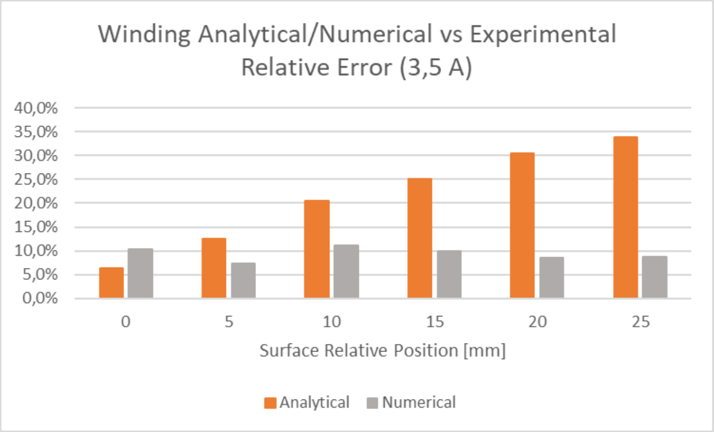

Figure E.27: Comparation between analytical and numerical EMG winding relative ERROR, considering 3.5 A.

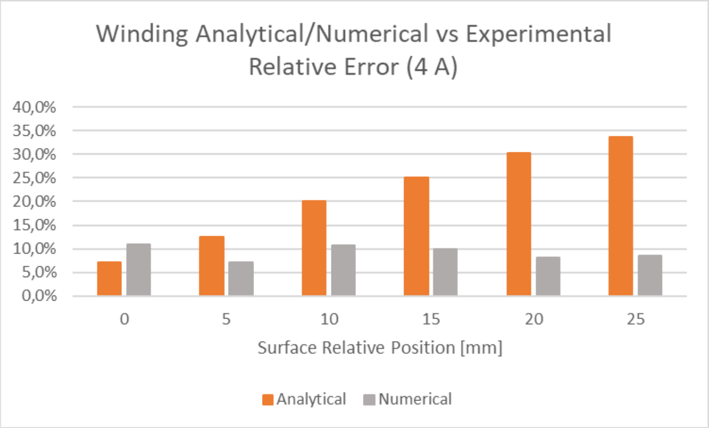

Figure E.28: Comparation between analytical and numerical EMG winding relative ERROR, considering 4 A.

E.4 EMG (with magnetic core) Numerical and Experimental Results

Experimental Measurements B [mT]									
	Nº of Turns	Current [A]							
		0,5	1	1,5	2	2,5	3	3,5	4
25 mm	315	1,35	2,34	3,26	4,18	5,08	5,98	6,91	7,98
	630	2,47	4,46	6,53	8,65	10,73	12,76	14,88	16,83
	945	3,45	6,43	9,54	12,51	15,56	18,54	21,47	24,28
	1260	4,22	7,92	11,97	15,69	19,33	23,21	26,85	30,4
	1575	5,79	10,78	16,04	21,21	26,37	31,5	36,4	41,4
	1890	6,48	12,78	19,09	25,33	31,4	37,2	43,1	48,6
	2205	7,67	14,83	22,27	29,58	36,4	43,5	50,1	56,5
	2520	8,89	17,35	25,69	34,1	42,1	50,2	58,1	65,5
	2835	10,2	20,2	29,7	39,3	48,7	57,8	66,5	74,5

Figure E.29: Experimental magnetic flux density data of EMG with magnetic core at 25 mm.

A FEMM 4.2

FEMM 4.2 Simulation B [mT]									
	Nº of Turns	Current							
		0,5	1	1,5	2	2,5	3	3,5	4
25 mm	315	1,24252	2,48503	3,72755	4,97007	6,21258	7,4551	8,69761	9,94012
	630	2,48503	4,97007	7,4551	9,94012	12,4251	14,9102	17,3952	19,8802
	945	3,72755	7,4551	11,1826	14,9102	18,6377	22,3652	26,0926	29,82
	1260	4,97007	9,94012	14,9102	19,8802	24,8501	29,82	34,7896	39,7586
	1575	6,21258	12,4251	18,6377	24,8501	31,0625	37,2741	43,4854	49,6974
	1890	7,4551	14,9102	22,3652	29,82	37,2741	44,7277	52,1817	59,6251
	2205	8,69761	17,3952	26,0926	34,7896	43,4854	52,1817	60,863	69,4822
	2520	9,94012	19,8802	29,82	39,7586	49,6974	59,6251	69,4822	79,0879
	2835	11,1826	22,3652	33,5472	44,7277	55,9059	67,0301	77,9136	88,0678

Figure E.30: FEMM 4.2 numerical magnetic flux density data of the EMG with magnetic core at 25 mm

Numerical vs Experimental Relative ERROR %									
Surface Relative Position [mm]	Current [A]								Position Relative ERROR Average
	0,5	1	1,5	2	2,5	3	3,5	4	
315	8,7%	5,8%	12,5%	15,9%	18,2%	19,8%	20,6%	19,7%	15,2%
630	0,6%	10,3%	12,4%	13,0%	13,6%	14,4%	14,5%	15,3%	11,8%
945	7,4%	13,8%	14,7%	16,1%	16,5%	17,1%	17,7%	18,6%	15,2%
1260	15,1%	20,3%	19,7%	21,1%	22,2%	22,2%	22,8%	23,5%	20,9%
1575	6,8%	13,2%	13,9%	14,6%	15,1%	15,5%	16,3%	16,7%	14,0%
1890	13,1%	14,3%	14,6%	15,1%	15,8%	16,8%	17,4%	18,5%	15,7%
2205	11,8%	14,7%	14,7%	15,0%	16,3%	16,6%	17,7%	18,7%	15,7%
2520	10,6%	12,7%	13,8%	14,2%	15,3%	15,8%	16,4%	17,2%	14,5%
2835	8,8%	9,7%	11,5%	12,1%	12,9%	13,8%	14,6%	15,4%	12,3%
Current Relative ERROR Average	9,2%	12,8%	14,2%	15,2%	16,2%	16,9%	17,6%	18,2%	15,031%

Figure E.31: Numerical vs Experimental relative ERROR of EMG with magnetic core at 25 mm.

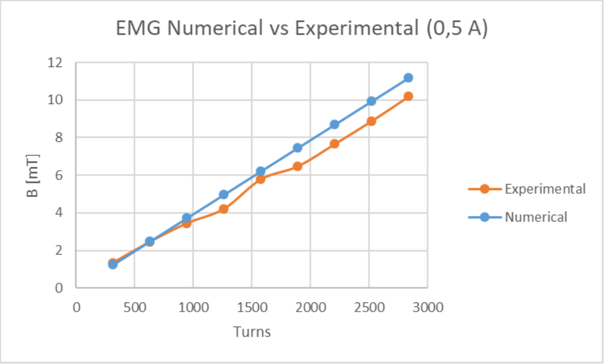

Figure E.32: Comparation between numerical and experimental magnetic flux density results of the EMG model

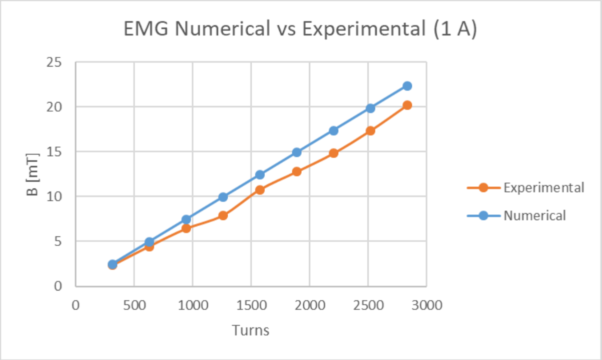

Figure E.33: Comparation between numerical and experimental magnetic flux density results of the EMG model (with magnetic core),

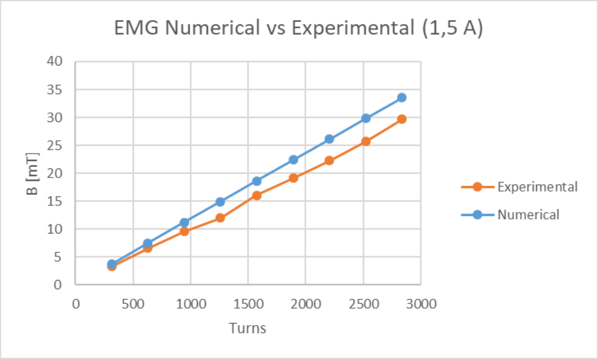

Figure E.34: Comparation between numerical and experimental magnetic flux density results of the EMG model (with magnetic

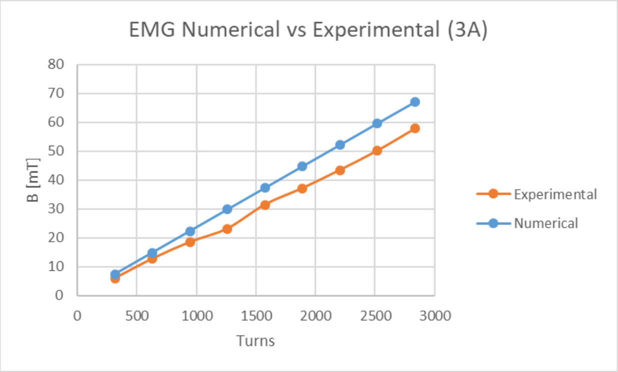

Figure E.35: Comparation between numerical and experimental magnetic flux density results of the EMG model (with magnetic

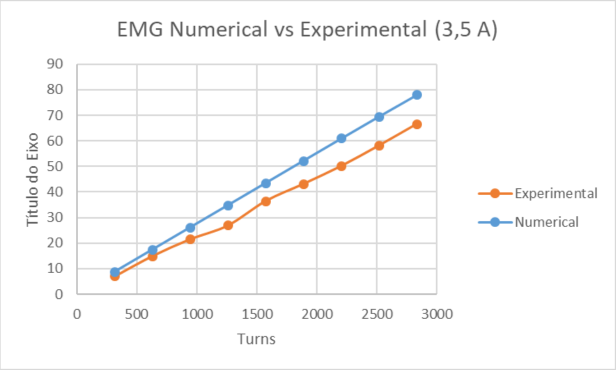

Figure E.36: Comparation between numerical and experimental magnetic flux density results of the EMG model (with magnetic

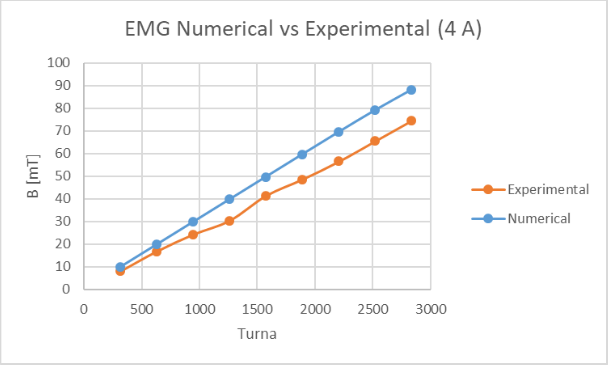

Figure E.37: Comparation between numerical and experimental magnetic flux density results of the EMG model (with magnetic